Luís de Souto Martins

Mestre em Engenharia Física

X-ray fluorescence analysis using a standardless method

Dissertação para obtenção do Grau de Doutor em

Engenharia Física

Orientador:	José Paulo Santos, Professor Catedrático, FCT-UNL
Co-orientadora:	Maria Luísa Carvalho, Professora Catedrática, FCT-UNL

Júri

Presidente:	Professora Maria Adelaide de Almeida Pedro de Jesus
Arguentes:	Professor Luís Filipe dos Santos Garcia Peralta
	Professor José Manuel Pires Marques
Vogais:	Professora Alda Sofia Pessanha de Sousa Moreno
	Professor Luís Manuel Cerqueira Lopes Alves
	Professor José Paulo Moreira dos Santos

FACULDADE DE CIÊNCIAS E TECNOLOGIA
UNIVERSIDADE NOVA DE LISBOA

Dezembro, 2019

Luís de Souto Martins

Mestre em Engenharia Física

X-ray fluorescence analysis using a standardless method

Dissertação para obtenção do Grau de Doutor em

Engenharia Física

Orientador:	José Paulo Santos, Professor Catedrático, FCT-UNL
Co-orientadora:	Maria Luísa Carvalho, Professora Catedrática, FCT-UNL

Júri

Presidente:	Professora Maria Adelaide de Almeida Pedro de Jesus
Arguentes:	Professor Luís Filipe dos Santos Garcia Peralta
	Professor José Manuel Pires Marques
Vogais:	Professora Alda Sofia Pessanha de Sousa Moreno
	Professor Luís Manuel Cerqueira Lopes Alves
	Professor José Paulo Moreira dos Santos

FACULDADE DE CIÊNCIAS E TECNOLOGIA
UNIVERSIDADE NOVA DE LISBOA

Dezembro, 2019

X-ray fluorescence analysis using a standardless method

To my family

Acknowledgements

First and foremost, I express my deepest gratitude to my supervisor Professor José Paulo Santos for his supervision, for his sharing of knowledge and scientific guidance, and for providing me with great working conditions, all of which I consider to have been essential in my growth as a scientist. Furthermore, I am also thankful to professor José Paulo Santos for the opportunities, advices, and knowledge he presented me, both inside and outside of the scientific scope, which allowed me to grow at a professional and personal level. I also express my deepest gratitude to my co-supervisor, Professora Maria Luísa Carvalho, for the essential guidance, support, and availability throughout the duration of my work, and specially by the sharing of her deep expertise of the experimental aspects of EDXRF technique, which were pivotal in this work.

I acknowledge the support of the Portuguese Foundation for Science and Technology (FCT) with the PhD grant PD/BD/105919/2014.

To all my colleagues, I am incredibly grateful for the constant and unwavering support they gave me, sharing with me their expertise and advices whenever, and for whatever, was need. Moreover, they provided me an extremely positive and productive work environment, as well as a caring and friendly out of office environment. To Sofia Pessanha I am particularly thankful for the sharing of expertise in the experimental aspects of EDXRF technique, as well as her experimental work with standard samples, which was an essential contribution for the present work. I express my gratitude to Jorge Machado and Mauro Guerra, which constantly shared their knowledge with me, having been vital in my handling of Geant4 and my understanding of atomic structure calculations, and contributing to my knowledge in other areas. To Patrícia Carvalho, besides being grateful for the sharing of knowledge, I am greatly thankful for her support through incessant encouragement, cheerfulness, and friendship. I am specially grateful to Pedro Amaro for his great dedication in closely following the development of my work, while sharing with me his knowledge, advices, and insight, which were highly helpful in all the different phases of my work. I am also thankful to my colleagues Micaela Fonseca, Pedro Cardoso, and David Fernandes. To Luíza Oliveira and Filipa Reis I express my gratitude for the support in all bureaucratic subjects as well as other subjects, and furthermore, for their constant cheerfulness.

To all my friends, I am thankful for the ongoing support and friendship. And above all, to my family, for always supporting me in all that I needed, my CatCat, my brother Jorge

Martins, my sister Ana Martins, my father Gaspar Martins, my mother Cristina Sebastião, Ana Rovisco, Victor Rodrigues, Maria "Miucha" Madalena, and Maria Madalena, my deepest gratitude for all the support, patience, and encouragement.

Abstract

Energy Dispersive X-ray Fluorescence spectrometry (EDXRF) is a non-destructive analytical technique that allows multi-element analysis of a large variety of materials in a relatively fast and simple way, and is used in a broad range of areas. This technique resorts to calibrated standard samples for each type of sample to be analysed, as well as the knowledge of Fundamental Parameters (FP). The use of standards have several drawbacks to consider such as the unavailability of standards for certain types of materials, the associated monetary costs, and inaccuracy of the standard's measurements. On the other hand, the inaccuracy of Fundamental Parameters limits the accuracy of the quantification. Furthermore, FP used by quantification software are included in built-in tabulation inaccessible to the user.

EDXRF spectrometers employed in triaxial geometry allow the experimental measurement of the Rayleigh-to-Compton scattering intensity ratio. The measurement of these ratios of standard samples permits a method for determination of the average atomic number Z_{avg} of unknown samples. In this work, using the Geant4 toolkit, a code is implemented to simulate the X-ray spectrum obtained from employing a triaxial geometry spectrometer, aiming for both elemental quantification from the characteristic peaks and the determination of Compton-to-Rayleigh scattering ratio. Simulation results are compared with experimental measurements of standard reference materials, showing a good agreement for the simulated peak intensities, as well as for the simulated scattering ratios. Zn K-shell FP are calculated using the multiconfiguration Dirac-Fock approach, presenting good agreement when comparing with the available values in literature. A comparison of K-shell fluorescence yield and partial fluorescence yield values is presented, regarding different references from which a comprehensive set of values can be used for atomic relaxation libraries. These comparisons point that further studies should be employed before changing Geant4 library for atomic relaxation.

Keywords: EDXRF, Monte Carlo, Atomic relaxation, Fundamental Parameters

Resumo

A espectroscopia de fluorescência de raios-X dispersiva em energia (EDXRF) é uma técnica analítica não-destrutiva que permite a análise multi-elementar de uma grande variedade de materiais de uma forma relativamente rápida e simples, e é utilizada numa ampla gama de áreas. Esta técnica recorre a padrões calibrados para cada tipo de material a analisar, assim como ao conhecimento de Parâmetros Fundamentais (PF). O uso de padrões tem várias desvantagens a considerar, como a indisponibilidade de padrões para certos tipos de materiais, os custos monetários associados, e a imprecisão das medidas dos padrões. Por outro lado, a imprecisão dos Parâmetros Fundamentais limita a precisão da quantificação. Além disso, os PF utilizados por software são incluídos em tabulações embutidas e inacessíveis ao utilizador. Os espectrómetros EDXRF utilizados em geometria triaxial permitem a medição experimental da razão da intensidade da dispersão Rayleigh-para-Compton. A medição destas razões permite um método para determinar o número atómico médio Z_{med} de amostras desconhecidas. Neste trabalho, utilizando o pacote de ferramentas Geant4, é implementado um código para simular o espectro de raios-X obtido por um espectrómetro em geometria triaxial, visando tanto a quantificação elemental através dos picos característicos, como a determinação do razão da intensidade Rayleigh-para-Compton. Os resultados das simulações são comparados com medidas experimentais para padrões, apresentando boa concordância tanto nas intensidades dos picos, assim nas razões de dispersão simuladas. São calculados PF para a camada-K do Zn utilizando a abordagem de multiconfigurações Dirac-Fock, apresentando boa concordância com os valores disponíveis na literatura. É apresentada uma comparação de rendimentos de fluorescência parciais e totais da camada-K, relativos a várias referências de onde conjuntos abrangentes de valores podem ser utilizados para bibliotecas para desexcitação atómica. Estas comparações reforçam que mais estudos deverão ser efetuados antes de mudar a biblioteca de desexcitação atómica do Geant4.

Palavras-chave: EDXRF, Monte Carlo, Desexcitação Atómica, Parâmetros Fundamentais

Contents

1 Introduction **1**

1.1 State of the art 1

1.2 Goals and Outline 4

2 Theoretical Background of EDXRF **7**

2.1 Physical processes in X-ray fluorescence technique 7

2.1.1 Photoelectric effect 7

2.1.2 Atomic relaxation 8

2.1.3 Rayleigh Scattering 13

2.1.4 Compton Scattering 14

2.1.5 Polarization in Compton and Rayleigh scattering 17

2.1.6 X-ray attenuation 19

2.1.7 Bremstrahlung emission 20

2.1.8 Electron impact ionization 20

3 EDXRF technique and analysis **21**

3.1 Experimental setup 22

3.1.1 Primary beam creation 22

3.1.2 Beam Collimation 24

3.1.3 X-ray Detection 25

3.2 X-ray spectrum 27

3.2.1 Characteristic peaks 28

3.2.2 Artifact features 28

3.2.3 Background 29

3.2.4 Coherent peak 29

3.2.5 Incoherent feature 29

3.2.6 Spectrum analysis 30

3.2.7 Methods for elemental quantification 31

3.2.8 Detection Limits, Precision and Accuracy 37

3.2.9 Triaxial Geometry 38

3.2.10 Analysis using the Coherent and Incoherent scattering features . . 40

4 Code for EDXRF standardless analysis **43**

4.1 Monte Carlo simulations . . . 43
4.2 A standardless XRF method using Geant4 . . . 44
4.2.1 Geant4 . . . 45
4.2.2 Validations of Geant4 physics processes implementation . . . 46
4.3 Experimental Setup . . . 49
4.4 Codes for simulation . . . 51
4.5 Basic code implementation . . . 56
4.5.1 First simulation . . . 56
4.5.2 Second simulation . . . 57
4.5.3 Simulation results . . . 58
4.6 Advanced code implementation . . . 63
4.6.1 First simulation . . . 63
4.6.2 Second simulation . . . 64
4.6.3 Simulation results . . . 66

5 Fundamental Parameters calculation 71
5.1 Theoretical background of atomic structure calculations . . . 71
5.2 Multiconfiguration Dirac-Fock calculations . . . 75
5.3 Calculation results . . . 76

6 Fundamental Parameters comparison 85
6.1 Overview of atomic parameters from different works . . . 86
6.1.1 Combination of Kostroun *et al.* Hartree-Slater radiationless transition probability calculations and Scofield's Dirac-Slater radiative transition probability calculations . . . 87
6.1.2 Scofield's radiative transition probability calculations based on the Dirac-Slater method . . . 87
6.1.3 Scofield's radiative transition probability calculations based on the Dirac-Fock method . . . 87
6.1.4 Chen *et al.* radiationless transition probability calculations based on the Dirac-Fock method . . . 88
6.1.5 EADL . . . 88
6.1.6 Salem *et al.* experimental K- and L-shell X-ray transition ratios . . . 88
6.1.7 Bambynek *et al* 1972 semi-empirical fittings to experimental data 89
6.1.8 Krause's 1979 compilation . . . 89
6.1.9 Bambynek *et al* 1984 semi-empirical fittings of experimental data 89
6.1.10 Hubbell *et al.* 1994 semi-empirical fittings of experimental data . 90
6.1.11 NIST Fundamental Parameters Database . . . 90
6.1.12 Combination of Chen *et al.* Dirac Fock transition probabilities and Scofield's Dirac-Slater transition probabilities . . . 90

6.1.13 Combination of Chen *et al.* Dirac Fock transition probabilities and Scofield's Dirac-Fock transition probabilities 91
6.1.14 Multiconfiguration Dirac-Fock values 92
6.1.15 Kahoul *et al.* 2012 empirical fittings 92
6.1.16 Daoudi *et al.* 2015 empirical fittings 93
6.1.17 Combination of semi-empirical or empirical K-shell fluorescence yield values with Salem *et al.* values 93
6.2 Comparison of values from the different works 94
6.2.1 K-shell Fluorescence Yield Comparison 94
6.2.2 K-L_2 and K-L_3 partial fluorescence yield comparison 99
6.2.3 K-M_2 and K-M_3 fluorescence yield comparison 102
6.3 Discussion 105

7 Conclusions **109**

Bibliography **113**

Appendices **133**

A Appendix **133**
A.1 MCDF transition probability calculations 133

B Appendix **137**
B.1 Fluorescence yield and partial fluorescence yield values 137

List of Figures

1.1 Setup CFAUL-eclipse II, in situ, at Museu Nacional de Arte Antiga, Portugal. Figure adopted from Pessanha work [1]. 2

2.1 Photoelectric cross-section, for Ag, as function of incident photon energy. Total cross-section and sub-shell cross-sections are represented. Figure adopted from [39].) 8
2.2 Radiative transition representation and nomenclature. Figure adapted from [41]. 10
2.3 Schematic representation of atomic relaxation cascade. In this example a vacancy in the K-shell is filled through the K-L_2 transition, leaving a vacancy in the L_2 sub-shell. The vacancy in the L_2 sub-shell is subsequently filled through the L-N_2 transition, leaving a vacancy in the N_2 sub-shell. Since N_2 is the valence sub-shell, the atomic system is in a de-excited state and the relaxation cascade finishes. Figure adapted from [41]. 11
2.4 K-shell and Auger yields as function of atomic number. 12
2.5 Klein-Nishina differential cross-section for different photon energy. 16
2.6 Klein-Nishina and Thomson differential cross-section for a linearly polarized and unpolarized 14 keV photon. 18
2.7 Klein-Nishina differential cross-section for a linearly polarized and unpolarized 1 MeV photon. 18
2.8 Cross-section of processes contributing to X-ray interacting with an atom of Cu. The shaded area corresponds to the X-ray energy range. 20

3.1 Schematic of EDXRF planar geometry setup. Figure adopted from [53]. . . . 22
3.2 Schematic of X-ray tube. 23
3.3 Example of spectrum produced by the X-ray tube. 24
3.4 Example of X-ray fluorescence spectrum. 30
3.5 Example of X-ray spectrum deconvolution and background subtraction. . . . 31
3.6 Schematic representation of a triaxial geometry EDXRF setup, using a secondary target. Figure adopted from Guimarães work [75]. 39
3.7 Comparison of EDXRF spectra obtained from planar and triaxial geometry. Figure adopted from Pessanha *et al.* [77]. 40

3.8 Compton-to-Rayleigh ratio as function of scattering angle. Values for different atomic numbers are presented. Figure adopted from Pessanha *et al.* work [4]. 41

4.1 Triaxial spectrometer at Laboratório de Física Atómica e Molecular, LIBPhys-UNL, Departamento de Física, FCT-UNL. a) View of the whole system. b) Top view of the sample holder, collimation tube and detector tube. c) Side view of sample holder, collimation tube and detector tube. 50

4.2 Source exciting the Mo secondary target. 50

4.3 Primary beam energy function used in the simulation. 53

4.4 Detector energy efficiency function. 55

4.5 Application of energy resolution (left figure) and efficiency (right figure) to the simulated spectrum. 55

4.6 Simulated setup used by the Basic code. 56

4.7 2D-histogram of z-component of polarization and energy for X-rays that leave the surface of the fluorescence target (Mo) within a solid angle accepted by the sample. Lines denoted as Mo K_α and Mo K_β correspond to Mo fluorescence photons, which can have any polarization value, as seen in the figure. The X-ray tube photons are polarized, as denoted by the red boxes in the figure. . 57

4.8 Comparison of simulated (red) and experimental (blue) spectra for the NBS-1571 orchard leaves. Fluorescence lines are identified by the element and transition 59

4.9 Comparison of simulated (red) and experimental (blue) spectra for the ISE-954 clay material. Fluorescence lines are identified by the element and transition. 61

4.10 Comparison of simulated (red) and experimental (blue) spectra for the BCR-B copper alloy. Fluorescence lines are identified by the element and transition. 62

4.11 Simulated setup used by the Advanced code. 64

4.12 2D-histogram of X- and Y-axis position of photon entering the sample. 65

4.13 2D-histogram of X-axis position and θ for photon reaching the sample. . . . 65

4.14 2D-histogram of Y-axis position and ϕ for photon reaching the sample. . . . 66

4.15 Experimental and simulated Rayleigh-to-Compton scattering ratio as function of the average atomic number. 68

6.1 Kostroun: values obtained from the combination of Kostroun *et al.* calculations [163] and Scofield's radiative Dirac-Slater calculations [105]. "DF,DS": values obtained from the combination of Chen *et al.* radiationless Diroc-Fock calculations [97] and Scofield's radiative Dirac-Slater calculations [93]. "DF": values obtained from the combination of Chen *et al.* radiationless Diroc-Fock calculations [97] and Scofield's radiative Dirac-Fock calculations [106]. "EADL": values obtained from the Evaluated Atomic Data Library [99]. 95

6.2 “Bambynek1972”: Values from Bambynek *et al.* earlier semi-empirical fit [154]. “Krause1979”: values from Krause’s semi-empirical fit [155]. “Bambynek1984”: values from Bambynek *et al.* later semi-empirical fit [156]. “NIST”: semi-empirical fit values presented in NIST’s Fundamental Parameters Database [38]. “Kahoul”: values from Kahoul *et al.* empirical fit [144]. “Daoudi”: values from Daoudi *et al.* empirical fit [157]. 97
6.3 "DF,DS": values obtained from the combination of Chen *et al.* radiationless Diroc-Fock calculations [97] and Scofield’s radiative Dirac-Slater calculations [93]. "DF": values obtained from the combination of Chen *et al.* radiationless Diroc-Fock calculations [97] and Scofield’s radiative Dirac-Fock calculations [106]. "EADL": values obtained from the Evaluated Atomic Data Library [99]. 99
6.4 "Bambynek1972": Values from Bambynek *et al.* earlier semi-empirical fit [154]. "Krause1979": values from Krause’s semi-empirical fit [155]. "Bambynek1984": values from Bambynek *et al.* later semi-empirical fit [156]. "NIST": semi-empirical fit values presented in NIST’s Fundamental Parameters Database [38]. "Kahoul": values from Kahoul *et al.* empirical fit [144]. "Daoudi": values from Daoudi *et al.* empirical fit [157]. 101
6.5 "DF,DS": values obtained from the combination of Chen *et al.* radiationless Diroc-Fock calculations [97] and Scofield’s radiative Dirac-Slater calculations [93]. "DF": values obtained from the combination of Chen *et al.* radiationless Diroc-Fock calculations [97] and Scofield’s radiative Dirac-Fock calculations [106]. "EADL": values obtained from the Evaluated Atomic Data Library [99]. 103
6.6 "Bambynek1972": Values from Bambynek *et al.* earlier semi-empirical fit [154]. "Krause1979": values from Krause’s semi-empirical fit [155]. "Bambynek1984": values from Bambynek *et al.* later semi-empirical fit [156]. "NIST": semi-empirical fit values presented in NIST’s Fundamental Parameters Database [38]. "Kahoul": values from Kahoul *et al.* empirical fit [144]. "Daoudi": values from Daoudi *et al.* empirical fit [157]. 104

List of Tables

4.1 Relative percentage difference between measured and simulated fluorescence lines peak intensities. The lines marked with calib were used for normalization of the counts of the simulated spectrum to the experimental spectrum. Uncertainty is presented for each values. 63

4.2 Average atomic number for samples composed by different weight fractions of HAp and HB. 67

5.1 Radiative transition probability values from this work's MCDF calculations, Scofield's Dirac-Hartree-Slater calculations [93], and Scofield's Dirac-Hartree-Fock calculations [106]. Values not presented in their references are presented in table as n.p.. All values are presented in milliatomic units; 1 milliatomic unit = $4.134 \times 10^{-13} s^{-1}$. 76

5.2 Radiative transition K-shell partial yield values, ω_{ij}, obtained from this work's MCDF calculations, Scofield's Dirac-Hartree-Slater calculations [93], Scofield's Dirac-Hartree-Fock calculations [106], and NIST Fundamental Parameters Database [38]. Values that could not be obtained, since transition probability values where not presented in their references, are presented in table as n.p.. 77

5.3 Indication of transitions corresponding to the line designations. 78

5.4 Radiative transition ratios obtained from this work's MCDF calculations, Scofield's Dirac-Hartree-Slater calculations [93], and Scofield's Dirac-Hartree-Fock calculations [106], empirical fit values from NIST Fundamental Parameters Database, and Salem empirical fit values *et al.* [108]. Values that could not be obtained due to lack of information are presented in table as n.p.. 79

5.5 Radiative transition Kβ/Kα ratios from several references. 79

5.6 Nonradiative transitions probabilities from this work's MCDF calculations, Chen *et al.* Dirac-Hartree-Fock calculations [95], and Safronova *et al.* Dirac-Hartree-Fock calculations [145]. Values not presented in their references are presented in table as n.p.. *Note: Chen *et al.* [95] does not present values for K-M_2M_2, K-M_2M_4 and K-M_2M_5 transitions. All values are presented in milliatomic units; 1 milliatomic unit = $4.134 \times 10^{-13} s^{-1}$. 80

5.7 Nonradiative K-LL, K-LX and K-XY transition probability values from this work's MCDF calculations, Chen *et al.* Dirac-Hartree-Fock calculations [95], and Safronova *et al.* Dirac-Hartree-Fock calculations [145]. K-LX/K-LL and K-XY/K-LL nonradiative transition ratios from this work's MCDF calculations, Chen *et al.* Dirac-Hartree-Fock calculations [95], Safronova *et al.* Dirac-Hartree-Fock calculations [145], and experimental values from Bellicard *et al.* [146]. Transition probability values are presented in milliatomic units; 1 milliatomic unit = $4.134 \times 10^{-13} s^{-1}$. 81
5.8 Nonradiative transition intensity relative to K-L_2L_3 ($^1D_2$). Values presented are from this work's MCDF calculations and experimental values from Freedman *et al.* [147]. 81
5.9 Comparison of K-shell fluorescence yield values from several works. 83

6.1 K-shell fluorescence yield average relative difference 96
6.2 $\omega_{K\text{-}L_2}$ fluorescence yield average relative difference 102
6.3 $\omega_{K\text{-}L_3}$ fluorescence yield average relative difference 102
6.4 $\omega_{K\text{-}M_2}$ fluorescence yield average relative difference 102
6.5 $\omega_{K\text{-}M_3}$ fluorescence yield average relative difference 102

A.1 Zn K-shell radiative transition probability values calculated using Multiconfiguration Dirac-Fock method. Calculations were performed with relaxed orbitals unless if "calculation notes" states that orbitals were frozen. Extra correlation state functions from the 1s orbital up to the 4p orbital were included in the calculations unless "calculation notes" presents a different orbital. In that case, the calculation was performed including extra correlation wavefunctions from the 1s orbital up to the orbital presented in "calculation notes". In the cases were no extra correlation state functions were included "calculation notes" states that no correlation was considered. Transition probabilities are presented in milliatomic units; 1 milliatomic unit = $4.134 \times 10^{-13} s^{-1}$. 133
A.2 Zn K-shell radiationless transition probability values calculated using Multiconfiguration Dirac-Fock method. Calculations were performed with relaxed orbitals unless if "calculation notes" states that orbitals were frozen. Extra correlation state functions from the 1s orbital up to the 4p orbital were included in the calculations unless "calculation notes" presents a different orbital. In that case, the calculation was performed including extra correlation wavefunctions from the 1s orbital up to the orbital presented in "calculation notes". In the cases were no extra correlation state functions were included "calculation notes" states that no correlation was considered. Transition probability values are presented in milliatomic units; 1 milliatomic unit = $4.134 \times 10^{-13} s^{-1}$. . . 134

B.1 Definitions and symbols of atomic quantities of present work and different references. 137

B.2 Continuation of Table I. 138
B.3 Continuation of Table II. 138
B.4 Theoretical K-shell fluorescence yield values. 139
B.5 Theoretical K-L_2 fluorescence yield values. 140
B.6 Theoretical K-L_3 fluorescence yield values. 141
B.7 Theoretical K-M_2 fluorescence yield values. 142
B.8 Theoretical K-M_3 fluorescence yield values. 143
B.9 Semi-empirical and empirical K-shell fluorescence yield values 144
B.10 Semi-empirical and empirical K-L_2 fluorescence yield values 145
B.11 Semi-empirical and empirical K-L_3 fluorescence yield values 146
B.12 Semi-empirical and empirical K-M_2 fluorescence yield values 147
B.13 Semi-empirical and empirical K-M_3 fluorescence yield values 148

Listings

Acronyms

DL	Detection Limits
EDXRF	Energy Dispersive X-Ray Fluorescence
EPDL97	Evaluated Photon Data Library 97
FWHM	Full Width at Half Maximum
Geant4	GEometry ANd Tracking 4
MCDF	multiconfiguration Dirac-Fock
MCHF	multiconfiguration Hartree-Fock
SDD	Silicon Drift detector

Symbols

A	transition probability
C_i'	absorption in air and detector window
μ	material linear attenuation coefficient
α_{ij}	coefficient correcting for absorption
$\boldsymbol{\alpha}$	Dirac matrix
$A_{ijk}^{(\mathrm{A})}$	transition probability for ijk radiationless transition
N_{A}	Avogadro number
$A_{ij}^{(\mathrm{R})}$	transition probability for ij radiative transition
$A_i^{(\mathrm{T})}$	total transition probability for the i sub-shell
$A_i^{(\mathrm{TA})}$	total radiationless transition probability for the i sub-shell
$A_i^{(\mathrm{TR})}$	total radiative transition probability for the i sub-shell
$A_i^{(\mathrm{att})}$	attenuation factor
a_i	radiationless yield (or Auger yield) for the i sub-shell
A_{w}	atomic wiight
β	Dirac matrix
c	light speed
c_i	element concentration
φ	configuration wave function
ρ	material density
ε_i	detector efficiency
$\hat{J}_{\mathrm{D}}$	direct operator
V_{D}	direct potential
$\frac{d\sigma^{\mathrm{C}}}{d\Omega}$	Compton scattering differential cross-section
$\frac{d\sigma^{\mathrm{KN}}}{d\Omega}$	Klein-Nishina differential cross-section
$\frac{d\sigma^{\mathrm{R}}}{d\Omega}$	differential cross-section for Rayleigh scattering
$\frac{d\sigma^{\mathrm{Th}}}{d\Omega}$	differential cross-section for Thomson scattering

E	photon energy
E_0	incident photon energy
$\boldsymbol{e}_0$	incident photon polarization vector
E_i	binding energy for i sub-shell
E_c	scattered photon energy
E_e	electron energy
E_γ	photon energy
$\mu'_\mathrm{s}(\lambda)$	effective mass absorption coefficient for incident photon energy
$\mu''_\mathrm{s}(\lambda)$	effective mass absorption coefficient for fluorescence
$\delta_{ij}(E_i)$	enhancement factor
ϵ	energy of an ionized state
ϵ_{ij}	coefficient correcting for enhancement
$\boldsymbol{e}$	scattered photon polarization vector
$\hat{K}_\mathrm{ex}$	exchange operator
V_ex	exchange potential
F	atomic form factor
F_ϵ	atomic form factors of excited states
g_i	instrumental factor
$G(i,j)$	two-body operator for the relativistic interaction between two electrons
h	planck constant
$\hat{H}$	Hamiltonian
$\hat{H}_\mathrm{D}$	one-electron Dirac Hamiltonian
$\hbar$	reduced Planck constant
I_0	initial beam intensity
I_d	beam intensity after crossing distance d
I_i	peak intensity for element i
$I_{(i)}(E)$	intensity emitted by a sample composed only by the element i
i_c	tube current
k	energy of scattered photon in units of the electron rest energy
k_0	energy of incident photon in units of the electron rest energy
$\boldsymbol{k}_0$	incident photon momentum vector

K_i	calibration factor
$\boldsymbol{k}$	scattered photon momentum vector
λ	wavelength
μ/ρ	material mass attenuation coefficient
w_i	mass fraction
m_e	electron mass
$a_i^{(\mathrm{m})}$	mixing coefficients
m	sample mass per unit area
N_B	counts relative to background
N_p	counts relative to peak
N_T	average number of counts
$V(\boldsymbol{r})$	nuclear potential
Ω	solid angle factor
p	momentum
ϕ	scattering azimuthal angle
$\rho(r)$	electronic charge distribution for radius r
P	photon polarization
q	recoil momentum
r_e	electron classical radius
R_i	peak relative intensity
$R_{\mathrm{C/R}}$	Compton-to-Rayleigh intensity ratio
S	incoherent scattering function
σ^C	Compton cross-section
σ	cross-section for all scattering and absorption processes
σ_B	standard deviation relative to background
σ_p	standard deviation relative to peak
σ_i^{pe}	i-shell photoelectric cross-section
σ_T	total counts standard deviation
$\phi_n(n)$	single-electron orbital

σ^{KN}	Klein-Nishina cross-section
σ^{R}	cross-section for Rayleigh scattering
σ_{X_i}	ionization cross-section
τ	mean life time
Γ	energy width
τ/ρ	photoelectric mass absorption coefficient
τ^{sct}/ρ	mass-scater coefficient
$\Gamma_i^{(\mathrm{TA})}$	total radiationless width for the i sub-shell
σ^{pe}	Total photoelectric cross-section
$\Gamma_i^{(\mathrm{TR})}$	total radiative width for the i sub-shell
Φ	angle between $\boldsymbol{e}_0$ and $\boldsymbol{e}$
V_{C}	critical voltage
V	tube voltage
$\psi(\boldsymbol{r}, t)$	electron wave-function in space-time coordinates
ω_i	fluorescence yield for the i sub-shell
ω_{ij}	partial fluorescence yield for the ij radiative transition
$\omega_{ij}^{(\mathrm{NA})}$	partial fluorescence yield for the ij radiative transition (normalized without accounting radiationless transitions)
x	momentum-transfer variable
Z	atomic number
Z_{avg}	average atomic number

Chapter 1

Introduction

1.1 State of the art

X-ray spectroscopy techniques are widely employed in elemental analysis. Energy Dispersive X-ray Fluorescence technique (EDXRF) is one of the most commonly used for elemental analysis, due to its several benefits, such as being non-destructive, relatively easy, fast, and low-cost when comparing with other analytical techniques. Hence, it has been employed in a broad range of areas such as: biology, geology, forensic sciences, cultural heritage, etc. The setups employed for EDXRF varies from bench-top, to hand-held, diversifying the employment of the technique. Furthermore, setups can be employed in a triaxial geometry using a secondary target, allowing a considerate improvement on the detection limits, which is very convenient for the analysis of trace elements. In Fig. 1.1 it is presented a spectrometer in a triaxial geometry being employed in cultural heritage studies.

Nowadays, the analysis of the EDXRF spectrum, and consequent elemental quantification, is achieved using codes or software dedicated for such purposes, which employ one of three different methods, namely, Comparison with Standards method, Influence Coefficient method, or Fundamental Parameters method. In Comparison with Standards, quantification is achieved resorting to a linear calibration using standards of similar composition to the unknown sample. This method considers that the matrix effects are the same among the different standards and the unknown sample, which is an approximation that limits to some extent the accuracy of the quantification [2]. Furthermore, the accuracy of the unknown sample quantification is dependent on the accuracy of the standards analysis. Other drawbacks that must be considered are the unavailability of standards for certain type of materials, and the monetary costs associated with obtaining the standards.

Figure 1.1: Setup CFAUL-eclipse II, in situ, at Museu Nacional de Arte Antiga, Portugal. Figure adopted from Pessanha work [1].

In both Fundamental Parameters method and the Influence Coefficient method, quantification is achieved by employing mathematical methods to solve the equations relating peak intensity I and concentration c. These equations account for the absorption and enhancement of all elements in the sample, the matrix effects, and include physics parameters related to the several physics processes occurring in the technique, the Fundamental Parameters (FP). While in the Influence Coefficient method approximations are performed to lower the complexity of the equations, in the FP method no considerations are employed, making it more accurate and, nowadays, the most employed method. The accuracy of the quantification is affected by the contribution included in the equations to be solved, and the accuracy of the Fundamental Parameters present in these equations. For more accurate results, other contribution are sometimes included in these equations, such as: tertiary- and higher-order fluorescence, enhancement by electrons, non-parallel beam geometries, sample inhomogeneity, among others. The inclusion of such contribution improves the accuracy of the FP method. Codes and software usually resort to built-in tabulations of Fundamental Parameter values, which are in almost all cases, if not all cases, inaccessible to the user. As such, the inaccuracy of Fundamental Parameters can not be addressed by simply changing the parameters values.

The FP are crucial not only in methods such as the FP method and Influence Coefficient method, but also in many other scientific areas. As such, the calculation of such parameters, using atomic structure calculations, has been the subject of many scientific

works, using Dirac-Hartree-Slater (DS) method, or the Dirac-Hartree-Fock (DF) method. While these approaches solve the multi-electronic atomic systems accounting for the electron-electron interaction, the interaction is not fully taken into account, for which several methods have emerged that better describe that interaction, allowing for more accurate results, such as the multiconfiguration Dirac-Fock method.

Although EDXRF analysis is performed in most cases by evaluation of the characteristic peaks in the X-ray spectrum, further analytical information can be obtained by exploiting the X-ray scattering features. A calibration curve of Compton-to-Rayleigh intensity ratios $R_{C/R}$ in function of average atomic number Z_{avg} can be obtained by evaluation the scattering features of several standards with the same material type, and under the same geometrical conditions [3, 4]. The Z_{avg} of an unknown similar sample can be obtained by direct correlating its measured $R_{C/R}$ ratio with Z_{avg} through the calibration curve. This method is quite sensitive for low-Z materials due to elastic and inelastic scattering different dependence on atomic number. It can be used in the identification and characterization of low-Z materials, as shown in Pessanha *et al.* [4] work. By comparing the measured $R_{C/R}$ for a sample with the calibration curve, this method allows for a calculation of light elements which are "invisible"in XRF, or even calculation of heavier impurities in light materials which may not be detected by XRF [5]. Using this method, materials can easily be distinguished from each other, by measuring the $R_{C/R}$ ratio. Such is useful for choosing samples to be used in experimental measurements. In light materials, even differences of Z_{avg} as low as 0.1 can be distinguished due to the method particular sensitivity in low-Z_{avg} materials. Furthermore, the method can be used to correct standards.

Nowadays, there are quite a number of codes and software for quantitative and qualitative EDXRF analysis using the FP method, such as NRLXRF [6, 7] (from Naval Research Laboratory), NBSGSC [7, 8] (from National Bureau of Standards, actual National Institute for Standards and Technology), XRFAES [9] (from Chalmers University of Technology), WinAxil (from Canberra, and originally included in the software package QXAS, sponsored by the International Atomic Energy Agency) [10], PyMCA [11, 12] (developed by the European Synchrotron Radiation Facility (ESRF) software group), among others. These codes and software mostly differ from one-another in the completeness of the physics models they employ. As such, some of them can be more suited for specific conditions such as the type of sample matrices to analyse, and the experimental setup conditions. Monte Carlo (MC) methods have also been employed in experiments involving X-ray fluorescence, providing assistance for the construction of X-ray spectrometers and analysis of the data acquired. Some of the simulations where performed from dedicated in-house codes, such as 3D μ X-ray [13], X-ray optics [14], and X-ray tomography [15, 16], while others were performed using general-purpose codes, such as MCNP [**mcnpRep**, 17], PENELOPE [18, 19], and GEometry ANd Tracking 4 (Geant4) [20–22]. Monte Carlo methods present several advantages for the simulation of X-ray fluorescence experiments. They can account for contributions that are usually not included in the FP equations,

such as electron contribution to the fluorescence emission, tertiary- and higher-order of enhancement, and non-parallel beam geometry. Furthermore, the method present advantages in describing inhomogeneous or irregular samples, and further variations of the experimental geometry. The disadvantages of this method are the increased computation time and required computational capacity. Regarding the EDXRF technique, Monte Carlo simulations have been applied for a quantitative analysis from the comparison of the simulated X-ray spectrum with the experimental spectrum, such as XMI-MSIM [23] and XRMC [24, 25]. MC simulations have also been applied in studies for in vivo measurements [26, 27] and in cultural heritage studies [28, 29].

MC simulations have also been applied to triaxial geometry spectrometers, such as in Lewis *et al.* [30, 31], Hugtenburg *et al.* [32] and Al-Ghorabie Fayez [33] works.

1.2 Goals and Outline

The motivation of the present work arises from what was presented in the previous section. The main goal is the implementation of a standardless EDXRF elemental quantification method, with the additional objectives to implement it for a triaxial geometry spectrometer (with associated lower limits of detection), and to extract Compton-to-Rayleigh scattering intensity ratios in order to determine the sample Z_{avg}. It is also aimed at accounting for several contributions to the peak intensity that are not always included in the Fundamental Parameter method, such as electron enhancement, non-parallel beam-geometry, tertiary- and higher-order fluorescence, etc. Also, the user must be able to change the Fundamental Parameters used in the method.

To accomplish all the aimed goals, a code is implemented using the Geant4 toolkit [20–22], benefiting from the toolkit's implemented Monte Carlo methods and availability to change the tabulated fundamental parameters. Geant4 implementation of several physics processes through MC methods allows that all contributions to the peak intensity are taken into consideration. And Geant4's geometry handling is ideal for the simulation of the triaxil spectrometer.

Even though MC codes have been used for optimization of triaxial spectrometers, there are no MC simulations dedicated to elemental quantification in EDXRF using this type of spectrometers. As such, the present work implements a novel code that not only allows an EDXRF elemental quantification method using this type of geometry, but also the analysis of the Z_{avg} through the evaluation of the Compton-to-Rayleigh scattering intensity ratio $R_{\text{C/R}}$. Furthermore, without the need to resort to standards, the quantification is not limited by drawbacks of Standard Comparison method, such as the possible unavailability of standards similar to the material to analyse, the costs associated, among other discussed in the previous section. Additionally, since Fundamental Parameters are very relevant not only to EDXRF technique, but also to other scientific areas, another goal of the present work is the calculation and comparison of FP relevant to EDXRF technique, and to other techniques where atomic relaxation is a relevant physics process.

The present work is divided in seven Chapters. In Chapter 2, the theoretical background of EDXRF is presented, focusing on the most relevant physics processes and interactions occurring in the technique; the photoelectric effect, atomic relaxation, Rayleigh and Compton scattering (with emphases in the contributions of photon polarization), Bremstrahlung emission, and electron impact ionization.

In Chapter 3, the EDXRF technique is presented with emphases for its experimental details (for both planar and triaxial geometry). It is also presented a typical X-ray spectrum and its different features, as well as the different methods used in elemental quantification. The method for analysis using the scattering features is presented as well.

In Chapter 4, it is presented an overview of Geant4 and its implementation and validation of several physics processes and Fundamental Parameters relevant to the present work simulations. Furthermore, the method developed in the present work is presented, for which two versions of the developed code are presented, the "Basic code", which aims at elemental quantification, and the "Advanced code", which aims at analysis of the Z_{avg} through the evaluation of the Compton-to-Rayleigh scattering intensity ratio $R_{C/R}$. It is presented simulations of the EDXRF spectra of standard samples for a triaxial spectrometer, using the Basic code, which are compared with the respective experimentally measured spectra. The standards correspond to low-Z, medium-Z, and high-Z matrices. These comparisons present relatively good agreement (better than 20 % for most cases) for the characteristic peak intensities. It also presented a calibration curve of Rayleigh-to-Compton scattering ratio, R_{RC}, as function of the average atomic number, Z_{avg}, obtained from the Advanced code triaxial geometry simulations, and compared with the equivalent experimentally measured calibration curve. The calibration curve is measured, from a set of model samples consisting of different proportions of reference materials of Hydroxyapatite (HAp)[$Ca_{10}(PO_4)_6(OH)_2$] (Sigma-Aldrich, lot #BCBS8492V), and boric acid [H_3BO_3]. The comparison of the curves show that most simulated values are close lying or within the experimental uncertainty margins. The agreement between simulated and experimental values is better than 10 % in most cases.

In Chapter 5, the theoretical background of atomic structure calculations is presented. Multiconfiguration Dirac-Fock calculations are performed to obtain Zn K-shell transition probability values. From these values, other fundamental parameters, such as K-shell fluorescence yield values, and partial fluorescence yield values, are obtained. It is presented a comparison of the calculated FP with the available theoretical, experimental, and empirical fitted values. Regarding radiative transition, these comparisons highlight very good agreement when comparing the MCDF calculated values with most available Dirac-Fock theoretical values, and when comparing with most experimental values. As for radiationless transitions, comparisons are limited to the few available results in literature, and while some calculated MCDF values are in agreement with the other theoretical and experimental values, others do not present a good agreement. The calculated K-shell K-shell fluorescence yield is higher than most compared experimental and theoretical values, although being in very good agreement with Ménesguen and Lépy [34] experimental

value.

In Chapter 6, it is presented a bibliography overview of works containing K-shell fluorescence yield values, and/or partial fluorescence yield values, or relevant atomic parameters from which those values can be obtained. With the values obtained from these works, it is presented a comparison of K-shell fluorescence yield, and partial K-shell fluorescence yield values, regarding the K-L_2, K-L_3, K-M_2, K-M_3 radiative transitions, in order to assess the values tabulated in EADL database, the database from which Geant4 and other codes and software resort for the simulation of atomic relaxation. These comparisons support that, as Pia *et al.* [35–37] had already concluded in earlier works, EADL does not present the state of the art partial fluorescence yield values. However, the comparisons also highlight that, contrary to what Pia *et al.* [35–37] works suggest, more studies should be performed before changing EADL library values. Furthermore, it is also concluded that NIST's Fundamental Parameters Database [38] K-shell fluorescence yield values are in high disagreement with all other values compared. Additionally, regarding the method employed for deriving partial transition yields, it is suggested that xraylib library should employ the method used in this Chapter, or alternatively, the similar method employed in Pia *et al.* works.

In Chapter 7 the conclusions of the present work are presented.

Chapter 2

Theoretical Background of EDXRF

2.1 Physical processes in X-ray fluorescence technique

Several physics processes occur during the fluorescence technique, whether in the production of the primary X-ray beam, the beam interaction with the sample, or the detection of the radiation. The understanding of such processes is crucial for the underlying performance of the technique and the quality of the X-ray spectrum that is obtained, as well as the interpretation of the different structures in the spectrum. The most relevant processes are: photoelectric effect, atomic relaxation, Rayleigh scattering, Compton scattering, Bremsstrahlung radiation emission, and electron impact ionization.

2.1.1 Photoelectric effect

The photoelectric effect occurs when an incoming photon interacts with an inner-shell atomic electron, resulting in the ejection of the electron from the ionized atom. For this to occur, the energy of the photon must be greater than the electron binding energy. In this process, the photon is absorbed and the photon energy is transferred to the ejected electron, leaving the atom ionized and in an excited state. The ejected electron is usually designated as a photoelectron, and its kinetic energy is the excess between the incident photon's energy and the binding energy of the sub-shell from which the electron was ejected.

The photoelectric absorption of the incident photon does not necessarily result in an ejected electron. The electron may transit from its bound state to a higher bound state if the photon energy is higher than the energy gap between states.

The total photoelectric cross-section σ^{pe} represents the probability that, for a given photon energy, an atomic electron is ejected, and is given by the sum of the photoelectric

cross-section for each i sub-shell σ_i^{pe}:

$$\sigma^{\text{pe}} = \sigma_{\text{K}}^{\text{pe}} + \sigma_{\text{L}_1}^{\text{pe}} + \sigma_{\text{L}_2}^{\text{pe}} + \sigma_{\text{L}_3}^{\text{pe}} + \sigma_{\text{M}_1}^{\text{pe}} + \ldots \tag{2.1}$$

Each of these sub-shell cross sections is null for photon energies lower than the respective sub-shell binding energy, and additionally, has a sudden increase at those energies, known as the absortion edges. For photon energy higher than the absortion edges the cross-section decreases with the photon energy. Therefore, the representation of the total photoelectric cross-sections, as function of the incoming photon energy, exhibits the characteristic sawtooth-like form near the absorption edges correspondent to the different sub-shells, as can be seen from Fig. 2.1. The absorption edges increases with atomic number. The chemical environment and temperature of the absorbing atom also cause small deviations and the rise of fine structures near the absorption edges.

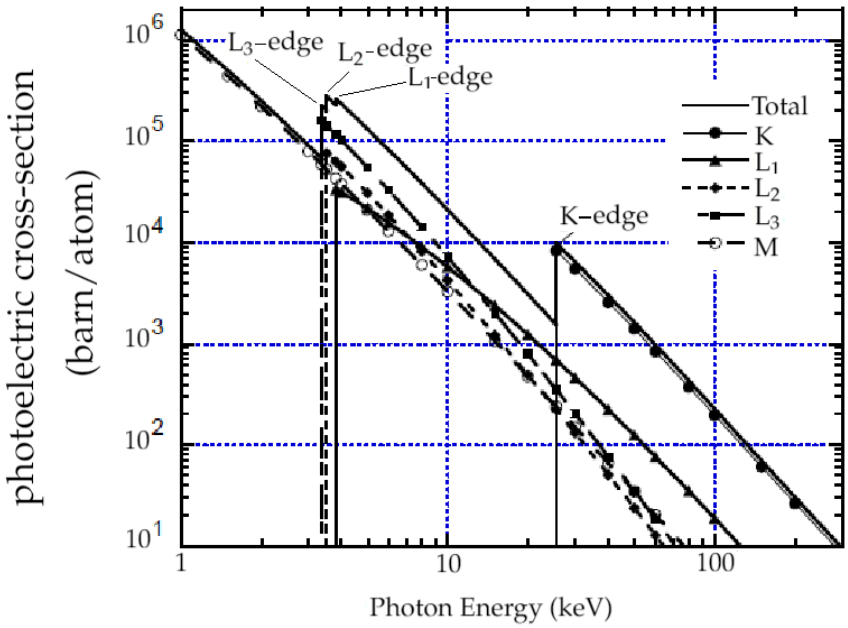

Figure 2.1: Photoelectric cross-section, for Ag, as function of incident photon energy. Total cross-section and sub-shell cross-sections are represented. Figure adopted from [39].)

2.1.2 Atomic relaxation

An atom in an excited atomic state may decay to a lower energy level through spontaneous photon emission. The probability, A, of this spontaneous transition has units of s^{-1}. This quantity is also usually designated as "transition rate" or "transition probability per unit of time". To avoid terminology confusion, in the present work, this quantity is always referred to as "transition probability". Since the energy width Γ and the mean life τ of the excited atomic state are related through Heisenberg uncertainty principle $\Gamma \times \tau = \hbar$, the transition probability of the state is therefore given as $A = 1/\tau = \Gamma/\hbar$ [40]. The excited

state can also transit to lower energy states through a radiationless transition. In this case, the energy of the transition is transferred to another atomic electron of an higher energy shell or sub-shell, resulting in its emission. If the electron transition occurs between shells, the radiationless transition is commonly denominated as Auger transition, and the emitted electron is the Auger electron. Other cases of radiationless transitions include the Coster-Kronig transition, in which the electron transition is intra-shell, and super Coster-Kronig transition, where, in addition to the previous case, the Auger electron is emitted from the same shell.

The most probable radiative transitions in the relaxation process are the so-called "allowed transitions", while the so-called "forbidden transitions" are much more unlikely to occur. These transitions differ from each other through the selection rules they follow, i.e., the sets of changes in the quantum numbers. In Fig. 2.2 the characteristic radiative transitions are presented, using the most common notations, the "Siegbahn notation", and the IUPAC (International Union of Pure and Applied Chemistry) notation.

After the atomic transition occurs, the atomic system may still be excited. In fact, the atomic system usually undergoes a sequence of transitions until it reaches the de-excited state, emitting photons and Auger electrons in the process. Such sequence is typically denominated as relaxation cascade or de-excitation cascade. The cascade is depicted in Fig. 2.3.

For a radiative transition where the electron transits from sub-shell j to sub-shell i, with binding energies E_i and E_j, respectively, the energy of the emitted photon is given as:

$$E_\gamma = E_j - E_i. \tag{2.2}$$

Since binding energies are specific for each sub-shell and element, the emitted photon energy is also specific for each element and each transition. For this reason, photons emitted in the atomic relaxation are usually termed as characteristic X-rays. Some different radiative transitions lead to the emission of characteristic X-rays with similar energies. As such, their corresponding measured spectrum lines are often indistinguishable, for which it is common to use a notation where multiple transitions are encompassed, for example, K-$M_{4,5}$ encompasses the K-M_4 and K-M_5 transitions.

In an experimental context, the particles that are used to excite the atoms are usually referred to as primary particles, and therefore, the characteristic photons emitted from the consequent atomic relaxation are frequently termed as secondary photons. In the specific cases where the primary particles are X-ray photons, such as in the X-ray fluorescence technique, the secondary photons are also usually referred to fluorescence photons.

For a radiationless transition where the electron transits from the j sub-shell to the i sub-shell, the Auger electron, emitted from the h sub-shell, has energy given by:

$$E_\mathrm{e} = E_j - (E_h + E_i), \tag{2.3}$$

where E_i, E_j, and E_h are the binding energies of i, j, and h sub-shells respectively.

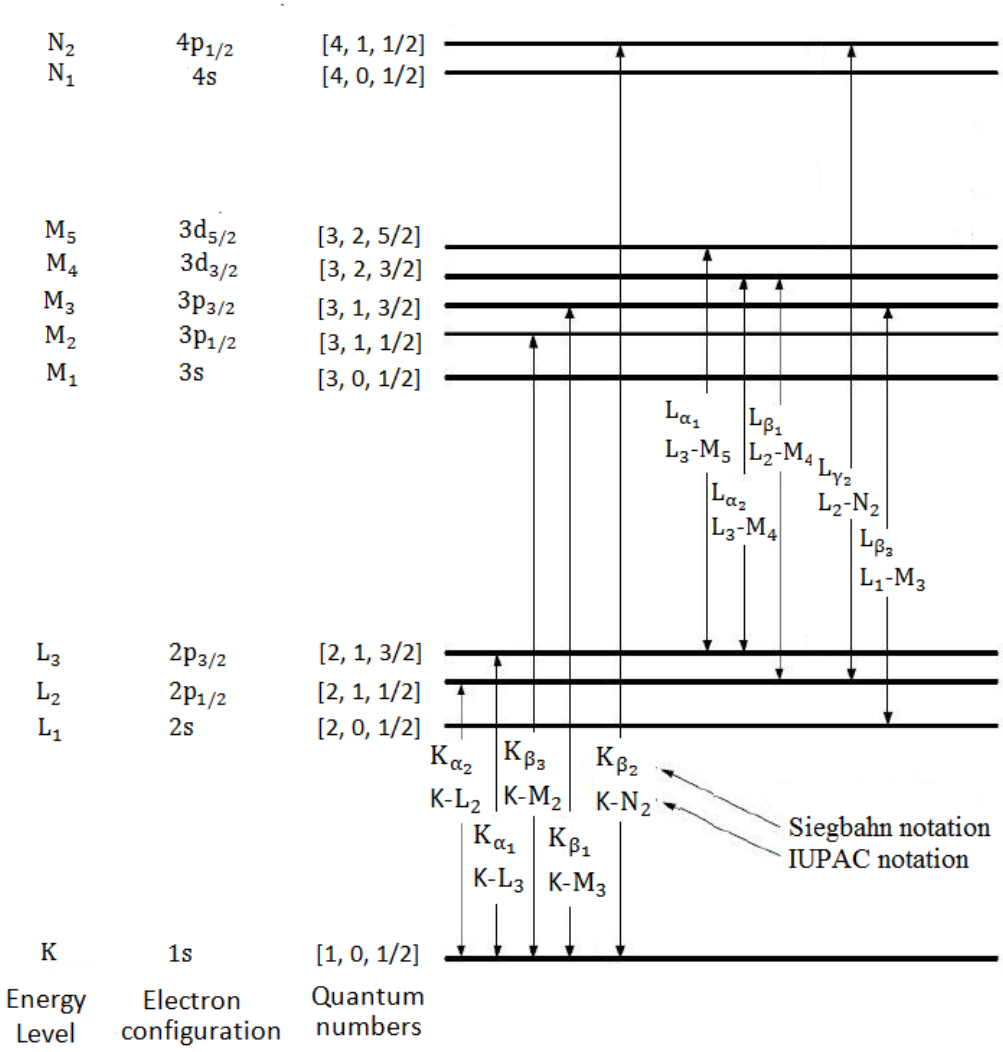

Figure 2.2: Radiative transition representation and nomenclature. Figure adapted from [41].

For an atomic state with an initial vacancy in the i sub-shell, the total radiative width $\Gamma_i^{(\mathrm{TR})}$ is the energy width associated with all radiative transitions that can fill the i sub-shell, and the total radiationless width $\Gamma_i^{(\mathrm{TA})}$ is the energy width associated with all radiationless transitions (including Auger, Coster-Kronig, and super Coster-Kronig transitions) that can fill the i sub-shell. The total state width is given as $\Gamma_i = \Gamma_i^{(\mathrm{TR})} + \Gamma_i^{(\mathrm{TA})}$. Likewise, the total transition probability of the state is given as $A_i^{(\mathrm{T})} = A_i^{(\mathrm{TR})} + A_i^{(\mathrm{TA})}$, where $A_i^{(\mathrm{TR})}$ is the total radiative transition probability, and $A_i^{(\mathrm{TA})}$ is the total radiationless transition probability. Both $A_i^{(\mathrm{TR})}$ and $A_i^{(\mathrm{TA})}$ are given as:

$$A_i^{(\mathrm{TR})} = \sum_{j(>i)} A_{ij}^{(\mathrm{R})}, \tag{2.4a}$$

$$A_i^{(\mathrm{TA})} = \sum_{j(>i)} \sum_{k(\geq j)} A_{ijk}^{(\mathrm{A})}, \tag{2.4b}$$

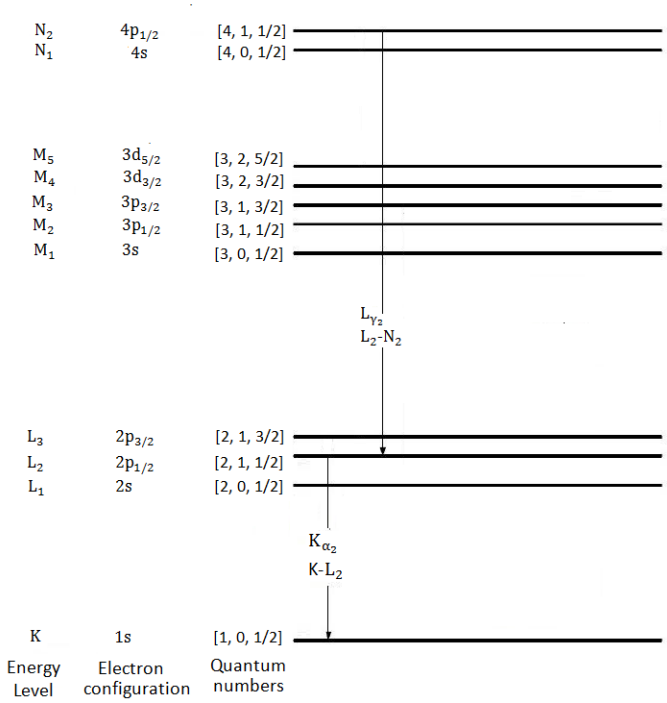

Figure 2.3: Schematic representation of atomic relaxation cascade. In this example a vacancy in the K-shell is filled through the K-L_2 transition, leaving a vacancy in the L_2 sub-shell. The vacancy in the L_2 sub-shell is subsequently filled through the L-N_2 transition, leaving a vacancy in the N_2 sub-shell. Since N_2 is the valence sub-shell, the atomic system is in a de-excited state and the relaxation cascade finishes. Figure adapted from [41].

where $A_{ij}^{(\mathrm{R})}$ is the transition probability of the radiative transition where the vacancy in sub-shell i is filled with an electron from sub-shell j, and $A_{ijk}^{(\mathrm{A})}$ is the transition probability of the radiationless transition where the vacancy in the i sub-shell is filled with an electron from the j sub-shell and an Auger electron is emitted from the k sub-shell. The fluorescence yield, ω_i, is the probability that an atomic state with a vacancy in the i sub-shell de-excites through a radiative transition. It can be given by:

$$\omega_i = \frac{\Gamma_i^{(\mathrm{TR})}}{\Gamma_i^{(\mathrm{T})}} = \frac{\Gamma_i^{(\mathrm{TR})}}{\Gamma_i^{(\mathrm{TR})} + \Gamma_i^{(\mathrm{TA})}}. \tag{2.5}$$

or,

$$\omega_i = \frac{A_i^{(\mathrm{TR})}}{A_i^{(\mathrm{T})}} = \frac{A_i^{(\mathrm{TR})}}{A_i^{(\mathrm{TR})} + A_i^{(\mathrm{TA})}} = \frac{\sum_{j(>i)} A_{ij}^{(\mathrm{R})}}{\sum_{j(>i)} A_{ij}^{(\mathrm{R})} + \sum_{j(>i)} \sum_{k(\geq j)} A_{ijk}^{(\mathrm{A})}}. \tag{2.6}$$

On the contrary, the probability that the atomic state deexcites through radiationless transition is the radiationless yield (or Auger yield), a_i, which can be obtained from

analogous equations to Eqs. 2.5 or 2.6. The sum of fluorescence yield and Auger yield is unity: $\omega_i + a_i = 1$. As presented in Fig. 2.4, the fluorescence yield increases with atomic number, while the Auger yield decreases. The fluorescence yield is higher for sub-shells

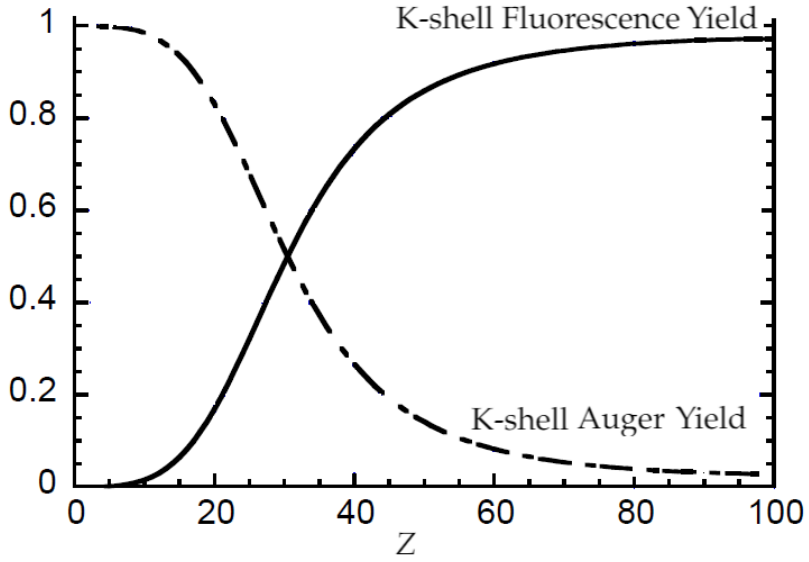

Figure 2.4: K-shell and Auger yields as function of atomic number.

with lower binding energies, i.e., for any element, the following condition is verified:

$$\omega_{\mathrm{K}} < \omega_{\mathrm{L}} < \omega_{\mathrm{M}} < \ldots \tag{2.7}$$

The partial fluorescence yield of a specific radiative transition (or set of transitions) can be calculated in a similar way as the fluorescence yield of the sub-shell. The partial fluorescence yield ω_{ij} of the transition ij, in which the vacancy in a i sub-shell is filled with an electron from the j sub-shell, with respective transition probability $A_{ij}^{(\mathrm{R})}$, is written as:

$$\omega_{ij} = \frac{A_{ij}^{(\mathrm{R})}}{A_i^{(\mathrm{T})}} = \frac{A_{ij}^{(\mathrm{R})}}{A_i^{(\mathrm{TR})} + A_i^{(\mathrm{TA})}} = \frac{A_{ij}^{(\mathrm{R})}}{\sum_{j(>i)} A_{ij}^{(\mathrm{R})} + \sum_{j(>i)} \sum_{k(\geq j)} A_{ijk}^{(\mathrm{A})}}, \tag{2.8}$$

representing the probability that the atom will de-excite through the specific transition ij instead of all other possible radiative and radiationless transitions. As expected, for any excited state, the sum of all partial radiative transition fluorescence yields equals the fluorescence yield of the sub-shell:

$$\sum_j \omega_{ij} = \omega_i. \tag{2.9}$$

Frequently, in literature [35–37], the radiationless transition rates $A_{ijk}^{(\mathrm{A})}$ are not included in Eq. 2.8. The values calculated this way have varying designations among the literature,

such as "transition probability", "transition intensity" or "partial fluorescence yield". In the present work, it is used the designation "partial fluorescence yield (normalized without accounting radiationless transitions)" and the symbol "$\omega_{ij}^{(\mathrm{NA})}$" (where NA stands for "No Auger") to represent it. The radiative transition partial fluorescence yield (normalized without accounting radiationless transitions) "$\omega_{ij}^{(\mathrm{NA})}$", for the radiative transition ij, is given as:

$$\omega_{ij}^{(\mathrm{NA})} = \frac{A_{ij}^{(\mathrm{R})}}{A_i^{(\mathrm{TR})}} = \frac{A_{ij}^{(\mathrm{R})}}{\sum_{j(>i)} A_{ij}^{(\mathrm{R})}}, \tag{2.10}$$

representing the probability that the atom will deexcite through a specific radiative transition ij instead of all other possible radiative transitions. The sum of all partial fluorescence yields (normalized without accounting radiationless transitions) is unity:

$$\sum_j \omega_{ij}^{(\mathrm{NA})} = 1. \tag{2.11}$$

For any radiative transition ij, the respective partial fluorescence yield ω_{ij}, and the respective partial fluorescence yield (normalized without accounting radiationless transitions) $\omega_{ij}^{(\mathrm{NA})}$, follow the relation:

$$\omega_{ij} = \omega_i \times \omega_{ij}^{(\mathrm{NA})}, \tag{2.12}$$

where ω_i is the fluorescence yield of the respective sub-shell.

2.1.3 Rayleigh Scattering

Rayleigh scattering is a process where photons are elastically scattered by bound electrons. In this process, the energy of a photon is transferred to an atomic electron, which transits from the initial state to a virtual state and back to the initial state through the emission of a photon, the scattered photon. Thus, the atom from which the photon is scattered does not get ionized or excited. The scattered photon has the same energy as the incident photon, although different direction. This process can be regarded as a collision between a photon and an atom as a whole, and it can be formally described as an absorption of the incident photon by a bound electron that transits to a virtual state, and a consequent emission of a photon with different direction. This process is more likely to occur for low energy photons and for scatterer atoms with high atomic number.

The differential cross-section for the Rayleigh scattering can be derived from the more simple process of the elastic scattering from one free electron, the Thomson scattering [3]. The differential cross-section for Thomson scattering is dependent only on the scattering angle θ, and is written as [42]:

$$\frac{d\sigma^{\mathrm{Th}}}{d\Omega}(\theta) = \frac{r_{\mathrm{e}}}{2}(1+\cos^2\theta)(\mathrm{cm}^2\mathrm{sr}^{-1}\mathrm{electron}^{-1}), \tag{2.13}$$

where r_{e} is the classical radius of the electron. In order to (approximately) consider the charge distribution of all atomic electrons at once, atomic form factors $F(q,Z)$ are

included, and thus the Rayleigh scattering differential cross-section is written as [42]:

$$\frac{d\sigma^{\mathrm{R}}}{d\Omega}(\theta) = \frac{d\sigma_{\mathrm{Th}}}{d\Omega}(\theta)[F(q,Z)]^2(\mathrm{cm}^2\mathrm{sr}^{-1}\mathrm{atom}^{-1}), \tag{2.14}$$

where $[F(q,Z)]^2$ is the probability that the Z electrons of an atom gets the recoil momentum, q, without absorbing any energy. The recoil momentum q is given as [42]:

$$q = 2E\sin\left(\frac{\theta}{2}\right), \tag{2.15}$$

where E is the energy of the incident photon. For an atom with spherically symmetric charge distributions, the atomic form factor can be given as [43]:

$$F(q,Z) = 4\pi\int_0^\infty \rho(r)\frac{\sin(qr)}{qr}r^2dr, \tag{2.16}$$

where $\rho(r)$ is the electronic charge distribution for radius r. Atomic form factors are also usually presented in terms of the momentum-transfer variable x, which is given by [42]:

$$x = \left[\sin\left(\frac{\theta}{2}\right)\right]/\lambda(\mathrm{\AA}^{-1}), \tag{2.17}$$

where λ is the incident photon wavelength. Thus, the form factor is presented as "$F(x,Z)$". The atomic form factor is approximately independent of the scattering angle up to about 2 keV. However, at higher energies, the atomic form factor decreases rapidly as the scattering angle increases. Atomic form factors can be obtained from Eq. 2.16 using atomic structure calculations based on Thomas-Fermi, Hartree-Slater, Hartree-Fock, or other atomic structure calculation models, or analytic expressions [42]. Calculations and tabulations of $F(x,Z)$ are available in literature, in works such as Hubbel *et al.* [42], Hubbel and Øverbø[44]. While the Thomson differential cross-section is independent of the photon energy, the Raleigh differential cross-section has a dependence introduced by the atomic form factor. For high energies, the Rayleigh differential cross-section is much higher for small scattering angles. In fact, for 1 MeV photons, more than half of the photons are scattered within a 5° angle. However, for lower photons energies, such as the ones common in X-ray fluorescence technique, the angular distribution becomes much broader. For elements of higher atomic number the broadening is even greater.

The Rayleigh cross-section is obtained from integrating the differential cross-section with respect to θ:

$$\sigma^{\mathrm{R}} = \int_\theta \frac{d\sigma^{\mathrm{R}}}{d\Omega}(\theta)d\theta = \int_\theta \frac{d\sigma_{\mathrm{Th}}}{d\Omega}(\theta)[F(q,Z)]^2d\theta, \tag{2.18}$$

The cross-section is higher for higher atomic elements.

2.1.4 Compton Scattering

In an inelastic scattering there is energy transfer between the incident particle and the medium from which it is scattered. The case in which a photon is inelastically scattered

by a charged particle is denominated Compton scattering (or Compton effect). The name arrives from Arthur Holly Compton's significant works [45, 46] which reinforced that light could not be considered purely as a wave. In Compton *et al.* works [45, 46], it was observed the scattering of X-ray photons in atomic electrons, and since the energy of the incident photons was so much larger than the binding energy of the atomic electron, the electrons were treated as being free and at rest. With this considerations, treating the photons as particles, and applying the conservation of momentum and conservation of energy to the collision of the incident photon with one electron, the Compton shift formula was derived, which relates the wavelength shift $\Delta\lambda$ of the incident photon and the scattering angle θ:

$$\Delta\lambda = \frac{h}{m_e c}(1 - \cos\theta), \tag{2.19}$$

where h is the Planck constant, and the quantity $\frac{h}{m_e c}$ is the Compton wavelength of the electron. Thus, from this formula, the wavelength shift for scattering in electrons is null for $\theta = 0$ and reaches a maximum value of $\frac{2h}{m_{ec}}$ when the photon is backscattered ($\theta = 180$). Compton's formula can be written in terms of energy energy transfer of the inelastically scattered photon [47]:

$$\Delta E = \frac{E_0 E_c}{m_e c^2} \cdot (1 - \cos\theta), \tag{2.20}$$

where ΔE is the energy difference between the incident and the scattered photon, E_0 the energy of the incident photon, $m_e c^2$ the electron rest-mass energy, and E_c the energy of the scattered photon. Due to the considerations that the electron is free and at rest, Compton's equation is not strictly valid for the case of atomic electrons. Dumond accounted for the Doppler shift due to the relative motions of the scattering body, source of radiation and observer [48]. Considering the electron momentum p_x and the angle between the direction of the electron and the normal to the scattering plane ψ, Dumond extended the equation [48]:

$$\Delta E = \frac{E_0 . E_c}{m_e . c^2}.(1 - \cos\theta) + \frac{2E_0 p_x}{m_e c} \cdot \sin\frac{\theta}{2} \cdot \cos\psi, \tag{2.21}$$

where the first term is the Compton shift (as given from Eq. 2.20), and the second term accounts for the shift due to the electron motion.

Using quantum electrodynamics theory, Klein and Nishina derived the expression for the differential cross-section that expresses the probability of an unpolarized X-ray photon being inelastically scattered into a solid angle $d\Omega$, by a free electron at rest [49]. This expression, know as Klein-Nishina function, can be written as [49]:

$$\frac{d\sigma^{\mathrm{KN}}}{d\Omega}(\theta, E) = \frac{r_e^2}{2}(\frac{k}{k_0})^2(\frac{k}{k_0} + \frac{k_0}{k} - \sin^2\theta)(\mathrm{cm} \cdot \mathrm{electron}^{-1} \cdot \mathrm{sr}^{-1}), \tag{2.22}$$

where $d\sigma^{\mathrm{KN}}/d\Omega$ is the Klein-Nishina differential cross-section, k_0 is the energy of the incident photon in units of the electron rest energy, k the energy of the scattered photon in units of the electron rest energy, θ the scattering angle, and r_e is the classical electron radius. The differential cross-section is minimum for $\theta = 90$. Due to the dependence on

photon energy, the differential cross-section exhibit significantly different behaviour in the range 1 keV < E < 1 MeV. Fig. 2.5 presents the Klein-Nishina differential cross-section for different photon energies, where it is highlighted that for 1 MeV photons, scattering angles in the range 90° < θ < 180° are very unlikely to occur. The lower the photon energy, the more the photons are scattered in these angles. The total Klein-Nishina cross-section

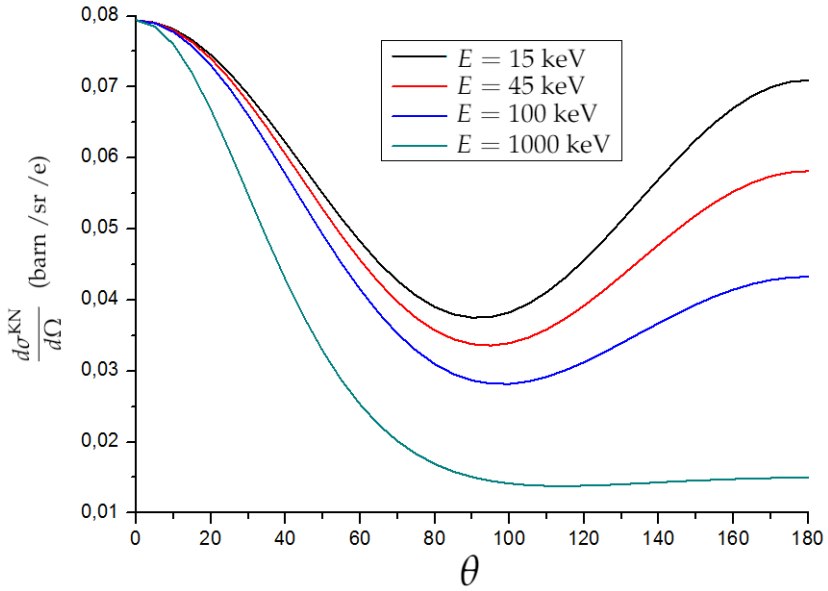

Figure 2.5: Klein-Nishina differential cross-section for different photon energy.

σ^{KN} is obtained by integrating the previous equation with respect to θ:

$$\sigma^{\mathrm{KN}} = 2\pi r_e^2 \left\{ \frac{1+k}{k^2} \left[\frac{2(1+k)}{1+2k} - \frac{\ln(1+2k)}{k} \right] + \frac{\ln(1+2k)}{2k} - \frac{1-3k}{(1+2k)^2} \right\}. \tag{2.23}$$

The Klein-Nishina approximation that the electrons are free and at rest is a good approximation for photons of the order of 1 MeV or higher, in particular if the photons are scattered from low-Z atoms. However, for lower energies, cross-sections of scattering by bound electrons must take into account the electron's binding energies. To account for such, a correction to the Klein-Nishina differential cross-section can be made by applying a factor, the incoherent scattering function $S(x,Z)$, which accounts for the binding effect from the bound electron [42]. As such, the Compton scattering differential cross-section $\frac{d\sigma^{\mathrm{C}}}{d\Omega}$ is given as:

$$\frac{d\sigma^{\mathrm{C}}}{d\Omega}(\theta,E) = \frac{d\sigma^{\mathrm{KN}}}{d\Omega}(\theta,E) S(q,Z), \tag{2.24}$$

where, q is the recoil momentum, and Z the atomic number of the atom. The incoherent scattering function can be written in terms of atomic form factors of excited states. The later are written as [50]:

$$F_\epsilon(\mathbf{q},Z) = \langle \epsilon | \sum_{j=1}^{Z} exp(i\mathbf{q}\cdot\mathbf{r}) | 0 \rangle, \tag{2.25}$$

where ϵ is the energy of an ionized state, and $\mathbf{r}$ the electron radius. The incoherent scattering function $S(q,Z)$ is written as a sum of the atomic form factors for the excited states:

$$S(\mathbf{q},Z) = \sum_{\epsilon>0} |F_\epsilon(\mathbf{q},Z)|^2. \tag{2.26}$$

As in the case of the atomic form factors, the incoherent scattering function is often represented as function of the momentum-transfer variable x (defined by Eq. 2.17). Calculations of $S(x,Z)$ can be performed from the same methods for $F(x,Z)$ calculations. Some works in literature [42, 44] present such calculations, as well as tabulations, for these values.

The Compton cross-section is obtained from integrating the differential cross-section with respect to θ:

$$\sigma^{\mathrm{C}}(E) = \int_\theta \frac{d\sigma^{\mathrm{C}}}{d\Omega}(\theta,E)d\theta = \int_\theta \frac{d\sigma_{\mathrm{KN}}}{d\Omega}(\theta,E)[S(q,Z)]^2 d\theta, \tag{2.27}$$

2.1.5 Polarization in Compton and Rayleigh scattering

The contribution of polarization is increasingly more important for lower photon energy. While for high-energy photons the scattering is virtually isotropic in the scattering azimuthal angle ϕ, for low-energy linearly polarized photons anisotropy is verified [51]. For the inelastic scattering of a linearly polarized photon by a free electron, where $\boldsymbol{k}_0$ and $\boldsymbol{e}_0$ are the incident photon momentum vector and polarization vector, respectively, and where $\boldsymbol{k}$ and $\boldsymbol{e}$ are the scattered photon momentum vector and polarization vector, respectively, the Klein-Nishina differential scattering cross-section can be written as [49]:

$$\frac{d\sigma^{\mathrm{KN}}}{d\Omega} = \frac{1}{4} r_0^2 \left(\frac{k}{k_0}\right)^2 \left(\frac{k}{k_0} + \frac{k_0}{k} - 2 + 4\cos^2\Phi\right), \tag{2.28}$$

where k_0 is the incident photon momentum, k the scattered photon momentum, and Φ is the angle between $\boldsymbol{e}_0$ and $\boldsymbol{e}$ [49]. The Thomson scattering of a linearly polarized photon can be written as [43]:

$$\frac{d\sigma^{\mathrm{Th}}}{d\Omega} = r_0^2 \cos^2\Phi, \tag{2.29}$$

The differential cross-sections from Eqs. 2.28 and 2.29 can also be written as function of the polar scattering angle θ and azimuthal scattering angle ϕ [52]:

$$\frac{d\sigma^{\mathrm{KN}}}{d\Omega} = \frac{1}{2} r_0^2 \left(\frac{k}{k_0}\right)^2 \left(\frac{k}{k_0} + \frac{k_0}{k} - 2\sin^2\theta\cos^2\phi\right), \tag{2.30}$$

$$\frac{d\sigma^{\mathrm{Th}}}{d\Omega} = r_0^2 (1 - \sin^2\theta\cos^2\phi). \tag{2.31}$$

The differential cross-sections for unpolarized photons can be obtained from Eqs. 2.30 and 2.31 by averaging with respect to the azimuthal scattering angle ϕ.

In Fig. 2.6, Klein-Nishina and Thomson differential cross-section are presented for different scattering angles, for photon energy E=14 keV. It can be seen that for this energy

the differential cross-sections are sensitive to the polarization, and they vanish for $\phi = 0$ and $\theta = 90$.

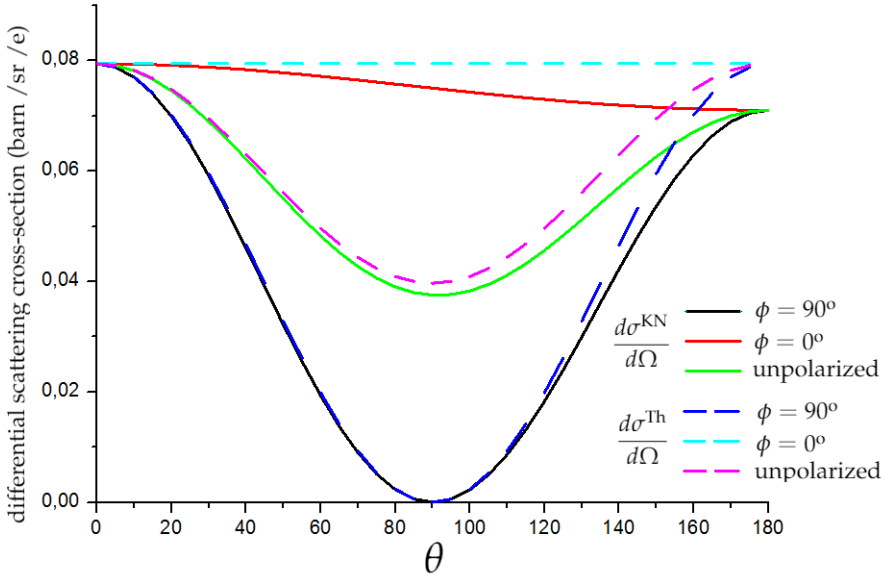

Figure 2.6: Klein-Nishina and Thomson differential cross-section for a linearly polarized and unpolarized 14 keV photon.

In Fig. 2.7, Klein-Nishina differential cross-section is presented for higher energy (E=1 MeV), where it is seen that the cross-section is much more insensitive to the polarization than in the case of low energy photons.

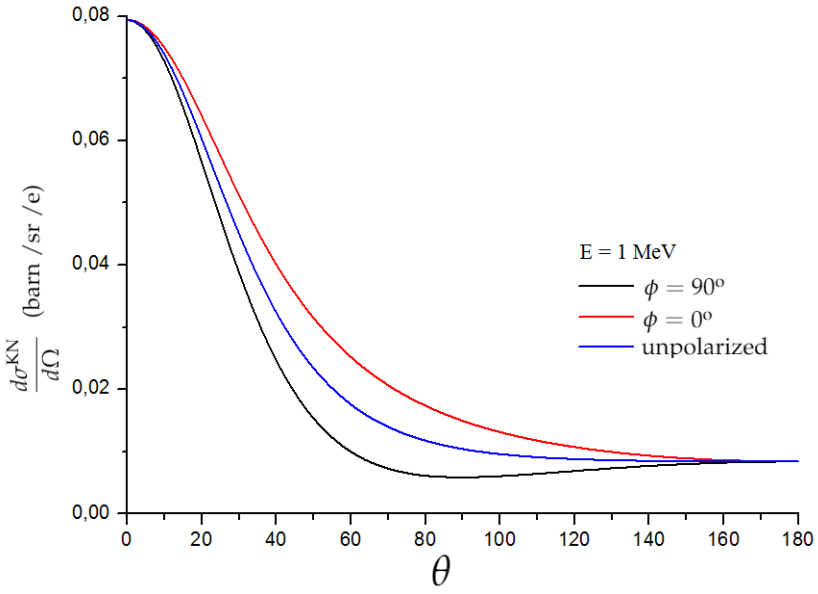

Figure 2.7: Klein-Nishina differential cross-section for a linearly polarized and unpolarized 1 MeV photon.

Differential cross-sections for Compton and Rayleigh scattering for polarized photons

can be obtained by applying atomic form factors F and the incoherent scattering function S, to Klein-Nishina and Thoson differential cross-sections, respectively, analogous to what was presented in Sections 2.1.3 and 2.1.4.

After the scattering, the scattered photon can be polarized or depolarized. The probability that the photon is depolarized can be given as [52]:

$$\left(\frac{k}{k_0}+\frac{k_0}{k}-2\right)/\left(\frac{k}{k_0}+\frac{k_0}{k}-2\sin^2\theta\cos^2\phi\right).$$

Photons with energies bellow 100 keV have low probabilities of being depolarized ($\leq 1\%$) depending on the scattering angles.

2.1.6 X-ray attenuation

An X-ray beam crossing a material will lose its intensity due to various radiation-matter interactions. For the typical energies of X-ray Fluorescence technique ($E < 100$ keV) the greater contributions for the attenuation are the photoelectric effect and the scattering. In medium and high Z elements the photoelectric effect is predominant, while in lower Z elements it is the Compton scattering. There is also a very small contribution of photon-nucleus interaction. The attenuation of the beam can be described by the Lambert-Beer law:

$$I_d = I_0 \exp[-(\mu/\rho)\rho d], \tag{2.32}$$

where I_0 is the initial beam intensity, I_d is the beam intensity after crossing distance d, ρ is the material's density, μ (cm^{-1}) is the material's linear attenuation coefficient, and μ/ρ (cm^2/g) is the mass-attenuation coefficient of the material. The attenuation due to the photoelectric effect is accounted by the photoelectric mass absorption coefficient, (τ/ρ), and the attenuation due to scattering (both elastic and inelastic) is accounted by the mass-scatter coefficient $(\tau^{\mathrm{sct}}/\rho)$. As such, for the mass-attenuation coefficient, the following expression applies:

$$(\mu/\rho) = (\tau/\rho) + (\tau^{\mathrm{sct}}/\rho). \tag{2.33}$$

The cross-section for all scattering and absorption processes, σ, can be related to the mass attenuation coefficient (μ/ρ) through the following expression:

$$\sigma = (\mu/\rho)\frac{A_{\mathrm{w}}}{N_{\mathrm{A}}}, \tag{2.34}$$

where A_{w} is the atomic weight of the material and N_{A} the Avogadro number. If the material is multi-elemental, the material's mass attenuation coefficient is obtained as:

$$(\mu/\rho) = \sum_i w_i(\mu/\rho)_i, \tag{2.35}$$

where, w_i and $(\mu/\rho)_i$ are the mass fraction and mass attenuation coefficient for an element i, respectively.

For the energies used in X-ray fluorescence technique (<100 keV), and medium Z elements, the predominant process in the X-ray attenuation is the photo-ionization, as shown in Fig. 2.8.

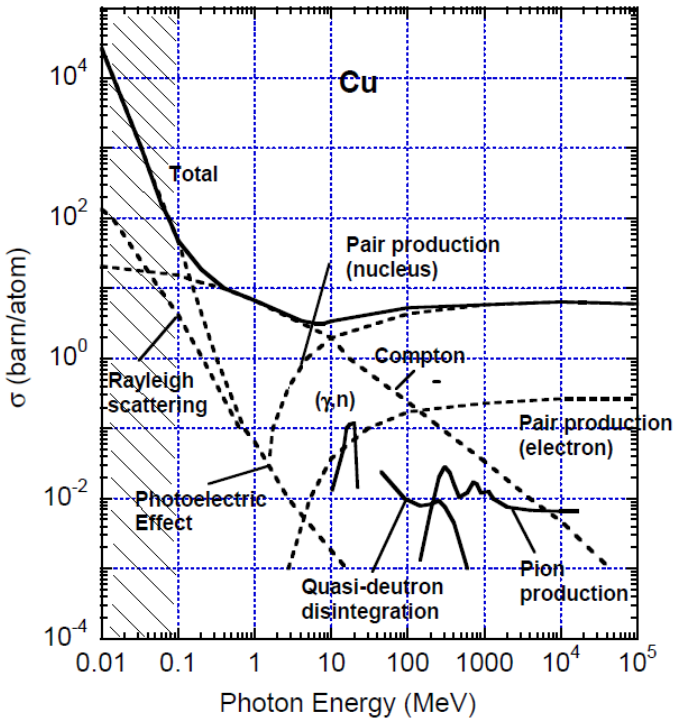

Figure 2.8: Cross-section of processes contributing to X-ray interacting with an atom of Cu. The shaded area corresponds to the X-ray energy range.

2.1.7 Bremstrahlung emission

When charged particles are decelerated by other charged particles, some of their kinetic energy is converted into Bremsstrahlung radiation. The spectrum of the emitted radiation energy is a continuum. In what concerns the X-ray fluorescence technique, this process is specially relevant in the creation of the primary beam, since it is one of the main physical processes occurring in the X-ray tube, where electrons are decelerated by atomic nucleus, producing Bremsstrahlung X-ray photons (see Section 3.1.1). Furthermore, it can also occur in the target material, due to the presence of photo-electrons and Auger electrons, which were created from the photoelectric effect and the atomic deexcitation, respectively. But while the contribution of the Bremsstrahlung radiation created in the X-ray tube is crucial to the understanding of the XRF spectrum, the contribution of the Bremsstrahlung radiation created in the sample is almost negligible to the X-ray spectrum.

2.1.8 Electron impact ionization

In electron impact ionization an atom is ionized by an incoming electron. As such, analogous to the photoelectric effect, instead of a photon, photo-electrons and Auger electrons created in the sample can contribute to the ionization, and consequent emission of characteristic X-rays in the sample. This contribution can be up to a few percent depending on the material and the energy of the primary X-ray beam.

Chapter 3

EDXRF technique and analysis

In 1901, Wilhelm Röntgen was awarded the nobel prize for the discovery of X-rays. From 1914 to 1924, half of the Nobel Prizes in physics were awarded to developments in X-ray spectroscopy, showing the potential of the technique. In 1950s, X-rays started to been used commercially for elemental analysis. Nowadays, X-ray spectroscopy techniques are widely used, being the Energy Dispersive X-Ray Fluorescence (EDXRF) technique one of the most common. There are many reasons for this technique to be so ubiquitous. One of the main appeals is that the technique is non-destructive, with a few exceptions, since the energy and intensity of the primary X-ray beam is rarely high enough to significantly change the sample. This allows for samples to be analysed again by this or other techniques, which is specially convenient when analysing standards. The sample preparation is in many cases minimal, requiring little or no treatment at all. The samples can be in solid, liquid, and gaseous states, while powder samples are also suitable for analysis. The technique is rather fast when compared with other analytical techniques, being able to obtain element quantification in a matter of minutes, depending on the sample and system. It is relatively easy to use due to the available software that implement quantification methods. The cost of the technique is also relatively low when compared with most of the analytical techniques, due to not only low need of sample preparation, the fact that it is non-destructive, but also the relatively inexpensive setups used to perform the technique. There are many types of experimental setups, from bench-top, to hand-held, which diversify the employment of the technique. For these reasons, the technique is used in a broad range of areas such as: biology, geology, forensic sciences, cultural heritage, etc. The ability to identify elements in the sample is very much influenced by experimental factors of the setup and sample, and in optimal conditions elements can be quantified with accuracy up to 99%. Some limitations must be taken into consideration in EDXRF technique. The sample's area that is analysed can not generally be smaller

than a few millimetres, thus making the technique not suitable for analysis of very small components, even if collimators and/or capillaries are used to focus the beam. Sample thickness must be above a few millimetres. Furthermore, the technique is not suitable for direct quantification of light elements, due to their very low fluorescence yield, which makes them "invisible" to the technique.

3.1 Experimental setup

Many different experimental setups are possible for EDXRF technique. The most common setup is a planar geometry, where some type of X-ray source is used to produce a primary beam that excites the sample, and the radiation emitted from the sample is detected using a detection system. Collimators can be used to focus the primary beam or the radiation being emitted by the sample to the detector. This geometry is presented in Fig. 3.1.

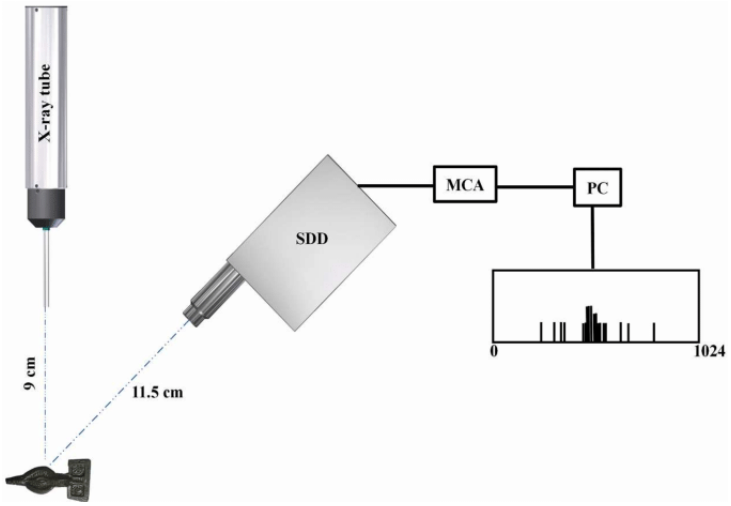

Figure 3.1: Schematic of EDXRF planar geometry setup. Figure adopted from [53].

3.1.1 Primary beam creation

In some techniques, the sample is excited using particle beams, as for example in Particle Induced X-ray Emission technique. Decades ago, it was common to use electron beams as the excitation source. Nowadays, X-rays are the most used excitation source in EDXRF. The X-ray primary beam is produced using an X-ray tube. There are many types of tubes, with different parameters, which lead to different characteristics of the produced X-ray beam. Nevertheless, the following description of the X-ray tube can generally be applied to all of them. Inside the X-ray tube, a heated filament emits electrons, which are accelerated and directed by a strong electric field, colliding into the anode. The electrons interact with the atoms of the anode, and as result of these interaction X-ray photons will be created and emitted from the tube, as shown in Fig 3.2.

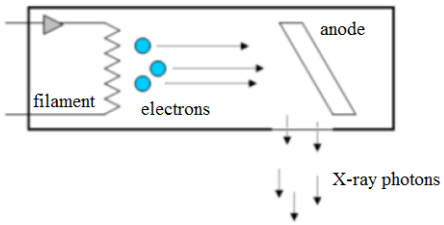

Figure 3.2: Schematic of X-ray tube.

The most important physical processes that lead to the creation of X-ray photons in the tube are the electron-impact ionization, Bremsstrahlung radiation emission, and atomic relaxation. If the kinetic energy of the accelerated electron is greater than the binding energy of an atomic electron, electron-impact ionization may occur, leaving the atom in excited state. The anode atoms may de-excite through emission of characteristic X-ray photons (see Section 2.1.2). Since the energy of the X-ray photons emitted in de-excitation are characteristic of the element, the energy spectrum of an X-ray tube will present characteristic lines specific to the anode's material. The intensity of a characteristic line in the spectrum is related to the tube current i_c, and applied voltage V, by the following expression [54]:

$$I = C i_c (V - V_C)^\gamma, \tag{3.1}$$

where C is a constant, γ a constant that depends on the emission line of the material, and V_C, the critical voltage, is the voltage needed to eject the corresponding atomic electrons from the filament.

The electrons reaching the anode can also decelerate due to the Coloumb field of the nucleus. In this process, the kinetic energy lost by the electron can be converted into Bremsstrahlung photons. Considering that electrons reaching the anode have kinetic energy E_{max}, the deceleration can lead to the emission of Bremsstrahlung photons with energy in the range $0 \leq E \leq E_{max}$. Thus, if the number of electrons is large enough, the spectrum of the resulting Bremsstrahlung radiation energy is continuum in the same energy range. The energy of the electrons reaching the anode, in an X-ray tube operating at voltage V_{max}, is given according to:

$$E_{max} = eV_{max}. \tag{3.2}$$

For a tube with current i_c, and atomic number of the anode material Z, the intensity distribution of the continuum Bremsstrahlung, for photon energies between E and E+dE, can be given as [55]:

$$N(E)dE = k i_c Z \left(\frac{E_{max}}{E} - 1 \right) dE, \tag{3.3}$$

where k is a constant. From this expression, it is highlighted that the intensity is inversely proportional to the energy of the photons, and as the energy aproaches E_{max} the intensity falls to zero. The shape of the intensity spectrum does not depend on the target material, and the maximum intensity is found at $E = \frac{2}{3} E_{max}$.

The spectrum of the emitted photon energy from an X-ray tube is thus a combination of the continuum spectrum due to the breamstrahlung radiation, and the characteristic peaks due the de-excitation of the anode material, as presented in Fig 3.3.

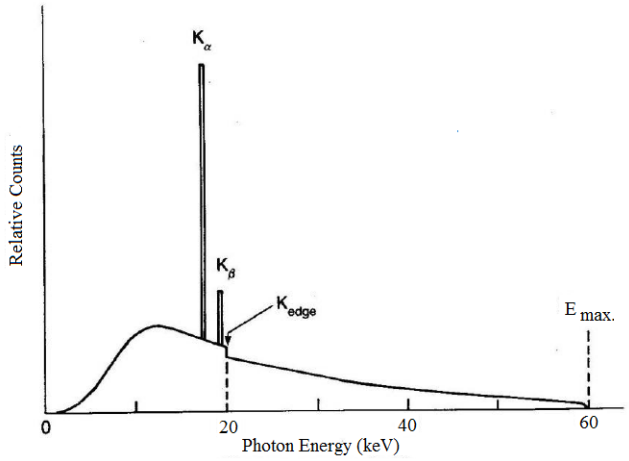

Figure 3.3: Example of spectrum produced by the X-ray tube.

Different applications require different X-ray tube spectra. The choice of the tube components should also be accordingly with the application. Anodes of higher atomic number material lead to more intensity of the Breamstrahlung continum. However, the choice of the anode material must consider that it should be a good heat conductor since the majority of the electrons energy is transferred to the anode as heat. For the choice of X-ray tube windows, materials with high transmission are usually considered, as to not absorb the intensity of the X-ray beam. The thickness of the window must be a compromise between being thick enough to avoid fracture (due to vacuum and heating) and thin enough not to considerably reduce the X-ray intensity. Many different types of X-ray tubes are available, with varying anode materials, window materials, cooling systems, and even window geometries.

3.1.2 Beam Collimation

The primary X-ray beam, created by the X-ray tube, usually has an angular distribution of 100º-150º (depending on the tube). Such angular distribution is very frequently too wide for X-ray fluorescence analysis. Collimators are usually positioned between the primary beam source and the target to focus the beam to a desired angle spread. The collimator absorbs (most of) the X-rays, except those that cross the collimator's hole. Thus, the collimator radius and the position of the collimator will determine the spread of the primary beam angle. It is common to use multiple collimators, whether between source and sample, or between sample and detector. The collimator material is chosen from elements which are not easily excited for energy values of the primary beam photons. The inconvenience of using collimators is the reduction of solid angle. As an alternative,

the focus of the beam can be achieved by the use of capillary and polycapillary lenses. In these lens, X-rays are transmitted through the capillares by total reflection. The cappilares are made so that the reflected angles are less than the critical angle for total reflection.

3.1.3 X-ray Detection

Detectors are instruments capable of gaining information about the radiation that passes through them. Detectors differ by the type of radiation they are able to detect, the physical principle of detection, and their structural characteristics such as the area, thickness, composition, and entrance window. Each detector is characterized by its working parameters, namely energy resolution, sensitivity, efficiency, and time resolution [56]. Different types of detectors operate under different physical principles. The choice of a type of detector to be used is determined by the mentioned characteristics, from which the most important are the type of radiation to be detected, the energy of the radiation, and the resolution.

In X-ray Fluorescence, the most commonly used EDXRF detectors are the Lithium drifted Silicon detector Si(Li), the Ge(Li), the high purity germanium (HPGe), and the more recent Peltier cooled Silicon Drift detector (SDD). The energy resolution of these detectors is low enough for adequately distinguish between characteristic lines of adjacent elements with $Z > 10$, in the energy range 1 keV to 50 keV for Si(Li) and SDD detectors, and in the energy range 6 keV to 200 keV for Ge(Li) and HPGe detectors [2, 57]. Although SDD detectors have better resolution, and higher counting rates, when compared with the others previously mentioned, the Si(Li) detectors are still to date the most commonly used semiconductor detector in EDXRF. As Si and Ge crystals of several centimetres are available, a very good efficiency is also assured.

The Si(Li) detector is a small cylinder p-i-n device with intrinsic (I) region, and its detector element is a single-crystal made of p-type silicon, doped with lithium in order to increase the electrical sensibility. The Si crystal is composed by a Li-drifted intrinsic region, which faces the specimen, and an adjacent Li-free region. Due to lithium high electropositivity, the p-type region is converted into a n-type region. The diode and the preamplifier are operated with cooling, which is performed using liquid nitrogen at boiling temperature, in order to minimize the electric noise and to not hinder the lithium ions mobility.

X-rays entering the detector element will interact in the deplection area, creating electron-hole pairs (mainly due to photoionization). For Si, the average generation energy of the electron-hole pairs is approximately 3.76 eV at 77K. The number of electron-hole pairs created (or the electron charge) is approximately proportional to the energy of the X-ray photon that entered the detector. The created electrons are directed by the external field into the preamplifier. The preamplifier, which is charge sensitive, collects the charge using a feedback capacitor, producing an output pulse with voltage proportional to the collected charge, which in turn is approximately proportional to the photon energy. The

signal is then shaped by a pulse processor, and analysed by a multichannel analyser (MCA), which will convert the analog voltage to a digital number. This digital number represents the channel, and channel corresponds to a small energy range. Each time a pulse is sent to the MCA, the counts of the respective channel are incremented, this way accumulating an energy spectrum [58].

The output signal of the detector system is not always proportional to the energy of the photon which entered the detector. In fact, there are several interactions in the detector that can result in an analog voltage which does not represent the energy of the detected photon, leading to artifacts in the collected spectrum. The most commonly occurring are: sum peaks, escape peaks, and incomplete charge collection. Sum peaks occur when two photons enter the detector with very little time difference, and as consequence the pulse created and measured is proportional to the sum of the two photon energies. In the X-ray spectrum this artifact is visible as a peak for which the energy is the sum of two other existing peaks, and as such, they can usually be identified.

A photon entering the detector may not deposit all of its energy in the detector. The ionization of the detector material will lead to emission of its characteristic X-rays. If one (or more) of the material's characteristic X-rays escape the detector, the energy accounted by the detection system will be the energy of the incoming photon subtracted by the energy of the material's characteristic X-rays. In the case of Si(Li)detectors, the characteristic K_α X-ray photons energy is 1.74 keV, and as such, the spectrum may exhibit peaks 1.74 keV lower than other existing peaks, the so-called Escape peaks. Characteristic X-rays other than the K_α may escape the detector, and more than one characteristic X-ray may escape. Nevertheless, the likelihood of such events is much smaller than the that of a single K_α X-ray escaping the detector, and as such, the X-ray spectrum usually only exhibits peaks for the single K_α escape.

Even if all energy is collected in the detector, the created electrons may not all be collected by the electrical contacts. As such there is an incomplete charge collection, with a measured signal lower than the one corresponding to the energy of the photon entering the detector. This results in peaks with low energy tails in the X-ray spectrum.

X-rays entering the detector may escape the detector through Compton scattering, depositing only some of their energy. Since the photon can transfer any amount of its energy in Compton scattering this effect results in a continuum contribution to the X-ray spectrum.

The energy resolution of a detection system is a result of the energy resolution of the detector (also denominated as intrinsic resolution), the amplifier, and multichannel analyser. This parameter measures the capacity of the system to distinguish photons with close energies. For a given energy in the spectrum, where a peak is presented, the energy resolution is expressed as the peak's Full Width at Half Maximum (FWHM) of the measured distribution. If the energy resolution is large enough, the distribution of the peak can be overlapped with the other close-laying peaks. The distribution in the

spectrum can be described as a Gaussian function, with the following expression [56]:

$$G(E) = \frac{N_0}{\sigma\sqrt{2\pi}} \exp\left[-0.5\left(\frac{E - E_0}{\sigma}\right)^2\right], \tag{3.4}$$

where σ is the standard deviation (σ = FWHM/2.35), N_0 the peak area, and E_0 the peak centroid.

The energy resolution can be written in a way associated with the statistical fluctuations in the conversion from energy to charge carriers in the detector. Considering that the detector has a conversion factor ϵ, from energy E to number of carriers n, the standard deviation of number of carriers is:

$$\sigma_n = \sqrt{\frac{E}{\epsilon}}. \tag{3.5}$$

Since σ and σ_n follow the relation $\sigma = \epsilon\sigma_n$, the FWHM can be written as:

$$\text{FWHM} = 2.35\sigma = 2.35\epsilon\sigma_n = 2.35\sqrt{E\epsilon}. \tag{3.6}$$

Following Poisson statistics, the variance of the generated charge in semiconductor detectors should be higher than the one that is verified. To account for such deviation, the Fano factor, F, is introduced in the standard deviation:

$$\sigma = \sqrt{F\bar{n}}, \tag{3.7}$$

where $\bar{n}$ is the average number of carriers. Accounting the Fano factor, the resolution is written as:

$$\text{FWHM} = 2.35\sqrt{FE\epsilon}. \tag{3.8}$$

Nowadays, the energy resolution of X-ray fluorescence detectors are lower than 200 eV.

Another very important parameter of the detection system is the detection efficiency. This parameter accounts for the fact that from all the photons that are emitted from the source, only a fraction will actually interact with the detector and deposit all of their energy. The efficiency of the detection system is composed by three contributions. The first, the geometrical efficiency, is related to the active area of the detector, the distance with respect to the source, and the solid angle. Second, the intrinsic efficiency, accounts for the fact that even photons entering the detector may leave without interacting with it. The intrinsic efficiency is thus related to the absorption coefficient of the detector material (for a given photon energy), and by the detector thickness. And third, the photopeak efficiency, accounting that even photons that interact with the detector may not deposit all of their energy [56].

3.2 X-ray spectrum

The X-ray spectrum obtained from XRF technique exhibits characteristic features related to the physical interactions occurring all along the analysis, from the X-ray primary beam production, the interaction with the sample, to the detection of the radiation and the

conversion of the output signal. The understanding of the different features is crucial for a good evaluation of the X-ray spectrum and the consequent analysis and quantification of the sample. The features visible in the spectrum are dependent on the sample analysed, and also on various experimental conditions, such as primary X-ray source, and detection system.

3.2.1 Characteristic peaks

The main features of the X-ray spectrum, the characteristic peaks are the result of the characteristic X-ray photons emitted from the sample, due to atomic de-excitation. The energy of the characteristic X-rays is given by a Lorentz distribution, with FWHM given by the Heisenberg principle, as explained in Section 2.1.2. In an ideal experimental system, the spectrum's characteristic peaks would follow this Lorentz distribution, but since there is a (nearly) Gaussian contribution from the detection system, the peak profile is a Voigt distribution, a convolution between the Gaussian and the Lorentz distributions. The width of the Lorentz distribution of K- and L-shell lines are of the 10 eV order, for elements in the range $Z < 50$, which is much smaller than the order of the width associated with the experimental system (100-200 eV). As such, the profile of the characteristic peaks can be considered a Gaussian function, as a first-order approximation [59]. This approximation is employed by most of software and codes that adjust profiles to the X-ray spectrum features. The characteristic peaks may present a tail in the low-energy side due to incomplete charge collection in the detector, as described in Section 3.1.3. To describe the tailed peaks, many functions can be used. Usually, codes and software add some kind of tail function to the Gaussian profile, usually an exponential function [60].

Even though the characteristic peaks of interest are those corresponding to elements present in the sample, depending on the experimental conditions, it is possible that the spectrum contains characteristic peaks of elements that are not in the sample. For example, elements present in the collimators, or even in air, can also be excited with enough intensity so that their characteristic X-ray photons reach the detector with significant intensity.

3.2.2 Artifact features

Peaks related to the artifact events occurring in the detection can be visible in the spectrum, as described in Section 3.1.3. Escape peaks may be visible for energies 1.74 keV lower than those of characteristic peaks, if Si(Li) detectors are used. Sum peaks can appear in energies that are the sum of two characteristic peak energies. Most software is able to recognize sum and escape peaks. But they do not reinstate their intensity to the respective characteristic peaks.

3.2.3 Background

The background of the spectrum is due to a large number of contributions. If the X-ray beam exciting the sample is polychromatic, the major contribution to the background is the scattering from the sample. Typical X-ray tubes produce a primary X-ray beam with an energy continuum due to Bremsstrahlung radiation (see Section 3.1.1); the scattering of those X-rays from the sample into the detector will lead to an energy continue in the X-ray spectrum. Furthermore, since Compton scattering (unlike Rayleigh scattering) leads to change in the photon's energy, the shape of the energy continue in the X-ray spectrum will not be the same as the shape of the primary beam energy continuum, thus difficultting the understanding of the spectrum background even if the primary beam's spectrum is very well known.

Furthermore, incomplete charge collection in the detector also contributes to the background, since the cumulative effect of all tails contributes to the continuum of the spectrum. This is specially significant for low energies, where the background is usually higher than what is predicted due to the scattering.

For all the reasons previously mentioned, the background shape is very complex to define. Different codes and software use different methods to define the background and subtract from to the spectrum.

3.2.4 Coherent peak

If the X-ray beam exciting the sample is mono-chromatic, or approximately mono-chromatic, the elastic scattering of the beam from the sample will result in it reaching the detector with the same energy. As such, the spectrum will exhibit a peak at that energy, the coherent peak, which can be also named as elastic peak or Rayleigh peak. The profile of this peak can be described as a Gaussian function since it is a resultant of the (almost) Gaussian contribution of the energy resolution of the detection system on the mono-chromatic scattered radiation.

3.2.5 Incoherent feature

Following the previous case, where the X-ray beam exciting the sample is mono-chromatic, the inelastic scattering of the beam results in another feature in the spectrum, the incoherent (or inelastic, or Compton) feature, which is usually also referred to as Compton peak. Since the inelastic scattered photon's energy is lower than the incident photon's energy, the Compton peak is found at the low-energy side of the Rayleigh peak, with an energy difference which can approximately be given by Eq. 2.21. Due to the relation of the scattering angle and energy loss in the scattering (as explained further in Section 2.1.4), the incoherent feature does not follow a Gaussian distribution. Due to the energy-angle relation, the shape will be affected by all experimental factors which affect the angles of the beams, such as the relative positions of source, sample and detector, and the

beam collimation, besides being affected by the sample material, energy of the excitation beam, and the detector's parameters. However, the shape can always approximately be described as a Gaussian distribution with a low energy tail. To do so, many different ways are employed by different codes and software.

3.2.6 Spectrum analysis

From the X-ray spectrum the elemental analysis is performed by identifying the characteristic peaks. In Fig. 3.4 it is presented a spectrum where the scattering peaks are present.

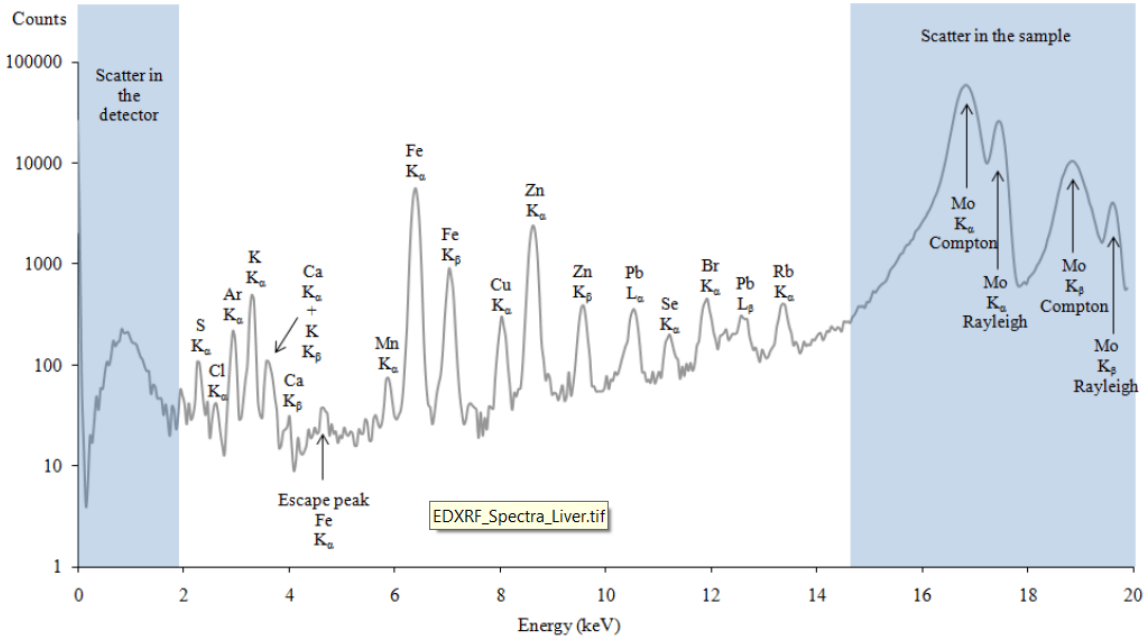

Figure 3.4: Example of X-ray fluorescence spectrum.

Since the energies of the X-ray photons emitted in the atomic de-excitation are specific to each element and atomic transition, each characteristic peak can be matched to an element. In practice, the matching of peak to element isn't always trivial. The identification can be hindered by the overlapped of peaks which are close in energy, or by peaks that are covered by the background, or other features such as the Compton peak. Nowadays, the identification of the elements from the peaks in the spectrum can be performed automatically by a large number of dedicated software or codes. Nevertheless, in many cases, after the automatic identification, a "manual" identification is usually performed, as to guarantee a correct analysis.

In addition to the elemental qualitative analysis, the main goal of the EDXRF technique (as well as other X-ray spectroscopy techniques) is the quantitative analysis. The quantitative analysis gives information about the relative amount of the elements in the sample, in terms of their concentration, usually in parts per million (ppm) or $\mu g.g^{-1}$. There are different methods to perform this type of analysis. For the choice of the method

to use, it must be taken into consideration the desired application, as well as the method's advantages and disadvantages. Most methods start with the identification and quantification of the characteristic peaks. For this, the different features of the spectrum must be identified and deconvoluted from one-another. Such is performed in many different ways, by many different existing software and codes. While the fitting of Gaussian or Voigt functions to the characteristic peaks can be relatively trivial, the mathematical description of the background usually presents a challenge, for the reasons discussed in Section 3.2.3. As consequence, there isn't a realist physical model that describes the background, for which usually softwares present more than one alternative to adjust a function to the background, and the alternative that improves the least-square fitting procedure is usually chosen. The different features of the spectrum are fitted, and a χ^2 value is obtained, i.e. the difference between the mathematical function and the spectrum. After the spectrum is de-convoluted and the different features are fitted, the background is usually removed from the spectrum and the area of each peak is then quantified. This procedure is shown in Fig. 3.5. The area of the peak is denominated as the peak intensity, and it is from this quantity that the respective element concentration can be obtained.

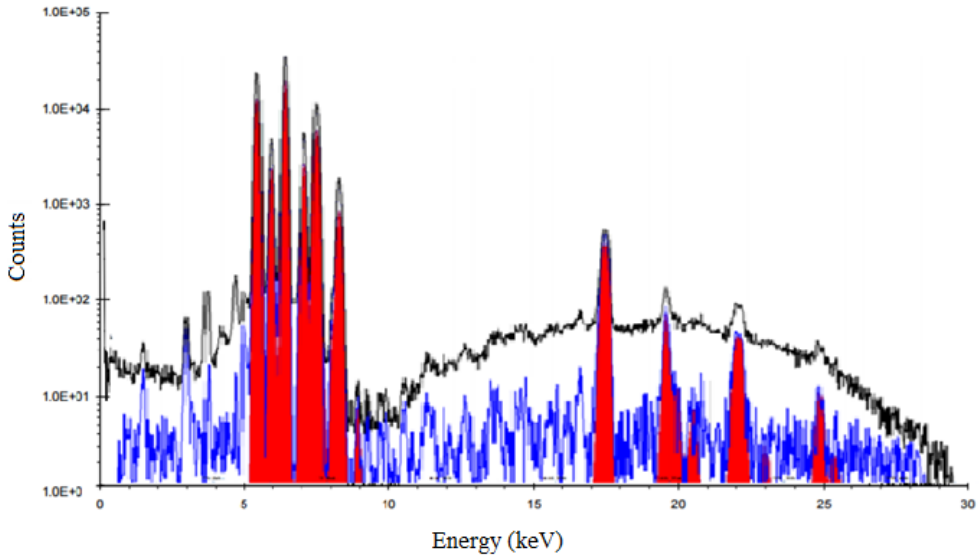

Figure 3.5: Example of X-ray spectrum deconvolution and background subtraction.

3.2.7 Methods for elemental quantification

The intensity I_i of a characteristic peak, relative to an element i, is not only the result of the primary X-ray fluorescence emitted from the element i, but also of effects with the other j elements present in the sample. The primary fluorescence can be absorbed by all elements in the sample, leading to excitation and possible de-excitation by emission of more X-ray fluorescence, such is usually described as secondary fluorescence. This can be repeated indefinitely, leading to third-order fluorescence, fourth-order fluorescence, etc, although each order is increasingly more uncommon. Other elements j can absorb

the characteristic X-rays from element i, reducing the intensity I_i of the peak related to element i, but it is also possible that fluorescence from other elements j excite the element i, contributing to it's fluorescence emission and increasing the intensity of the characteristic peak I_i [54, 61]. The amount of X-ray emission and absorption for each element is directly proportional their concentrations c. For these reasons, the relation of I_i and c_i is not linear, and it must account for the effects that all elements j have on the peak intensity I_i, the matrix effects. The accurate description of this relation, accounting for matrix effects, was the subject of many works since the 1950s [62–64]. In 1955, Sherman proposed the equation for the peak intensity of an X-ray line with energy E_i, related to the X-rays emitted by an element i, with known concentration c_i, in a sample being excited by a poly-chromatic X-ray beam, and accounting for all matrix effects [65]. This became known as the Sherman equation, and its importance is demonstrated by the fact that it became the theoretical basis of all modern methods for the correction of matrix effects. Sherman's equation, in its original form, is written as [65]:

$$I_i(E_i) = g_i c_i \int_{E_{\text{edge},i}}^{E_0} \frac{I_0(E)\mu_i(E)}{\mu'_s(E) + \mu''_s(E_i)} \left[1 + \sum_j c_j \delta_{ij}(E)\right] dE. \tag{3.9}$$

where g_i is a instrumental factor, dependent on the experimental conditions. In the previous equation, $\mu'_s(\lambda)$ is the effective mass absorption coefficient of the sample for the incident energy E, accounting for all the absorption of the incident beam in the sample, and $\mu''_s(\lambda)$ is the effective mass absorption coefficient of the sample for the characteristic X-ray energy E_i, accounting for all the absorption of the characteristic X-rays in the sample. $\delta_{ij}(E_i)$ is an enhancement factor that accounts for how much the characteristic X-rays of element j, with energy E, enhance the emission of characteristic X-rays of element i, with energy E_i. These quantities are dependent on several fundamental parameters, such as sub-shell fluorescence yields, jump-ratios, etc. Their derivation is defined further in Sherman's original work [65].

In the 80s, Rousseau presented the Fundamental Algorithm [66, 67], which was deduced directly from the Sherman equation with algebraic manipulation and no approximations. A later work from Rousseau and Bouchard presented an experimental verification on the algorithm [68]. Rousseau presented the new equation [66]:

$$c_i = R_i \frac{1 + \sum_j \alpha_{ij} c_j}{1 + \sum_j \epsilon_{ij} c_j}, \tag{3.10}$$

which is written as function of the peak's relative intensity R_i, this quantity is given as:

$$R_i = I_i(E)/I_{(i)}(E), \tag{3.11}$$

where $I_{(i)}(E)$ is the intensity emitted by a sample composed only by the element i. Although the Fundamental Algorithm (Eq. 3.10) and Sherman's equation (Eq. 3.9) are different in form, both represent exactly the same since the former was derived with only

algebraic manipulation from the later. The coefficients from Eq. 3.10, α_{ij} and ϵ_{ij}, are coefficients correcting for absorption and enhancement effects, respectively. Eq. 3.10 shows that the concentration c_i is proportional to the relative measured intensity R_i, and the α_{ij} coefficients, which includes all mass absorption coefficients, correct for all absorption effects caused by element j on the element i, and the coefficients ϵ correct for all enhancement to element i caused by element j. Written in this form, the Fundamental Algorithm makes it easier to understand the physical principles behind Sherman's equation. The derivation of the Fundamental Algorithm from Sherman's equation, and the definition and derivation of α_{ij} and ϵ_{ij} are presented in several of Rousseau's works [61, 66, 69].

As an alternative to Sherman's equation, or the Fundamental Algorithm, the relation between the intensity of the respective I_i and the respective concentration c_i can be written as [9]:

$$I_i = I_0 K_i m c_i A_i^{(\mathrm{att})}, \tag{3.12}$$

where I_i is the peak intensity, I_0 the intensity of the beam exciting the sample, K_i a calibration factor, $A_i^{(\mathrm{att})}$ the attenuation factor, m the sample's mass per unit area given in (g.cm^{-2}), and c_i the element's concentration. For an homogeneous sample, the sample's mass per unit area is given as:

$$m = \rho x, \tag{3.13}$$

where ρ is the sample's mass density (g.cm^{-3}) and x the sample thickness (cm). The calibration factor K_i is given by the following expression:

$$K_i = \Omega \varepsilon_i C_i' \omega_i \sigma_{X_i} P_{n->m}, \tag{3.14}$$

where Ω is the detector solid angle, σ_{X_i} is the ionization cross-section, ω_i the fluorescence yield, $P_{n->m}$ the transition probability from a sub-shell n to a sub-shell m, C_i' the absorption in air and in the detector window, and ε_i the detector efficiency. The attenuation factor $A_i^{(\mathrm{att})}$, from Eq. 3.12 accounts for the matrix effects, and it can be written as [54]:

$$A_i^{\mathrm{att}} = \frac{1 - \exp\left[-\sum_j c_j \left(\frac{\frac{\mu}{\rho}(E_{1,j})}{\sin\phi_1} + \frac{\frac{\mu}{\rho}(E_{i,j})}{\sin\phi_2}\right) m\right]}{\sum_j c_j \left(\frac{\frac{\mu}{\rho}(E_{1,j})}{\sin\phi_1} + \frac{\frac{\mu}{\rho}(E_{i,j})}{\sin\phi_2}\right) m}, \tag{3.15}$$

where $(\mu/\rho)(E_1, j)$ is the mass attenuation coefficient of the element j for the energy E_1 exciting the sample, $\mu/\rho(E_i, j)$ is the mass attenuation coefficient of the element j and for the energy of the energy E_i of the characteristic X-ray photons, emitted by element i, ϕ is the angle of the radiation exciting the sample, and ϕ_2 the angle of the emitted radiation.

The determination of the element concentration from the respective peak intensity can be achieved either through mathematical methods to solve the equations presented in this section, through comparison with standard samples, or a combination of both.

3.2.7.1 Comparison with standards

Quantification can be achieved by using standard reference materials with similar composition to those of the unknown sample. By measuring the peak intensity I_i for several standards in which the element's i concentration, c_i, is known, a linear calibration $c_i(I_i)$ can be obtained [2]. This assumes that the composition of the standards are similar enough to consider that the matrix effects are approximately the same for each standard. Considering the composition of the unknown sample is similar to that of the standards, a direct correlation can be made from the linear calibration, where the measured peak intensity will correspond to the element concentration. This is usually referred to as "comparison with standards" method, and it is performed by many quantification software. There are several disadvantages and limitations to this method. The consideration that the matrix effects are the same among the different standards and the unknown sample is an approximation that limits to some extent the accuracy of the quantification [2]. This method becomes increasingly less accurate, with the more different the samples's composition is compared to the standard material. Also, the accuracy of the unknown sample quantification is dependent on the accuracy of the standards analysis. Furthermore, it does not consider possible heterogeneity, and the difference in density between standards and the unknown sample. Other drawbacks that must be considered are the unavailability of standards for certain type of materials, and the monetary costs associated with obtaining the standards.

3.2.7.2 Fundamental Parameter method and Influence Coefficient method

As an alternative to comparison with standards, the Fundamental Parameters method or the Influence Coefficient methods can be employed. These methods aims to achieve quantification employing mathematical methods to solve the equations relating peak intensity I and concentration c (as in Eqs. 3.9 or 3.12). Both methods start from an equation that describes the intensity of the characteristic peak as function of the respective element concentration and several fundamental parameters. In the case of a poly-chromatic beam, the equation employed by the method describes the intensity of the characteristic peak with an integral that describes the contribution all beam energies in the generation of fluorescence, such as for example, the Sherman equation (Eq. 3.9). Usually, several elements have unknown concentrations, and as such, there are set of equations to be solved. The difference of Fundamental Parameters method and Influence Coefficient method (or α-method) lies on the approach to solve these equations.

In the Influence Coefficient method the integration over the many energy values of the beam, as in Eq. 3.9, is replaced by the evaluation of the integrand at a single, effective, excitation wavelength, usually denominated the "effective wavelength", which is dependent on the sample composition. As such, the non-linear equations are transformed into linear equations. The new linear equations include influence coefficients α_{ij} which account for the influence of the elements j in the fluorescence emission of element i [70]. These

coefficients were derived by Sherman in 1953 [71]. From there on, much work was performed to derive the number of coefficients that should be included in the description of multi-element samples, and on the determination of the effective excitation wavelength. The effects of third elements are accounted by either including more coefficients, or by calibrating in various concentration ranges. For this method to work, all the sample's elements must be accounted for in the calibration. The calibration is performed recurring to a series of standards which are of similar composition to the analysed sample. As such, the method is fit for the analysis of samples from which most of the element's concentration is known, but is not fit for truly unknown samples. Furthermore, it is restricted to bulk materials. This method was a good alternative in times where personal computers where not as available, and as powerful, as nowadays, for which the linearisation of the equations was necessary.

Unlike the Influence Coefficient method, in the Fundamental Parameter method no simplifications are performed to solve the equations. The inter-element effects are not introduced by coefficients, but rather, they are calculated for each sample composition. Since no approximations are performed, the Fundamental Parameter method has the potential to be more accurate than the Influence Coefficient method, and since nowadays the solution of the integral equations are achievable with modern day computers [72], this method as became widely more used in X-ray fluorescence analysis. Several codes and software perform this method. Although there may be differences between how each software or code performs the method, the basis is generally as follows in the next paragraphs, as explained further in De Boer and Brouwer work [72].

The experimental factor g (as presented in Eq. 3.9) can be obtained from a calibration, measuring the spectrometer response for each fluorescence energy of interest. Such is performed by measuring the characteristic peak intensities I_m for one or more standards samples, and comparing with the respective calculated theoretical intensities I_t. Considering that I_t contains all matrix effects, the instrumental factor is related to I_t and I_m:

$$I_m = gI_t. \tag{3.16}$$

This experimental factor will include detector efficiency, and will not be dependent on the sample composition.

The composition of the unknown sample is performed in an iterative way, starting from a first guessed sample composition, and sample thickness, as input. From these, peak intensities $I_{t,i}$ are calculated from the set of equations, and multiplied by the instrumental factor g_i. The theoretical intensities are compared with the measured intensities $I_{\mathrm{m},i}$, and a χ^2 value is calculated:

$$\chi^2 = \sum_i \left(\frac{I_{m,i} - f_i I_{t,i}}{\sigma_i} \right)^2, \tag{3.17}$$

where the standard deviation σ of the intensities are obtained from the uncertainty in the instrumental factor, accounting for statistics and experimental uncertainties. Element

concentrations c_i are changed iteratively, and the theoretical intensity is recalculated, until a minimum value of χ^2 is reached. In this approach, more than one characteristic peak intensities (measured and calculated) can be introduced for a single element. With such inclusion, there are more peak intensities values, N_{peak}, than the number of unknown parameters N_{unknown} (element concentrations and sample thickness). The number of degrees of freedom v is given as:

$$v = N_{\text{peak}} - N_{\text{unkwon}}. \tag{3.18}$$

This method can also be employed to layered samples. In this case, the unknown parameters are the element's concentrations and the thickness of each layer, which are obtained through the same iterative procedure applied to each layer.

In the equations solved by the Fundamental Parameters method (such as Eq. 3.9 or 3.12) there are a large number of underlying Fundamental Parameters, such as: absorption coefficients, emission energies, absorption energies, fluorescence yields, jump ratios, etc. Codes and software recur to internal tabulations of such parameters. The uncertainties of some fundamental parameters are often large. Nevertheless, even for parameters with accuracy from 5% to 10%, the FP method can produce results with accuracy within 1% if standards are used. This is explained by the fact that the calibration with standards to obtain the instrumental factor g (Eq. 3.9) will eliminate the uncertainties in the FP parameters. Furthermore, uncertainties in FP parameters largely cancel with each other in the peak intensity equation.

When compared with the Influence Coefficient method, the FP method is more suitable for quantification of samples where the full composition is unknown, due to the fact that the inter-element effects are calculated for each case. Even in the cases where only some of the element's concentrations are unknown, which is the case where the Influence Coefficient method is more suitable, the FP method can compete. Although the FP method has the potential to achieve quantification with accuracy lower than 1%, especially when allied with the use of standards for calibration, there are several shortcomings that need to be considered. The equation describing peak intensity account only for primary- and secondary-order fluorescence. For some specific sample composition, tertiary- and higher-order fluorescence can have significant contribution to the enhancement of the characteristic peaks of interest. Enhancement by electrons is also not accounted. In some cases, electron impact ionization by photo-electrons or Auger electrons can significantly contribute to the ionization of the element's of interest, and consequently to its fluorescence emission. The equation also assumes a parallel incident beam and parallel emitted beam. And while the sample is considered homogeneous, or composed by homogenous layers, some lateral inhomogeneities may exist. Most of this limitations are somewhat corrected by the calibration with standards because uncertainties in the calculation of the intensities of the standards cancel those in the calculation of the unknown samples. Some software and codes implement the FP method with models that address some of this limitations, such as: accounting for tertiary-order fluorescence,

angle spread of the beam, 3D inhomogeneities in the sample, electron contribution to the emission, etc, increasing the accuracy of the method. Nevertheless, the built-in tabulations of Fundamental Parameter values in the existing software are in almost all cases, if not all cases, inaccessible to the user. As such, the inaccuracy of Fundamental Parameters can not be addressed by simply changing the parameters values.

3.2.8 Detection Limits, Precision and Accuracy

In order to check the suitability of an analytical technique to measure a given element in a given kind of matrix, the precision, accuracy and detection limits have to be taken into account. The method precision is obtained by measuring several times the peak intensity, to take into account the statistical fluctuations of the measurements. The detection limit value represent the lowest statistically significant concentration value for a given element to be able to be quantified from a given matrix. If n measurements of the total counts for a specific energy are performed, the total counts will fluctuate due to statistics. The average number of total counts is given as:

$$N_{\mathrm{T}} = \sum_{i=0}^{n} N_i/n. \tag{3.19}$$

Since the counts follow a Poisson distribution, the average total counts have the following standard deviation:

$$\sigma_{\mathrm{T}} = \sqrt{N_{\mathrm{T}}}. \tag{3.20}$$

If these counts correspond to an energy (or channel) of a characteristic peak, the total counts are the sum of counts relative to the characteristic peak, N_{p}, and the background, N_{B}. As such, in this case, σ_{T} may be written as:

$$\sigma_{\mathrm{T}} = \sigma_{\mathrm{p}} + \sigma_{\mathrm{B}}, \tag{3.21}$$

where σ_{p} is the standard deviation relative to the peak counts, and σ_{B} is the standard deviation relative to the background counts. If the number of occurrences is sufficiently large the Poisson distribution can be described as a Gaussian distribution [73]. In order for the peak to be significantly distinguished from the background, N_{p} must be distinguishible from N_{B}, which happens with 97% probability, according to Gaussian distribution properties, for $N_{\mathrm{p}} > N_{\mathrm{B}} + 3\sigma_{\mathrm{B}}$ [59]. The Detection Limits (DL), can be given by subtracting N_{B} to the previous equation [74]:

$$DL = c_i \frac{3\sigma_{\mathrm{B}}}{I_{\mathrm{P}_i}} = c_i \frac{3\sqrt{N_{\mathrm{B}}}}{N_{\mathrm{P}}}, \tag{3.22}$$

where c_i the concentration of element i, and I_{P_i} is the characteristic peak intensity related to element i. For higher counting time, and consequentially higher counting rates, the detection limit is lower. The detection limit is directly proportional to the background counts, and as such, spectrum with lower background allow for better detection limits. Since c_i must be known, the calculation of detection limits is performed by measuring standards.

3.2.9 Triaxial Geometry

In the planar geometry setup, unless a mono-chromatic (or nearly mono-chromatic) beam is used, the X-ray spectrum obtained will contain the signal of the background radiation reaching the detector, which increases the detection limits. Furthermore, because of the relatively difficult mathematical description of the background, the de-convolution between background and characteristic peaks may contain some uncertainty, which will reflect in uncertainty on the quantification procedure. For these reasons, mechanisms to minimize the background are employed in some setups, by (approximately) monocromatizing the excitation beam. One way in which such can be achieved is by using filters in the X-ray tube output, which will attenuate the lower energy radiations emitted by the tube. For this, the filters material should have atomic numbers for which the lower energy attenuation is relatively high, and the high-energy attenuation is relatively low.

Another way to monocromatize the excitation beam is by using a secondary target. With this method, the primary excitation beam (the beam emitted from the X-ray tube) does not excite the sample to analyse, but instead excites the secondary target. And it is the radiation emitted from the secondary target, the secondary beam, that will excite the sample. The secondary beam radiation is mainly composed by the secondary target's characteristic X-ray fluorescence radiation, and by the primary beam radiation which is scattered from the secondary target to the sample. Although the secondary beam is not entirely monochromatic, it is much more monochromatic than the primary beam. This is explained by the fact the fluorescence X-rays component of the secundary beam are mainly the fluorescence photons emitted from the secondary target's K-L_2 and K-L_3 transitions, due to their higher transition probabilities, and for which emitted photons have similar energies. Furthermore, only a small component of the polychromatic primary beam scatters from the secondary target into the sample. It should be noted that the choice of the secondary target material must take into account that its material must be able to be excited by the primary beam energies, and its K-L_2 and K-L_3 fluorescence X-rays must have enough energy to excite the sample.

As complement to the use a secondary target, a triaxil geometry can be employed in order to reduce further the polychromatic continuum radiation from the X-ray tube reaching the detector. In this geometry, as presented in Fig. 3.6, the X-ray tube, secondary target, and sample, form a 90º angle.

This way, the primary beam X-rays scattered from the secondary target into the target are minimized, since Klein-Nishina cross-section is lower for this angle (see Sections 2.1.4 and 2.1.5). For the same reason, the secondary target, sample, and detector, also form a 90º angle, minimizing the scattering from the sample into the detector. The primary beam's Bremsstrahlung radiation that is scattered from the secondary target to the sample becomes polarized almost entirely in the direction perpendicular to that of the scattering plane. For photons with such polarization, the differential scattering cross-section becomes null for scattering angles $\theta = 90$, $\phi = 0$ (see Section 2.1.5), and as such, the X-ray

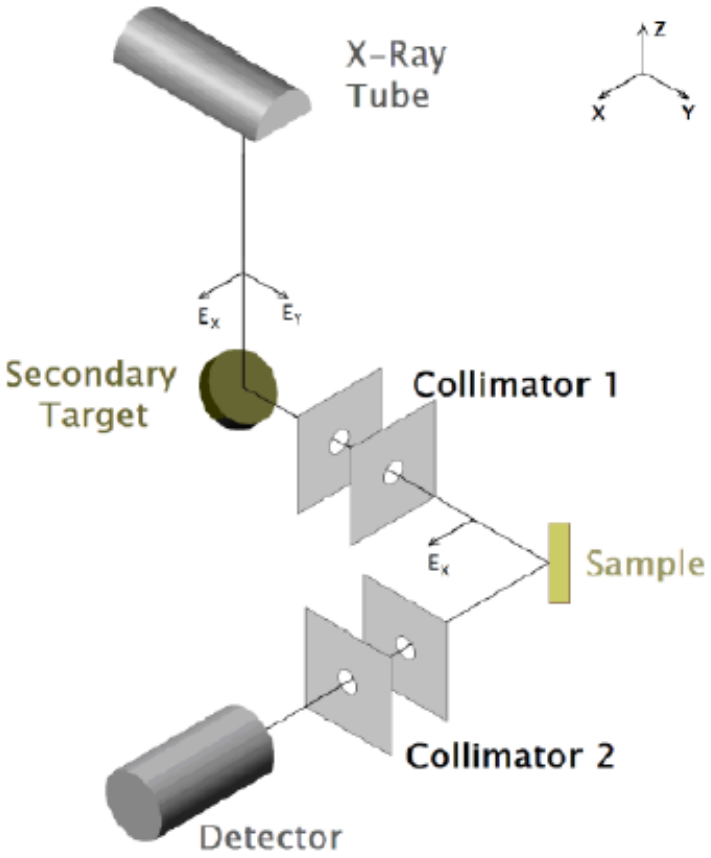

Figure 3.6: Schematic representation of a triaxial geometry EDXRF setup, using a secondary target. Figure adopted from Guimarães work [75].

tube polychromatic radiation scattering from the sample to the detector is extremely minimized due to polarization cut-off [76]. The secondary target fluorescence has polarization with isotropic direction, and as such, unlike the primary beam bremsstrahlung radiation, it can be scattered into the detector, resulting in Coherent and Incoherent features in the XRF spectrum. To ensure a good minimization of the scattering, the beams must be collimated, although even so there is always scattered radiation reaching the detector. The more restricted the collimation, the more the intensity loss of the beams. Furthermore, the secondary beam intensity is much lower than the primary beam intensity. For these reasons, EDXRF with this type of geometry will result in spectrum with much lower intensity when comparing with a spectrum obtained in the planar geometry. Fig. 3.7 highlights the difference in spectra obtained from using this geometry compared to a typical XRF spectrum obtained from a planar geometry.

As seen if Fig. 3.7 the spectrum background is greatly reduced when comparing with the characteristic peaks, thus improving detection limits (as can be seen from Eq. 3.22). With this method, limits of detection of tens of ppm (or $\mu g.g^{-1}$) can be achieved for several elements of interest to cultural heritage studies [78, 79] and toxicology studies [80,

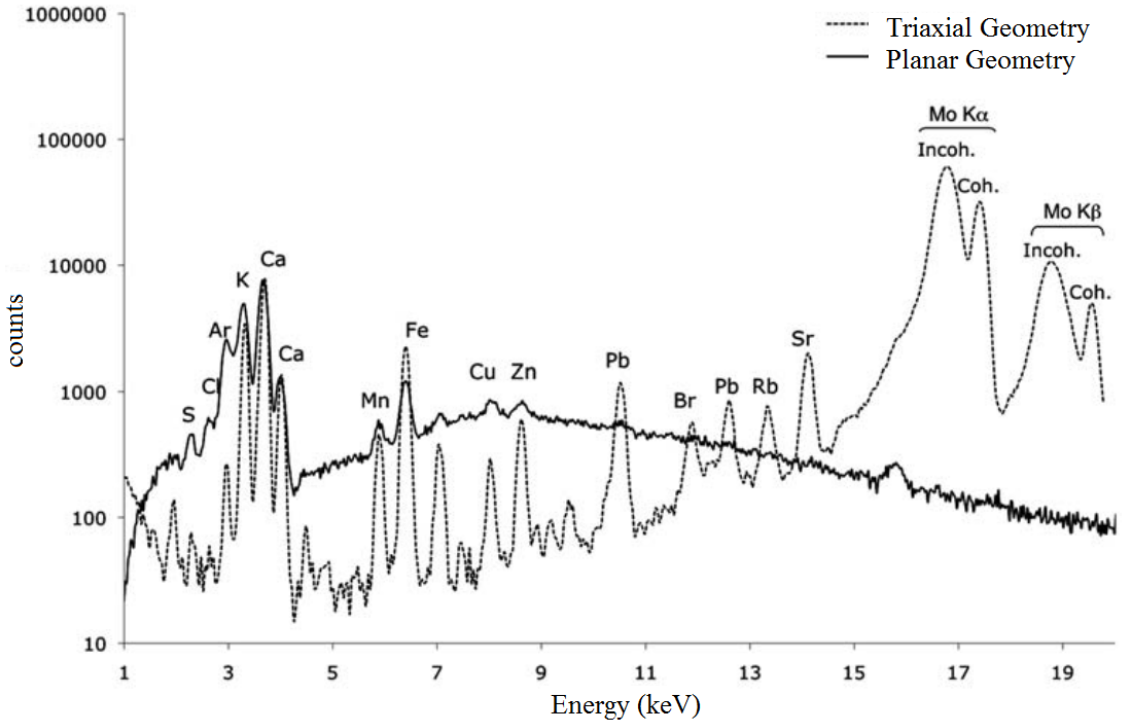

Figure 3.7: Comparison of EDXRF spectra obtained from planar and triaxial geometry. Figure adopted from Pessanha *et al.* [77].

81]. The advantages of the method have triggered recent the development and investment of triaxial geometry spectrometers (NEXCG,1 SPECTRO Xepos2 and Epsilon-53) by different manufacturers.

3.2.10 Analysis using the Coherent and Incoherent scattering features

Although XRF analysis is performed in most cases by evaluation of the characteristic peaks in the X-ray spectrum, further analytical information can be obtained by exploiting the X-ray scattering features. For experimental conditions in which the sample is excited by a nearly, or completely, monochromatic beam, the Rayleigh Scattering and Compton Scattering features are clearly distinguishable in the spectrum. Due to Rayleigh and Compton scattering different dependencies on the atomic number of the sample's elements, the evaluation of their respective features in the spectrum can lead to information of the average atomic number, Z_{avg}, of the sample [3].

For the Rayleigh scattering differential cross-section, the dependency with atomic number comes only from the form factor dependence, since Thomson differential cross-section is only dependent on scattering angle and energy (as explained in Section 2.1.3). Equivalently, for the Compton scattering differential cross-section, the dependency with atomic number comes only from the incoherent function dependency, since Klein-Nishina differential cross-section depends only on energy and scattering angle (see Section 2.1.4). The Compton-to-Rayleigh ratio can be obtained by dividing the respective differential

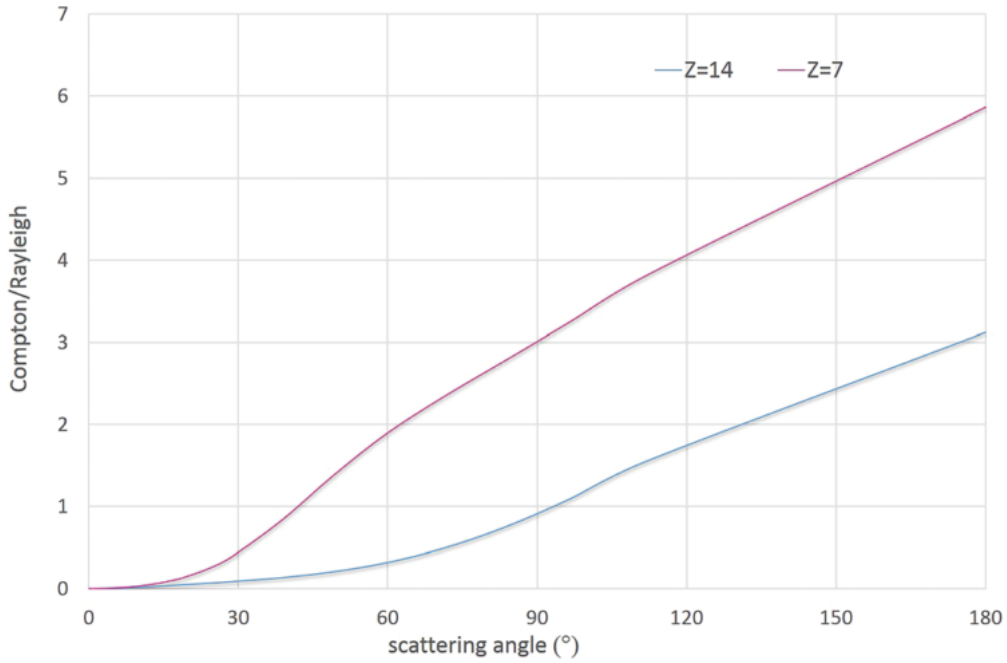

Figure 3.8: Compton-to-Rayleigh ratio as function of scattering angle. Values for different atomic numbers are presented. Figure adopted from Pessanha *et al.* work [4].

cross-sections. Fig. 3.8 presents the dependency of this ratio with the scattering angle, for different atomic numbers.

For energies bellow approximatly 10 keV, the Compton scattering is insignificant when compared with Rayleigh scattering. For energies of above 15 keV, Compton scattering is predominant for very low Z values. However, Rayleigh scattering increases more rapidly with Z, and it quickly becomes predominant as Z increases. For energy values of dozens of keV, the ratio can be quite sensitive to variations of the atomic number Z.

The specific dependence of this ratio on atomic number makes it an useful feature for analysis. Furthermore, this ratio can be extracted in a relatively easy way from the X-ray spectrum by dividing the intensity of the respective features, specially if the scattering peaks are at higher energies. A calibration curve of Compton-to-Rayleigh intensity ratios $R_{C/R}$ in function of average atomic number Z_{avg} can be obtained by evaluation the scattering features of several standards with the same material type, and under the same geometrical conditions [3, 4]. Partially unknown samples with the same type of material can then be analysed and to the measured Compton-to-Rayleigh intensity ratio an average atomic number Z_{avg} can be corresponded through the calibration curve. There are several advantages to this method of analysis, particularly for lighter matrices. It allows for an indirectly extraction of light elements, which are "invisible" to the X-ray spectrum. Furthermore, the method is particularly sensitive for light matrices, as a small variation of Z_{avg} leads to a high variation of the ratio [3]. Such is due to the fact that, for low atomic numbers, the Rayleigh scattering increases much more rapidly than the Compton scattering. This method can be used in the identification and characterization

of low-Z materials, as shown in Pessanha *et al.* [4] work. By comparing the measured $R_{C/R}$ for a sample with the calibration curve, this method allows for a calculation of light elements which are "invisible"in XRF, or even calculation of heavier impurities in light materials which may not be detected by XRF [5]. Using this method, materials can easily be distinguished from each other, by measuring the $R_{C/R}$ ratio. Such is useful for choosing samples to be used in experimental measurements. In light materials, even differences of Z_{avg} as low as 0.1 can be distinguished due to the method particular sensitivity in low-Z_{avg} materials. Furthermore, the method can be used to correct standards.

When comparing this method with methods that evaluate the Compton and Rayleigh scattering independently, this method has the advantage that experimental factors, such as acquisition times, detector acceptance angles, etc, do not have to be taken into account, since they are the same for both type of scatterings, as thus are cancelled in the calculation of the Compton-to-Rayleigh ratio.

For these reasons, evaluating the Compton-to-Rayleigh ratio allows for an analytical method that further improves and complements the usual characteristic peak based quantitative analysis, particularly for low average atomic number samples.

Chapter 4

Code for EDXRF standardless analysis

4.1 Monte Carlo simulations

While there is no consensus on the definition of Monte Carlo methods, they can generally be defined as algorithms that consist in repeated random sampling and statistical analysis as a method for obtaining numerical results, which are usually approximate solutions of deterministic problems. While there are a wide range of MC methods, they all generally follow the following steps. First, the statistical properties of the possible inputs are determined. Following these properties, a large set of possible inputs is generated. These set are then used to perform deterministic calculations. And finally, the results are statistically analyzed. The definition of Monte Carlo simulations is also non consensual. However, they are generally described as simulations which use MC methods, usually employed to model complex problems with a large number of random variables, where analytical or numerical solutions usually do not exist or are too difficult to implement. As such, they are random experimentations, as the results of these experiments are not well known. These simulations typically include many unknown parameters, which are difficult to experimentally obtain. While the simulations are based on random numbers to implement random sampling, it is not always necessary that the numbers are truly random. In fact, most MC simulations are performed using pseudorandom sequences, which allow for testing, and running simulations with the same outcomes more than once.

Monte Carlo methods were first employed by scientists at the nuclear weapons project at Los Alamos Scientific Laboratory, having been central to the simulations required for the Manhattan Project and to the development of the hydrogen bomb. The method was named for the Monaco resort town which was renowned for its casinos. While at a earlier stage these methods were mainly employed in physics, physical chemistry, and operations

research, nowadays, MC methods and MC simulations are used to model physical and conceptual systems in a much wider range of areas, including finance, mathematics, game theory, engineering, insurance, among many others.

4.2 A standardless XRF method using Geant4

There are quite a number of codes and software for quantitative and qualitative EDXRF analysis using the FP method, such as NRLXRF [6, 7] (from Naval Research Laboratory), NBSGSC [7, 8] (from National Bureau of Standards), XRFAES [9] (from Chalmers University of Technology), WinAxil (from Canberra) [10], PyMCA [11, 12] (developed by the European Synchrotron Radiation Facility (ESRF) software group), among others. Most of the software used nowadays implement the Fundamental Parameters method as well as the comparison with standards method. The existing codes and software mostly differ from one-another in the completeness of the physics models they employ. As such, some of them can be more suited for specific conditions such as the type of sample matrices to analyse, and the experimental setup conditions.

In the last decade, simulations performed with Monte Carlo methods have been applied to experiments involving X-ray fluorescence. These simulations provided assistance in the construction of X-ray spectrometers and analysis of the data acquired. Some of the simulations where performed from dedicated in-house codes, such as 3D μ X-ray [13], X-ray optics [14], and X-ray tomography [15, 16], while others were performed using general-purpose codes, such as MCNP [**mcnp**, 17], PENELOPE [18, 19], and Geant4 [20–22]. Regarding EDXRF technique, many Monte Carlo simulations have been applied for a quantitative analysis from the comparison of the simulated X-ray spectrum with the experimental spectrum, such as XMI-MSIM [23] and XRMC [24, 25]. MC simulations have also been applied in studies for in vivo measurements [26, 27] and in cultural heritage studies [28, 29].

MC simulations have also been applied to triaxial spectrometers. Examples of such works are Lewis *et al.* [30, 31], Hugtenburg *et al.* [32] and Al-Ghorabie Fayez [33].

Monte Carlo methods present several advantages for the simulation of EDXRF. They can account for contributions that are usually not included in the FP equations, such as electron contribution to the fluorescence emission, tertiary- and higher-order of enhancement, and non-parallel beam geometry. Furthermore, the method present advantages in describing inhomogeneous or irregular samples, and further variations on the experimental geometry. The disadvantages of this method are the increased computation time and required computational capacity.

Even though MC codes have been used for optimization of triaxial spectrometers, there are no MC simulations dedicated to elemental quantification in EDXRF using the spectrometers available nowadays. This consideration, added to the fact that FP tabulations in the existing codes are in almost all cases inaccessible to the user, form the motivation of the present work, where the aim is to implement a standardless EDXRF

elemental quantification method using a triaxial geometry, and for which FP can be altered by the user in order to improve the accuracy of the quantification. Furthermore, one of the possibilities for the codes that is aimed in the present work is the analysis of Compton-to-Rayleigh scattering ratio (see Section 3.2.10). It should be noted that even though codes and software which do not consider a triaxial spectrometer can aim at this method of analysis of the scattered peaks, by considering the primary X-ray beam energy as the fluorescence energies of a secondary target, the accuracy achieved will always be limited by the fact that the accurate polarization of the secondary beam is not included.

To achieve the aim of the present work, a code is implemented using the Geant4 toolkit [20–22], benefiting from the toolkit's implemented Monte Carlo methods and availability to change the tabulated fundamental parameters.

4.2.1 Geant4

Geant4 [20–22] is a toolkit written for the simulation of the passage of particles through matter, using Monte Carlo methods. The toolkit was created in C++, as open source, by a worlwide collaboration of physicists and software engineers. The functionalities of Geant4 include the tracking of the particles, implementation of different physic models, storage of hit information, description of the geometry, among others. Geant4 implements a wide range of physic processes, such as electromagnetic, hadronic, and optical processes, for a wide range of particles, elements, and materials, and over a wide range of energies. In some cases the energy range of implementation cover from 1 eV to 1 TeV. A variety of packages is available in the toolkit, each one specializing in different particles, energy ranges they handle, or on the different approaches in physics modelling. The models that describe the physics processes are exposed to the user, who can choose what available models will describe which process, and in some cases, for which range of energy. The toolkit offers an easy handle of complex geometries, which allied to the exposed wide range of physic models and processes, makes it easily adaptable for use in different type of applications. Due to it's versatility, it has been used in applications for a wide range of fields, such as particle physics, nuclear physics, accelerator design, space engineering and medical physics and it is currently used by many research projects around the world.

Geant4 was initially designed for application in high-energy physics, more specifically, for experiments concerning CERN. Nowadays, although it continues to be more used in high-energy physics applications, it gained increased focus on the development of physics processes and models for low-energy physics. For the simulations involving low-energy physics, the Geant4 Low Energy Electromagnetic package [82, 83] was created. This package handles physics processes for electrons, photons, charged hadrons and ions, in energy ranges that extend down to below 1 keV and with a detailed description of particle interaction by taking into account the atomic structure of matter [84]. To extend the use of the Geant4 to the simulation of experiments regarding X-ray or Auger emission, the Low Energy Electromagnetic package incorporates a model that handles atomic relaxation

[84].

4.2.2 Validations of Geant4 physics processes implementation

Geant4 implementations of physics models are usually accompanied by validations through comparison of simulated and experimental results [85]. Nevertheless, since Geant4 is mainly used in high-energy applications, validations of physics processes at low-energy (< 100 keV) are less available in literature. For the present work, the main physical processes of interest are the photo-ionization, atomic relaxation, Compton scattering and Rayleigh scattering, at low energy ranges. In literature, there are validation of Geant4 simulation of EDXRF simulated spectra, through comparison with experimental spectra. A collaboration project with the European Space Agency is in progress to perform G4 simulations for astrophysical studies [86, 87]. In other studies, the data acquired by X-ray fluorescence microprobe with synchrotron radiation was compared with G4 simulations [88]. There are also validations focusing specifically on the physics processes relevant to EDXRF simulation, which are presented throughout the present section.

Mass attenuation coefficients of composite materials were validated by Medhat *et al.* [89].

4.2.2.1 Atomic Relaxation

The simulation of atomic relaxation by the Low Energy Electromagnetic package [82, 83] is divided in two stages that are implemented independently. The first stage is the vacancy creation by a primary process, and the second stage is the relaxation cascade. The vacancy creation stage is handled by the *LowEnergyElectromagnetic* class, which is responsible for the primary interaction processes such as: the photoelectric effect, Compton scattering and ionization, which are implemented through multiple models and are capable of calculating their cross-sections for atomic shells or sub-shells at various levels of detail [84].

After the creation of a vacancy, the second stage is triggered and the relaxation cascade starts. This stage is handled by the *Atomic relaxation class* [90]. During the cascade, secondary photons or electrons are generated through radiative and radiationless transitions. The selection of the transitions is based on the respective transition partial fluorescence yield values, and the energy of the emitted fluorescence photon (also commonly termed as secondary photon) is calculated taking into account the atomic electrons binding energies. For such, the partial fluorescence yield values and binding energy values are tabulated in Geant4's library G4EMLOW. The values are derived from the Evaluated Atomic Data Library (EADL) [91]. The 2014 version of EADL can be found online [92]. The partial fluorescence yield values from EADL are derived from Scofield's relativistic Hartree-Slater calculations [93] for radiative transitions, and Chen *et al.* [94–98] relativistic Hartree-Slater calculations for radiationless transitions complemented by Hubbel's corrections

[99] to avoid the over-prediction of the strength of Coster-Kronig transitions resulting from Dirac-Hartree-Slater calculations.

4.2.2.2 Validation of Geant4 secondary particle energy values

Guatelli *et al.* presented a test [100] to the precision of secondary X-ray and Auger electron energies resulting from the Geant4's Atomic Relaxation simulation model by comparing the data against the experimental measurements on the NIST Standard Reference Data [101]: the X-ray energies are from X-ray Transition Energies Database [102] and the Auger electron energies are from X-ray Photoelectron Spectroscopy Database [103]. The X-ray Transition Energies Database [102] is a compilation of experimental measurements and values from other existing experimental databases. The relative differences are in most cases smaller than 0.5%, and in the worst cases comprised within 1 – 2%.

In more recent studies, X-ray K-L_2 energies from EADL tabulation were compared by Pia *et al.* [37] with other binding energy tabulations, and with high precision experimental measurements from Deslattes [102]. This comparison showed that EADL exhibits relatively worse accuracy than other tabulations analysed in this study when comparing with the experimental measurements of Deslattes *et al.* [102]. Pia *et al.* suggest that Geant4 simulation of X-ray fluorescence energies could be improved by modifying the tabulated values in G4EMLOW4 to values from other binding energy tabulations.

It should be noted that EADL has recently (in 2017) altered the binding energy values for their tabulations. Nevertheless, these values are still not used in the most recent version of Geant4 library G4EMLOW.

4.2.2.3 Validation of Geant4 partial fluorescence yield values

Auger fluorescence yields tabulated in Geant4 were validated in a study by Incerty *et al.* [104].

Several studies from Pia *et al* present comparisons [35], [36], [37] between radiative transition partial fluorescence yield values (normalized without accounting radiationless transitions), from EADL tabulations against the values obtained from different sources, namely Scofield's Hartree-Slater calculations [93, 105], Scofield's Hartree-Fock calculations [106, 107], and experimental values obtained from Salem *et al.* fit to experimental data [108]. The result of this evaluation highlights that transition probabilities calculated using Scofield's Hartree-Fock values are in better agreement with experimental measurements than transition probabilities calculated using Scofield's Hartree-Slater values. Furthermore, even though EADL values are derived from Scofield's Hartree-Slater calculations, in some cases large deviations are found between the two. Since in these cases EADL values are inconsistent with the experimental data, Pia *et al.* suggest that such deviations are probably due to accidental treatment on the data by EADL's part.

Pia *et al* conclude [37] that EADL data doesn't provide the state-of-the-art radiative transition probabilities. Since Geant4 uses EADL's data, the revision to its values would

contribute to improve the accuracy on its simulation of processes like X-ray fluorescence.

Pia *et al.* comparisons focus on partial fluorescence yield values which are normalized without accounting radiationless transitions (see Sections 2.1.2, Eq. 2.10). However, the EADL library and Geant4's library G4EMLOW present partial fluorescence yield values which are normalized accounting radiationless transitions (see Sections 2.1.2., Eq. 2.8). Thus, in the present work it is presented a comparison of the later values, as well as total K-shell fluorescence yields, obtained from several references. This comparison is presented in Chapter 6.

4.2.2.4 Validation of Geant4 photoionization cross-section values

Geant4 Livermore model [109] for photoionization recurs to tabulated cross-section in G4 library G4EMLOW. The tabulated values are according to Evaluated Photon Data Library 97 (EPDL97) [110]. For energy values up to 1 MeV, EDPL97 includes data obtained from Scofield's Hartree-Slater calculations of subshell cross-sections [111]. The same data is employed in NIST database, extended up to 1.5 MeV. Other G4 models for photo-ionization employ different tabulations of data for these cross-section, but since the Livermore model is more adequate for low energy ranges we restrict the discussion to the later model.

Validation studies comparing Geant4 photoionization cross-section against other databases were performed by Cirrone *et al.* [112]. Very good agreement is found between the G4 Livermore and the NIST database at low energy values, however such is to be expected since both use the same data for energy values bellow 1 MeV.

In a more recent study from Han *et al.* [113], cross-section data libraries and parametrization methods were quantitatively evaluated through comparison with experimental measurements, demonstrating statistically that better accuracy is found for EPDL tabulations.

4.2.2.5 Validation of Geant4 Rayleigh scattering implementation

For the Rayleigh scattering, Geant4 Livermore model [109] recurs to G4 library G4EMLOW for tabulations of cross-section and tabulations of atomic form factors, which are derived from EPDL97 [110]. The atomic form factors are obtained from Hubbel *et al.* nonrelativistic Hartree-Fock calculations [42] and the total cross-section values are obtained from the numerical integration of the Thomson scattering formula, the atomic form factors, and the anomalous scattering factors [114] which were numerically integrated (unlike what is presented in Sections 2.1.3, Eq. 2.18).

In Cirrone *et al.* studies [112], the comparison between G4 Livermore Rayleigh cross-section and NIST XCOM database [115] shows significant disagreement at low energies. This discrepancy is justified by the fact that XCOM values are obtained from the numerical integration of the Thomson formula and Hubbel and Øverbø relativistic atomic form factors [44] (as in Sections 2.1.3, Eq. 2.18).

The relativistic atomic form factors employed in XCOM proved to be in better agreement with experimental values than the non-relativistic form factors employed by EPDL97. Thus, Geant4 Rayleigh cross-section could improve by adopting the relativistic form factor values. Furthermore, G4 sampling of the scattering angle in Rayleigh scattering is calculated using the tabulated form factors, and as such, the adoption of the relativistic values could also improve the simulation accuracy regarding the scattering angles.

4.2.2.6 Validation of Geant4 Compton scattering implementation

For the Compton scattering, Geant4 Livermore model [109] recurs to G4 library G4EMLOW for tabulations of cross-section and tabulations of the incoherent scattering function, which are derived from EPDL97 [110]. The incoherent function values are obtained from Hubbel *et al.* non-relativistic Hartree-Fock calculations [42] and the total cross-sections are obtained from the numerical integration of Klein-Nishina formula and the incoherent function (see Sections 2.1.4, Eq. 2.27), including radiative and double Compton-scattering corrections. NIST XCOM database [115] Compton cross-sections are obtained using the same values and the same calculations, and as such, the cross-sections are in good agreement with those of G4, in Cirrone *et al.* studies [112]. In a later Hubbel and Øverbø work [44], relativistic incoherent function values proved to be in better agreement with experimental values than the non-relativistic values from Hubbel *et al.* [42].

Later works [116–118] showed that, when compared to form factor approaches (see Sections 2.1.3 and 2.1.4), values obtained from the double differential cross-section obtained using the S-matrix in the relativistic impulse approximation approach are in better agreement with experimental data, in the order of a few percent.

4.3 Experimental Setup

The code developed in the present work aims to simulate the EDXRF spectrometer with the triaxial geometry spectrometer installed in the Laboratório de Física Atómica e Molecular, LIBPhys-UNL, Departamento de Física, FCT-UNL. The spectrometer is self-constructed and consists on three main components, the X-ray source, the sample arrangement, and the detector system (see Fig 4.1).

For the X-ray source, a commercial X-ray tube (Philips PW1140/00, 100 kV, 80 mA), with a tungsten anode, is operated at 50 kV and 20 mA. A molybdenum secondary target is used with the tube. The radiation emitted from the tube (the primary beam) is continuum due to Bremsstrahlung radiation, and it excites the Mo secondary target, as presented in a schematic representation in Fig. 4.2.

Between the primary beam source and the secondary target, a silver filter is placed. The filter attenuate the low energy bremsstrahlung of the primary beam which will not contribute to the excitation of the secondary target, but could contribute to the background of the measured X-ray spectrum.

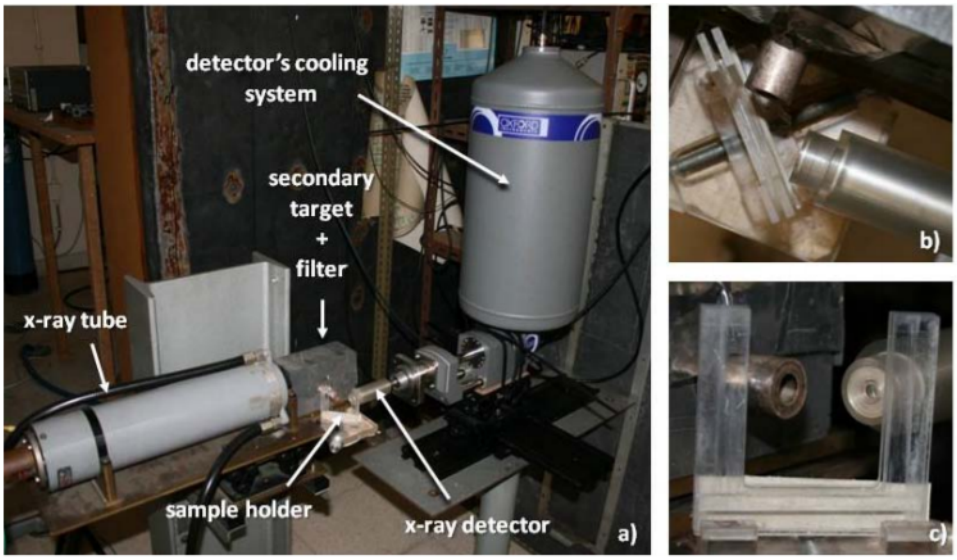

Figure 4.1: Triaxial spectrometer at Laboratório de Física Atómica e Molecular, LIBPhys-UNL, Departamento de Física, FCT-UNL. a) View of the whole system. b) Top view of the sample holder, collimation tube and detector tube. c) Side view of sample holder, collimation tube and detector tube.

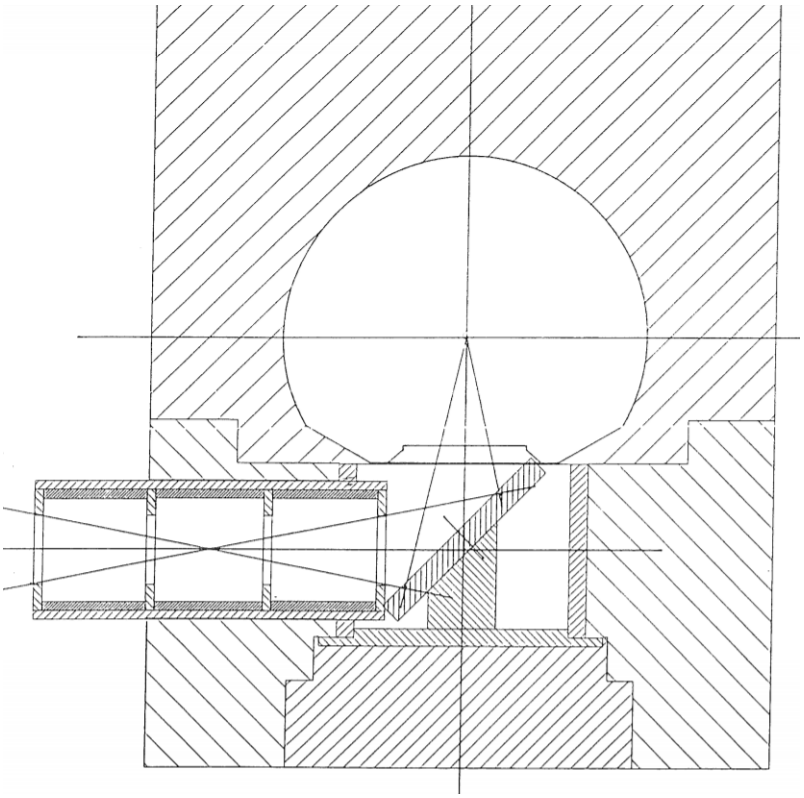

Figure 4.2: Source exciting the Mo secondary target.

The distance between the primary X-ray beam source and secondary target is approximately 2.5 cm. A collimator tube is placed in the path between secondary target and sample, in order to collimate the secondary X-ray beam coming from the secondary target. The collimators internal radius is approximately 4 mm, and the collimator tube length is 39 mm. The sample arrangement is constructed as to have the less possible material exposed to the X-ray secondary beam, besides the sample. The distance between sample and secondary target is approximately 42 mm. The detector used is an Oxford nitrogen cooled Si(Li) 30 mm^2 × 5 mm detector with a 8 μm beryllium window. The detector's energy resolution is 129 eV at 3 keV, 150 eV at 6.3 keV, and 220 eV at 17 keV. The distance between detector and sample is 4 cm, approximately. Two collimators near the detector collimate the beam direction coming from the sample, and their internal radius are approximately 4 mm, which ensure that X-rays only enter the detector in the active area.

4.4 Codes for simulation

The codes implemented in the present work using Geant4 are constructed to simulate the X-ray spectrum obtained from the triaxial spectrometer described in Section 4.3. The future aim of these codes is to implement a method of analysis through an iterative routine where the simulated sample composition is altered in each iteration and the simulated and experimental X-ray spectra are compared. The iteration process will finish when convergence between experimental and simulated spectrum is achieved. For an iterative process, computation time and capacity are specially crucial. Hence, several considerations were taken in the code in order to optimize computational time.

Two different codes were implemented in the present work, namely "Basic code" and "Advanced code". Both codes follow the same basis, but they are implemented using different considerations to simplify the simulations (particularly on the simulated setup geometry), and thus, they are distinguished from each other by an accuracy-computation time trade-off. The first code was implemented for the typical triaxial EDXRF analysis where the aim is the quantification of the X-ray spectrum characteristic peaks and consequent elemental quantification. The second code was implemented for the analysis of the sample average atomic number Z_{avg} using the Compton-to-Rayleigh scattering ratio. The motivation for the second code arose from the fact that the level of simplifications on implemented in the first code did not allow for a satisfactory simulation of the scattering ratio.

In both codes, the same G4 physical models and classes where used. G4 current more accurate electromagnetic physics package for low energy is the *G4EmStandardPhysics_option4*. However, the package's models that implement the physics processes do not account for photon's polarization. Since photon polarization is crucial for the simulation of a triaxial geometry spectrometer, the *G4EmLivermorePolarizedPhysics* was used instead. This package account for polarization of photons for the physics processes more relevant to the

EDXRF simulation. The class resorts to data values tabulated on G4EMLOW6.48 library, which are obtained from the ENDL evaluated data libraries: EADL (Evaluated Atomic Data Library), EPDL (Evaluated Photon Data Library, and EEDL (Evaluated Electron Data Library). From these data, Geant4 calculate cross-sections and samples the final states resulting from the interaction of photons, electrons and ions with matter. G4 particle cuts define length threshold values to assess if the created particles will be discarded (depositing their energy in the local material). The assessment is based on whether the created particle energy is enough for it to travel beyond the cut value. Low cut values improve the accuracy of the simulation but increase computation time. In the present work, simulations with several cut values were performed, and the values chosen for both implemented codes were the lowest for which no significant change in the simulations were verified.

In both codes, the overall simulation of the X-ray spectrum was divided in two sequential simulations. In the first simulation the primary beam excites the secondary target, and the secondary beam reaching the sample is obtained, where some information regarding the beam is stored in external files. In the second simulation, the information in the external files is used to recreate the secondary beam. The second simulation consist on the secondary beam exciting the sample and the detection of the radiation emitted from the sample, simulating the EDXRF spectrum. In a future iterative method, only the second simulation will be included in the iterative process, since the first simulation only has to be performed once. The choice of dividing in two sequential simulations was supported by the very high ratio of primary X-ray photons created to X-ray photons reaching the sample, which lead to unsustainable computation time and memory usage. This ratio is understandably high due to the low cross-sections values of scattering and fluorescence processes, and due to the loss in beam intensity in the collimators.

The following description of the code in this subsection applies for the basis of both codes implemented in the present work. In the first simulation, the primary beam is created, and the X-ray tube was not simulated as it would result in a substantial increase of computation time. Furthermore, since the program simulates a triaxial geometry, where polarization cut-off occurs, the accurate energy of the primary photons is much less relevant to the simulated X-ray spectrum, which will mainly consist on the sample fluorescence and secondary target fluorescence scattered by the sample into the detector. Thus, the primary X-ray photons are generated using Geant4 user *PrimaryGeneratorAction* class, where the energy attributed to the X-rays are according to the analytical algorithm of Pella *et al.* [119]. The attribution of energy values is performed by sampling from an external file with the primary source energy function, which is presented in Fig. 4.3.

For the primary photon direction, an opening angle between $0° < \Omega < 25°$ is randomly selected. This angle range follows the experimental angle, and for all possible angles the photon reaches the secondary target (see Fig. 4.2). Another angle is randomly selected, with any possible value. From these angles, the x-, y-, and z-components of the photon direction are obtained. The primary photon polarization is attributed without preferential

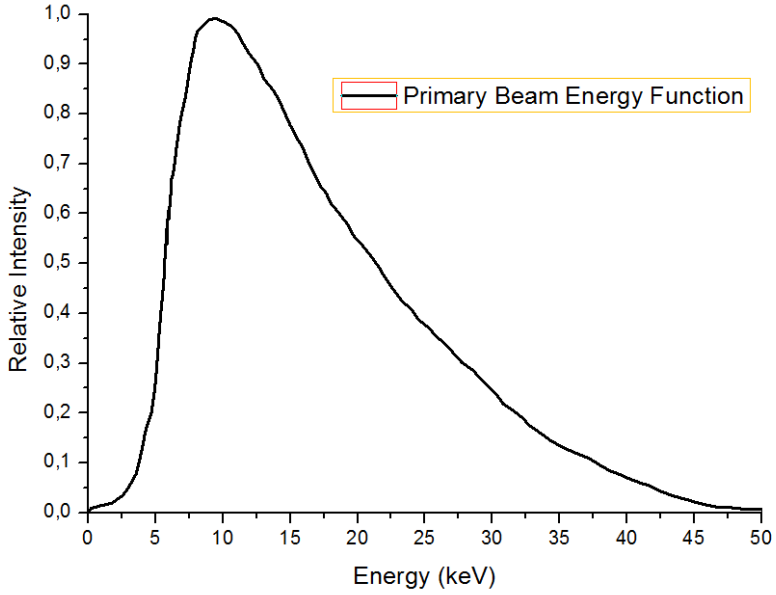

Figure 4.3: Primary beam energy function used in the simulation.

direction. For this, a random direction orthogonal to the photon momentum direction is calculated using rotation matrices.

As result of the interactions of the primary beam with the Mo secondary target, radiation will be emitted from the secondary target and some will reach the sample. The radiation reaching the sample is usually termed as secondary beam. At this phase, geometry simplifications are considered in the simulated setup between secondary target and sample, with different considerations for the two codes. In this phase no simplifications in the physics interactions or X-ray paths are implemented, with the exception of those inherent to Geant4, such as particle cuts. All physical interactions, and the paths for all particles, from the creation of the primary beam to the radiation reaching the sample, are handled in a standard way by Geant4's physical process packages and tracking actions. X-ray photons reaching the sample at this stage are discarded (or "killed" using G4 terminology), and some of their attributes are stored in histograms files using the Geant4 built-in ROOT [120] functionalities. This procedure was implemented with a Geant4's user *SteppingAction* class to retrieve the attributes of the photons reaching the sample, and an original class created in the present work (Analysis class) to analyse and store the information in external ROOT [120] files through Geant4's ROOT classes, following some of G4 examples available online. The quantity of different photon attributes that are stored at this stage differs from the first to the second code implemented in this work. Other than photons, attributes of particles reaching the sample are not stored. This consideration does not hinder the accuracy of the simulation since the amount of electrons reaching the sample are negligible, due to air path between secondary target and sample.

At a first stage of the code development, it was observed the peculiar feature of X-ray photons with null polarization component in any direction. Upon further investigation

it was concluded that X-ray fluorescence photons were being generated with null polarization by the Atomic Relaxation package. It was verified that Geant4 only attributed non-null polarization values to this photons after they where involved in any kind of interaction. As a solution to this problem, a random polarization direction, orthogonal to the photon direction, was attributed to the fluorescence photons generated. The implementation of this procedure was achieved using an user *SteppingAction* class. For this, it was considered that polarization of fluorescence photons is isotropic, which although is not true in all cases, is a good approximation for the purposes of the simulation.

In the second simulation, the beam exciting the sample, the secondary beam, is recreated. It should be noted that the primary photons of this second simulation are now the secondary beam photons. The attributes of the photons reaching the sample, which were stored in external files in the first simulation, are now used to generate the primary photons of the second simulation. While some of this attributes are sampled from the external files, others are calculated by the code, depending on the code in question. With this consideration, practically all primary X-ray photons generated in the second simulation will reach the sample, optimizing the needed computational time of the overall simulation.

The secondary beam excites the sample and some of the radiation will reach the detector. Other than the secondary beam recreation, in the second simulation, no simplifications in the physics interactions or X-ray paths are implemented, with the exception of those inherent to Geant4.

For the simulation of the X-ray spectrum, all the energy deposited in the detector is stored in an histogram. For this, the *ConstructSDandField* function from the *DetectorConstruction* class, and an user *EventAction* class are used. The details of detector charge collection are not implemented in the simulation. Therefore, there is no simulation of charge collection efficiency or low energy tails. Only the efficiency factors arising from the interaction of photons with detector elements are simulated. To account for charge collection mechanisms, the energy broadening due to energy resolution is applied to the simulated spectrum at the end of the simulation. Such is performed by applying a convolution of a Gaussian, with the experimental FWHM, to each of the channel counts in the histogram. To account for detector efficiency, the counts of each channel are multiplied by the respective experimental detector efficiency function (presented in Fig. 4.4), which is stored in an external ROOT file. It is worthwhile noting that while the various interactions of X-rays in the detector are simulated in the present work, the detector's dead layer is not included in the simulations since the thickness of the layer is unclear. As such, the efficiency function used in the present work accounts only for the contribution of the detector's dead layer. In Fig. 4.5, it is presented an example where the contribution of detector energy resolution (left figure) and detector efficiency (right figure) are applied to the simulated spectrum.

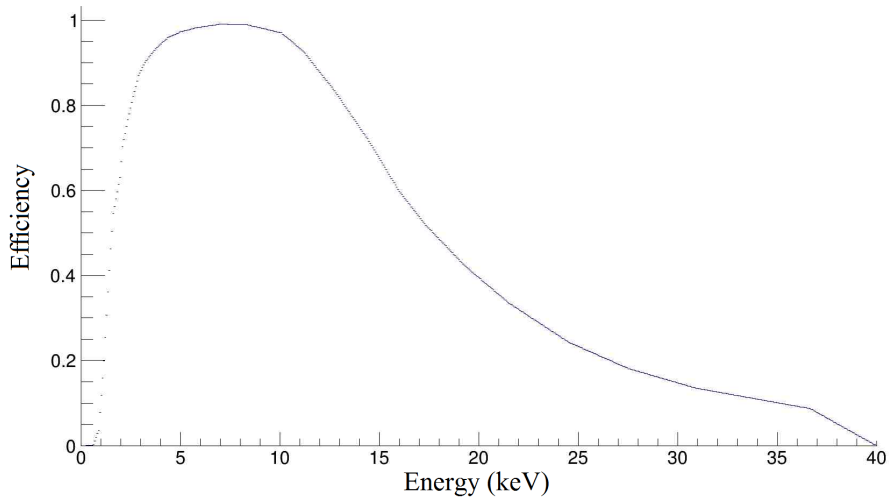

Figure 4.4: Detector energy efficiency function.

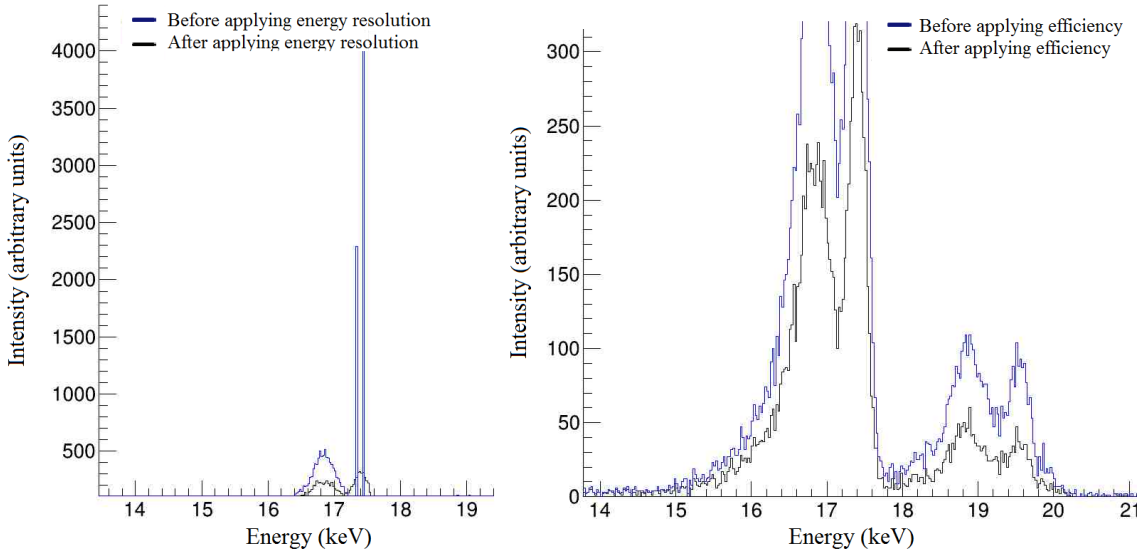

Figure 4.5: Application of energy resolution (left figure) and efficiency (right figure) to the simulated spectrum.

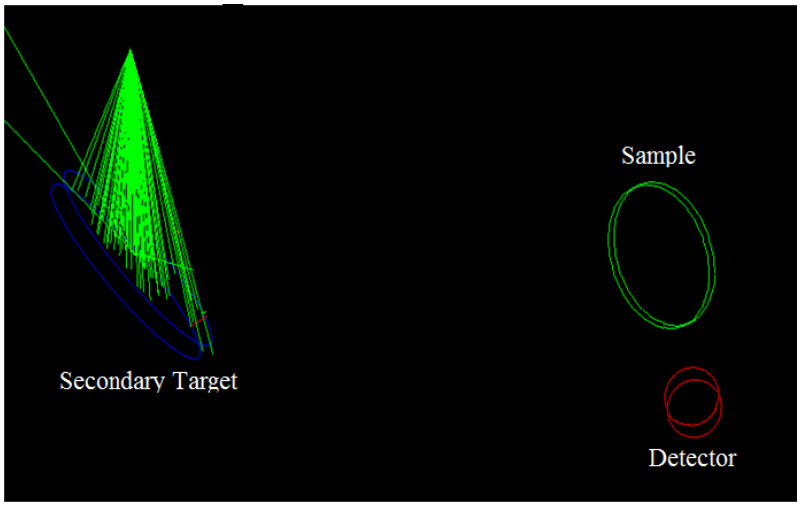

Figure 4.6: Simulated setup used by the Basic code.

4.5 Basic code implementation

The presence of collimators in the simulation's geometry result in a significant increase of computation time since photon's interactions with the collimator material are included in the simulation. Furthermore, photons interacting with collimator do not contribute significantly to the secondary beam reaching the sample. This is justified by the fact that the probability that they are scattered from the collimator into the sample is relatively low. For these reasons, in this code, collimators were not considered in the simulated geometry. In Fig. 4.6 it is presented the simulated setup.

4.5.1 First simulation

Since no collimators are included in the simulation, an evaluation of the photon momentum direction unitary vector, $\boldsymbol{p}$, was performed for the photons exiting the secondary target, in order to define an approximation for the solid angle of acceptance. Being the x-axis oriented in the direction from secondary target to sample, for the Cartesian coordinate system of the simulation, a threshold value was chosen for the x-component of the momentum direction, p_x, of photons reaching the detector. For the choice of the threshold value, an analysis of the p_x values of photons reaching the sample was performed, and it was observed $p_x > 0.98$ for the great majority. Thus, in this code, photons exiting the Mo secondary target with $p_x < 0.98$ are discarded from the simulation. For $p_x > 0.98$, some of the photon's attributes are stored in ROOT histograms, and the photons are discarded, ending the first simulation. This procedure was implemented using an user *SteppingAction* class. The z-component of the polarization, P_z and the energy, E, are stored in a 2D-histogram in a ROOT file. It should be noted that due to the simplification presented, in the first simulation of this code, the photons are discarded without actually reaching the sample, for which no interactions of the photons with the sample occur at this stage.

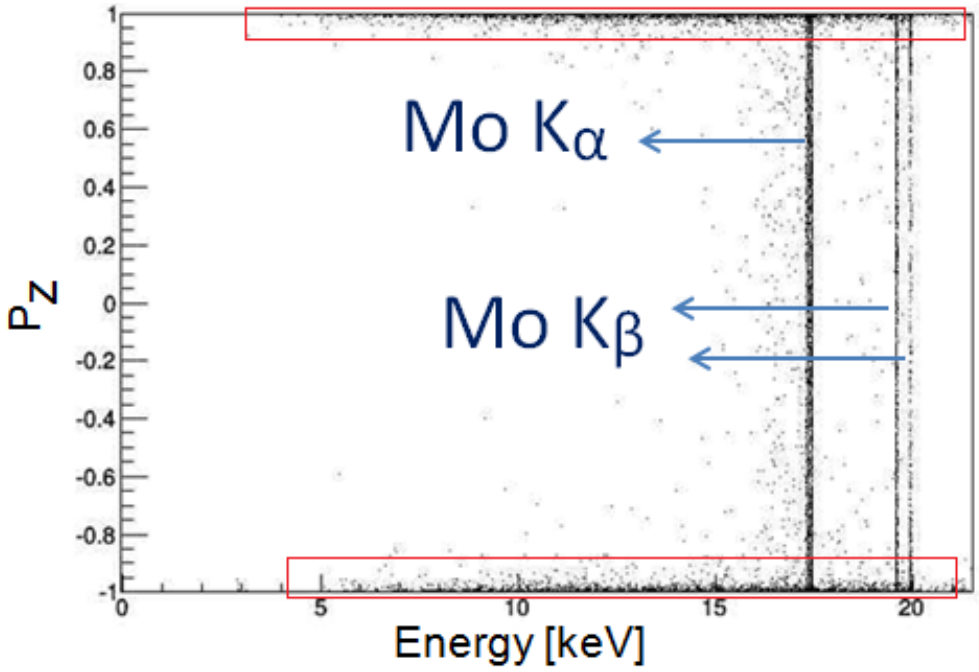

Figure 4.7: 2D-histogram of z-component of polarization and energy for X-rays that leave the surface of the fluorescence target (Mo) within a solid angle accepted by the sample. Lines denoted as Mo K_α and Mo K_β correspond to Mo fluorescence photons, which can have any polarization value, as seen in the figure. The X-ray tube photons are polarized, as denoted by the red boxes in the figure.

The correction to the fluorescence photons with null polarization values is applied, as described in Section 4.4. With this correction, the 2D-histogram obtained is typically as presented in Fig. 4.7. It can be seen that the continuum background radiation from the X-ray tube which reached the sample is mostly polarized along the z-axis, as expected. The secondary target fluorescence K_α and K_β lines are visible as narrow lines. The z-component of the polarization for the fluorescence lines takes all possible values, although not isotropically. The scatter points at lower energies than fluorescence lines correspond to fluorescence photons that were incoherently scattered. Coherently scattered fluorescence photons contribute to the narrow lines, since no energy is transferred in the scattering. The photons which are more mainly polarized in along the z-axis are less probable to scatter from the sample into the detector (as explained in Sections 2.1.5 and 3.2.9).

4.5.2 Second simulation

For the second simulation, the 2D-histogram from the first simulation is used as input for the recreation of the secondary beam. The primary photon energy and z-component of the polarization are sampled from the histogram. This procedure is implemented using the *PrimaryGeneratorAction* class and the originally created *Analysis* class. The x- and

y-component of the polarization are randomly generated with no preferential direction, in a way that the polarization vector is normalized to unity. For the momentum direction, the p_x value is randomly generated between the threshold value and unity $0.98 \leq p_x \leq 1$, to ensure that the photon direction is in the solid angle of the sample. The p_y and p_z components are randomly attributed without preferential direction, and in a way that the momentum direction vector is normalized to unity and is orthogonal to the polarization vector. The initial position of the photon is randomly attributed in the secondary target's surface that is exposed to the primary beam. All of this considerations ensure that all, or almost all, primaries generated in the second simulation reach the sample.

To optimize time computation, no collimators were considered between the sample and the detector. Other than the previous fact, the detector distance to the sample, and the geometry of the detector, are as in the experimental setup.

In this second simulation, the excitation of the sample, the storage of energy deposited in the detector, and the acquisition of the X-ray spectrum, are performed as explained in Section 4.4. For computation time optimization, the correction performed to the null-polarization fluorescence photons is not applied in the second simulation. Such is justified by the fact that the increase of accuracy in the simulated X-ray spectrum by correcting the polarization of the fluorescence photons emitted from the sample can be considered negligible.

The solid angle consideration implemented in this program (at both the first and second simulations) neglects the fact that photons exit the secondary target in different spacial positions, and as such, each photon has a different value of p_x that would allow for it to reach the sample. This affects the accurate simulation of the photons direction. Also contributing to the inaccuracy of the photons direction in the simulation is the consideration that photons are emitted from a random position of the secondary target surface and the fact that no collimators are included in the simulation. However, for the analysis of peak intensities, the secondary beam photon directions are not crucial since X-ray fluorescence emission is (approximatly) isotropic, and the loss in accuracy in the simulation of the scattering peaks will not greatly influence the simulated characteristic peak. Thus, considering the time optimization improvement with this simplifications, these were considered justifiable.

4.5.3 Simulation results

To test the accuracy of this code, simulation of spectra for reference materials were performed and compared with the experimental spectra. The chosen reference materials have similar matrices to those of materials used in toxicology and cultural heritage studies. The standard NBS-1571 orchard leaves and the standard NBS-1577a bovine liver were chosen as representative cases of organic matrices with low atomic number. In these matrices, the amount of by C, H and O, is roughly 90 %. For matrices with medium atomic number it was chosen to measure the standard ISE-954 clay material, which is

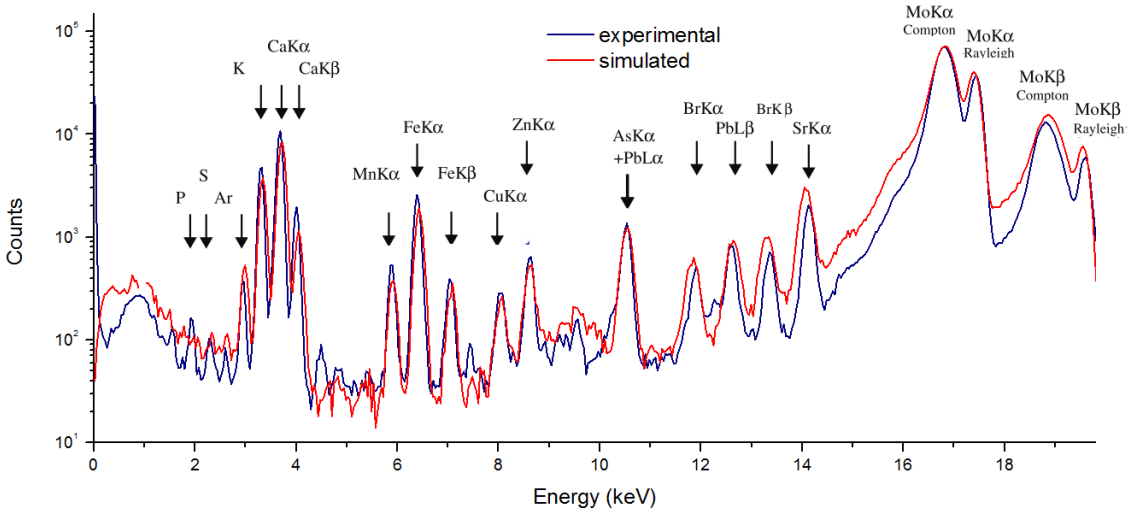

Figure 4.8: Comparison of simulated (red) and experimental (blue) spectra for the NBS-1571 orchard leaves. Fluorescence lines are identified by the element and transition

mainly composed by O (50%), Si (25%) and Al (11%), and the standard NIST-1400 bone ash, which is mainly Ca (38%), O (20%) P (18%) and C (14%). For heavy atomic number matrices, the standard BCR-B was chosen, which is a copper alloy (80% made of Cu).

In order to define the sample composition in the simulations the elements and respective weigh percentage were attributed to the sample using the respective documentation of the reference standard materials, whether certified or non-certified values. This was performed using the *DetectorConstruction* class.

For the standard NBS-1571 (orchard leaves) the certificate does not mention weight percentages, thus, they were calculated according to the weight proportions of cellulose ($C_6H_{10}O_5$). The material density was considered the same as cellulose (1.5 g/cm^3). For the standard 1577a (bovine liver), the elements weight fraction were attributed assuming the same proportions of similar materials implemented in Geant4, like *G4_Tissue_SOFT_ICPR*. The material density was considered to be the same as the typical organic materials available in Geant4 (1.03 g/cm3). For the ISE-954 (clay material), the weight fractions and density were considered the same as Geant4 material G4_concrete. For the NIST-1400 (bone ash) material the weight fractions of H, C and O, and the density (1.8 g/cm^3), were considered similar to Geant4 material G4_BONE_COMPACT_ICRU. The BCR-B (copper alloy) density was considered a typical value of Cu-Sn brass material (8.5 g/cm^3).

Fig. 4.8 presents the comparison between the simulated and experimental spectra for NBS-1571 (orchard leaves). The simulated spectrum was normalized to the experimental Compton peak of Mo K_α. It can be seen that Compton peaks of Mo K_α and K_β are more intense than the Rayleigh peaks. Such is to be expected due to the low average atomic number of the sample ($Z_{\text{avg}} \approx 7$ for orchard leaves and $Z_{\text{avg}} \approx 6.9$ for bovine leaver), since in low Z_{avg} materials the differential cross-section for Compton scattering is higher than Rayleigh's, for these values of energy and scattering angles.

In both comparisons (orchard leaves and bovine liver), the relative differences for the Compton to Rayleigh peak ratio is 10% for K_α, and 4% for K_β.

As for the characteristic peaks, all fluorescence lines from the experimental spectrum are present in the simulated spectrum. When comparing the background of the spectra some discrepancies are observed. For low energy (0 to 4 keV), the simulated spectrum background is higher by a factor of approximately 1.5 at 1 keV. This discrepancy might be attributed to the fact that the charge collection efficiency of the detector is not simulated. The simulated spectrum background is also higher at higher energies (13 to 16.3 keV). This is due to the multiple Compton scattering in the sample [121] as pointed out by Dimmock *et al.*. [88]. Several simulations with different sample length, sample density, and detector length did not present a significant change in the background. A possible contribution to the background, at 2 keV, is the escape peak of the Ca K_α.

In Table 4.1, it is presented the peak intensity relative difference between experiment and simulated spectra for orchard leaves. The values presented are for the reference materials and the uncertainties are obtained from the amplitude uncertainties after the fit is performed. For NBS-1571, the agreement is better than 25% for all peaks, with the exception of Ca K_β and the peaks over the Compton tail, where the difference is about 60%. It should be noted that other K_β lines are in agreement, which indicates that the discrepancy in Ca K_β should not be attributed to inaccuracy in fundamental parameters. The discrepancy can be attributed to matrix effects or simulation artifacts. The fact that Br is not certified can also contribute to the deviation. The good agreement for Zn and Cu, with only with 35 $\mu g.g^{-1}$ and 12 $\mu g.g^{-1}$ respectively, indicates that the simulation can be applied in cases where these are trace elements. The agreement of the peak intensities for the simulated and experimental spectra for the bovine leaver (NBS-1577a) is also good, except for the peaks at the Compton tail.

In Fig. 4.9 the simulated and experimental spectra for the clay material are presented. In this case, the simulated spectrum was normalized to the Fe K_α experimental peak. As expected, for this medium atomic number material, the Compton peak is no longer as intense, when compared with the Rayleigh peak, as in the case of the low atomic number materials. It should be noted that with the normalization to Fe K_α, the simulated scattered peaks are lower than the experimental by a factor of approximatly 2. A study from Owens *et al.* [87] reported discrepancies on the Compton peak for a direct monochromatic excitation beam incident on a sample with medium atomic number. Works in literature have shown that the double differential cross-section obtained using the S-matrix in the relativistic impulse approximation approach gives better agreement with experimental data compared to form factor approaches. Although Geant4 employs the form factor approach through the *G4EmLivermorePolarizedPhysics* class, such would only account for a few percent of deviation, and thus cannot justify the discrepancy in the simulated peaks.

As can be seen from Table 4.1, most simulated peaks are in good agreement with experimental, for both medium atomic number materials, ISE-954 (clay material) and

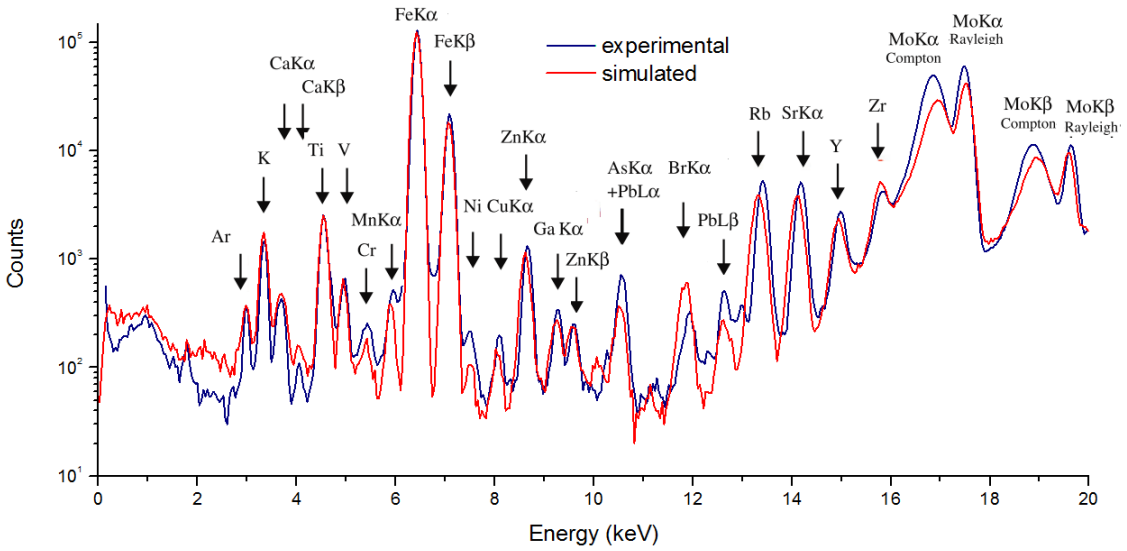

Figure 4.9: Comparison of simulated (red) and experimental (blue) spectra for the ISE-954 clay material. Fluorescence lines are identified by the element and transition.

NIST-1400 (bone ash). Regarding ISE-954 (clay material), the simulated Pb L_α peak intensity is in disagreement with the measured intensity, presenting 70 % relative difference, and as consequence, a great disagreement is also found for the As K_α + Pb L_α peak, for which the relative difference is 68 %. For the Ni K_α, Br K_α, and Zr K_α peaks, the relative differences are 30 %, 30 % and 39 %. As for the remaining ISE-954 peaks, the relative differences are lower than 30 %, and very good agreement is observed specifically for Ca K_α, Fe K_β, and Zn K_α peaks, for which relative differences are 7 %, 6 %, and 3 %, respectively. Unlike in the case of the orchard leaves, the Ca K_β peak is in agreement with experiment, which indicates that the disagreement in orchard leaves is not due to fundamental parameters.

In Fig. 4.10 the simulated and experimental spectra for BCR-B (copper alloy) are presented. As expected, for this higher atomic number material, the Compton peak is much lower than the Rayleigh peaks. Like in the case of medium atomic number materials, the simulated Rayleigh scattering peaks are lower than the experimental by a factor of approximation 2. The simulated spectrum is normalized to the experimental Cu K_α. As presented in Table 4.1, most characteristic peaks are in good agreement with the experimental. The exception are for Fe K_β and Ni peaks, which present 44 % and 40 % relative difference between measured and simulated intensity. Such disagreement might be due to fact that the quantities of these elements are not certified. The relative percentage difference between simulated and experimental Zn K_α, Cu K_β, and Mn K_α peaks are 27 %, 28 %, and 17 % respectively. Better agreement is found for most of the remaining peaks, for which relative differences are within 11 %, with Sn standing out with only 5 % relative difference. Great disagreement is found for the Compton peak, which can be attributed to the fact that the detector sum peaks of the very intense Cu

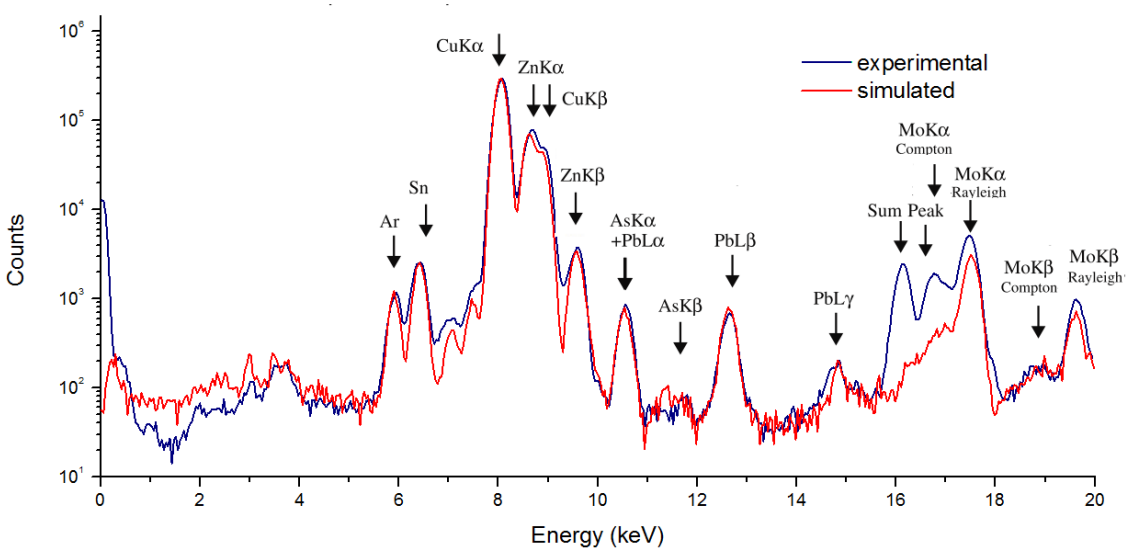

Figure 4.10: Comparison of simulated (red) and experimental (blue) spectra for the BCR-B copper alloy. Fluorescence lines are identified by the element and transition.

and Zn peaks are not simulated. In the measured spectrum, the structure composed by the Compton peak and sum peaks is approximately 4 times higher than the simulated Compton peak.

The simulation performed with this version of the code presented relatively good agreement (better than 20 % for most cases) for the characteristic peak. Some of the exceptions to this are clearly due to the fact that some detector related contributions like sum peaks or efficiency charge collection are not simulated. Other exceptions are due to matrix effects like multiple Compton scattering (observed in the low Z_{avg} materials). The greatest disagreement is found for the simulated scattering peaks, which in part can be attributed to the codes's several approximations affecting the accuracy of the simulated scattering angles. The agreement for peaks that lie on the Compton tail are particularly affected by the disagreement in the simulated scattering peaks. Nevertheless, in a future code where iterative simulations are performed until convergence is found between the simulated and experimental spectra, the optimization of time-computation computational is crucial. Although this simulations are achieved through a compromise between accuracy (of scattering peaks and some peaks lying on the Compton tail) and computation-time, good agreement is found for most of the characteristic peaks, justifying that this version of the code can be employed in future analytical investigation, for most of the elements considered in this study, and for this type of matrices.

Lines	NBS-1571	NBS-1577a	Δ(%) ISE-954	NIST-1400	BCR-B
P				23 ± 1	
K Kα	12 ± 2	16 ± 3	22 ± 4		
Ca Kα	10 ± 1	23 ± 18	7 ± 16	calib	
Ca Kβ	35 ± 9			15 ± 1	
Sn					5 ± 15
Ti Kα			11 ± 5		
V Kα			21 ± 11		
Mn Kα	13 ± 17	8 ± 32	28 ± 37		17 ± 3
Fe Kα	17 ± 4	25 ± 4	calib	12 ± 3	11 ± 1
Fe Kβ	6 ± 18	20 ± 19	6 ± 1	6 ± 15	44 ± 11
Ni Kα			30		40
Cu Kα	15 ± 33	11 ± 2	20 ± 23		calib
Zn Kα	10 ± 14	6 ± 2	3 ± 10	25 ± 3	27 ± 1
Cu Kβ		10 ± 11			28 ± 1
Ga Kα			20 ± 25		
Zn Kβ		26 ± 10	11 ± 23	26 ± 15	10 ± 1
As Kα + Pb Lα	21 ± 5		68 ± 17		9 ± 3
Br Kα	40 ± 11	33 ± 11	30 ± 14		
Pb Lβ	35 ± 7		70 ± 25		11 ± 3
Rb Kα	60 ± 7	50 ± 5	20 ± 1		
Sr Kα	63 ± 2		15 ± 1	28 ± 1	
Y Kα			12 ± 3		
Zr Kα			39 ± 2	20 ± 1	

Table 4.1: Relative percentage difference between measured and simulated fluorescence lines peak intensities. The lines marked with calib were used for normalization of the counts of the simulated spectrum to the experimental spectrum. Uncertainty is presented for each values.

4.6 Advanced code implementation

In the Advanced code, no simplification in the simulated setup geometry is implemented. Thus, the collimation tube is included, which increases substantially the computation-time needed for the simulation of the secondary beam due to the fact that now interactions with the collimator are simulated. In Fig. 4.11 the simulated setup is presented.

4.6.1 First simulation

The generation of the primary photons is as described in Section 4.4. In this simulation, unlike in the case of the Basic code, the photons emitted from the secondary target are not evaluated by their momentum. Instead, the simulations is performed without including any consideration about the photons emitted from the secondary target. As such, some of these photons will reach the sample while other will reach the collimators, where most

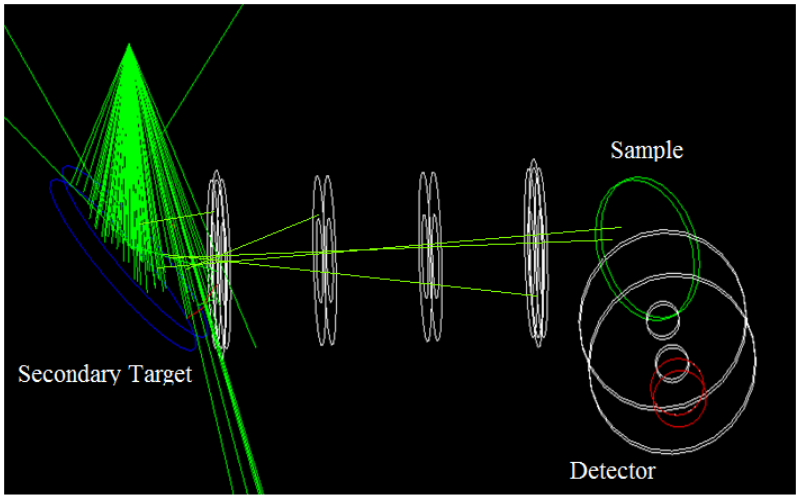

Figure 4.11: Simulated setup used by the Advanced code.

of them will be annihilated. One way to reduce computation time at this phase is to discard the photons that reach the collimators, as not to include their interaction in the simulation. Nevertheless, such approach was not employed in the present work since it would affect the accuracy of the simulated secondary beam, due to the discard of photons that can possibly be scattered from the collimation tube into the sample. It should be noted that for a future program that iteratively simulates the spectrum, only the second simulation is included in the iterative process, and as such, the trade of computation time for accuracy on the first simulation is well justified.

When the photons reach the sample some attributes are stored in histograms in external ROOT files, and they are discarded, ending the simulation. Differing from the Basic code, at this stage more attributes are stored. Besides the 2D-histogram of z-component polarization and energy, the spatial position and direction angles are also stored. The x- and y-components of position are stored in one 2D-histogram, as presented in Fig. 4.12).

The photon angle θ (defined from the x- and z-components of direction), and the x-component of position are stored in a 2D-histogram, as presented in Fig. 4.13. Similarly, the photon's angle ϕ (defined from the x- and y-components of direction) and the y-component of position are also stored in a 2D-histogram, as presented in Fig. 4.14.

4.6.2 Second simulation

The simulation starts with the re-creation of the secondary. For the generation of the primary photons, the energy and the z-component of the polarization are sampled from the 2D-histogram. For the attribution of the photon spacial initial position, the x- and y-component of the position are sampled from the 2D-histogram, and the z-component is obtained from the linear relation with the x-component. The angle θ is sampled from

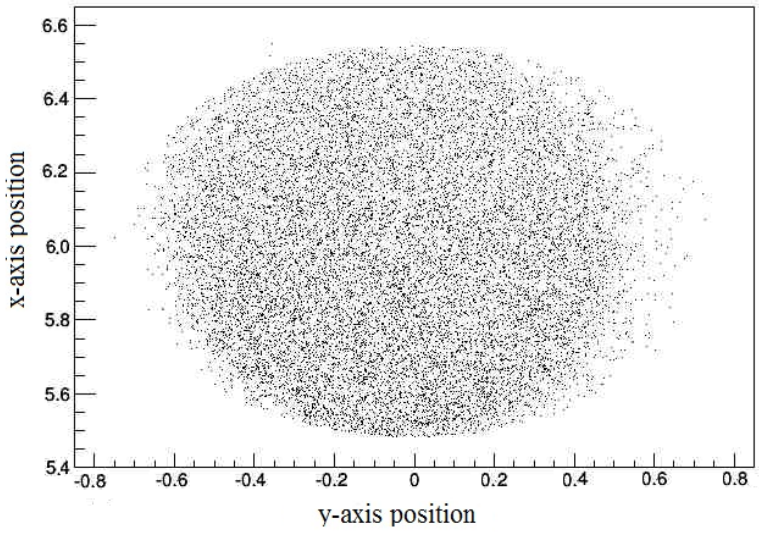

Figure 4.12: 2D-histogram of X- and Y-axis position of photon entering the sample.

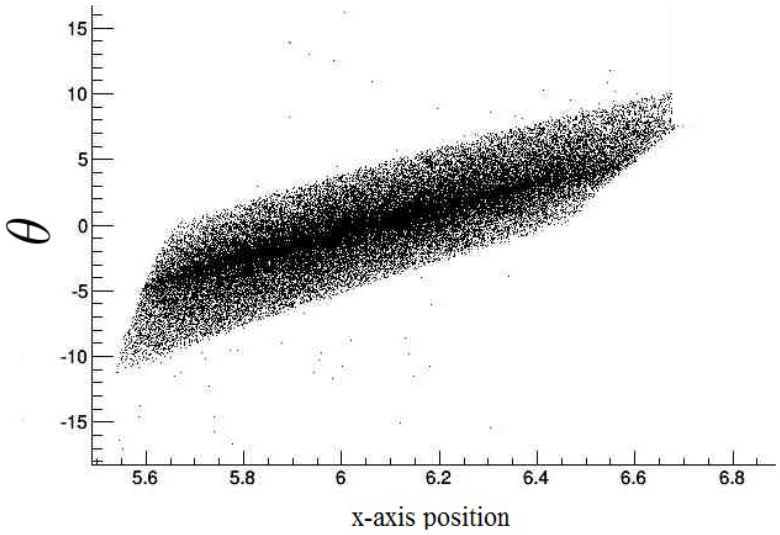

Figure 4.13: 2D-histogram of X-axis position and θ for photon reaching the sample.

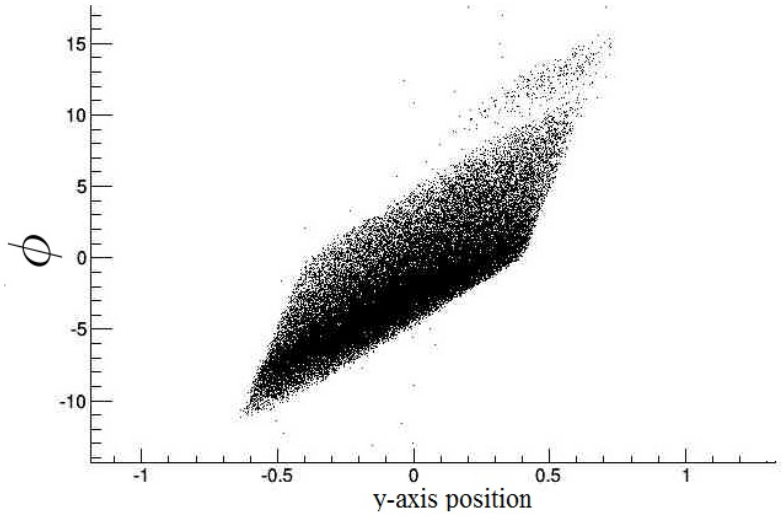

Figure 4.14: 2D-histogram of Y-axis position and ϕ for photon reaching the sample.

the 2D-histogram using the x-component of the position as input, and the angle ϕ is sampled from the 2D-histogram using the y-component of the position as input, and the momentum direction is obtained from θ and ϕ. By taking into account these relations between position and momentum direction, the simulation can better describe the scattering angles of photon scattered from the sample into the detector than the Basic code.

The x- and y-components of the polarization are attributed without preferential direction, in a way that the polarization vector is normalized to unity and is orthogonal to the momentum direction vector. Unlike in the Basic code, primary photons are not generated in the secondary target, they are generated directly on the sample surface.

The excitation of the sample, detection of the X-rays, and creation of the X-ray spectrum, are as described in Section 4.4. Besides how the secondary beam is recreated, the only difference to the Basic code in this second simulation is the inclusion of the collimators.

4.6.3 Simulation results

To test the accuracy of the program the calibration curve of Rayleigh-to-Compton scattering ratio, R_{RC}, as function of the average atomic number, Z_{avg}, was compared between simulated and experimental spectra. The calibration curve is measured, from a set of model samples consisting of different proportions of reference materials of Hydroxyapatite (HAp)[$Ca_{10}(PO_4)_6(OH)_2$] (Sigma-Aldrich, lot #BCBS8492V), and boric acid (HB) [H_3BO_3]. Although the boric acid material is not certified, no significant impurities have been found in the spectrum. As presented in a previous study [122], the calibration curve $R_{\mathrm{RC}}(Z_{\mathrm{avg}})$ for this type of materials, can establish a methodology for the analysis and characterization of hydroxyapatite-based materials such as dental tissues and human

HAp	HB	Z_{avg}
0	100	7.13
5	95	7.48
10	90	7.83
15	85	8.17
20	80	8.52
25	75	8.87
30	70	9.21
35	65	9.56
40	60	9.91
45	55	10.25
50	50	10.60
55	45	10.95
60	40	11.29
65	35	11.64
70	30	11.99
75	25	12.33
80	20	12.68
85	15	13.03
90	10	13.37
95	5	13.72
100	0	14.07

Table 4.2: Average atomic number for samples composed by different weight fractions of HAp and HB.

tissues. The measurements were carried out in Laboratório de Física Atómica e Molecular, LIBPhys-UNL, Departamento de Física, FCT-UNL. The mixtures for the samples were chosen in order to get calibration curve to be in the range $7.13 < Z_{avg} < 14.07$. For each model sample, two replicas of pellets were obtained from the powdered materials, in order to reduce uncertainties due to inhomogeneity. The average atomic number for each model sample is calculated from the following expression:

$$Z_{avg} = \sum_i w_i Z_i, \tag{4.1}$$

where w_i and Z_i are the mass fraction and atomic number for the element i, respectively. For each model sample pellet replica, a second measurement of the spectrum was performed after rotating the pellet, to further reduce uncertainties due to inhomogeneity. As such, 4 experimental measurements are performed for each model sample material.

The calibration curve was obtained from the ratio of the scattering peaks higher net count. In Table 4.2 the HAp and HB weight fractions of each model sample are presented, along with the sample Z_{avg}.

The simulated samples were composed by the same elements and respective weight fractions of the experimental model samples. For this, the HAp and HB materials were created using the *DetectorConstruction* class and the samples were attributed different weight fractions on these materials (the values presented in Table 4.2), in similarity to the

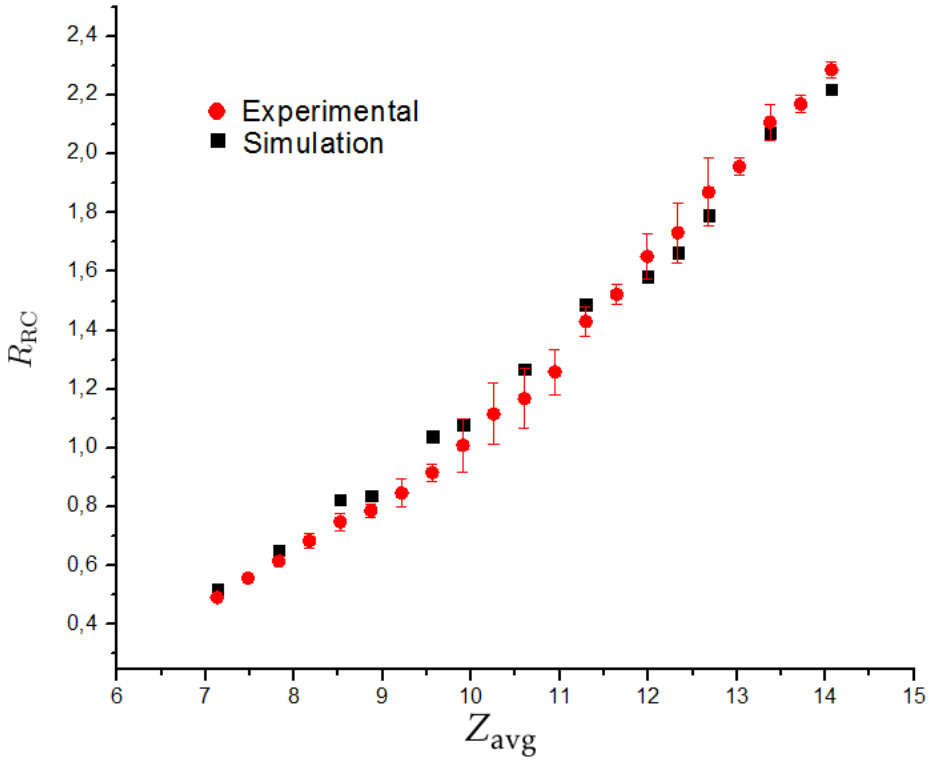

Figure 4.15: Experimental and simulated Rayleigh-to-Compton scattering ratio as function of the average atomic number.

experimental method. The measured densities presented discrepant values between different pellets of the same model material. Such can likely be attributed to the grounding process of the pellets. As such, for the simulations, it was considered material densities of 2.2 g/cm^3, which corresponds to an average measured density. Different density values were tested in the range $1.2 < \rho < 3$ and no significant change to the simulated scattering ratio was verified. The generation of the simulated sample is performed using the user *DetectorConstruction* class.

In Fig. 4.15 the simulated and experimental calibration curves are compared. Relatively good agreement is found between the simulated and experimental ratios, considering that Geant4 resorts to non-relativistic form factors and incoherent function values for the calculation of Rayleigh and Compton cross-sections. The simulated ratio values, in the range $7.13 \leq Z_{avg} \leq 8.86$, are around 6 % higher than the experimental values. In the range $11.98 \leq Z_{avg} \leq 14.07$, the simulated values are less then 4 % lower than the experimental values. Best agreement is found for $Z_{avg} = 13.37$ and $Z_{avg} = 14.06828$, for which the simulated values are 1.69 % and 2.92 % lower than the experimental values, respectively. For the intermediate range $8.86 \leq Z_{avg} \leq 11.98$, worse agreement is found. For $Z_{avg} = 9.56$, $Z_{avg} = 9.91$, $Z_{avg} = 10.60$, and $Z_{avg} = 11.29$, the simulated values are higher than the experimental values by 13.97 %, 7.08 %, 8.62 %, and 4.14 %, respectively.

Nevertheless, most simulated values are close lying or within the experimental uncertainty margins. It is worthwhile mentioning that the simulated values are always higher than the experimental in the range $7.13 \leq Z_{\text{avg}} \leq 11.29$, and lower than the experimental ones in the range $11.99 \leq Z_{\text{avg}} \leq 14.07$. The ratios for lower Z_{avg} values present worse agreement than for higher Z_{avg} values. Since lower Z_{avg} value model samples are mostly composed of boric acid, and since the HB material is not certified, it is suspected that the fact R_{RC} value are in worse agreement for lower Z_{avg} samples can be due to impurities in the HB material.

The relatively good agreement obtained for the simulated Rayleigh-to-Compton ratios demonstrate that this code has the potential to be applied in similar future analytical investigations, especially if fundamental parameters are changed in Geant4 library G4EMLOW.

Chapter 5

Fundamental Parameters calculation

The measurements and calculations of atomic transition probability values have been the subject of many scientific works. From transition probability values, important quantities can be calculated, such as ratios of transition intensities, partial fluorescence yields, and shell fluorescence yields. Although there are numerous calculations of atomic transition probability values in literature (more frequently of the K-shell), the majority of the existing works present calculations for few selected transitions. Up until the 1970s there were relatively few comprehensive relativistic calculations of transition probability values. Such changed when Scofield presented radiative probability values calculated for the majority of transitions and elements, first using Dirac-Hartree-Slater theory [93], and later using Dirac-Hartree-Fock theory [106]. In the same decade Chen *et al.* [95, 97] presented probability values for nonradiative transition, calculated for the majority of possible transitions and elements, using Dirac-Hartree-Fock theory. Scofield's and Chen *et al.*'s benchmark comprehensive calculations allowed for libraries, such as the Evaluated Atomic Data Library [92, 123], to present comprehensive sets of partial fluorescence yields, which are useful regarding simulations of atomic relaxation, and other aplications.

5.1 Theoretical background of atomic structure calculations

The Schröedinger equation is a wave equation that describe spin-1/2 particles such as electrons, and is written as:

$$\hat{H}\left|\psi(\boldsymbol{r},t)\right\rangle = E\left|\psi(\boldsymbol{r},t)\right\rangle, \tag{5.1}$$

where $\hat{H}$ is the Hamiltonian, E the energy, $\boldsymbol{r}$ is the electron position vector, and $\psi(\boldsymbol{r},t)$ the electron wave-function in space-time coordinates. The Dirac equation presents the relativistic alternative to the Schröedinger equation by including the relativistc behaviour

of the particle. The Dirac Hamiltonian for one electron, $\hat{H}_{\mathrm{D}}$, is given as:

$$\hat{H}_D = mc^2\beta + c\boldsymbol{\alpha}.\boldsymbol{p} + V(\boldsymbol{r}), \tag{5.2}$$

where $\boldsymbol{r}$ is the electron position vector, $\psi(\boldsymbol{r},t)$ the electron wave-function in space-time coordinates, m the electron rest mass, $\boldsymbol{p}$ the momentum operator, $\boldsymbol{\alpha}$ and β the Dirac matrices and $V(\boldsymbol{r})$ the nuclear potencial. All state-of-the-art atomic calculations aim to solve the multi-electronic Hamiltonian, where the electron-electron interactions must be taken into account. The Hamiltonian for the multi-electronic atomic system can be written as:

$$\hat{H} = \sum_{i=1}^{N} \hat{H}_D(r_i) + \sum_{i<j=1}^{N} G(i,j), \tag{5.3}$$

where $G(i,j)$ is the two-body operator for the relativistic interaction between the electron i and the electron j, and is written as:

$$G(i,j) = \frac{1}{r_{ij}} - \frac{1}{2r_{ij}}\left[\boldsymbol{\alpha}_1 \cdot \boldsymbol{\alpha}_2 \frac{(\boldsymbol{\alpha}_1 \cdot \boldsymbol{r}_{ij})(\boldsymbol{\alpha}_2 \cdot \boldsymbol{r}_{ij})}{r_{ij}^2}\right] \tag{5.4}$$

where the first term accounts for the Coulomb interaction, the second term (the Breit term) accounts for retardation, and $r_{ij} = |\boldsymbol{r}_i - \boldsymbol{r}_j|$. An additional term can be present in the Breit term to account for magnetic interaction. In non-relativist methods, operator G only includes the Coulomb interaction term.

One of the first approaches to solve multi-electronic atomic systems was performed by Hartree [124]. The total wave function of an atomic system with N electrons was assumed to be expressed as a product of one-electron orthonormal orbitals $\phi_n(n)$:

$$\left|\psi(1,2,...,\mathrm{N})\right\rangle = \left|\phi_1(1)\phi_2(2)...\phi_N(N)\right\rangle, \tag{5.5}$$

where variables 1,2,..., indicate position and spin, and the underscripted labels indicate quantum numbers. Through the variational principle to minimize the energy, the energy of each single-electron orbital $\phi(k)$ is given by the Hartree equation:

$$\begin{aligned} &-\frac{\hbar^2}{2}\nabla_1^2\left|\phi_k(1)\right\rangle - \frac{Zq_e^2}{r_1}\left|\phi_k(1)\right\rangle + \\ &\left(\sum_{i\neq j}\int \phi_j^*(2)\frac{q_e^2}{r_{12}}\phi_j(2)dv_2\right)\left|\phi_k(1)\right\rangle = \epsilon_k\left|\phi_k(1)\right\rangle, \quad k = 1,2,...,N \end{aligned} \tag{5.6}$$

where dv_2 is the integration on coordinates. These equations are similar to the Schröedinger equation, but while in the later the only potencial is the Coulomb potencial due to the atomic nucleus, in the Hartree equations, the Hartree potencial is added to account for the effect of electronic interaction. The Hartree potencial is written as

$$V_{\mathrm{H}}(r_1) = \int \rho_j(2)\frac{q_e^2}{r_{12}}dv_2, \tag{5.7}$$

where $\rho_k(2) = \sum_{j \neq k} \phi_j^*(2)\phi(2)$, is the charge density due to all other electrons. This potencial represents the electrostatic potencial at the point r_1 generated by a charge distribution ρ_k. With this approximation Hartree considered that the Coulomb repulsion between electrons could be accounted as an average field that contains the combined repulsion from all other electrons on the electron that we are considering. The Hartree potencial is not known *a priori* since it depends on the electrons charge density distribution, which in turn depend on the solutions of the Hartree equations. The solution to the Hartree potencial, the energy and the wave functions may be achieved using an iterative method by applying the variational principle to the expected value of the Hamiltonian ($\delta\langle\psi|\hat{H}|\psi\rangle = 0$). The iterative method usually begins with an initial guess of the orbitals, from which the charge density is calculated. The Hartree potencial is then calculated from the charge density and the Hartree equations are solved, and from the solution arise new orbitals. The new orbitals are now used as the initial guess and the process is repeated until convergence is achieved. Usually, convergence is considered to be achieved if the starting orbitals and the final orbitals differ only bellow some threshold. This way the Hartree potencial is then consistent with the orbitals that generate it, for which this is usually called as *self consistent field*.

In closed-shell atoms, and even in some open-shell atoms, the Hartree potencial V_H can be considered to be central by spherically averaging the charge density ρ_k. This way the potencial depends only on the distance between the electron and the nucleus. This approximation is named the *central field approximation* and it simplifies the solution of the Hartree equations. The multi-electron wave function ψ_N written as a simple product of one-electron orbitals $\phi_n(n)$ does not guarantee antisymmetry of the wave function. Slater later introduced the way of writing the multi electron wave function ψ_N in the form of a determinante (the Slater determinant) [125]:

$$\psi(r_1, r_2, ..., r_N) = \frac{1}{\sqrt{N!}} \begin{vmatrix} \phi_1(r_1) & \phi_2(r_1) & ... & \phi_N(r_1) \\ \phi_1(r_2) & \phi_2(r_2) & ... & \phi_N(r_2) \\ ... & ... & ... & ... \\ \phi_1(r_N) & \phi_2(r_N) & ... & \phi_N(r_N) \end{vmatrix}. \tag{5.8}$$

In this way the electrons are indistinguishable, the Pauli Exclusion Principle is ensured, and the wave function is antisymmetric. With the inclusion of these wave functions in the Hartree method for solving the multi electronic system, the method became known as the Hartree-Slater method, and the potencial as the Hartree-Slater potencial. It's relativistic counterparts are know as Dirac-Hartree-Slater (or Dirac-Slater) method. Many calculations of atomic structure were performed using the Hartree-Slater and Dirac-Slater methods, but the approximations used in the description of the electron-electron interaction seemed to produce results that were in many cases significantly diverted from the experimental ones. In what became known as Hartree-Slater-Fock method (or Hartree-Fock method) [126] a different approach was used to consider the contribution of all electrons to the potencial. As in Hartree-Slater method, it is considered that each electron

is affected by an average field created by all other electrons, however, in the Hartree-Fock method, the average field is represented by the direct and exchange operators, $\hat{J}_{\mathrm{D}}$ and $\hat{K}_{\mathrm{ex}}$, such that the average potential is given as:

$$V_{\mathrm{HF}}(r) = V_{\mathrm{D}}(r) + V_{\mathrm{ex}}(r), \tag{5.9}$$

where V_{D} is the direct potential, due to the electron repulsion, and V_{ex} is the exchange potential, which accounts for the exchange of two electrons, due to the anti-symmetrization of the electron wave-functions. With this inclusion, Hartree-Fock accounts for more of the electron-electron interaction than the Hartree-Slater methods, and have generally been shown to be more accurate. The relativistic counterpart of the Hartree-Fock method is usually referred to as Dirac-Hartree-Fock method, or Dirac-Fock method.

The Dirac-Slater and Dirac-Fock approaches do not fully describe the Coulomb repulsion between electrons. To obtain high precision results the electronic correlation needs to be fully taken into account. For this many methods have emerged, such as multiconfiguration Hartree-Fock (MCHF), configuration-interaction (CI), many-body perturbation theory (MBPT) as well as their relativistic versions, relativistic configuration-interaction (RCI), multiconfiguration Dirac-Fock (MCDF), and relativistic many-body perturbation theory (RMBPT). In RCI (or CI) and MCDF (or MCHF), electronic correlation is included by writing the wave function of the atomic system ψ as a linear combination of configuration wave functions φ, which are wave functions for different possible configuration states: $\psi(1,2,...,N) = \sum_i a_i^{(\mathrm{m})}\varphi_i$, where $a_i^{(\mathrm{m})}$ are mixing coefficients. For example, the wave function for He in the ground state can be written as:

$$\psi(\mathrm{He}) = a_1^{(\mathrm{m})}\varphi(1s^2) + a_2^{(\mathrm{m})}\varphi(2p^2), \tag{5.10}$$

where $a_1^{(\mathrm{m})}$ and $a_2^{(\mathrm{m})}$ are the mixing coefficients, $\varphi(1s^2)$ is the minimum configuration state function, and $\varphi(1s^1 2p^1)$ and $\varphi(2p^2)$ are extra correlations state functions. The configuration wave functions are written as a combination of one-electron orbitals using the Slater determinants, as in the non multiconfiguration methods. These methods follow a similar procedure as the Hartree-Fock method. The mixing coefficients are obtained by minimizing the energy. In RCI the wave functions are frozen and only the mixing coefficients are altered during the iteration process. In MCDF methods, both wave functions and mixing coefficients are altered in the iteration process, allowing some degree of freedom for the variation of the wave functions. The multiconfiguration Dirac-Fock method is described in detail in other works [127–130].

For all methods mentioned in the present chapter, contributions for the energy can be added (and usually are), such as Breit correction and Gaunt correction to electron-electron interaction, retardation effects, vacuum polarization, etc. These contributions can be included self-consistently or can be calculated as perturbation through perturbation theory after self consistence has been achieved.

Hartree-Fock and Dirac-Fock approaches have widely been employed in atomic structure calculations, for which there is in literature comprehensive calculations for wide

ranges of elements and atomic transitions. While the more recent approaches (MCDF, RCI, RMBPT) allow more accurate results, results obtained with these methods are not as abundant in literature due to the methods increased complexity. In the present work, the MCDF method is employed in atomic structure calculations, to more accurately describe the electron-electron interactions. The calculations are presented in the following section.

5.2 Multiconfiguration Dirac-Fock calculations

Zn K-shell transition probability values are calculated using the MCDFGME code [127], developed by J.P. Desclaux and P. Indelicato. This code implements the Multiconfiguration Dirac-Fock method including various contributions self-consistently, like Coulomb interaction, Breit corrections, vacuum polarizations, etc. It also includes quantum electrodynamics contributions. One of the many capacities of the code is the calculations of radiative and radiationless transition probability values and the energies of the emitted X-rays and Auger electrons. The energy and wave function for the initial configuration, the Zn with a hole in the K-shell ($1s^1 2s^2 2p^6 3s^2 3p^6 4s^2 3d^{10}$), and the energies and wave functions of all possible final configurations attained through radiative or radiationless transitions are calculated independently, including in most cases all possible extra correlation states up to the 4p orbital. From these, radiative and radiationless transitions probability values for all possible radiative and radiationless transitions are calculated. In the calculation of radiative transition, correlation up to the 4p orbital is included (for both the initial and final state) in all transitions, with the exception of the K-N_1 transition where in the final state ($1s^2 2s^2 2p^6 3s^2 3p^6 4s^1 3d^{10}$) only selected extra correlation configurations up to the 4p orbital are included to be able to achieve convergence. Furthermore, also for the K-N_1 transition probabilities calculation, to achieve convergence some orbitals are frozen during the iterative process. Except for the previous exception, full relaxation was allowed for both initial and final states. Since the wave functions of the initial and final states are calculated independently, the spin-orbitals are not orthogonal. To account for the non-orthogonality, a formalism described by Lowdin [131] is used by the MCDFGME code. Due to convergence problems, several nonradiative transition probability values are calculated including only selected extra correlation configurations up to the 4p orbital. In some transitions only selected extra correlation configurations up to the 4s orbital are included. For the nonradiative transition between $1s^1 2s^2 2p^6 3s^2 3p^6 4s^2 3d^{10}$ and $1s^2 2s^2 2p^6 3p^6 4s^2 3d^{10}$ no extra correlation states were included. Additionally, for many nonradiative transitions, the orbitals were frozen during the iterative process. In all calculations, Breit interaction (including its magnetic and retardation components) and vacuum polarization contributions are included in the self-consistent field method. The calculated radiative transition probability values are presented in Table A.1 (in Appendix A) and the calculated radiationless transition probability values are presented in Table A.2 (in Appendix A). From these values, K-shell transition partial fluorescence yield, transition intensity ratios, and the K-shell fluorescence yield values are derived.

5.3 Calculation results

The present work radiative transition probability values, calculated using the multiconfiguration Dirac-Fock method, are compared in Table 5.1 with Scofield's Dirac-Hartree-Slater [93], Dirac-Hartree-Fock results [93], and Casteleiro *et al.* MCDF calculations [132]. In Casteleiro *et al.* MCDF calculations no multi-configuration wavefunctions beyond intermediate coupling are not included, unlike in the present work calculations. Good agreement is found with Scofield's Dirac-Hartree-Fock values. When comparing with the later, the calculated MCDF values differ by about 2 % higher for the K-L_2 and K-L_3 transitions, and are 1.1 % higher for the K-M_2 and K-M_3 transitions, as well as for the total radiative transition rate. When comparing with Scofield's Dirac-Hartree-Slater values worse agreement is found for these transitions. The agreement with Casteleiro *et al.* [132] values is even better than with DF values.

Table 5.1: Radiative transition probability values from this work's MCDF calculations, Scofield's Dirac-Hartree-Slater calculations [93], and Scofield's Dirac-Hartree-Fock calculations [106]. Values not presented in their references are presented in table as n.p.. All values are presented in milliatomic units; 1 milliatomic unit = $4.134 \times 10^{-13} s^{-1}$.

Radiative transition	DS [93]	DF [106]	MCDF (Casteleiro *et al.*)	MCDF (present work)
K-L_1	2.07×10^{-5}	n.p.	2.59×10^{-5}	2.47×10^{-5}
K-L_2	8.28	8.59	8.77	8.76
K-L_3	16.1	16.7	17.1	17.07
K-M_1	4.08×10^{-6}	n.p.	5.24×10^{-6}	5.18×10^{-6}
K-M_2	1.024	1.17	1.19	1.185
K-M_3	2.00	2.29	2.33	2.318
K-M_4	1.39×10^{-3}	n.p.	1.59×10^{-3}	1.50×10^{-3}
K-M_5	2.00×10^{-3}	n.p.	2.17×10^{-3}	2.17×10^{-3}
K-N_1	2.46×10^{-7}	n.p.	3.50×10^{-7}	3.36×10^{-7}
Total	27.4	29.0	29.4	29.33

From the radiative transition probability values, radiative transition partial fluorescence yield values (normalized without accounting radiationless transitions) are calculated as in Eq. 2.10. The values obtained are presented in Table 5.2, where they are compared with the theoretical values from Scofield's Dirac-Hartree-Slater calculations [93], theoretical values from Scofield's Dirac-Hartree-Fock calculations [106], and the empirical values present in NIST's Fundamental Parameters Database [38]. The partial fluorescence yield values presented in NIST's Fundamental Parameters Database [38] are obtained from empirical fitting functions to Salem *et al.* collection of K-shell experimental transition intensity ratios [108], and some treatment to the data to convert from transition ratios to partial fluorescence yield values. It is worthwhile mentioning that Salem *et al.* collection [108] is still to this date the most complete source of experimental X-ray transition intensity ratios, in what concerns K-shell and L-shell transitions. Although

Table 5.2: Radiative transition K-shell partial yield values, ω_{ij}, obtained from this work's MCDF calculations, Scofield's Dirac-Hartree-Slater calculations [93], Scofield's Dirac-Hartree-Fock calculations [106], and NIST Fundamental Parameters Database [38]. Values that could not be obtained, since transition probability values where not presented in their references, are presented in table as n.p..

ω_{ij}	MCDF	DS [93]	DF [106]	NIST [38]
K-L_1	8.43×10^{-7}	7.54×10^{-7}	n.p.	3.16×10^{-4}
K-L_2	0.298	0.302	0.299	0.294
K-L_3	0.582	0.588	0.581	0.576
K-M_1	1.76×10^{-7}	1.49×10^{-7}	n.p.	n.p.
K-M_2	0.040	0.037	0.041	0.044
K-M_3	0.079	0.073	0.080	0.085
K-M_4	$5.10E \times 10^{-5}$	5.05×10^{-5}	n.p.	n.p.
K-M_5	7.39×10^{-5}	7.30×10^{-5}	n.p.	n.p.
K-$M_{4,5}$	1.25×10^{-4}	1.23×10^{-4}	n.p.	8.16×10^{-4}
K-N_1	1.15×10^{-8}	8.96×10^{-9}	n.p.	n.p.

Scofield's Hartree-Fock reference [106] do not present transition probability values for the K-L_1, K-M_1, K-M_4, K-M_5, and K-N_1 transitions, these values can be considered negligible when comparing with the sum of all possible radiative transition probabilities. Thus, partial fluorescence yield values obtained from the Hartree-Fock probability values are calculated (from Eq. 2.10) using only the K-L_2, K-L_3, K-M_2 and K-M_3 transitions. NIST's Fundamental Parameters Database does not present partial fluorescence yield values for K-M_1, K-M_4, K-M_5, and K-N_1 transitions, although it presents values for K-$M_{4,5}$ transition, which is equivalent to the sum of K-M_4 and K-M_5 values. From Table 5.2, it is shown that this work's MCDF partial fluorescence yield values for K-L_2, K-L_3, K-M_2, K-M_3 transitions are in close agreement with the empirical values from NIST Fundamental Parameters Database [38], while for K-L_1 and K-$M_{4,5}$ transitions the same can not be said.

Radiative transition ratios obtained from this work's multiconfiguration Dirac-Fock calculations are compared in Table 5.4 with ratios obtained from Scofield's Dirac-Hartree-Slater calculations [93], Scofield's Dirac-Hartree-Fock calculations [106], and the empirical-fit values from NIST Fundamental Parameters Database [38]. The designations for the transitions used in Tables 5.4 are presented in Table 5.3. Since there is in literature a large quantity of experimental and theoretical results for Kβ/Kα intensity ratio, we present these values in a separate table, Table 5.5. In this table, the present work values are compared with other theoretical values, experimental values, and values obtained from empirical fittings to the experimental values. The theoretical values are those obtained from Scofield's Dirac-Hartree-Slater calculations [93], Scofield's Dirac-Hartree-Fock calculations [106], Kup *et al.* MCDF calculations [133], and Casteleiro *et al.* MCDF calculations. It should be noted that in both Kup *et al.* and Casteleiro *et al.* MCDF calculations, multi-configuration wavefunctions beyond intermediate coupling are not included, unlike in the calculations of the present work. The experimental values presented are from

several works from 2001 to 2011 [134–143]. In Table 5.5, the values obtained through empirical fittings to the experimental data are those of Salem *et al.* [108], NIST Fundamental Parameters Database [38], and Kahoul *et al.* [144]. Salem *et al.* fittings use experimental data up to 1974. NIST Fundamental Parameters Database uses the same data as Salem *et al.*, but since NIST database only presents the radiative transition probabilities and not the ratios, we obtained them by calculating the ratios of the respective transition probabilities. Kahoul *et al.* uses experimental values from the period 2001-2011 (these experimental values are also presented in Table 5.5). As presented in Table 5.4, this work's values are in good agreement with Scofield's Hartree-Fock values [106]. When comparing against NIST's database ratios [38], relatively good agreement is presented for the $K\alpha_2/K\alpha_1$, $K\beta_3/K\beta_1$, and $K\beta'_1/K\alpha_1$ ratios, but strong disagreement is found for the $K\alpha_3/K\alpha_1$ and $K\beta_5/K\beta_1$ ratios.

From the comparison of $K\beta/K\alpha$ ratios, presented in Table 5.5, it is noticeable that Kup *et al.* [133] value is equal to the present work MCDF value, even though in their calculations no multiconfiguration wavefunctions were included except those of intermediate coupling. When comparing the present work's MCDF value with the theoretical values from Scofield, closer agreement is found with Scofield's Dirac-Hartree-Fock value [106]. Even though NIST Fundamental Parameters Database [38] uses Salem *et al.* ratios [108], their value differ from one-another. This discrepancy can be due to NIST's database treatment to Salem *et al.* data. The present work value is in good agreement with Salem *et al.* empirical fit value [108] and with Kahoul *et al.* empirical fit value [144].

Table 5.3: Indication of transitions corresponding to the line designations.

$K\alpha$	All K-L transition
$K\alpha_1$	K-L_3
$K\alpha_2$	K-L_2
$K\alpha_3$	K-L_1
$K\beta_1$	K-M_3
$K\beta_3$	K-M_2
$K\beta_5$	K-M_4+K-M_5
$K\beta'_1$	All K-M transitions
$K\beta'_2$	K-N and all higher shells
$K\beta$	K-M and all higher shells

Nonradiative transition probability values calculated in the present work are compared in Table 5.6 with Chen *et al.* Dirac-Hartree-Fock values [95] and with Safronova *et al.* Dirac-Hartree-Fock values [145]. In this table, transitions are grouped according with the holes in the shells in order to help the readability. As presented in Table 5.6, this work's values of radiationless transition probability values are often lower than Chen *et al.* [95] values and often higher than Safronova *et al.* values [145].

K-LX and K-LL transition probability values, and (K-LX)/(K-LL) and (K-XY)/(K-LL) ratios are compared in Table 5.7 with Chen *et al.* Dirac-Hartree-Fock values [95], Safronova

Table 5.4: Radiative transition ratios obtained from this work's MCDF calculations, Scofield's Dirac-Hartree-Slater calculations [93], and Scofield's Dirac-Hartree-Fock calculations [106], empirical fit values from NIST Fundamental Parameters Database, and Salem empirical fit values *et al.* [108]. Values that could not be obtained due to lack of information are presented in table as n.p..

Transition Intensity Ratio	MCDF	DS [93]	DF [106]	NIST [38]	Salem [108]
$K\alpha_2/K\alpha_1$	0.513	0.514	0.5142	0.511	0.510
$K\beta_3/K\beta_1$	0.511	0.511	0.5108	0.518	n.p.
$K\beta_1'/K\alpha_1$	0.205	0.188	0.2135	0.224	n.p.
$K\beta_2'/K\alpha_1$	1.97×10^{-8}	1.53×10^{-8}	n.p.	n.p.	n.p.
$K\alpha_3/K\alpha_1$	1.45×10^{-6}	1.28×10^{-6}	n.p.	5.49×10^{-4}	n.p.
$K\beta_1/K\alpha_1$	0.136	0.124	0.1370	0.147	n.p.
$K\beta_5/K\beta_1$	1.58×10^{-3}	1.69×10^{-3}	n.p.	9.64×10^{-3}	n.p.

Table 5.5: Radiative transition $K\beta/K\alpha$ ratios from several references.

		$K\beta/K\alpha$
Theoretical	MCDF	0.136
	Scofield (DS), 1974 [93]	0.1241
	Scofield (DF), 1974 [106]	0.141
	Casteleiro *et al.* (MCDF), 2010 [132]	0.136
	Kup *et al.* (MCDF), 2017 [133]	0.136
Experimental	Ertuğrul, Sögüt, *et al.*, 2001 [134]	0.136 ± 0.01
	Sogut *et al.*, 2002 [135]	0.1254 ± 0.0102
	Ertugrul, 2002 [136]	0.158 ± 0.005
	Öz, 2006 [137]	0.141 ± 0.01
	Han *et al.*, 2007 [138]	0.126 ± 0.01
	Cevik *et al.*, 2007 [139]	0.136 ± 0.005
	Ertuğral *et al.*, 2007 [140]	0.1379 ± 0.005
	Yalçin, 2007 [141]	0.1225 ± 0.0007
	Yalçin, 2007 [141]	0.1267 ± 0.0011
	Kup Aylikci *et al.*, 2010 [142]	0.12 ± 0.0061
	Kup Aylikci *et al.*, 2011 [143]	0.12 ± 0.0061
Empirical fit (-1974)	Salem *et al.*, 1974 [108]	0.138
Empirical fit (-1974)	NIST, 2002 [38]	0.148
Empirical fit (2001-2011)	Kahoul *et al.*, 2011 [144]	0.1285 ± 0.0051

Table 5.6: Nonradiative transitions probabilities from this work's MCDF calculations, Chen *et al.* Dirac-Hartree-Fock calculations [95], and Safronova *et al.* Dirac-Hartree-Fock calculations [145]. Values not presented in their references are presented in table as n.p.. *Note: Chen *et al.* [95] does not present values for K-M_2M_2, K-M_2M_4 and K-M_2M_5 transitions. All values are presented in milliatomic units; 1 milliatomic unit = $4.134 \times 10^{-13} s^{-1}$.

Nonradiative transitions	1s $n1$ $n2$	Safronova [145]	Chen [95]	MCDF
K-L_1L_1	1s 2s 2s	1.817	2.084	1.402
K-L_1L_2+K-L_1L_3	1s 2s 2p	5.918	6.423	5.829
K-L_1M_1	1s 2s 3s	0.490	0.564	0.811
K-L_1M_2+K-L_1M_3	1s 2s 3p	0.764	0.840	0.883
K-L_1M_4+K-L_1M_5	1s 2s 3d	0.031	0.040	0.023
K-L_1N_1	1s 2s 4s	n.p.	0.043	0.031
K-L_2L_2+K-L_2L_3+ K-L_3L_3	1s 2p 2p	14.64	15.51	15.93
K-L_2M_1+K-L_3M_1	1s 2p 3s	0.687	0.741	0.633
K-L_2M_2+K-L_2M_3+ K-L_3M_2+K-L_3M_3	1s 2p 3p	3.299	3.501	3.512
K-L_2M_4+K-L_2M_5+ K-L_3M_4+K-L_3M_5	1s 2p 3d	0.247	0.319	0.188
K-L_2N_1+K-L_3N_1	1s 2p 4s	n.p.	0.055	0.047
K-M_1M_1	1s 3s 3s	0.033	0.038	0.044
K-M_1M_2+K-M_1M_3	1s 3s 3p	0.089	0.097	0.088
K-M_1M_4+K-M_1M_5	1s 3s 3d	0.003	n.p.	0.003
K-M_1N_1	1s 3s 4s	n.p.	0.006	0.014
K-M_2M_2+K-M_2M_3+ K-M_3M_3	1s 3p 3p	0.187	0.194*	0.198
K-M_2M_4+K-M_2M_5+ K-M_3M_4+K-M_3M_5	1s 3p 3d	0.023	0.020*	0.026
K-M_2N_1+K-M_3N_1	1s 3p 4s	n.p.	0.008	0.006
K-M_4M_4+K-M_4M_5+ K-M_5M_5	1s 3d 3d	n.p.	n.p.	0.001
K-M_4N_1+K-M_5N_1	1s 3d 4s	n.p.		0.000
Total		28.231	30.484	29.665

Table 5.7: Nonradiative K-LL, K-LX and K-XY transition probability values from this work's MCDF calculations, Chen *et al.* Dirac-Hartree-Fock calculations [95], and Safronova *et al.* Dirac-Hartree-Fock calculations [145]. K-LX/K-LL and K-XY/K-LL nonradiative transition ratios from this work's MCDF calculations, Chen *et al.* Dirac-Hartree-Fock calculations [95], Safronova *et al.* Dirac-Hartree-Fock calculations [145], and experimental values from Bellicard *et al.* [146]. Transition probability values are presented in milliatomic units; 1 milliatomic unit = $4.134 \times 10^{-13} s^{-1}$.

	Safronova [145]	Chen [95]	MCDF	Experimental [146]
K-LL	22.38	24.02	23.16	
K-LX	5.518	6.103	6.128	
K-XY	0.335	0.363	0.380	
K-LX/K-LL	0.247	0.254	0.265	0.30 ± 0.02
K-XY/K-LL	0.015	0.015	0.016	0.019 ± 0.005

et al. Dirac-Hatree-Fock values [145], and experimental values from Bellicard *et al.* [146]. It is presented in Table 5.7 that K-LL total value is lower than Chen *et al* value and higher than Safronova. As for K-LX and K-XY total probability values, these presented values are higher than the other compared. Thus, K-LX/K-LL and K-XY/K-LL ratios from this work are higher than the other compared values.

This work's ratios of radiationless transitions intensity relative to the K-L_2L_3 ($^1D_2$) transition are presented in Table 5.8, where they are compared with experimental results from Freedman *et al.* [147]. The values are in most cases in good agreement with the presented experimental results.

Table 5.8: Nonradiative transition intensity relative to K-L_2L_3 ($^1D_2$). Values presented are from this work's MCDF calculations and experimental values from Freedman *et al.* [147].

Relative Intensity Transition	MCDF	Experimental [147]
K-L_1L_1 ($^1S_0$)	0.114	0.058
K-L_1L_2 ($^1P_1$)	0.298	0.28
K-L_1L_2 ($^3P_0$)	0.024	<0.03
K-L_1L_3 ($^3P_1$)	0.080	0.046
K-L_1L_3 ($^3P_2$)	0.072	<0.02
K-L_2L_2 ($^1S_0$)	0.090	<0.1
K-L_2L_3 ($^1D_2$)	1.000	1.000
K-L_3L_3 ($^3P_0$)	0.040	∼0.04
K-L_3L_3 ($^3P_2$)	0.165	0.2

From these work's calculated radiative and radiationless transition probability values (presented in Tables A.1 and A.2 in Appendix A, respectively), the Zn K-shell fluorescence yield value is calculated from Eq. 2.6. The present work K-shell fluorescence yield is compared in Table 5.9 with other values obtained from theoretical calculations, experimental measurements, and empirical fittings to experimental values. The theoretical

values are from EADL library [99], Chen *et al.* Dirac-Hartree-Fock calculations [97], Kup *et al.* MCDF calculations [133], and Casteleiro *et al.* MCDF calculations. It should be noted that in both Kup *et al.* and Casteleiro *et al.* MCDF calculations, multi-configuration wavefunctions beyond intermediate coupling are not included, unlike in the calculations of the present work. The experimental values are from several works from 2000 to 2010 [34, 136, 138, 142, 148–153]. The empirical fitting values are from several works [38, 144, 154–157]. The fluorescence yield value from this work is higher than all other theoretical values compared in Table 5.9. Such is to be expected when comparing with values presented in EADL [99] and Chen *et al.* work [97], since the calculated total radiative transition probability $A^{(TA)}$ is higher than the value used in those references, which is Scofield's Dirac-Slater value [93] in EADL [91], and Scofield's Dirac-Fock value [106] in Chen *et al.* work. And since the calculated total radiationless transition probability $A^{(TA)}$ is lower than value from Chen *et al.* work, which is the same Chen *et al.* work, and in EADL. From the previous statements, the fact that the present work value is higher than the other theoretical values can be verified from Eq. 2.6. It should be noted that while the calculated total radiative transition probability $A^{(TA)}$ is in good agreement with Scofield's Dirac-Fock value (as seen in Table 5.1), the calculated total radiationless transition probability $A^{(TA)}$ is not in so much good agreement with Chen *et al.* Dirac-Fock value (as presented in Table 5.6). It also worthwhile mentioning that is known that performing atomic structure calculation using the multiconfiguration Dirac-Fock approach generally have more limitation in achieving accurate results for radiationless transition calculations than for radiative transition calculations. Since Kup *et al.* and Casteleiro *et al.* do not include multi-configuration wavefunctions beyond intermediate coupling, their respective radiationless transition calculations are likely to be more accurate, and as such, the same can be said of the calculated K-shell fluorescence yield. The calculated K-shell fluorescence yield is also higher than the compared experimental values, with the exception being when comparing with the value measured by Söğüt [153] value, which is one of the most recent measurements. Furthermore, the value is in very good agreement with Ménesguen and Lépy [34] experimental value. All empirical fit values are lower than the calculated MCDF value. Interestingly, the most recent values obtained through empirical fittings, which are those of Daoudi *et al.* and Kahoul *et al.*, are significantly lower than all the theoretical values, with the exception of values from EADL, which are the only theoretical values calculated using the Dirac-Hartree-Slater method, instead of the Dirac-Hartree-Fock method.

Table 5.9: Comparison of K-shell fluorescence yield values from several works.

		ω_K
Theoretical	MCDF	0.497
	EADL [99]	0.466
	DF [97]	0.488
	Kup *et al.* [133]	0.485
	Casteleiro *et al.* [132]	0.485
Experimental	Şimşek *et al.*, 2000 [148]	0.482±0.022
	Durak and Özdemir, 2001 [149]	0.482±0.032
	Ertugrul, 2002 [136]	0.460±0.013
	Şimşek *et al.*, 2002 [150]	0.488±0.021
	Gudennavar *et al.*, 2003 [151]	0.464±0.010
	Yashoda *et al.*, 2005 [152]	0.471±0.018
	Han *et al.*, 2007 [138]	0.477±0.038
	Aylikci *et al.*, 2010 [142]	0.485±0.024
	Aylikci *et al.*, 2010 [142]	0.460±0.023
	Aylikci *et al.*, 2010 [142]	0.459±0.023
	Aylikci *et al.*, 2010 [142]	0.458±0.023
	Aylikci *et al.*, 2010 [142]	0.467±0.023
	Ménesguen and Lépy, 2001 [34]	0.495±0.022
	Söğüt, 2010 [153]	0.525±0.050
Empirical fit	Bambynek, 1972 [154]	0.479
	Krause, 1979 [155]	0.474
	Bambynek, 1984 [156]	0.486
	NIST, 2002 [38]	0.469
	Kahoul *et al.*, 2012 [144]	0.463
	Daoudi *et al.*, 2015 [157]	0.473

Chapter 6

Fundamental Parameters comparison

Many codes and software of elemental analysis and Monte Carlo simulation of atomic relaxation (softwares based on the AXIL package [158, 159], PENELOPE [160–162], PyMCA [12], among many others) rely on the data available in literature regarding atomic relaxation, such as transition probabilities, fluorescence yields, partial fluorescence yields and radiationless transition yields. The accuracy of these codes and softwares are strongly related to the accuracy of the data used. On the other hand, the simulation of atomic relaxation relies on data libraries with tabulated partial fluorescence yield values of radiative transitions, commonly derived from the Evaluated Atomic Data Library (EADL). However, recent studies from Pia *et al.* support that the data library EADL could be improved by adopting Scofield's Hartree-Fock calculations instead of current Scofield's Hartree-Slater calculations (see Section 4.1.2). These studies compare the partial fluorescence yield values without accounting radiationless transitions (see Section 2.1.2, Eq. 2.10). Since EADL library and Geant4's library G4EMLOW present partial fluorescence yield values that are normalized accounting radiationless transitions (see Sections 2.1.2., Eq. 2.8), in the present chapter it is presented a comparison of the later values, regarding the K-L_2, K-L_3, K-M_2, K-M_3 radiative transitions, in order to assess the partial fluorescence yields presented in EADL. Furthermore, total K-shell fluorescence yield values are also compared. The values included in these comparison are obtained from several references, either extracted directly from its references, or are derived from atomic parameters presented in these references. Additionally, it is presented comprehensive partial fluorescence yield values obtained from the combination of semi-empirical and empirical fitting functions from different references.

In literature, several references can be found containing values related to atomic transitions, such as: transition rates, ratios of emission rates (where the values may be the ratio of single or several transitions), shell fluorescence yields, fluorescence widths, Auger

yields, Auger widths, etc. These values were obtained through experimental measurements, theoretical calculations, or semi-empirical fittings to the available data. Although total shell fluorescence yield and partial fluorescence yield values can generally be derived from these data, there is no comparison of comprehensive libraries with partial fluorescence yield values, possibly due to the different nomenclatures used in the literature. Thus, in this chapter, it is also presented a bibliography overview of works containing partial fluorescence yield values, or relevant atomic parameters from which partial fluorescence yields can be obtained. The references include libraries and articles, in which the atomic parameter values were theoretically calculated, experimentally measured, or obtained with semi-empirical and empirical fitting formulas.

The quantities presented in this chapter, as mentioned, have various designations in literature. In fact, the various references that are presented in Section 6.1 often use different designations and symbols than the ones used in the present work. To help readability, in Tables B.1 to B.3 (in Appendix B), is presented a comparison of the different designations and symbols used in the present work, with the ones used in the references presented in Section 6.1. To simplify, the variable subscripts corresponding to the shells and sub-shells are omitted. Also to simplify, the transition probability A, presented in the first column of Table B.1, can refer to either the transition probability $A_{ij}^{(\mathrm{R})}$ of a radiative transition ij, or the transition probability $A_{ijk}^{(\mathrm{A})}$ of a radiationless transition ijk (see Section 2.1.2). This simplification was chosen because most of the works that are listed in Tables B.1 to B.3 do not use different symbols or nomenclature to differ between radiative and radiationless transition probability.

6.1 Overview of atomic parameters from different works

Here, it is presented references containing K-shell fluorescence yields, transition probabilities, partial fluorescence yields, or other atomic parameters, from which K-shell fluorescence yield values ω_{K} and partial fluorescence yield values $\omega_{\mathrm{K\text{-}L_2}}$, $\omega_{\mathrm{K\text{-}L_3}}$, $\omega_{\mathrm{K\text{-}M_2}}$ and, $\omega_{\mathrm{K\text{-}M_3}}$ can be obtained; whether they are libraries, articles, product of theoretical calculations, experimental measurements or the result of combined theoretical and experimental values. Although a huge number of theoretical calculations and experimental results can be found in literature, it is selected and described the ones from which comprehensive values can be obtained for large range of transitions and large range of atomic number, which are the ones relevant to the comparisons made in the present work.

The nomenclature of the atomic parameters in the references presented in this chapter may differ from the nomenclature in the present work. Throughout this chapter, each quantity is referred to using the designations of the present work. The designations used in the original references are presented in Tables B.1 to B.3.

6.1.1 Combination of Kostroun *et al.* Hartree-Slater radiationless transition probability calculations and Scofield's Dirac-Slater radiative transition probability calculations

In 1971, Kostroun *et al.* [163] calculated nonrelativistic K-shell radiationless transition probabilities for selected elements using the Hartree-Slater method. In order to derive theoretical total K-shell fluorescence yields, Kostroun *et al.* [163] combined their results with Scofield's earlier Dirac-Slater radiative transition probabilities [105], which were calculated without considering the finite extent of the nuclear charge distribution. In Kostroun *et al.* work, calculations were only performed for selected elements, the values for the remaining elements where obtained through fits.

In the present work, it is present the K-shell fluorescence yield values ω_K extracted directly from Kostroun *et al.* work. These values are compared with values from other works in Section 6.2, and presented in Table B.4 (from Appendix B). Throughout this work, these values are referred to as "Kostroun".

6.1.2 Scofield's radiative transition probability calculations based on the Dirac-Slater method

In 1969, using relativistic Hartree-Slater theory, or Dirac-Slater theory (see Section 5.1), Scofield calculated K- and L-shell radiative transition probabilities [105] for selected transitions, and selected elements in the range $13 < Z < 92$. In these calculations, the electrons were treated relativistically and the effect of retardation was included (the second term of operator G from Eq. 5.4). The electrons were considered as moving independently with their mutual interactions accounted for by a central potential (thus not including the exchange potential from Eq. 5.9). All multipoles of the radiation field and all transitions from occupied states of the atom were included. Scofield presents the radiative transition probabilities calculated using this model for K- and L-shell transitions [105]. As mentioned in Section 6.1.1, the calculations in this work did not considered the finite extent of the nuclear charge distribution.

In 1974, Scofield presented K- and L-shell radiative transition probabilities calculated using an improved model, by including nuclear charge distribution of finite extent [93]. In this later work, it is presented values for elements with atomic number ranging $5 \leq Z \leq 104$ and for all possible radiative transitions.

6.1.3 Scofield's radiative transition probability calculations based on the Dirac-Fock method

Using relativistic Hartree-Fock theory, or Dirac-Fock theory (as presented in Section 5.1), Scofield calculated K- and L-shell radiative transition probabilities. In Scofield's work, the exchange potential V_{ex} was included (as in Eq. 5.9). In his work, the values for K-shell are presented for selected transitions, and for selected elements with atomic number ranging

$10 \leq Z \leq 98$ [106]. The values for L-shell radiative transition probabilities are presented for selected elements with atomic number ranging $18 \leq Z \leq 94$ [107]. In other works [164], it is presented L-shell radiative transition probabilities for more selected elements, which were obtained by interpolation of the probabilities calculated by Scofield.

6.1.4 Chen *et al.* radiationless transition probability calculations based on the Dirac-Fock method

Chen *et al.* theoretical approach consists on calculating the radiationless transition probabilities from relativistic perturbation theory, for frozen orbitals, in the Dirac-Hartree-Fock (or Dirac-Fock) approach (thus including the exchange potential in Eq. 5.9). Using this approach, Chen *et al.* present calculated radiationless transition probabilities for K- and L-shell, for selected elements with atomic number in the range $18 \leq Z \leq 96$ [95]. In a later work, Chen *et al* present radiationless K-shell atomic level widths [97] and present radiationless L-shell atomic level widths. [94, 96] for selected elements.

6.1.5 EADL

The EADL library [99] contains partial fluorescence yield and radiationless transition yield values, which the Geant4 includes in its library. The radiative transition partial transition yield values are based on Scofield's theoretical approaches [93, 105] (which were presented in Sections 6.1.1 and 6.1.2) and the radiationless transition yield values are based on Chen's theoretical approaches [94–98] (which were presented in Section 6.1.4) complemented by Hubbel's corrections [99] to avoid the over-prediction of the strength of Coster-Kronig transitions resulting from Dirac-Hartree-Slater calculations. The 2014 version of EADL can be found online [92]. Recent changes have been performed to EADL library, regarding the binding energy values.

In the present work, it is presented K-shell partial fluorescence yield values $\omega_{\text{K-L}_2}$, $\omega_{\text{K-L}_3}$, $\omega_{\text{K-M}_2}$, $\omega_{\text{K-M}_3}$, extracted directly from the EADL library [99]. It is also presents K-shell fluorescence yield values ω_{K} obtained by summing over all radiative transition fluorescence yields, as in Eq. 2.9. These values are compared with values from other works in Section 6.2, and presented in Tables B.4 to B.8 (in Appendix B). Throughout this work these values are referred to as "EADL".

6.1.6 Salem *et al.* experimental K- and L-shell X-ray transition ratios

Salem *et al.* compiled selected experimental data for K- and L-shell transition rates, and through least-squares fitting, generated most probable values of K- and L-shell X-ray radiative transition rate ratios [108]. From these ratios, partial fluorescence yield values (normalized without accounting radiationless transitions) $\omega_{ij}^{(\text{NA})}$ can be obtained, as was performed in Pia *et al.* works [35–37], and in NIST's Fundamental Parameters Database [38].

6.1.7 Bambynek *et al* 1972 semi-empirical fittings to experimental data

In 1972, Bambynek *et al.* [154] fitted a collection of selected K-shell fluorescence yield experimental values, using a semi-empirical fitting formula. The formula and the fitting parameters are presented in Hubbell *et al.* comparisons of several compilations [165].

It is presented Bambynek *et al.* [154] K-shell fluorescence yield values ω_K, which where extracted directly from Hubbell *et al.* work [165]. These values are compared with values from other works in Section 6.2, and presented in Table B.9 (in Appendix B).

Throughout the work, the values obtained in the present section are referred to as "Bambynek1972".

6.1.8 Krause's 1979 compilation

Krause generated a consistent set of values of K- and L-shell radiative and radiationless yields using the information available up to 1979 on several atomic parameters (fluorescence yields, auger yields, transitions probabilities, level withs, etc) [155]. In Krause's work, all pertinent data available in literature, including experimental, theoretical and semi-empirical values, was compiled and evaluated in order to generate K- and L-shell radiative and radiationless yields.

It is presented the K-shell fluorescence yield ω_K values from Krause's compilation [155]. The values are extracted directly from Hubbell *et al.* comparisons of several compilations [165]. These values are compared with values from other works in Section 6.2, and presented in Table B.9 (in Appendix B).

Throughout the work, the values obtained in the present section are referred to as "Krause1979".

6.1.9 Bambynek *et al* 1984 semi-empirical fittings of experimental data

In 1984, Bambynek *et al.* presented a new evaluation [156] of K-shell fluorescence yield values by introducing about 100 new measurements to the Bambynek *et al.* 1972 work [154]. As such, new fitting parameters where obtained, and new fitted values. Hubbell *et al.* comparisons of several compilations [165] present Bambynek's new fitting parameters, new fitted values, and comparisons against Bambynek 1972 [154] fitted values.

In the present work, it is presented Bambynek *et al.* K-shell fluorescence yield values ω_K, which where extracted directly from Hubbell *et al.* comparisons of several compilations [165]. These values are compared with values from other works in Section 6.2, and presented in Table B.9 (in Appendix B).

Throughout the work, the values obtained in this section are referred to as "Bambynek1984".

6.1.10 Hubbell *et al.* 1994 semi-empirical fittings of experimental data

In 1994, Hubbel *et al.* compiled the measured K-shell, L-shell, and higher atomic shell X-ray fluorescence yield data generated between the period 1978 - 1993 [165]. From the compiled data K-, L- and M-shell fluorescence yields were produced by fitting the selected data (the selection criteria and fitting procedure is explained in their work). They compared their fitted values with earlier fitted and theoretical values. Hubbel *et al*. fits for K-shell fluorescence yields ω_K are presented in NIST Fundamental Parameters Database [38] even though an erratum [166] informs about extensive anomalies to their fitted values, and as such they advise that the values obtained from Bambynek's 1984 work [156] should be used instead, regarding K-shell fluorescence yield values.

6.1.11 NIST Fundamental Parameters Database

Elam accomplished the compilation of a comprehensive database of atomic fundamental parameters relevant to X-ray spectroscopy [38], which is available in the NIST's web-page. The radiative K-shell fluorescence yield ω_K, tabulated in the database were calculated from the fits to several experimental values by Hubbel *et al*. [165], discussed in the previous section. The radiative L-shell fluorescence yield tabulated in the database are from Krause's revision to experimental and theoretical values [155] with modifications proposed by Jitschin [167].

The database also presents partial fluorescence yield values (normalized without accounting radiationless transitions) $\omega^{(NA)}$ for K- and L-shell transitions that were calculated using the emission rate ratios presented by Salem *et al* work [108]; the fit process to the data is explained with detail in Elam *et al.*'s work [38].

In the present work, it is presented K-shell fluorescence yields values ω_K, extracted directly from the NIST Fundamental Parameters Database [38]. These values are compared with values from other works in Section 6.2, and presented in Table B.9 (in Appendix B). Throughout the work, the values obtained in this section are referred to as "NIST".

6.1.12 Combination of Chen *et al.* Dirac Fock transition probabilities and Scofield's Dirac-Slater transition probabilities

In the present work, it is calculated K-shell fluorescence yield values ω_K and K-shell partial fluorescence yield values $\omega_{K\text{-}L_2}$, $\omega_{K\text{-}L_3}$, $\omega_{K\text{-}M_2}$ and, $\omega_{K\text{-}M_3}$, using the same references as EADL, i.e. using Scofield's more recent Dirac-Hartree-Slater calculations of radiative transitions probabilities [93] (which were presented in Section 6.1.2) and Chen's Dirac-Hartree-Fock calculations of radiationless transition probabilities (which were presented in Section 6.1.4).

Two different works from Chen *et al.* [95, 97] (presented in Section 6.1.4) can be used to obtain the K-shell total radiationless transition probability $A_K^{(TA)}$. Chen *et al.* later work presents the K-shell total radiationless width $\Gamma_K^{(TA)}$, from which the K-shell

total radiationless transition probability $A_K^{(TA)}$ can be derived. The total radiationless transition probability $A_K^{(TA)}$ calculated in Chen *et al* earlier work [95] differs from the calculated value in a later work [97]. Nevertheless, the K-shell fluorescence yield values calculated using the different references have deviations of less than 0.1%, and as such, both references are equivalent. It was opted of using Chen *et al.* later work [97].

Since Chen *et al.* present values for selected elements, in the present work, values for other elements are derived through fits to the available data.

Thus, K-shell fluorescence yields ω_K and radiative transition partial fluorescence yield values $\omega_{K\text{-}L_2}$, $\omega_{K\text{-}L_3}$, $\omega_{K\text{-}M_2}$ and, $\omega_{K\text{-}M_3}$ are calculated using Eq. 2.6 and Eq. 2.8, respectively, where the radiative transition probabilities $A_{Kj}^{(R)}$, and the total radiative transition probability $A_K^{(TR)}$ is obtained from Scofield's later Dirac-Slater work [93], and the total radiationless transition probability $A_K^{(TA)}$ is obtained from Chen *et al.* later Dirac-Fock work [97]. This combination with Scofield's transition probabilities to derive K-shell fluorescence yield values ω_K had already been performed in Chen *et al.* later work [97]. Unlike EADL, in the present work, Hubbel's corrections [168] are not included in any calculations since the procedure of how the EADL library applies these corrections is unclear.

The values obtained in this section are compared with values from other works in Section 6.2, and presented in Appendix B, Tables B.4 to B.8.

Throughout the work, the values obtained in this section are referred to as "DF,DS", since they are a combination of Dirac-Fock and Dirac-Slater calculations.

6.1.13 Combination of Chen *et al.* Dirac Fock transition probabilities and Scofield's Dirac-Fock transition probabilities

In the present work, K-shell fluorescence yield values ω_K and K-shell partial fluorescence yield values $\omega_{K\text{-}L_2}$, $\omega_{K\text{-}L_3}$, $\omega_{K\text{-}M_2}$ and, $\omega_{K\text{-}M_3}$ are calculated from the combination of Scofield's radiative transitions Dirac-Hartree-Fock calculations [106] (presented in Section 6.1.3) and Chen *et al.* later radiationless transitions Dirac-Hartree-Fock calculations [97] (presented in Section 6.1.4). This combination of values is similar to the combination presented in Section 6.1.12, however, in this case, Scofield's Dirac-Fock values are used instead of Scofield's Dirac-Slater values, as suggested in Pia *et al.* works.

In Scofield's Dirac-Fock work [106], it is presented radiative transition probabilities $A^{(R)}$ for a limited number of transitions, and limited number of elements, as well as total radiative transition probability $A^{(TR)}$. From this information, the partial fluorescence yields (normalized without accounting radiationless transitions) $\omega^{(NA)}$ can be obtained using Eq. 2.10. As far as we know, the xraylib database [169] uses this method, with the exception that the values had to be normalized to satisfy Eq. 2.11. This method is limited to the transitions presented in Scofield's work. Pia *et al.* performed a different approach to obtain $\omega^{(NA)}$ values from Scofield's Dirac-Fock work [106]. Since Scofield's work also present radiative transition probability ratios, Pia *et al.* wrote equations to extract the

$\omega^{(\mathrm{NA})}$ values from these ratios. Since no transition probability ratio relative to K-$L_{4,5}$ transitions is presented in Scofield's Dirac Fock work, Pia *et al.* made an approximation, by assuming that the K-$M_{4,5}$/K-M_2 Dirac-Fock ratio should be equal to the experimental K-$M_{4,5}$/K-M_2 ratio of Salem *et al.* work [108]. This approximation was justified by the fact that Scofield's Dirac-Slater K-$M_{4,5}$/K-M_2 probability ratio was in good agreement with the experimental ratio, and as such, the Dirac-Fock ratio, although not presented, should also be in good agreement. In the present work, the method employed by Pia *et al.* is followed, but with a different approximation. Since Scofield's Dirac-Slater K-$M_{4,5}$/K-M_3 ratio was in better agreement with the experimental values, it was assumed the Dirac-Fock K-$M_{4,5}$/K-M_3 ratio to be equal to the Dirac-Slater K-$M_{4,5}$/K-M_3 ratio. With this method, $\omega^{(\mathrm{NA})}$ values can be obtained for all possible radiative transitions. The method performed in the present work, and the method performed in the xraylib result in different $\omega^{(\mathrm{NA})}_{\mathrm{K\text{-}L_2}}$, $\omega^{(\mathrm{NA})}_{\mathrm{K\text{-}L_3}}$, $\omega^{(\mathrm{NA})}_{\mathrm{K\text{-}M_2}}$, $\omega^{(\mathrm{NA})}_{\mathrm{K\text{-}M_3}}$ values. In fact, regarding the $\omega^{(\mathrm{NA})}_{\mathrm{K\text{-}L_2}}$, $\omega^{(\mathrm{NA})}_{\mathrm{K\text{-}L_3}}$, $\omega^{(\mathrm{NA})}_{\mathrm{K\text{-}M_2}}$, $\omega^{(\mathrm{NA})}_{\mathrm{K\text{-}M_3}}$ values, the method in the present work (and the method performed in Pia *et al.* works [35–37]) produces values that are overall in slightly closer agreement with the experimental values from Salem *et al.* work [108] than the values obtained from the xraylib method.

The K-shell fluorescence yield ω_{K} is calculated using Eq. 2.6, where the total radiationless transition probability $A^{(\mathrm{TA})}_{\mathrm{K}}$ is from Chen *et al.* Dirac-Fock work [97] (presented in Section 6.1.2), and the total radiative transition probability $A^{(\mathrm{TR})}_{\mathrm{K}}$ is from Scofield's Dirac-Fock work [106] (presented in Section 6.1.3).

The partial fluorescence yields $\omega_{\mathrm{K\text{-}L_2}}$, $\omega_{\mathrm{K\text{-}L_3}}$, $\omega_{\mathrm{K\text{-}M_2}}$, $\omega_{\mathrm{K\text{-}M_3}}$ are calculated from $\omega^{(\mathrm{NA})}_{\mathrm{K\text{-}L_2}}$, $\omega^{(\mathrm{NA})}_{\mathrm{K\text{-}L_3}}$, $\omega^{(NA)}_{\mathrm{K\text{-}M_2}}$, $\omega^{(\mathrm{NA})}_{\mathrm{K\text{-}M_3}}$, using Eq. 2.12.

These values obtained on this section are compared with values from other works in Section 6.2, and presented in Appendix B, in Tables B.4 to B.8. Throughout this work, these values are referred to as "DF", as they are a result of Dirac-Fock calculations.

6.1.14 Multiconfiguration Dirac-Fock values

It is presented K-shell fluorescence yield values ω_{K} calculated using the Multiconfiguration Dirac-Fock method, for selected elements. The values were calculated by different authors [133, 170–173].

These values are compared with values from other works in Section 6.2, and presented in Table B.4 (in Appendix B). Throughout the present work, these values are referred to as "MCDF".

6.1.15 Kahoul *et al.* 2012 empirical fittings

In 2012, Kahoul *et al.* [144] compiled experimental data of the K-shell fluorescence yields from the period 1960-2011. From this data, they deduced empirical K-shell fluorescence yield values ω_{K} from polynomial fittings of the weighted-mean and unweighted-mean values of all the compiled data. The data was separated in three atomic number ranges,

$11 \leq Z \leq 20$, $21 \leq Z \leq 50$ and $51 \leq Z \leq 99$, and a polynomial fitting was performed independently for each range.

The values are extracted directly from Kahoul *et al.* work, and are compared with values from other works in Section 6.2, and presented in Table B.9 (in Appendix B). These values are referred to as "Kahoul2012", throughout the present work.

6.1.16 Daoudi *et al.* 2015 empirical fittings

In 2015, Daoudi *et al.* [157] compiled experimental data of the K-shell fluorescence yield values up to the date, relying on existing compilations, and adding new data published in the period 2012-2015. This compilation included 737 experimental values, with atomic number range $3 \leq Z \leq 99$. The data was separated in three atomic number ranges, $11 \leq Z \leq 20$, $21 \leq Z \leq 50$ and $51 \leq Z \leq 99$, and an empiric polynomial fitting was performed independently for each range.

The K-shell fluorescence yield values ω_{K} are extracted directly from Daoudi *et al.* work [157],and are compared with values from other works in Section 6.2, and presented in Table B.9 (in Appendix B). Throughout the present work, these values are referred to as "Daoudi2015".

6.1.17 Combination of semi-empirical or empirical K-shell fluorescence yield values with Salem *et al.* values

From the references regarding semi-empirical or empirical fittings presented so far ("Bambynek1972"[154], "Krause1979" [155], "Bambynek1984"[156], "NIST"[38], "Kahoul2012" [144] and "Daoudi2015"[157]), semi-empirical and empirical values regarding K-shell fluorescence yield ω_{K} were obtained. In the present work, calculations of partial fluorescence yields $\omega_{\mathrm{K\text{-}L_2}}$, $\omega_{\mathrm{K\text{-}L_3}}$, $\omega_{\mathrm{K\text{-}M_2}}$, $\omega_{\mathrm{K\text{-}M_3}}$ are performed for each of these references using Eq. 2.12, where the partial fluorescence yield values (normalized without accounting radiationless transitions) $\omega^{(\mathrm{NA})}$ are those obtained from Salem *et al.* work [108], which are tabulated in NIST Fundamental Parameters Database. As an example, to derive the $\mathrm{K\text{-}L_2}$ partial fluorescence yield $\omega_{\mathrm{K\text{-}L_2}}$ from Daoudi *et al.*'s K-shell fluorescence yield ω_{K}, it is written:

$$\omega_{\mathrm{K\text{-}L_2}}^{\mathrm{Daoudi,Salem}}(Z) = \omega_{\mathrm{K}}^{\mathrm{Daoudi}}(Z) \times \omega_{\mathrm{K\text{-}L_2}}^{(\mathrm{NA})\mathrm{Salem}}(Z).$$

Salem *et al.* values are used because they are still up to date considered the most complete references of K- and L-shell experimental transition probability ratios, they are used in Pia *et al.*'s comparisons, and their relevance is reinforced by the fact that they are used in the NIST Fundamental Parameters Database.

Using this formalism, it is presented partial fluorescence yield values $\omega_{\mathrm{K\text{-}L_2}}$, $\omega_{\mathrm{K\text{-}L_3}}$, $\omega_{\mathrm{K\text{-}M_2}}$, $\omega_{\mathrm{K\text{-}M_3}}$, for each of the semi-empirical and empirical values.

These values are compared with values from other works in Section 6.2, and presented in Tables B.10 to B.13 (in Appendix B). Throughout the present work these values are

referred to as "Bambynek1972,Salem", "Krause1979,Salem", "Bambynek1984,Salem", "NIST,Salem", "Kahoul2012,Salem" and "Daoudi2015,Salem".

6.2 Comparison of values from the different works

It is presented a comparison of the K-shell fluorescence yield values ω_{K}, and the K-shell partial fluorescence yield values $\omega_{\mathrm{K\text{-}L_2}}$, $\omega_{\mathrm{K\text{-}L_3}}$, $\omega_{\mathrm{K\text{-}M_2}}$, $\omega_{\mathrm{K\text{-}M_3}}$, that were obtained from the different references as explained in Section 6.1.

Regarding the K-shell fluorescence yield ω_{K}, five different theoretical values are presented: "Kostroun" [163], "EADL" [99], "DF,DS"[93, 97], "DF"[97, 106] and "MCDF"[133, 170–172], as well as values from four semi-empirical fittings: "Bambynek1972" [154], "Krause1979" [155], "Bambynek1984" [156], and "NIST" [38], and values from two empirical fittings: "Kahoul2012" [144] and "Daoudi2015" [157].

In what concerns the theoretical partial fluorescence yield values $\omega_{\mathrm{K\text{-}L_2}}$, $\omega_{\mathrm{K\text{-}L_3}}$, $\omega_{\mathrm{K\text{-}M_2}}$, $\omega_{\mathrm{K\text{-}M_3}}$, the theoretical values presented are "EADL"[99], "DF,DS"[93, 97] and "DF"[97, 106]; the values from Kostroun work [163] are not presented since they were calculated non-relativistically. As to semi-empirical and empirical values, as explained in Section 6.1.17, the semi-empirical values presented are: "Bambynek1972,Salem" [108, 154], "Krause1979,Salem" [108, 155], "Bambynek1984,Salem" [108, 156] and "NIST,Salem" [38, 108], and the empirical values: "Kahoul2012,Salem" [108, 144] and "Daoudi2015,Salem" [108, 157].

Relative difference between values from different references are also presented. For an element with atomic number Z, and a radiative transition ij, the relative difference of the partial fluorescence yield from reference 1 and reference 2 is given as:

$$\Delta\omega_{ij}^{\mathrm{ref1,ref2}}(Z) = \frac{(\omega_{ij}^{\mathrm{ref1}}(Z) - \omega_{ij}^{\mathrm{ref2}}(Z)) \times 100\%}{\frac{\omega_{ij}^{\mathrm{ref1}}(Z) + \omega_{ij}^{\mathrm{ref2}}(Z)}{2}}. \tag{6.1}$$

The average relative difference is given by averaging the absolute value of the relative difference for all elements available in both references:

$$\Delta\omega_{ij}^{\mathrm{ref1,ref2}} = \frac{\sum_{Z} |\Delta\omega_{ij}^{\mathrm{ref1,ref2}}(Z)|}{N}, \tag{6.2}$$

where N is the number of elements.

6.2.1 K-shell Fluorescence Yield Comparison

6.2.1.1 Theoretical K-shell fluorescence yield values

The K-shell fluorescence yield theoretical values are presented in Figs. 6.1.a and 6.1.b (the values are divided for two atomic ranges to better visualization), and in Appendix B (Table B.4). The same theoretical K-shell fluorescence yield values are normalized to their corresponding "DF" values and presented in Fig. 6.1.c.

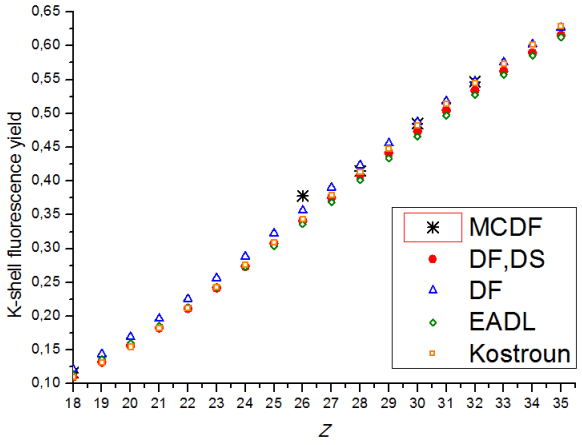

(a) Theoretical K-shell fluorescence yield values ($18 \leq Z \leq 35$)

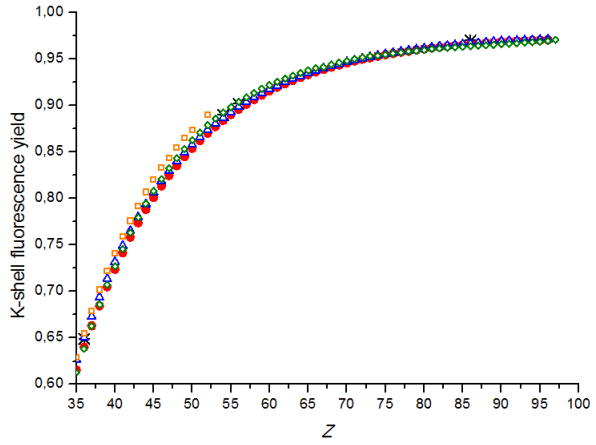

(b) Theoretical K-shell fluorescence yield values ($35 \leq Z \leq 96$))

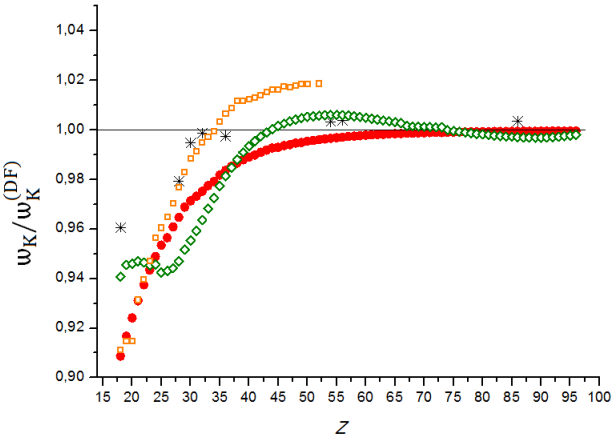

(c) Theoretical K-shell fluorescence yield values normalized to "DF" values

Figure 6.1: Kostroun: values obtained from the combination of Kostroun *et al.* calculations [163] and Scofield's radiative Dirac-Slater calculations [105]. "DF,DS": values obtained from the combination of Chen *et al.* radiationless Diroc-Fock calculations [97] and Scofield's radiative Dirac-Slater calculations [93]. "DF": values obtained from the combination of Chen *et al.* radiationless Diroc-Fock calculations [97] and Scofield's radiative Dirac-Fock calculations [106]. "EADL": values obtained from the Evaluated Atomic Data Library [99].

From the comparisons in Figs. 6.1.a and 6.1.b it is highlighted that the K-shell fluorescence yield values increase monotonically with increasing atomic number for all theoretical references. While "Kostroun" values are in relatively good agreement with "DF,DS" values for low atomic numbers, their disagreement increases as atomic number increases. The "EADL" values are in good agreement with "DF,DS" values, which is to be expected since they are calculated using the transition probabilities from the same references (with the excetion that the EADL library introduces a correction that we did not introduce in "DF,DS" calculations). "DF,DS" and "DF" values are obtained using the same reference for radiationless transition probabilities, but using different references from Scofield regarding the radiative transitions probabilities. Scofield's radiative transition probabilities calculated using the Dirac-Fock method are overall higher than those calculated using the Dirac-Slater method. As such, "DF" K-shell fluorescence yield values are overall higher than "DF,DS" values, as shown in Fig. 6.1.c. For low atomic numbers, "DF,DS" and "DF" values differ by almost 10% difference, but as the atomic number increases they become more and more in agreement. In fact, for $42 < Z < 74$ they differ less than 1%, and from $75 < Z < 96$ they differ less than 0.1%

The "MCDF" values are in better agreement with "DF" values among other theoretical values.

6.2.1.2 Semi-empirical and empirical K-shell fluorescence yield values

The semi-empirical and empirical K-shell fluorescence yield values are compared in Fig. 6.2.a and Fig. 6.2.b (the values are divided for two atomic ranges for better visualization). The same values are presented in Table B.9 (in Appendix B). Table B.9 also presents, for each atomic number, the minimum and the maximum value from the compared references, and the relative difference from those values, with the intent of presenting the highest deviations of the available semi-empirical and empirical references. In Fig. 6.2.c and Fig. 6.2.d, the semi-empirical and empirical values are normalized to the corresponding theoretical "DF" values, and "DF,DS" values, respectively.

Table 6.1: K-shell fluorescence yield average relative difference

$\Delta\omega_K(\%)$	DS,DF	DF
Bambynek 1972	0.93245	0.85845
Krause 1979	0.74575	1.1053
Bambynek1984	1.30666	0.15352
NIST	2.10472	2.7279
Kahoul 2012	1.02286	1.80249
Daoudi 2015	0.88204	1.47661

Unlike the theoretical values presented in Fig. 6.1, some of the semi-empirical and empirical values presented in Fig. 6.2.a and Fig. 6.2.b exhibit non-monotonically behaviour with increasing atomic number. Such is highlighted in Fig. 6.2.b zooms, where it

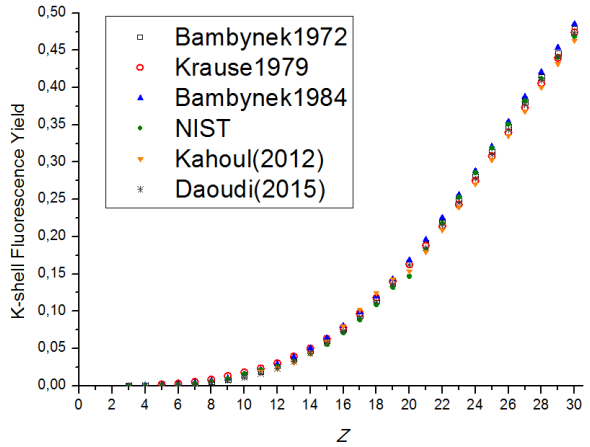

(a) Semi-empirical and empirical K-shell fluorescence yield values ($3 \leq Z \leq 30$)

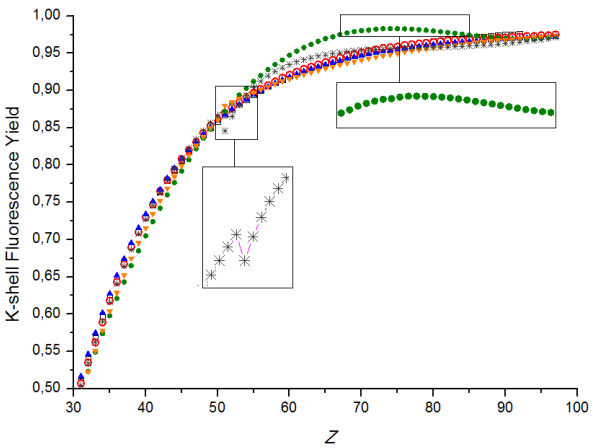

(b) Semi-empirical and empirical K-shell fluorescence yield values ($31 \leq Z \leq 98$)

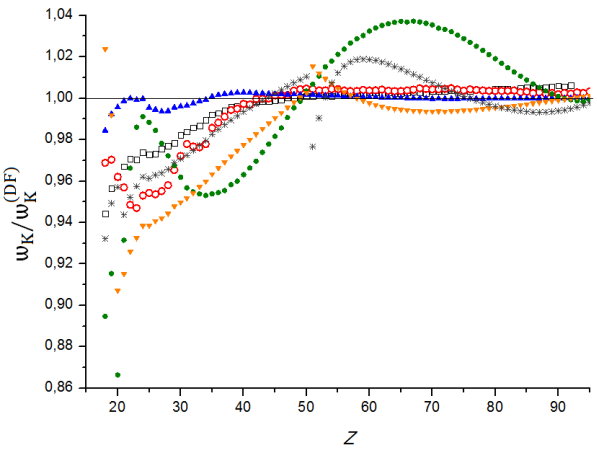

(c) Semi-empirical and empirical K-shell fluorescence yield values normalized to "DF" values

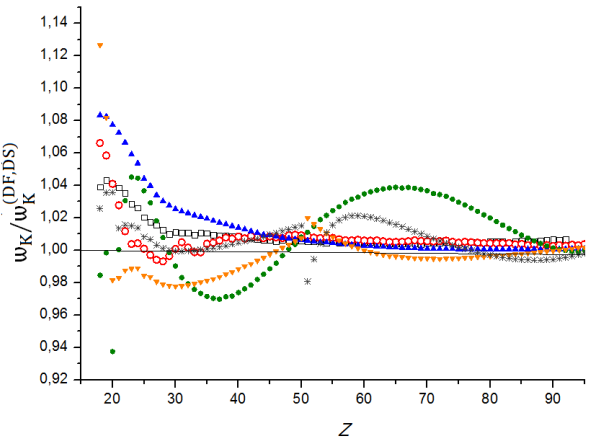

(d) Semi-empirical and empirical K-shell fluorescence yield values normalized to "DF,DS" values

Figure 6.2: "Bambynek1972": Values from Bambynek *et al.* earlier semi-empirical fit [154]. "Krause1979": values from Krause's semi-empirical fit [155]. "Bambynek1984": values from Bambynek *et al.* later semi-empirical fit [156]. "NIST": semi-empirical fit values presented in NIST's Fundamental Parameters Database [38]. "Kahoul": values from Kahoul *et al.* empirical fit [144]. "Daoudi": values from Daoudi *et al.* empirical fit [157].

is visible that in the range $70 < Z < 85$ NIST's values decrease as atomic number increases, and that "Daoudi" values decrease for $Z = 50$. The decrease in "Daoudi" values can be explained by the fact that they divided the experimental results in three ranges of atomic number and performed different fittings for each range. From Fig. 6.2.b (and Table B.9) it is visible that in the range $60 < Z < 80$ "NIST" values are in clear disagreement with all other semi-empirical and empirical values. The different semi-empirical and empirical K-shell fluorescence yield values present worse agreement between each other for low atomic numbers. In the range $3 < Z < 18$, differences higher than 10% can be found between some of the references. As the atomic number increases, better agreement is generally found between the different references. Such is to be expected, since experimental measurement of K-shell fluorescence yields for low atomic numbers generally result in higher uncertainties due to the higher predominance of radiationless transition in these elements. In the range $19 < Z < 50$ the difference between the different values is comprised between 10% to 1%, and in the range $51 < Z < 99$ the agreement is comprised between 1% to 0.4%.

The comparison in Fig. 6.2.c highlights that "Bambynek1984" values are in excellent agreement with "DF" values; their relative difference is always lower than 0.2%. "Bambynek1972" and "Krause1979" values are also in good agreement with the "DF" values, especially in the $Z > 40$ range, where they converge to the "DF" values as the atomic number increases. The more recent empirical and semi-empirical values, "NIST", "Kahoul2012", and "Daoudi2015", present worse agreement with "DF" values than "Bambynek1972", "Krause1979", "Bambynek1984" values. In the range $0 < Z < 40$ the semi-empirical and empirical values are generally lower than "DF" values. The "NIST" values present the worst agreement with the "DF" values.

From Fig. 6.2.d one can see that "Bambynek1972", "Krause1979" and "Bambynek1984" values are in good agreement with "DF,DS" values, and their agreement increases with increasing atomic number. "Kahoul2012" and "Daoudi2015" values are also in good agreement but their values do not converge to those of "DF,DS" values as the atomic number increases. As for the "NIST" values, they present the worse agreement with "DF,DS" values.

It is worthwhile mentioning that from the comparisons presented in this section, the K-shell fluorescence yield values from "DF,DS", "DF", "EADL", "Bambynek1972", "Krause1979" and "Bambynek1984", converge as atomic number increases, presenting very good agreement in the range $Z > 40$, while the most recent values "NIST", "Kahoul" and "Daoudi2015" do not exhibit this behaviour.

In Table 6.1 the average relative difference between each semi-empirical and empirical values and the "DF,DS" and "DF" values is presented. From this table it is shown that the "Bambynek 1972" and "Bambynek 1984" values are in closer agreement with the "DF" values, while all the other references are in better agreement with the "DF,DS" values. Although, with the exception of "NIST" values, all values are in good agreement with the "DF" and "DF,DS" values, presenting average relative difference lower than 2%. The

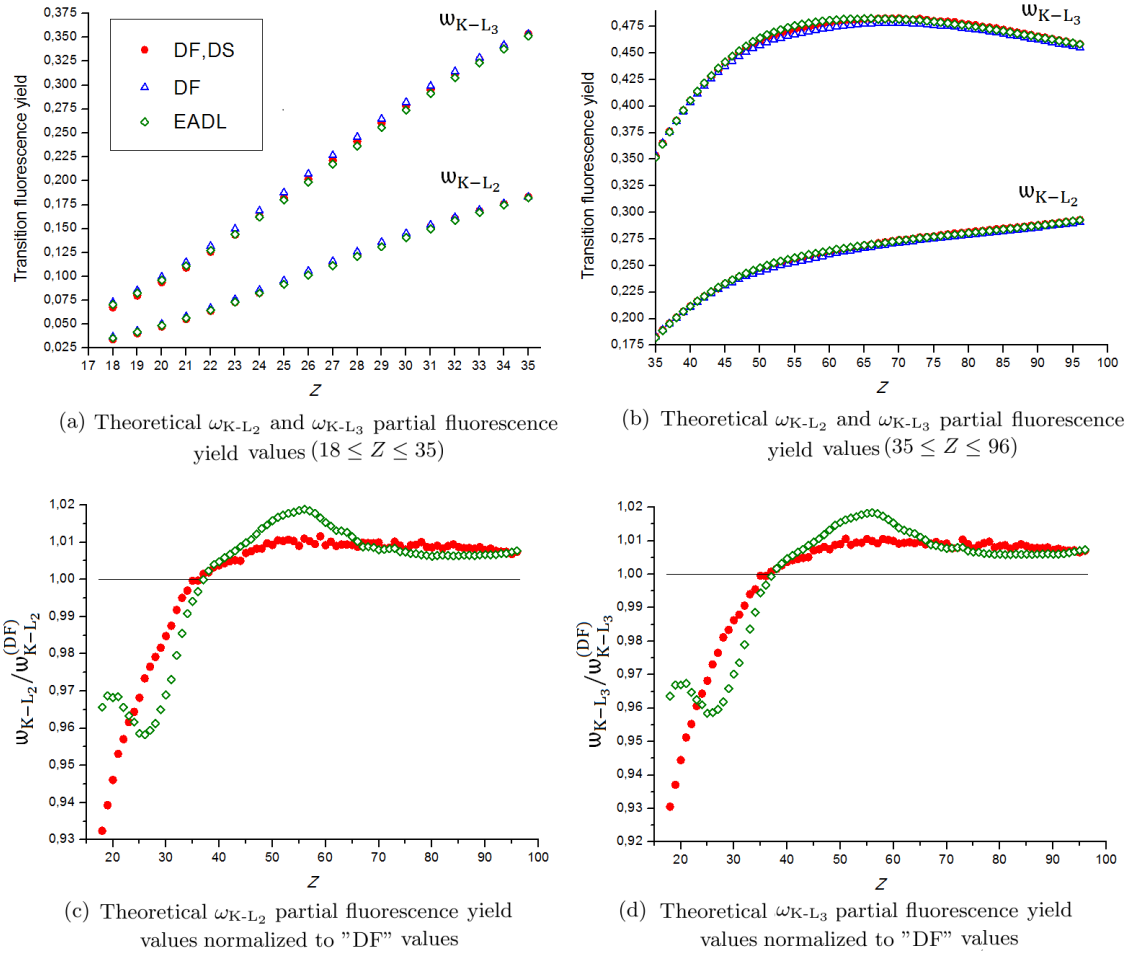

(a) Theoretical $\omega_{K\text{-}L_2}$ and $\omega_{K\text{-}L_3}$ partial fluorescence yield values ($18 \leq Z \leq 35$)

(b) Theoretical $\omega_{K\text{-}L_2}$ and $\omega_{K\text{-}L_3}$ partial fluorescence yield values ($35 \leq Z \leq 96$)

(c) Theoretical $\omega_{K\text{-}L_2}$ partial fluorescence yield values normalized to "DF" values

(d) Theoretical $\omega_{K\text{-}L_3}$ partial fluorescence yield values normalized to "DF" values

Figure 6.3: "DF,DS": values obtained from the combination of Chen *et al.* radiationless Diroc-Fock calculations [97] and Scofield's radiative Dirac-Slater calculations [93]. "DF": values obtained from the combination of Chen *et al.* radiationless Diroc-Fock calculations [97] and Scofield's radiative Dirac-Fock calculations [106]. "EADL": values obtained from the Evaluated Atomic Data Library [99].

"Bambynek 1984" values are in excellent agreement with "DF" values, presenting less than 0.2% difference.

6.2.2 K-L_2 and K-L_3 partial fluorescence yield comparison

6.2.2.1 Theoretical K-L_2 and K-L_3 partial fluorescence yield values

The theoretical partial fluorescence yields $\omega_{K\text{-}L_2}$ and $\omega_{K\text{-}L_3}$ of "DF,DS", "DF", and "EADL" values are compared in Fig. 6.3.a and Fig. 6.3.b (values are divided in two ranges of atomic number to better visualization), and presented in Tables B.5 and B.6 (in Appendix B). In Fig. 6.3.c and Fig. 6.3.d, the "DF,DS" and "EADL" partial fluorescence yields $\omega_{K\text{-}L_2}$ and $\omega_{K\text{-}L_3}$ are normalized to the "DF" values.

From Fig. 6.3.a and 6.3.b (and Tables B.5 and B.6) it is highlighted that "DF,DS" partial

fluorescence yields $\omega_{K\text{-}L_2}$ and $\omega_{K\text{-}L_3}$ are lower than "DF" values in the range $18 < Z < 36$, and higher than "DF" values in the range $36 < Z \leq 97$. For low atomic numbers the difference between "DF,DS" and "DF" references is significantly high for both $\omega_{K\text{-}L_2}$, and $\omega_{K\text{-}L_3}$, the difference is close to 7% for $Z = 18$. For high atomic numbers better agreement is shown, in the range $Z > 60$ the difference is always lower than 1%.

6.2.2.2 Semi-empirical and empirical K-L_2 and K-L_3 partial fluorescence yield values

In Figs. 6.4.a and 6.4.b, the semi-empirical and empirical $\omega_{K\text{-}L_2}$ and $\omega_{K\text{-}L_3}$ partial fluorescence yield values are compared (the values are divided in two ranges of atomic number for better visualization), which are obtained from the combination of semi-empirical or empirical K-shell fluorescence yield values with Salem *et al.* transition probability values (as explained in Section 6.1.17). The same values are presented in Tables B.10 and B.11. In Figs. 6.4.c and 6.4.d, $\omega_{K\text{-}L_2}$ and $\omega_{K\text{-}L_3}$ values of semi-empirical and empirical references are normalized to the respective "DF" values, and, in Figs. 6.4.e and 6.4.f, are normalized to the respective "DF,DS" values.

The values presented in Figs. 6.4.a and 6.4.b (also presented in Tables B.10 and B.11) exhibit significantly high relative differences from each other, especially at low atomic numbers. In the range $3 \leq Z < 20$ differences of 10% to 100% are found between some of the references. As the atomic number increases better agreement is observed. In the range $20 < Z < 80$, the values have relative differences within 10%, and in the range $80 < Z < 96$ lower than 2%.

The comparisons in Figs. 6.4.c, 6.4.d, 6.4.e and 6.4.f, show that at low atomic numbers, better agreement is seen in the comparison with "DF,DS" values, with the exception of the "Bambynek1984, Salem" values, which are in better agreement with "DF" values. For higher atomic numbers the semi-empirical and empirical values are generally in better agreement with "DF" values.

Table 6.2 presents the average relative difference between each semi-empirical or empirical $\omega_{K\text{-}L_2}$ values and the "DF,DS" and "DF" values. In Table 6.3 the same is presented, but regarding $\omega_{K\text{-}L_3}$ values. From these tables, it is inferred that all semi-empirical and empirical values are in closer agreement with "DF,DS" values than the "DF" values, with the exception of "Bambynek1984, Salem" (for both $\omega_{K\text{-}L_2}$ and $\omega_{K\text{-}L_3}$), and "Kahoul 2012" (for $\omega_{K\text{-}L_2}$). It is worthwhile noting that the average deviation between the semi-empirical and empirical values in relation to "DF,DS" or "DF" values is for all cases lower than 3%, and in many cases lower than 1%.

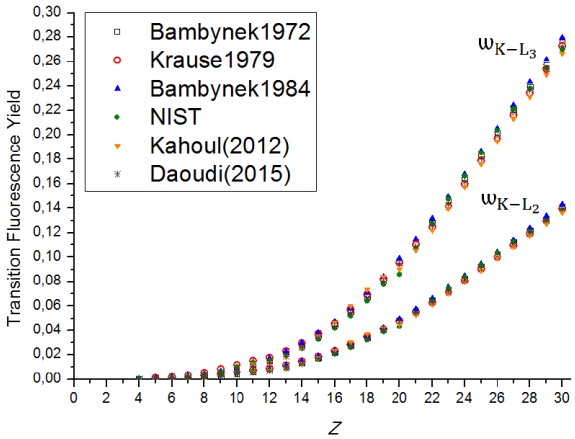

(a) Semi-empirical and empirical $\omega_{K\text{-}L_2}$ and $\omega_{K\text{-}L_3}$ partial fluorescence yield values $(4 \leq Z \leq 30)$

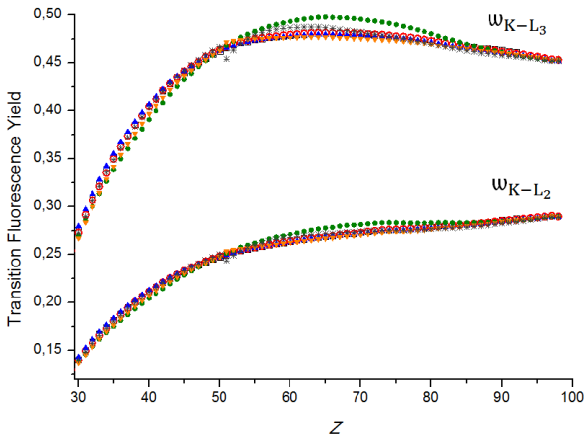

(b) Semi-empirical and empirical $\omega_{K\text{-}L_2}$ and $\omega_{K\text{-}L_3}$ partial fluorescence yield values $(30 \leq Z \leq 98)$

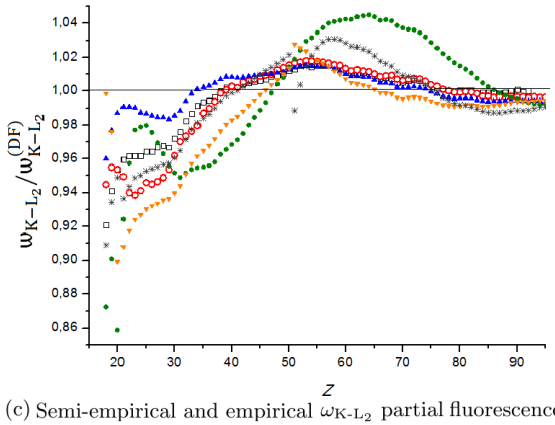

(c) Semi-empirical and empirical $\omega_{K\text{-}L_2}$ partial fluorescence yield values normalized to "DF" values

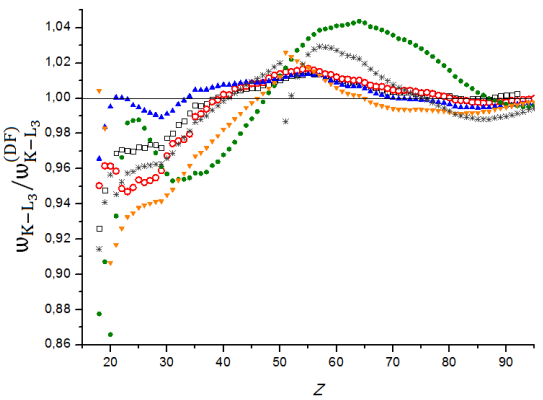

(d) Semi-empirical and empirical $\omega_{K\text{-}L_3}$ partial fluorescence yield values normalized to "DF" values

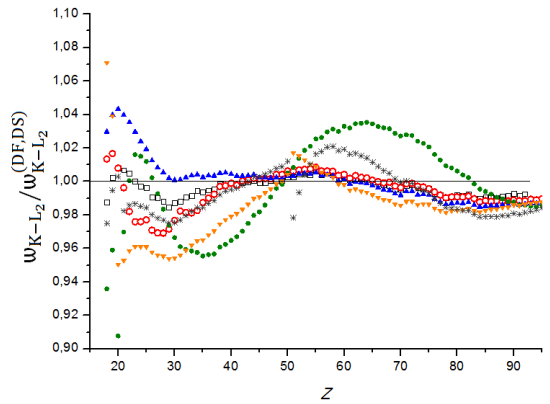

(e) Semi-empirical and empirical $\omega_{K\text{-}L_2}$ partial fluorescence yield values normalized to "DF,DS" values

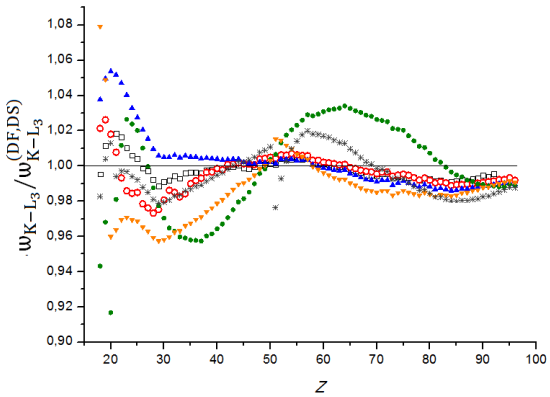

(f) Semi-empirical and empirical $\omega_{K\text{-}L_3}$ partial fluorescence yield values normalized to "DF,DS" values

Figure 6.4: "Bambynek1972": Values from Bambynek *et al.* earlier semi-empirical fit [154]. "Krause1979": values from Krause's semi-empirical fit [155]. "Bambynek1984": values from Bambynek *et al.* later semi-empirical fit [156]. "NIST": semi-empirical fit values presented in NIST's Fundamental Parameters Database [38]. "Kahoul": values from Kahoul *et al.* empirical fit [144]. "Daoudi": values from Daoudi *et al.* empirical fit [157].

Table 6.2: $\omega_{K\text{-}L_2}$ fluorescence yield average relative difference

$\Delta\omega_{K\text{-}L_2}(\%)$	DS,DF	DF
Bambynek 1972	1.10103	1.3122
Krause 1979	1.39625	1.57368
Bambynek1984	1.43885	0.89263
NIST	2.86495	3.11976
Kahoul 2012	2.53726	2.12996
Daoudi 2015	1.87931	2.08348

Table 6.3: $\omega_{K\text{-}L_3}$ fluorescence yield average relative difference

$\Delta\omega_{K\text{-}L_3}(\%)$	DS,DF	DF
Bambynek 1972	0.5014	1.10359
Krause 1979	0.81386	1.38566
Bambynek1984	1.06974	0.62827
NIST	2.18804	2.90847
Kahoul 2012	1.87117	1.98114
Daoudi 2015	1.16017	1.84538

Table 6.4: $\omega_{K\text{-}M_2}$ fluorescence yield average relative difference

$\Delta\omega_{K\text{-}M_2}(\%)$	DS,DF	DF
Bambynek 1972	7.51496	3.38598
Krause 1979	7.1521	3.41098
Bambynek1984	7.87296	3.66588
NIST	6.99792	3.79644
Kahoul 2012	6.35466	3.9817
Daoudi 2015	6.82589	2.92917

Table 6.5: $\omega_{K\text{-}M_3}$ fluorescence yield average relative difference

$\Delta\omega_{K\text{-}M_3}(\%)$	DS,DF	DF
Bambynek 1972	6.66471	3.36447
Krause 1979	6.13335	3.35167
Bambynek1984	6.88758	3.11984
NIST	5.92833	3.61726
Kahoul 2012	5.37293	4.10008
Daoudi 2015	5.77349	2.9606

6.2.3 K-M_2 and K-M_3 fluorescence yield comparison

6.2.3.1 Theoretical K-M_2 and K-M_3 partial fluorescence yield values

A comparison of the theoretical partial fluorescence yield values $\omega_{K\text{-}M_2}$ and $\omega_{K\text{-}M_3}$ is presented in Figs. 6.5.a and 6.5.b (values are divided in two ranges of atomic number for better visualization). The same values are presented in Tables B.7 and B.8. In Figs. 6.5.c and 6.5.d, these values are normalized to the respective "DF" values.

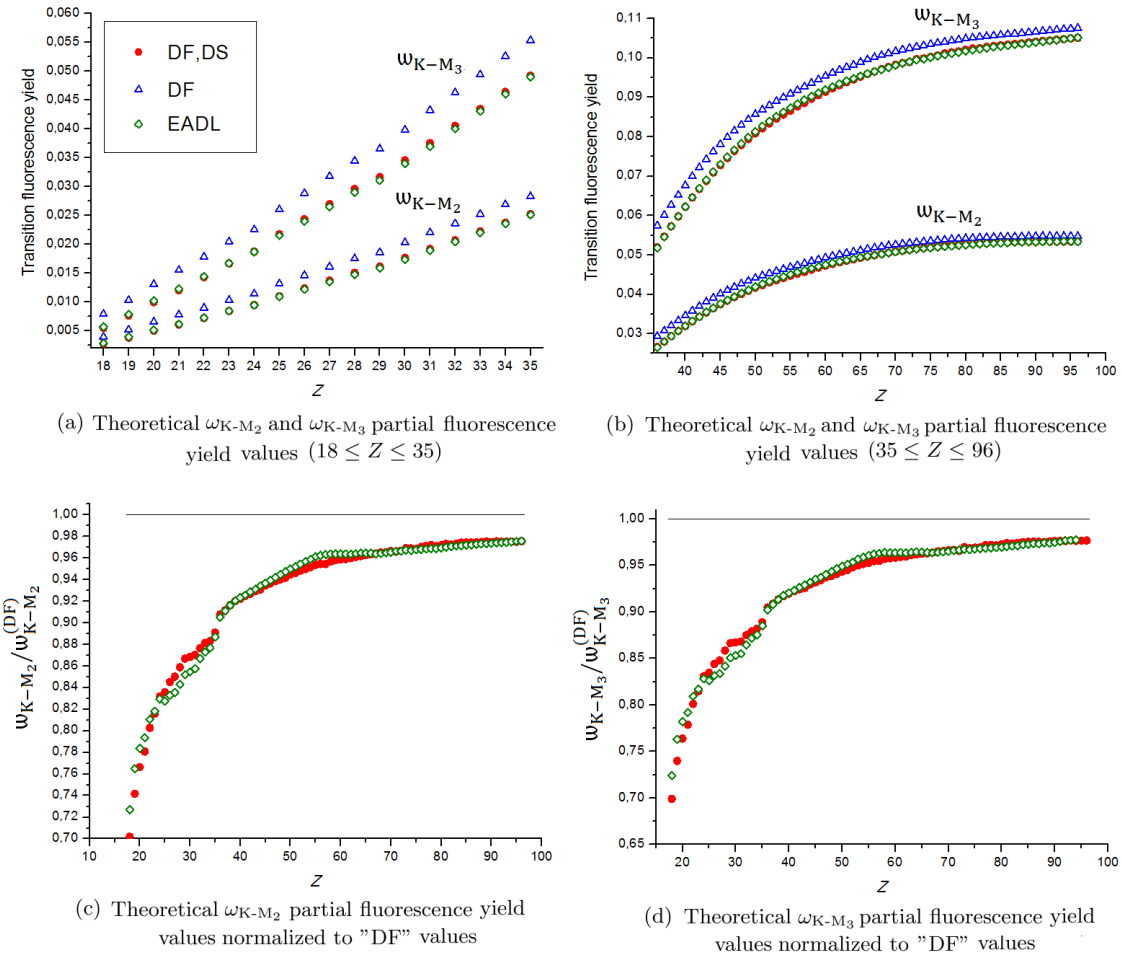

(a) Theoretical $\omega_{\text{K-M}_2}$ and $\omega_{\text{K-M}_3}$ partial fluorescence yield values ($18 \leq Z \leq 35$)

(b) Theoretical $\omega_{\text{K-M}_2}$ and $\omega_{\text{K-M}_3}$ partial fluorescence yield values ($35 \leq Z \leq 96$)

(c) Theoretical $\omega_{\text{K-M}_2}$ partial fluorescence yield values normalized to "DF" values

(d) Theoretical $\omega_{\text{K-M}_3}$ partial fluorescence yield values normalized to "DF" values

Figure 6.5: "DF,DS": values obtained from the combination of Chen *et al.* radiationless Diroc-Fock calculations [97] and Scofield's radiative Dirac-Slater calculations [93]. "DF": values obtained from the combination of Chen *et al.* radiationless Diroc-Fock calculations [97] and Scofield's radiative Dirac-Fock calculations [106]. "EADL": values obtained from the Evaluated Atomic Data Library [99].

Figure 6.5 indicates that the partial fluorescence yields $\omega_{\text{K-M}_2}$ and $\omega_{\text{K-M}_3}$ from "DF" values are higher than the respective "DF,DS" values for all atomic numbers. These values are in higher disagreement at low atomic numbers, where at $Z = 18$ the relative difference is around 35%. At higher atomic numbers the agreement improves, and at $Z = 95$ the difference is lower than 3%.

6.2.3.2 Semi-empirical and empirical K-M_2 and K-M_3 partial fluorescence yield values

In Figs. 6.6.a and 6.6.b, the semi-empirical and empirical partial fluorescence yields $\omega_{\text{K-M}_2}$ and $\omega_{\text{K-M}_3}$ are compared (the values are divided in two ranges of atomic number for better visualization). The same values are presented in Tables B.12 and B.13. These

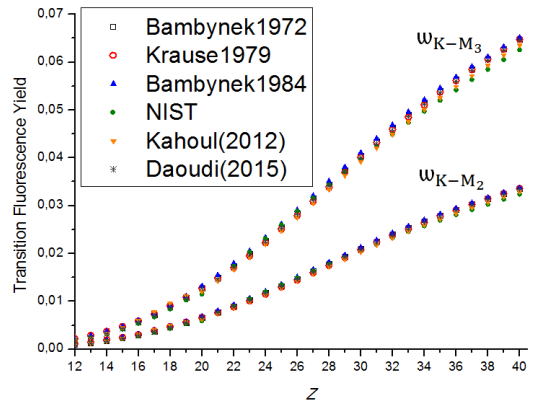

(a) Semi-empirical and empirical $\omega_{K\text{-}M_2}$ and $\omega_{K\text{-}M_3}$ partial fluorescence yield values $(12 \leq Z \leq 40)$

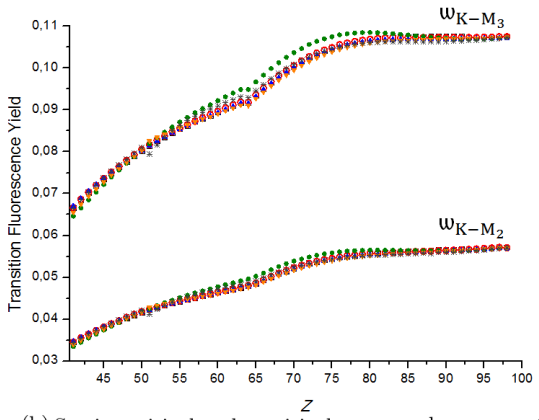

(b) Semi-empirical and empirical $\omega_{K\text{-}M_2}$ and $\omega_{K\text{-}M_3}$ partial fluorescence yield values $(40 \leq Z \leq 98)$

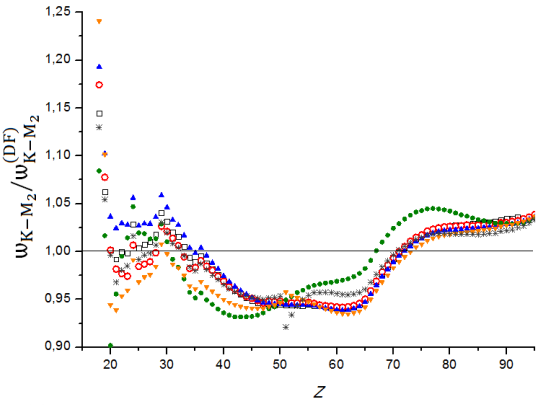

(c) Semi-empirical and empirical $\omega_{K\text{-}M_2}$ partial fluorescence yield values normalized to "DF" values

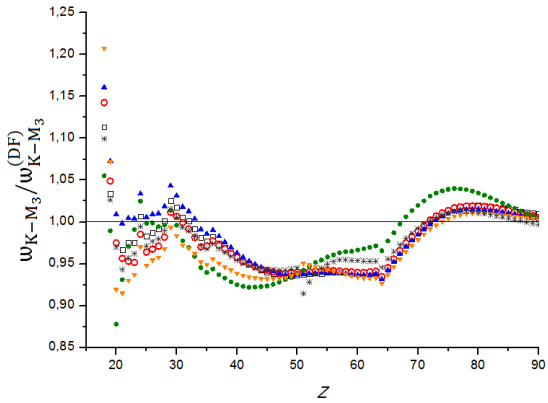

(d) Semi-empirical and empirical $\omega_{K\text{-}M_3}$ partial fluorescence yield values normalized to "DF" values

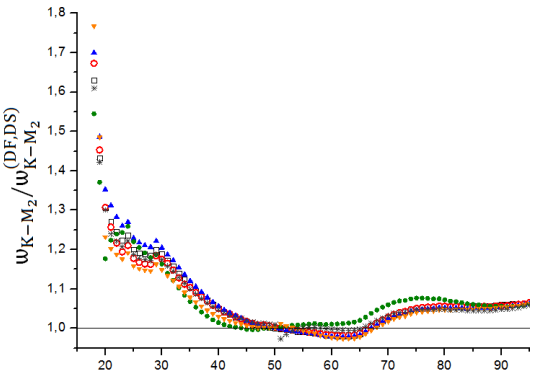

(e) Semi-empirical and empirical $\omega_{K\text{-}M_2}$ partial fluorescence yield values normalized to "DF,DS" values

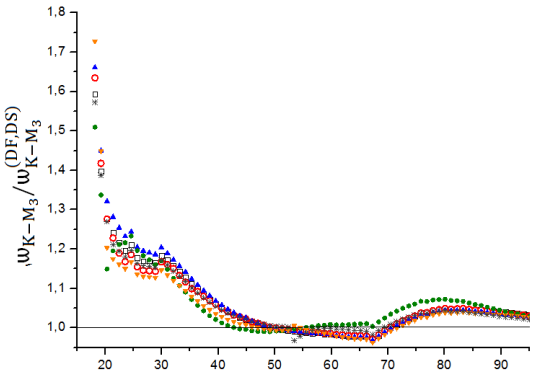

(f) Semi-empirical and empirical $\omega_{K\text{-}M_3}$ partial fluorescence yield values normalized to "DF,DS" values

Figure 6.6: "Bambynek1972": Values from Bambynek *et al.* earlier semi-empirical fit [154]. "Krause1979": values from Krause's semi-empirical fit [155]. "Bambynek1984": values from Bambynek *et al.* later semi-empirical fit [156]. "NIST": semi-empirical fit values presented in NIST's Fundamental Parameters Database [38]. "Kahoul": values from Kahoul *et al.* empirical fit [144]. "Daoudi": values from Daoudi *et al.* empirical fit [157].

values are obtained from the combination of semi-empirical or empirical K-shell fluorescence yield values with Salem *et al.* transition probability values (as presented in Section 6.1.17). From these figures and tables, it is clear that the semi-empirical and empirical partial fluorescence yields exhibit significantly high differences between each other, especially at low atomic numbers. In the range $3 \leq Z < 20$ some references present 10% to 100% difference to other references. As the atomic number increases better agreement is observed between all references. In the range $20 < Z < 80$, the values are comprised within 10% difference from each other, and in the range $80 < Z < 96$, differences are lower than 2%.

The $\omega_{\text{K-M}_2}$ and $\omega_{\text{K-M}_3}$ semi-empirical and empirical values are normalized with the respective "DF" theoretical values in Figs. 6.6.c and 6.6.d, and with the respective theoretical "DF,DS" values in Figs. 6.6.e and 6.6.f. These comparisons highlight that the empirical and semi-empirical values are higher than "DF,DS" values for almost all atomic numbers. Better agreement is found when comparing with the "DF" values.

Table 6.4 presents the average relative difference between each semi-empirical or empirical $\omega_{\text{K-M}_2}$ values and the "DF,DS" and "DF" values. In Table 6.5 the same is presented, but regarding $\omega_{\text{K-M}_3}$ values. From these tables, it is shown that all semi-empirical and empirical values are in closer agreement with "DF" values.

6.3 Discussion

The comparisons between all theoretical, empirical, and semi-empirical K-shell fluorescence yield values, ω_{K}, from the different references exhibit that NIST's Fundamental Parameters Database values disagree with the other references, especially in the atomic number range $60 \leq Z \leq 80$. As such, it is suggested a change to values obtained from other references.

The ω_{K}, $\omega_{\text{K-L}_2}$, $\omega_{\text{K-L}_3}$, $\omega_{\text{K-M}_2}$, $\omega_{\text{K-M}_3}$ partial fluorescence yields values from EADL and from Dirac-Fock/Dirac-Slater calculations ("DF,DS") exhibit some disagreement even though they were obtained from the same references. Pia et al. [35–37] had already pointed out this disagreement in their comparisons of partial fluorescence yields (normalized without accounting for radiationless transitions). Part of this disagreement can be due to the fact that while EADL includes Hubbel's corrections to avoid the over-prediction of the strength of Coster-Kronig transitions resulting from Dirac-Slater calculations, such corrections are not implemented in the present work.

Pia *et al.* work [35–37] highlighted that partial fluorescence yields (normalized without accounting for radiationless transitions) $\omega_{ij}^{(\text{NA})}$ obtained from Scofield's Hartree-Fock work [106] are in better agreement with the experimental values of Salem *et al.* [108], and as such, EADL should adopt Scofield's Hartree-Fock values. In the present work, the comparison consisted in partial fluorescence yields ω_{ij} that were normalized accounting for radiationless transitions, as are presented in EADL. The comparisons from the present work highlight that regarding ω_{K}, $\omega_{\text{K-L}_2}$ and $\omega_{\text{K-L}_3}$ values, when comparing the

values obtained from using Scofield's Dirac-Slater calculations "DF,DS", and the values obtained using Scofield's Dirac-Fock calculations "DF", the "DF,DS" values are actually in better agreement with most of the semi-empirical and empirical values. The exception to the previous statement is the case of Bambynek *et al.* 1984 semi-empirical values, which are in excellent agreement with "DF" values. As for the $\omega_{\text{K-M}_2}$ and $\omega_{\text{K-M}_3}$ partial fluorescence yields, the "DF" values are in better agreement with all semi-empirical and empirical values. The comparisons in the present work do not support that the change in the EADL library, regarding what Scofield's values are adopted, will make EADL's partial fluorescence yield values in better agreement with the semi-empirical and empirical values available in literature. It is worthwhile mentioning that, as it was presented in Pia *et al.* studies, when comparing partial fluorescence yield values (normalized without accounting for radiationless transitions) $\omega_{ij}^{(\text{NA})}$ obtained from Scofield's Dirac-Fock work and Scofield's Dirac-Slater work, the ones obtained from Dirac-Fock work are clearly in better agreement with the experimental values of Salem *et al.*. Such is to be expected since Dirac-Fock calculations have long been shown to be more accurate than Dirac-Slater calculations. Since $\omega_{ij}^{(\text{NA})}$ values and ω_{ij} differ only in including, or not, the randiationless transition probability values (see Eqs. 2.8 and 2.10), it is suspected that the fact that comparisons of ω_{ij} values do not show a clear better agreement for Dirac-Fock calculations can be due to inaccuracy of the total radiationless transition probability $A_i^{(\text{TA})}$. As such, it is suggested that change in EADL regarding partial yield values should be backed up with further studies.

The present work introduced a method to obtain partial fluorescence yields $\omega_{\text{K-L}_2}$, $\omega_{\text{K-L}_3}$, $\omega_{\text{K-M}_2}$ and $\omega_{\text{K-M}_3}$ from the combination of semi-empirical or empirical fitting functions with Salem *et al.* [108] ratios (as described in Section 6.1.17). This method can be a viable alternative of obtaining comprehensive values for data libraries, covering a large range of atomic number and a large range of transitions, as an alternative to relying in the existing theoretical data. However, some of the existing empirical and semi-empirical values present significant deviations between each other, especially at low atomic numbers, where differences around 100 % can be found between some of the references. In the range $Z > 20$ the deviations between the different references are comprised within 10% to a few percent.

From the comparisons of the present work, it is concluded that the "DF" values are in excellent agreement with Bambynek *et al.* 1984 semi-empirical values. In fact, no pair of references presented better agreement.

The method used in this work to obtain partial fluorescence yield values (normalized without accounting for radiationless transitions), which is based on Pia *et al.* method [35–37], allows to obtain values for all radiative transitions. The method used in the xraylib library is limited to those transitions that the transition probability values [169] are presented in Scofield's work [106]. Furthermore, the $\omega_{\text{K-L}_2}^{(NA)}$, $\omega_{\text{K-L}_3}^{(NA)}$, $\omega_{\text{K-M}_2}^{(NA)}$ and $\omega_{\text{K-M}_3}^{(NA)}$ values obtained using this method are slightly in better agreement with the experimental

values of Salem *et al.* [108]. Thus, it is suggested that the xraylib library [169] could consider using the method described in the present work, or the method used in Pia *et al.* work [35–37].

Chapter 7

Conclusions

In the present work, X-ray fluorescence analysis using a standardless method was achieved using Geant4 toolkit [20–22] for the the implementation of a code that performs the simulation of an EDXRF spectrum using a triaxial geometry spectrometer. By accurately describing the contribution of photon polarization in the scattering, the code is able to accurately simulate a typical EDXRF spectrum in a triaxial geometry, where the background is lower (lowering the detection limits of the elements), and where the scattering features are visible. As such, the developed code is suitable not only for a method of quantitative analysis from the characteristic peak intensities, but also for a method of analysis of the sample Z_{avg} through the evaluation of the Compton-to-Rayleigh scattering intensity ratio $R_{\text{C/R}}$. Even though Monte Carlo codes have been used for optimization of triaxial spectrometers, to our knowledge, there were no Monte Carlo simulations dedicated to elemental quantification in EDXRF technique using spectrometers in such geometry. Furthermore, from what it is known, the developed code is a novelty in what regards Monte Carlo simulations of EDXRF spectrometers including the analysis of the sample Z_{avg} through the evaluation of the Compton-to-Rayleigh scattering intensity ratio $R_{\text{C/R}}$. Since Geant4 implements several physics processes, and due to its handling of geometry, several contributions for the fluorescence peaks that are not always included in FP methods are included in these work simulations, such as: non-parallel beam geometries, tertiary- and higher-order fluorescence, electron enhancement of the fluorescence emission, etc. However, in the present work some geometry approximations had to be applied in the code, in order to reduced computation time and memory usage, which led to the development of two different versions of the code.

For the validation of the developed Basic code, simulations of the EDXRF spectra of

standard samples for a triaxial spectrometer were performed and compared with the respective experimentally measured spectra. The standards correspond to low-Z, medium-Z, and high-Z matrices. These comparisons present relatively good agreement (better than 20 % for most cases) for the characteristic peak intensities, with some of the exceptions to this good agreement being due to the fact that some detector related contributions are not simulated (such as sum peaks).

For the validation of the developed Advance code, a calibration curve of Rayleigh-to-Compton scattering ratio, R_{RC}, as function of the average atomic number, Z_{avg}, was obtained from the simulation of triaxial geometry spectra, and compared with the equivalent experimentally measured calibration curve. For both simulated and experimental curves, the curve was obtained from a set of model samples consisting of different proportions of reference materials of Hydroxyapatite (HAp)[$Ca_{10}(PO_4)_6(OH)_2$] (Sigma-Aldrich, lot #BCBS8492V), and boric acid [H_3BO_3]. The mixtures of the samples were chosen in order to have a calibration curve in the range $7.13 < Z_{avg} < 14.07$. The comparison of the curves show that most simulated values are close lying or within the experimental uncertainty margins. The agreement between simulated and experimental values is better than 10 % in most cases.

Using the multiconfiguration Dirac-Fock approach, all possible Zn K-shell radiative and radiationless transition probability values were calculated. From these values, other fundamental parameters, such as K-shell fluorescence yield value, transition intensity ratios, and partial fluorescence yield values, were obtained. Regarding radiative transition, the comparison between the calculated MCDF values and other values highlight a very good agreement when comparing transition probability values with Dirac-Fock values, and when comparing partial fluorescence yield values with the available Dirac-Fock values and experimental values. Most of the radiative transition intensity ratios compared are also in good agreement with the experimental values. Regarding radiationless transitions, some calculated values are in agreement with the other theoretical and experimental values, while other do not present a good agreement. Such comparisons are limited due to the lack of experimental and theoretical values. The calculated K-shell fluorescence yield is higher than the compared experimental and theoretical values, with the exception being when comparing with the value measured by Söğüt [153] value, which is one of the most recent measurements. Furthermore, the value is in very good agreement with Ménesguen and Lépy [34] experimental value.

It was presented a bibliography overview of works containing K-shell fluorescence yield values, and/or, partial fluorescence yield values, or relevant atomic parameters from which the former can be obtained. From the values obtained from these references, it was also presented a comparison of K-shell fluorescence yield, and partial K-shell fluorescence yield values, regarding the K-L_2, K-L_3, K-M_2, K-M_3 radiative transitions, in order to assess the values presented in EADL database, the database from which Geant4 and other codes and software resort for the simulation of atomic relaxation. These comparisons support one of the conclusions presented in Pia *et al.* works, namely that EADL does not present

the state of the art partial fluorescence yield values. However, these comparisons do not support Pia *et al.* suggestions that EADL should adopt the values from Scofield's Dirac-Fock work instead of values from Scofield's Dirac-Slater works. The comparison presented in this chapter show that more studies should be performed before changing EADL library values. Furthermore, it was suggested that xraylib library should adopt the method for deriving partial fluorescence yield values (normalized without accounting for radiationless transitions) employed in the present work, or the similar method from Pia *et al.* works, as these allow to obtain values for more transitions, and which are generally more accurate when comparing with experimental values. Furthermore, it is also concluded that NIST's Fundamental Parameters Database [38] K-shell fluorescence yield values are in high disagreement with all other values compared.

Bibliography

[1] S. Pessanha. "Non-Destructive Characterization of Artworks in Paper Support Using Spectroscopic Techniques." Doctoral dissertation. Universidade de Lisboa, 2013. URL: https://repositorio.ul.pt/handle/10451/10516.

[2] R. Jenkins, R. Gould, and D. Gedcke. *Quantitative x-ray spectrometry*. New York: Marcel Dekker Inc, 1981, p. 586. ISBN: 9780824712662. URL: https://doi.org/10.1002/xrs.1300110214.

[3] V. D. Hodoroaba and V. Rackwitz. "Gaining improved chemical composition by exploitation of compton-to-rayleigh intensity ratio in XRF analysis." In: *Analytical Chemistry* 86.14 (2014), pp. 6858–6864. ISSN: 15206882. DOI: 10.1021/ac5000619.

[4] S. Pessanha, S. Silva, L. Martins, J. P. Santos, and J. M. Silveira. "Suitability of the Compton-to-Rayleigh ratio in X-ray fluorescence spectroscopy: Hydroxyapatite-based materials characterization." In: *Journal of Analytical Atomic Spectrometry* 34.5 (2019), pp. 854–859. ISSN: 13645544. DOI: 10.1039/c8ja00370j. URL: https://pubs.rsc.org/en/content/articlepdf/2019/JA/C8JA00370J.

[5] V.-D. Hodoroaba and V. Rackwitz. "Gaining improved chemical composition by exploitation of compton-to-rayleigh intensity ratio in XRF analysis." In: *Analytical Chemistry* 86.14 (2014), pp. 6858–6864. ISSN: 15206882. DOI: 10.1021/ac5000619.

[6] J. W Criss. *NRLXRF : a Fortran program for X-ray fluorescence analysis : users' reference manual and general documentation*. Washington, D.C, 1977.

[7] W. T. Elam and J. R. Sieber. "An update to nrlxrf and nbsgsc." In: *Advances in X-Ray Analysis* 43.c (2000), pp. 442–448. URL: https://www.semanticscholar.org/paper/AN-UPDATE-TO-NRLXRF-AND-NBSGSC-Elam-Sieber.

[8] G. Tao, P. Pella, and R. Rousseau. *NBSGSC - a FORTRAN program for quantitative x-ray fluorescence analysis. Technical note (final)*. Tech. rep. United States: National Bureau of Standards, 1985.

[9] A. Rindby. "Software for energy-dispersive X-ray fluorescence." In: *X-Ray Spectrometry* 18.3 (1989), pp. 113–118. ISSN: 10974539. DOI: 10.1002/xrs.1300180308. URL: http://doi.wiley.com/10.1002/xrs.1300180308.

[10] *Canberra. WinAxil*. URL: http://www.canberra.com/products/438012.asp (visited on 09/20/2019).

[11] "A multiplatform code for the analysis of energy-dispersive X-ray fluorescence spectra." In: *Spectrochimica Acta Part B: Atomic Spectroscopy* 62.1 (2007), pp. 63–68. DOI: 10.1016/j.sab.2006.12.002. URL: http://pymca.sourceforge.net/index.html.

[12] P. Walter, M. Cotte, E. Papillon, J. Susini, and V. Solé. "A multiplatform code for the analysis of energy-dispersive X-ray fluorescence spectra." In: *Spectrochimica Acta Part B: Atomic Spectroscopy* 62.1 (2006), pp. 63–68. ISSN: 05848547. DOI: 10.1016/j.sab.2006.12.002.

[13] M. Czyzycki, D. Wegrzynek, P. Wrobel, and M. Lankosz. "Monte Carlo simulation code for confocal 3D micro-beam X-ray fluorescence analysis of stratified materials." In: *X-Ray Spectrometry* 40.2 (2011), pp. 88–95. ISSN: 00498246. DOI: 10.1002/xrs.1300. URL: http://doi.wiley.com/10.1002/xrs.1300.

[14] E. Bergbäck Knudsen, A. Prodi, J. Baltser, M. Thomsen, P. Kjær Willendrup, M. Sanchez Del Rio, C. Ferrero, E. Farhi, K. Haldrup, A. Vickery, R. Feidenhans'l, K. Mortensen, M. Meedom Nielsen, H. Friis Poulsen, S. Schmidt, and K. Lefmann. "McXtrace: A Monte Carlo McXtrace: software package for simulating X-ray optics, beamlines and experiments." In: *Journal of Applied Crystallography* 46.3 (2013), pp. 679–696. ISSN: 16005767. DOI: 10.1107/S0021889813007991. URL: http://scripts.iucr.org/cgi-bin/paper?S0021889813007991.

[15] V. Scot, J. E. Fernandez, L. Vincze, and K. Janssens. "3D extension of the Monte Carlo code MCSHAPE for photon-matter interactions in heterogeneous media." In: *Nuclear Instruments and Methods in Physics Research, Section B: Beam Interactions with Materials and Atoms* 263.1 SPEC. ISS. (2007), pp. 204–208. ISSN: 0168583X. DOI: 10.1016/j.nimb.2007.04.205. URL: https://linkinghub.elsevier.com/retrieve/pii/S0168583X07008634.

[16] V. Scot and J. E. Fernandez. "The Monte Carlo code MCSHAPE: Main features and recent developments." In: *Spectrochimica Acta - Part B Atomic Spectroscopy* 108 (2015), pp. 53–60. ISSN: 05848547. DOI: 10.1016/j.sab.2015.02.005. URL: https://www.sciencedirect.com/science/article/abs/pii/S0584854715000531.

[17] T. Trojek and T. Čechák. "Use of MCNP code in energy dispersive X-ray fluorescence." In: *Nuclear Instruments and Methods in Physics Research, Section B: Beam Interactions with Materials and Atoms* 263.1 SPEC. ISS. (2007), pp. 72–75. ISSN: 0168583X. DOI: 10.1016/j.nimb.2007.04.063. URL: https://www.sciencedirect.com/science/article/pii/S0168583X07008294.

[18] J. Baró, J. Sempau, J. M. Fernández-Varea, and F. Salvat. "PENELOPE: An algorithm for Monte Carlo simulation of the penetration and energy loss of electrons and positrons in matter." In: *Nuclear Inst. and Methods in Physics Research, B* 100.1 (1995), pp. 31–46. ISSN: 0168583X. DOI: 10.1016/0168-583X(95)00349-5. URL: https://www.sciencedirect.com/science/article/pii/0168583X95003495.

[19] X. Llovet, J. M. Fernández-Varea, J. Sempau, and F. Salvat. "Monte Carlo simulation of X-ray emission using the general-purpose code PENELOPE." In: *Surface and Interface Analysis*. Vol. 37. 11. John Wiley & Sons, Ltd, 2005, pp. 1054–1058. DOI: 10.1002/sia.2096. URL: http://doi.wiley.com/10.1002/sia.2096.

[20] S. Agostinelli et al. "GEANT4 - A simulation toolkit." In: *Nuclear Instruments and Methods in Physics Research, Section A: Accelerators, Spectrometers, Detectors and Associated Equipment* 506.3 (2003), pp. 250–303. ISSN: 01689002. DOI: 10.1016/S0168-9002(03)01368-8. arXiv: 1005.0727v1.

[21] J. Allison et al. "Geant4 developments and applications." In: *IEEE Transactions on Nuclear Science* 53.1 (2006), pp. 270–278. ISSN: 00189499. DOI: 10.1109/TNS.2006.869826. URL: http://ieeexplore.ieee.org/document/1610988/.

[22] J. Allison et al. "Recent developments in GEANT4." In: *Nuclear Instruments and Methods in Physics Research, Section A: Accelerators, Spectrometers, Detectors and Associated Equipment* 835 (2016), pp. 186–225. ISSN: 01689002. DOI: 10.1016/j.nima.2016.06.125. URL: https://www.sciencedirect.com/science/article/pii/S0168900216306957.

[23] L. Vincze, K. Janssen, and F. Adams. "A general Monte Carlo simulation of energy-dispersive X-ray fluorescence spectrometers-I. Unpolarized radiation, homogeneous samples." In: *Spectrochimica Acta Part B: Atomic Spectroscopy* 48.4 (1993), pp. 553–573. ISSN: 05848547. DOI: 10.1016/0584-8547(93)80060-8. URL: https://www.sciencedirect.com/science/article/abs/pii/0584854793800608.

[24] U. Bottigli, A. Brunetti, B. Golosio, P. Oliva, S. Stumbo, L. Vincze, P. Randaccio, P. Bleuet, A. Simionovici, and A. Somogyi. "Voxel-based Monte Carlo simulation of X-ray imaging and spectroscopy experiments." In: *Spectrochimica Acta - Part B Atomic Spectroscopy* 59.10-11 (2004), pp. 1747–1754. ISSN: 05848547. DOI: 10.1016/j.sab.2004.03.016.

[25] B. Golosio, T. Schoonjans, A. Brunetti, P. Oliva, and G. L. Masala. "Monte Carlo simulation of X-ray imaging and spectroscopy experiments using quadric geometry and variance reduction techniques." In: *Computer Physics Communications* 185.3 (2014), pp. 1044–1052. ISSN: 00104655. DOI: 10.1016/j.cpc.2013.10.034. URL: https://linkinghub.elsevier.com/retrieve/pii/S0010465513003834.

[26] J. D. Wallace. "The Monte Carlo modelling of in vivo X-ray fluorescence measurement of lead in tissue." In: *Physics in Medicine and Biology* 39.10 (1994), pp. 1745–1756. ISSN: 00319155. DOI: 10.1088/0031-9155/39/10/015. URL: http://stacks.iop.org/0031-9155/39/i=10/a=015?key=crossref.e49e81482fafe5ded0f65b094b4f5687.

[27] M. Zamburlini, S. H. Byun, A. Pejović-Milić, W. V. Prestwich, and D. R. Chettle. "Evaluation of MCNP5 and EGS4 for the simulation of in vivo strontium XRF measurements." In: *X-Ray Spectrometry* 36.2 (2007), pp. 76–81. ISSN: 00498246. DOI: 10.1002/xrs.942. URL: http://doi.wiley.com/10.1002/xrs.942.

[28] G. Piga, A. Brunetti, B. Lasio, S. Enzo, and A. Malgosa. "XRF investigation on skeletal remains from King Peter III of Aragon (1239-1285 A.D.) and Queen Blanche of Anjou (1280-1310 A.D.)" In: *Applied Physics A: Materials Science and Processing* 114.3 (2014), pp. 647–653. ISSN: 09478396. DOI: 10.1007/s00339-014-8272-z. URL: http://link.springer.com/10.1007/s00339-014-8272-z.

[29] M. Manso, N. Schiavon, I. Queralt, A. M. Arruda, J. M. Sampaio, and A. Brunetti. "Alloy characterization of a 7th Century BC archeological bronze vase - Overcoming patina constraints using Monte Carlo simulations." In: *Spectrochimica Acta - Part B Atomic Spectroscopy* 107 (2015), pp. 93–96. ISSN: 05848547. DOI: 10.1016/j.sab.2015.03.001. URL: https://www.sciencedirect.com/science/article/abs/pii/S0584854715000750.

[30] D. G. Lewis. "Optimization of a polarized source for in vivo X-ray fluorescence analysis of platinum and other heavy metals." In: *Physics in Medicine and Biology* 39.1 (1994), pp. 197–206. ISSN: 00319155. DOI: 10.1088/0031-9155/39/1/012. URL: http://stacks.iop.org/0031-9155/39/i=1/a=012?key=crossref.af47bf73e78fbb35aa0c26a1dad9a495.

[31] D. Lewis, G. Lewis, and C. Oggt. "Adaptation of the Egs4 Monte Carlo Fode for the Design of a Polarized Source for X-Ray Fluorescence Analysis of Platinum and Other Heavy Metals In Vivo." In: *Advances in X-ray Analysis* 38 (1994), pp. 579–585. ISSN: 0376-0308. DOI: 10.1154/s0376030800018267. URL: https://www.cambridge.org/core/product/identifier/S0376030800018267/type/journal{_}article.

[32] R. P. Hugtenburg, J. R. Turner, D. M. Mannering, and B. A. Robinson. "Monte Carlo methods for the in vivo analysis of cisplatin using x-ray fluorescence." In: *Applied Radiation and Isotopes* 49.5-6 (1998), pp. 673–676. ISSN: 09698043. DOI: 10.1016/S0969-8043(97)00230-3. URL: https://www.sciencedirect.com/science/article/pii/S0969804397002303.

[33] H. Al-Ghorabie Fayez. "EGS4 Monte Carlo simulation of a 90°geometry polarized X-ray fluorescence system." In: *Radiation Physics and Chemistry* 55.4 (1999),

pp. 377–384. ISSN: 0969806X. DOI: 10.1016/S0969-806X(99)00207-8. URL: https://linkinghub.elsevier.com/retrieve/pii/S0969806X99002078.

[34] Y. Ménesguen and M.-C. Lépy. "Mass attenuation coefficients in the range 3.8E11keV, K fluorescence yield and Kβ/Kα relative X-ray emission rate for Ti, V, Fe, Co, Ni, Cu and Zn measured with a tunable monochromatic X-ray source." In: *Nuclear Instruments and Methods in Physics Research Section B: Beam Interactions with Materials and Atoms* 268.16 (2010), pp. 2477–2486. ISSN: 0168-583X. DOI: 10.1016/J.NIMB.2010.05.044. URL: https://www.sciencedirect.com/science/article/pii/S0168583X10004623.

[35] M. G. Pia, P. Saracco, and M. Sudhakar. "Validation of fluorescence transition probability calculations." In: *IEEE Nuclear Science Symposium Conference Record* (2009), pp. 181–188. ISSN: 10957863. DOI: 10.1109/NSSMIC.2009.5401813. arXiv: 0912.1717.

[36] M. G. Pia, P. Saracco, and M. Sudhakar. "Validation of K and L shell radiative transition probability calculations." In: *IEEE Transactions on Nuclear Science* 56.6 (2009), pp. 3650–3661. ISSN: 00189499. DOI: 10.1109/TNS.2009.2033793.

[37] M. G. Pia, M. Augelli, M. Begalli, C.-H. Kim, L. Quintieri, P. Saracco, H. Seo, M. Sudhakar, G. Weidenspointner, and A. Zoglauer. "Conceptual challenges and computational progress in X-ray simulation." In: *SNA+MC 2010 Conference*. 2010. arXiv: 1012.3303. URL: http://arxiv.org/abs/1012.3303.

[38] W. T. Elam, B. D. Ravel, and J. R. Sieber. "A new atomic database for X-ray spectroscopic calculations." In: *Radiation Physics and Chemistry* 63.2 (2002), pp. 121–128. ISSN: 0969806X. DOI: 10.1016/S0969-806X(01)00227-4.

[39] O. R. N. Laboratory. *ZZ PHOTX, Photon Interaction Cross-Section Library for 100 Elements*.

[40] W. Bambynek, B. Crasemann, R. W. Fink, H. U. Freund, H. Mark, C. D. Swift, R. E. Price, and P. V. Rao. "X-Ray Fluorescence Yields, Auger, and Coster0Kronig Transition Probabilities." In: *Reviews of Modern Physics* 44.4 (1972), pp. 716–813. ISSN: 0034-6861. DOI: 10.1103/RevModPhys.44.716.

[41] E. Badea, L. Miu, P. Budrugeac, M. Giurginca, A. Mašić, N. Badea, and G. Della Gatta. "Study of deterioration of historical parchments by various thermal analysis techniques complemented by SEM, FTIR, UV-Vis-NIR and unilateral NMR investigations." In: *Journal of Thermal Analysis and Calorimetry* 91.1 (2008), pp. 17–27. ISSN: 13886150. DOI: 10.1007/s10973-007-8513-x. URL: http://link.springer.com/10.1007/s10973-007-8513-x.

[42] J. H. Hubbell, W. J. Veigele, E. A. Briggs, R. T. Brown, D. T. Cromer, and R. J. Howerton. "Atomic form factors, incoherent scattering functions, and photon scattering cross sections." In: *Journal of Physical and Chemical Reference Data* 4.3 (1975), pp. 471–538. ISSN: 0047-2689. DOI: 10.1063/1.555523. URL: http://aip.scitation.org/doi/10.1063/1.555523.

[43] P. P. Kane, L. Kissel, R. H. Pratt, and S. C. Roy. "Elastic scattering of γ-rays and X-rays by atoms." In: *Physics Reports* 140.2 (1986), pp. 75–159. ISSN: 03701573. DOI: 10.1016/0370-1573(86)90018-9. URL: https://www.sciencedirect.com/science/article/abs/pii/0370157386900189?via{\%}3Dihub.

[44] J. H. Hubbell and I. Overbo. "Relativistic atomic form factors and photon coherent scattering cross sections." In: *Journal of Physical and Chemical Reference Data* 8.1 (1979), pp. 69–106. ISSN: 15297845. DOI: 10.1063/1.555593.

[45] A. H. Compton. "A Quantum Theory of the Scattering of X-rays by Light Elements." In: *Physical Review* 21.5 (1923), pp. 483–502. ISSN: 0031899X. DOI: 10.1103/PhysRev.21.483. URL: https://link.aps.org/doi/10.1103/PhysRev.21.483.

[46] A. H. Compton. "The spectrum of scattered x-rays." In: *Physical Review* 22.5 (1923), pp. 409–413. ISSN: 0031899X. DOI: 10.1103/PhysRev.22.409. URL: https://link.aps.org/doi/10.1103/PhysRev.22.409.

[47] J. D. BERNAL. "X-Rays in Theory and Experiment." In: *Nature* 136 (1935), pp. 661–662. DOI: 10.1038/136661a0.

[48] J. W. M. Dumond. "The Linear Momenta of Electrons in Atoms and in Solid Bodies as Revealed by X-Ray Scattering." In: *Reviews of Modern Physics* 5.1 (1933), pp. 1–33. ISSN: 0034-6861. DOI: 10.1103/RevModPhys.5.1. URL: https://link.aps.org/doi/10.1103/RevModPhys.5.1.

[49] O. Klein and Y. Nishina. "Über die Streuung von Strahlung durch freie Elektronen nach der neuen relativistischen Quantendynamik von Dirac." In: *Zeitschrift für Physik* 52.11-12 (1929), pp. 853–868. ISSN: 0044-3328. DOI: 10.1007/BF01366453. URL: http://link.springer.com/10.1007/BF01366453.

[50] J. H. Hubbell. "Review and history of photon cross section calculations." In: *Physics in Medicine and Biology* 51.13 (2006), R245–R262. ISSN: 13616560. DOI: 10.1088/0031-9155/51/13/R15. URL: http://stacks.iop.org/0031-9155/51/i=13/a=R15?key=crossref.35275dfe439b3b728cfed9869ac94b34.

[51] H. Heitler. *The Quantum Theory of Radiation*. Ed. by Oxford. Oxford: Oxford, 1954, pp. 217–219.

[52] Y. Namito, S. Ban, and H. Hirayama. "Implementation of linearly-polarized photon scattering into the EGS4 code." In: *Nuclear Instruments and Methods in Physics Research, A* 332.1-2 (1993), pp. 277–283. ISSN: 01689002. DOI: 10.1016/0168-9002(93)90770-I.

[53] A. M. Gójska and E. A. Miśta. "Analysis of the elemental composition of the artefacts from the Kosewo archaeological site." In: *Acta Physica Polonica A* 130.6 (2016), pp. 1415–1419. ISSN: 1898794X. DOI: 10.12693/APhysPolA.130.1415. URL: http://przyrbwn.icm.edu.pl/APP/PDF/130/a130z6p24.pdf.

[54] R. Tertian and F. Claisse. *Principles of quantitative X-ray fluorescence analysis*. London: Heyden, 1982.

[55] R Klockenkamper. *Total-reflection x-ray fluorescence analysis*. New York: Wiley, 1996.

[56] F. Scholze, A. Longoni, C. Fiorini, L. Strüder, N. Meidinger, R. Hartmann, N. Kawahara, and T. Shoji. "X-Ray Detectors and XRF Detection Channels." In: *Handbook of Practical X-Ray Fluorescence Analysis*. Berlin, Heidelberg: Springer Berlin Heidelberg, 2007, pp. 199–308. DOI: 10.1007/978-3-540-36722-2_4. URL: http://link.springer.com/10.1007/978-3-540-36722-2{_}4.

[57] G. F. Knoll and H. W. Kraner. "Radiation Detection and Measurement." In: *Proceedings of the IEEE* 69.4 (1981), p. 495. ISSN: 15582256. DOI: 10.1109/PROC.1981.12016.

[58] R. Cesareo. "X-ray physics: Interaction with matter, production, detection." In: *Rivista del Nuovo Cimento* 23.7 (2000), pp. 1–183. ISSN: 0393697X. DOI: 10.1118/1.1496103. URL: http://doi.wiley.com/10.1118/1.1496103.

[59] R. v. R. Grieken and A. Markowicz. *Handbook of X-ray spectrometry : methods and techniques*. Marcel Dekker, 1993, p. 704. ISBN: 0824784839. URL: https://inis.iaea.org/search/searchsinglerecord.aspx?recordsFor=SingleRecord{\&}RN=25013766.

[60] P van Espen and P. Lemberge. "EDXRF spectrum evaluation and quantitative analysis using multivariate and nonlinear techniques." In: *Advances in X-Ray Analysis* 43 (2000), pp. 560–569.

[61] R. M. Rousseau and J. a. Boivin. "The fundamental algorithm: A natural extension of the Sherman equation Part 1: Theory." In: *The Rigaku Journal* 15.1 (1998), pp. 13–28. URL: http://www.rigaku.com/downloads/journal/volume15-1.html.

[62] E. Gillam and H. T. Heal. "Some problems in the analysis of steels by X-ray fluorescence." In: *British Journal of Applied Physics* 3 (1952), pp. 353–358.

[63] H. J. Beattie and R. M. Brissey. "Calibration Method for X-Ray Fluorescence Spectrometry." In: *Analytical Chemistry* 36 (1954), p. 980.

[64] J. Sherman. "Paper No. 73." In: *Pittsburgh Conference on Analytical Chemistry and Apllied Spectroscopy*. 1953.

[65] J. Sherman. "The theoretical derivation of fluorescent X-ray intensities from mixtures." In: *Spectrochimica Acta* 7.C (1955), pp. 283–306. ISSN: 03711951. DOI: 10.1016/0371-1951(55)80041-0. URL: https://www.sciencedirect.com/science/article/pii/0371195155800410.

[66] R. M. Rousseau. "Fundamental algorithm between concentration and intensity in XRF analysis 1—theory." In: *X-Ray Spectrometry* 13.3 (1984), pp. 115–120. ISSN: 10974539. DOI: 10.1002/xrs.1300130306. URL: http://doi.wiley.com/10.1002/xrs.1300130306.

[67] R. M. Rousseau. "Fundamental algorithm between concentration and intensity in XRF analysis 2—practical application." In: *X-Ray Spectrometry* 13.3 (1984), pp. 121–125. ISSN: 10974539. DOI: 10.1002/xrs.1300130307. URL: http://doi.wiley.com/10.1002/xrs.1300130307.

[68] R. M. Rousseau and M. Bouchard. "Fundamental algorithm between concentration and intensity in XRF analysis. 3—Experimental verification." In: *X-Ray Spectrometry* 15.3 (1986), pp. 207–215. ISSN: 10974539. DOI: 10.1002/xrs.1300150311. URL: http://doi.wiley.com/10.1002/xrs.1300150311.

[69] R. M. Rousseau. "The Fundamental Algorithm : an Exhaustive Study of the Claisse-Quintin Algorithm and the Tertian and Lachance Identities Part II : Application." In: *The Rigaku Journal* 15.2 (1998), pp. 14 –26.

[70] R. Sitko and B. Zawisza. "X-Ray Fluorescence Spectrometry." In: *X-Ray Spectroscopy* (2012), pp. 137–162. ISSN: 978-953-307-967-7. DOI: 10.5772/1422. URL: http://www.intechopen.com/books/x-ray-spectroscopy/quantification-in-x-ray-fluorescence-spectrometry.

[71] H. a. V. Sprang. "Fundamental parameter methods in XRF spectroscopy." In: *Advances in X-Ray Analysis* 42.C (2000), pp. 1–10. URL: https://www.researchgate.net/publication/237249511{_}Fundamental{_}parameter{_}methods{_}in{_}XRF{_}spectroscopy.

[72] D. K. G. de Boer and P. Brouwer. "Fundamental Parameter-Based X-ray Fluorescence Analysis of Thin and Multilayer Samples." In: *Advances in X-ray Analysis* 33 (1990), pp. 237–245. DOI: 10.1007/978-1-4613-9996-4_26. URL: https://www.researchgate.net/publication/286027743{_}Fundamental{_}Parameter-Based{_}X-Ray{_}Fluorescence{_}Analysis{_}of{_}Thin{_}and{_}Multilayer{_}Samples.

[73] G. W. Corder and D. I. Foreman. *Nonparametric statistics for non-statisticians : a step-by-step approach*. Ed. by John Wiley & Sons. Oxford: Wiley-Blackwell, 2009, p. 247.

[74] P. J. Custódio, M. L. Carvalho, F. Nunes, S. Pedroso, and A. Campos. "Direct analysis of human blood (mothers and newborns) by energy dispersive X-ray fluorescence." In: *Journal of Trace Elements in Medicine and Biology* 19.2-3 (2005), pp. 151–158. ISSN: 0946672X. DOI: 10.1016/j.jtemb.2005.09.002. URL: https://www.sciencedirect.com/science/article/pii/S0946672X05001045.

[75] D. Guimarães. "Measurement of Lead Concentration in Biological Tissues by Atomic Spectroscopy Techniques." Doctoral dissertation. Universidade Nova de Lisboa, 2011. URL: https://run.unl.pt/handle/10362/6805.

[76] A. H. Compton and C. F. Hagenow. "A Measurement of the Polarization of Secondary X-Rays." In: *Journal of the Optical Society of America* 8.4 (1924), p. 487. ISSN: 0030-3941. DOI: 10.1364/josa.8.000487. URL: https://www.osapublishing.org/abstract.cfm?URI=josa-8-4-487.

[77] S. Pessanha, A. Guilherme, and M. L. Carvalho. "Comparison of matrix effects on portable and stationary XRF spectrometers for cultural heritage samples." In: *Applied Physics A: Materials Science and Processing* 97.2 (2009), pp. 497–505. ISSN: 09478396. DOI: 10.1007/s00339-009-5251-x.

[78] M. Manso, M. Costa, and M. L. Carvalho. "Comparison of elemental content on modern and ancient papers by EDXRF." In: *Applied Physics A: Materials Science and Processing* 90.1 (2008), pp. 43–48. ISSN: 09478396. DOI: 10.1007/s00339-007-4235-y. URL: http://link.springer.com/10.1007/s00339-007-4235-y.

[79] S. Pessanha, A. Guilherme, and M. L. Carvalho. "Comparison of matrix effects on portable and stationary XRF spectrometers for cultural heritage samples." In: *Applied Physics A: Materials Science and Processing* 97.2 (2009), pp. 497–505. ISSN: 09478396. DOI: 10.1007/s00339-009-5251-x. URL: http://link.springer.com/10.1007/s00339-009-5251-x.

[80] M. L. Carvalho, L. Ascensão, T. Magalhães, and A. Casimiro. "EDXRF and TXRF Application to cadmium toxicity in Acer pseudoplatanus L. cells: Cytological features and cation interactions." In: *X-Ray Spectrometry* 34.5 (2005), pp. 406–410. ISSN: 00498246. DOI: 10.1002/xrs.832. URL: http://doi.wiley.com/10.1002/xrs.832.

[81] D. Guimarães, M. L. Carvalho, V. Geraldes, I. Rocha, and J. P. Santos. "Study of lead accumulation in bones of Wistar rats by X-ray fluorescence analysis: Aging effect." In: *Metallomics* 4.1 (2012), pp. 66–71. ISSN: 17565901. DOI: 10.1039/c1mt00149c. URL: http://xlink.rsc.org/?DOI=C1MT00149C.

[82] S. Chauvie, S. Guatelli, V. Ivanchenko, F. Longo, A. Mantero, B. Mascialino, P. Nieminen, L. Pandola, S. Parlati, L. Peralta, M. Pia, M. Piergentili, P. Rodrigues, S. Saliceti, and A. Trindade. "Geant4 low energy electromagnetic physics." In: *IEEE Symposium Conference Record Nuclear Science 2004.* Vol. 3. C. 2004, pp. 1881–

1885. ISBN: 0-7803-8701-5. DOI: 10.1109/NSSMIC.2004.1462612. URL: http://ieeexplore.ieee.org/lpdocs/epic03/wrapper.htm?arnumber=1462612.

[83] H. Araujo, A. Howard, S. Chauvie, S. Guatelli, A. Mantero, B. Mascialino, M. Pia, M. Piergentili, S. Saliceti, V. Ivanchenko, F. Longo, P. Nieminem, L. Pandola, S. Parlati, L. Peralta, P. Rodrigues, and A. Trinidade. "Geant4 Low Energy Electromagnetic Physics." In: *The Monte Carlo method: versatility unbounded in a dynamic computing world*. 2005, P23.

[84] S. Guatelli, A. Mantero, B. Mascialino, P. Nieminen, and M. G. Pia. "Geant4 atomic relaxation." In: *IEEE Transactions on Nuclear Science* 54.3 (2007), pp. 585–593. ISSN: 00189499. DOI: 10.1109/TNS.2007.896214.

[85] *PhysicsValidationTaskForce < Geant4 < TWiki*. URL: https://twiki.cern.ch/twiki/bin/view/Geant4/PhysicsValidationTaskForce (visited on 09/06/2019).

[86] A. Mantero, B. Bavdaz, A. Owens, T. Peacock, and M. G. Pia. "Simulation of X-ray fluorescence and application to planetary astrophysics." In: *IEEE Nuclear Science Symposium Conference Record*. Vol. 3. IEEE, 2003, pp. 1527–1529. ISBN: 0-7803-8257-9. DOI: 10.1109/NSSMIC.2003.1352167. URL: http://ieeexplore.ieee.org/document/1352167/.

[87] A. Owens, B. Beckhoff, M. Kolbe, M. Krumrey, A. Mantero, M. Mantler, A. Peacock, M. G. Pia, D. Pullan, U. G. Schneider, and G. Ulm. "Measuring and interpreting X-ray fluorescence from planetary surfaces." In: *Analytical Chemistry* 80.22 (2008), pp. 8398–8405. ISSN: 00032700. DOI: 10.1021/ac8009627. URL: https://pubs.acs.org/doi/10.1021/ac8009627.

[88] M. R. Dimmock, M. D. De Jonge, D. L. Howard, S. A. James, R. Kirkham, D. M. Paganin, D. J. Paterson, G. Ruben, C. G. Ryan, and J. M. C. Brown. "Validation of a Geant4 model of the X-ray fluorescence microprobe at the Australian Synchrotron." In: *Journal of Synchrotron Radiation*. Vol. 22. 2. 2015, pp. 354–365. DOI: 10.1107/S1600577515000223. URL: http://scripts.iucr.org/cgi-bin/paper?S1600577515000223.

[89] M. E. Medhat and V. P. Singh. "Mass attenuation coefficients of composite materials by Geant4, XCOM and experimental data: Comparative study." In: *Radiation Effects and Defects in Solids* 169.9 (2014), pp. 800–807. ISSN: 10294953. DOI: 10.1080/10420150.2014.950264. URL: http://www.tandfonline.com/doi/abs/10.1080/10420150.2014.950264.

[90] S. Guatelli, A. Mantero, B. Mascialino, P. Nieminen, and M. G. Pia. "Geant4 atomic relaxation." In: *IEEE Transactions on Nuclear Science* 54.3 (2007), pp. 585–593. ISSN: 00189499. DOI: 10.1109/TNS.2007.896214. URL: http://ieeexplore.ieee.org/document/4237414/.

[91] S. T. Perkins and D. E. Cullen. *ENDL Type Formats for the LLNL Evaluated Atomic Data Library (EADL), Evaluated Electron Data Library (EEDL), and Evaluated Photon Data Library (EPDL)*. Tech. rep. LAWRENCE LIVERMORE NATIONAL LABORATORY, 2002.

[92] *2014 Evaluated Atomic Data Library (EADL) in ENDL Format*. 2014. URL: https://www-nds.iaea.org/epics2014/ENDL/EADL/getza.htm (visited on 02/20/2019).

[93] J. H. Scofield. "Relativistic hartree-slater values for K and L X-ray emission rates." In: *Atomic Data and Nuclear Data Tables* 14.2 (1974), pp. 121–137. ISSN: 0092640X. DOI: 10.1016/S0092-640X(74)80019-7. URL: http://www.sciencedirect.com/science/article/pii/S0092640X74800197.

[94] M. H. Chen, E. Laiman, B. Crasemann, M. Aoyagi, and H. Mark. "Relativistic L-shell Auger and Coster-Kronig rates and fluorescence yields." In: *Physical Review A* 19.6 (1979), pp. 2253–2259. ISSN: 10502947. DOI: 10.1103/PhysRevA.19.2253.

[95] M. H. Chen, B. Crasemann, and H. Mark. "Relativistic radiationless transition probabilities for atomic K- and L-shells." In: *Atomic Data and Nuclear Data Tables* 24.1 (1979), pp. 13–37. ISSN: 10902090. DOI: 10.1016/0092-640X(79)90037-8.

[96] M. H. Chen, B. Crasemann, and H. Mark. "Widths and fluorescence yields of atomic L-shell vacancy states." In: *Physical Review A* 24.1 (1981), pp. 177–182. ISSN: 10502947. DOI: 10.1103/PhysRevA.24.177. arXiv: arXiv:1011.1669v3.

[97] M. H. Chen, B. Crasemann, and H. Mark. "Relativistic K-shell Auger rates, level widths, and fluorescence yields." In: *Physical Review A* 21.2 (1980), pp. 436–441. ISSN: 10502947. DOI: 10.1103/PhysRevA.21.436.

[98] M. H. Chen, B. Crasemann, and H. Mark. "Radiationless transitions to atomic M1,2,3 shells: Results of relativistic theory." In: *Physical Review A* 27.6 (1983).

[99] S. Perkins, D. Cullen, M. Chen, J. Rathkopf, J. Scofield, and J. Hubbell. *Tables and Graphs of Atomic Subshell and Relaxation Data Derived from the LLNL Evaluated Atomic Data Library (EADL), Z=1-100*. Tech. rep. LAWRENCE LIVERMORE NATIONAL LABORATORY, 1991, UCRL–50400. DOI: 10.2172/10121422.

[100] S. Guatelli, A. Mantero, B. Mascialino, M. G. Pia, and V. Zampichelli. "Validation of Geant4 atomic relaxation against the NIST reference data." In: *IEEE Nuclear Science Symposium Conference Record* 3 (2007), pp. 1516–1518. ISSN: 10957863. DOI: 10.1109/NSSMIC.2006.354186.

[101] *NIST Standard Reference Data [Online] https://www.nist.gov/srd*. URL: https://www.nist.gov/srd.

[102] R. D. Deslattes, E. G. Kassler, P. Indelicato, L. De Billy, E. Lindroth, and J. Anton. "X-ray transition energies: New approach to a comprehensive evaluation." In: *Reviews of Modern Physics* 75.1 (2003), pp. 35–99. ISSN: 00346861. DOI: 10.1103/RevModPhys.75.35. URL: http://link.aps.org/doi/10.1103/RevModPhys.75.35.

[103] A. V. Naumkin, A. Kraut-Vass, and C. J. Powell. *NIST X-ray photoelectron spectroscopy database [Online]*. 2008. URL: https://srdata.nist.gov/xps/.

[104] S. Incerti, B. Suerfu, J. Xu, V. Ivantchenko, A. Mantero, J. M. Brown, M. A. Bernal, Z. Francis, M. Karamitros, and H. N. Tran. "Simulation of Auger electron emission from nanometer-size gold targets using the Geant4 Monte Carlo simulation toolkit." In: *Nuclear Instruments and Methods in Physics Research, Section B: Beam Interactions with Materials and Atoms* 372 (2016), pp. 91–101. ISSN: 0168583X. DOI: 10.1016/j.nimb.2016.02.005. URL: https://www.sciencedirect.com/science/article/pii/S0168583X16001221.

[105] J. H. Scofield. "Radiative Decay Rates of Vacancies in the K and L Shells." In: *Physical Review* 179.1 (1969), pp. 9–16. ISSN: 0031899X. DOI: 10.1103/PhysRev.179.9.

[106] J. Scofield. "Exchange corrections of K x-ray emission rates." In: *Physical Review A* 9.3 (1974), pp. 1041–1049. ISSN: 0556-2791. DOI: 10.1103/PhysRevA.9.1041.

[107] J. H. Scofield. "Hartree-Fock values of L x-ray emission rates." In: *Physical Review A* 10.5 (1974), pp. 1507–1510. DOI: https://doi.org/10.1103/PhysRevA.10.1507.

[108] S. I. Salem, S. L. Panossian, and R. A. Krause. "Experimental K and L relative x-ray emission ratess." In: *Atomic Data and Nuclear Data Tables* 14.2 (1974), pp. 91–109. ISSN: 10902090. DOI: 10.1016/S0092-640X(74)80017-3.

[109] J. Apostolakis, S. Giani, M. Maire, P. Nieminen, M. G. Pia, and L. Urban. "Geant4 Low Energy Electromagnetic models for electrons and photons." In: *European Organization for Nuclear Research* CERN-OPEN-.August (1999), pp. 1–11. DOI: 10.15161/oar.it/1448986129.49.

[110] D. E. Cullen, J. H. Hubbell, L. Kissel, and L. L. N. Laboratory. *EPDL97: the evaluated photo data library '97 version*. Tech. rep. 5. Livermore, CA: Lawrence Livermore National Laboratory (LLNL), 1997, pp. 1–35. DOI: 10.2172/295438. URL: http://www.osti.gov/servlets/purl/295438-uZu33l/webviewable/http://www.osti.gov/bridge/servlets/purl/295438-uZu33l/webviewable/.

[111] J. H. Scofield. *Theoretical photoionization cross sections from 1 to 1500 keV, Lawrence Livermore Laboratory Report UCRL-51326*. Tech. rep. U.S. Atomic Energy Commission: Lawrence Livermore Laboratory, 1973, pp. 1–374. DOI: 10.2172/4545040. URL: http://www.osti.gov/servlets/purl/4545040/.

[112] G. A. P. Cirrone, G. Cuttone, F. Di Rosa, L. Pandola, F. Romano, and Q. Zhang. "Validation of the Geant4 electromagnetic photon cross-sections for elements and compounds." In: *Nuclear Instruments and Methods in Physics Research, Section A: Accelerators, Spectrometers, Detectors and Associated Equipment* 618.1-3 (2010), pp. 315–322. ISSN: 01689002. DOI: 10.1016/j.nima.2010.02.112.

[113] M. C. Han, H. S. Kim, M. G. Pia, T. Basaglia, M. Batic, G. Hoff, C. H. Kim, and P. Saracco. "Validation of Cross Sections for Monte Carlo Simulation of the Photoelectric Effect." In: *IEEE Transactions on Nuclear Science* 63.2 (2016), pp. 1117–1146. ISSN: 00189499. DOI: 10.1109/TNS.2016.2521876. arXiv: 1601.06514. URL: http://arxiv.org/abs/1601.06514http://dx.doi.org/10.1109/TNS.2016.2521876.

[114] D. Cullen. *Program SCATMAN: A code designed to calculate photon coherent scattering anomalous scattering factors and cross sections*. Tech. rep. Lawrence Livermore National Laboratory, UCRL-ID-103422, 1989.

[115] M.J. Berger, J.H. Hubbell, S.M. Seltzer, J. Chang, J.S. Coursey, R. Sukumar, D.S. Zucker and K. Olsen. *XCOM: Photon Cross Sections Database*. 1999. URL: https://physics.nist.gov/PhysRefData/Xcom/html/xcom1.html (visited on 08/29/2019).

[116] A. Reineking, R. Wenskus, A. Baumann, D. Schaupp, P. Rullhusen, F. Smend, and M. Schumacher. "Compton scattering: Test of the double differential cross section in the relativistic impulse approximation." In: *Physics Letters A* 95.1 (1983), pp. 29–31. ISSN: 03759601. DOI: 10.1016/0375-9601(83)90773-9. URL: https://www.sciencedirect.com/science/article/abs/pii/0375960183907739.

[117] R. Wenskus, A. Baumann, P. Rullhusen, D. Schaupp, F. Smend, and M. Schumacher. "Relativistic double differential cross sections for Compton scattering by bound electrons: Test at low photon energies and predictions at intermediate photon energies." In: *Zeitschrift für Physik A Atoms and Nuclei* 320.2 (1985), pp. 179–184. ISSN: 03402193. DOI: 10.1007/BF01881265. URL: http://link.springer.com/10.1007/BF01881265.

[118] G. A. Carlsson, C. A. Carlsson, K. Berggren, and R. Ribberfors. "Calculation of scattering cross sections for increased accuracy in diagnostic radiology. I. Energy broadening of Compton scattered photons." In: *Medical Physics* 9.6 (1982), pp. 868–879. ISSN: 00942405. DOI: 10.1118/1.595195. URL: http://www.ncbi.nlm.nih.gov/pubmed/7162473http://doi.wiley.com/10.1118/1.595195.

[119] P. A. Pella, L. Feng, and J. A. Small. "An analytical algorithm for calculation of spectral distributions of x-ray tubes for quantitative x-ray fluorescence analysis." In: *X-Ray Spectrometry* 14.3 (1985), pp. 125–135. ISSN: 10974539. DOI: 10.1002/xrs.1300140306. URL: http://doi.wiley.com/10.1002/xrs.1300140306.

[120] R. Brun and F. Rademakers. "ROOT - An object oriented data analysis framework." In: *Nuclear Instruments and Methods in Physics Research, Section A: Accelerators, Spectrometers, Detectors and Associated Equipment* 389.1-2 (1997), pp. 81–86. ISSN: 01689002. DOI: 10.1016/S0168-9002(97)00048-X. URL: https://linkinghub.elsevier.com/retrieve/pii/S016890029700048X.

[121] L. Vincze, K. Janssens, F. Adams, M. L. Rivers, and K. W. Jones. "A general Monte Carlo simulation of ED-XRF spectrometers. II: Polarized monochromatic radiation, homogeneous samples." In: *Spectrochimica Acta Part B: Atomic Spectroscopy* 50.2 (1995), pp. 127–147. ISSN: 05848547. DOI: 10.1016/0584-8547(94)00124-E. URL: https://www.sciencedirect.com/science/article/pii/058485479400124E.

[122] S. Pessanha, A. Guilherme, and M. L. Carvalho. "Comparison of matrix effects on portable and stationary XRF spectrometers for cultural heritage samples." In: *Applied Physics A: Materials Science and Processing* 97.2 (2009), pp. 497–505. ISSN: 09478396. DOI: 10.1007/s00339-009-5251-x. URL: http://link.springer.com/10.1007/s00339-009-5251-x.

[123] D. Cullen, S. T. {Perkins}, D. E. {Cullen}, M. H. {Chen}, J. H. {Hubbell}, J {Rathkopf}, and J {Scofield}. *Tables and Graphs of Atomic Subshell and Relaxation Data Derived from the LLNL Evaluated Atomic Data Library (EADL), Z = 1 -100*. 1991.

[124] D. R. Hartree. "The Wave Mechanics of an Atom with a Non-Coulomb Central Field." In: *Mathematical Proceedings of the Cambridge Philosophical Society* 24.1 (1928), pp. 89–110. DOI: https://doi.org/10.1017/S0305004100011919.

[125] J. C. Slater. "Note on Hartree's Method." In: *Physical Review* 35.2 (1930), p. 210. DOI: https://doi.org/10.1103/PhysRev.35.210.2. URL: https://journals.aps.org/pr/abstract/10.1103/PhysRev.35.210.2.

[126] D. R Hartree and W. Hartree. "Self-consistent field, with exchange, for beryllium." In: *Proceedings of the Royal Society A: Mathematical, Physical and Engineering Sciences* 150.869 (1935), pp. 9–33. DOI: https://doi.org/10.1098/rspa.1935.0085.

[127] J. P. Desclaux. "A multiconfiguration relativistic DIRAC-FOCK program." In: *Computer Physics Communications* 9.1 (1975), pp. 31–45. ISSN: 00104655. DOI: 10.1016/0010-4655(75)90054-5.

[128] P. Indelicato. "Projection operators in multiconfiguration Dirac-Fock calculations: Application to the ground state of heliumlike ions." In: *Physical Review A* 51.2 (1995), pp. 1132–1145. DOI: 10.1103/PhysRevA.51.1132. URL: link.aps.org/doi/10.1103/PhysRevA.51.1132.

[129] I. P. Grant, B. J. Mckenzie, P. R. Norrington, and D. F. Mayers. "AN ATOMIC MULTICONFIGURATIONAL DIRAC-FOCK PACKAGE." In: *Computer Physics Communications* 21.2 (1980), pp. 207–231. DOI: https://doi.org/10.1016/0010-4655(80)90041-7. URL: https://www.sciencedirect.com/science/article/pii/0010465580900417.

[130] J. P. Marques, M. C. Martins, A. M. Costa, P. Indelicato, F. Parente, and J. P. Santos. "Theoretical determination of K X-ray transition energy and probability values for highly charged (He- through B-like) Nd, Sm, Gd, Dy, Er, and Yb ions." In: *Radiation Physics and Chemistry* 154.October 2017 (2019), pp. 17–20. ISSN: 18790895. DOI: 10.1016/j.radphyschem.2018.02.003. URL: https://doi.org/10.1016/j.radphyschem.2018.02.003.

[131] P. O. Löwdin. "Quantum theory of many-particle systems. I. Physical interpretations by means of density matrices, natural spin-orbitals, and convergence problems in the method of configurational interaction." In: *Physical Review* 97.6 (1955), pp. 1474–1489. ISSN: 0031899X. DOI: 10.1103/PhysRev.97.1474. URL: https://link.aps.org/doi/10.1103/PhysRev.97.1474.

[132] C. Casteleiro, F. Parente, P. Indelicato, and J. P. Marques. "Relativistic K shell decay rates and fluorescence yields for Zn , Cd and Hg." In: *The European Physical Journal D* 56.1 (2010), pp. 1–6. DOI: 10.1140/epjd/e2009-00259-5. URL: link.springer.com/10.1140/epjd/e2009-00259-5.

[133] N. Kup Aylikci, J. Sampaio, A. Kahoul, V. Aylikci, I. Karahan, M. Guerra, J. Santos, J. Marques, and E. Tiraşoğlu. "The investigation of K-shell fluorescence parameters of Zn-Fe alloys with different grain size and microstrain values." In: *X-Ray Spectrometry* 46.4 (2017), pp. 242–251. DOI: 10.1002/xrs.2763.

[134] M Ertugrul, Ö Sögüt, Ö Simsek, and E Büyükkasap. "Measurement of Kβ/Kα intensity ratios for elements in the range $22 < Z < 69$ at 59.5 keV." In: *Journal of Physics B: Atomic, Molecular and Optical Physics* 34.5 (2001), pp. 909–914. ISSN: 0953-4075. DOI: 10.1088/0953-4075/34/5/316. URL: http://stacks.iop.org/0953-4075/34/i=5/a=316?key=crossref.c28db1dfd3085e80bbb7d6e853c12b03.

[135] O. Sogut, E. Büyükkasap, and H. Erdoğan. "Chemical-effect variation of Kβ/Kα X-ray intensity ratios in 3d elements." In: *Radiation Physics and Chemistry* 64.5-6 (2002), pp. 343–348. ISSN: 0969-806X. DOI: 10.1016/S0969-806X(01)00644-2. URL: https://www.sciencedirect.com/science/article/abs/pii/S0969806X01006442.

[136] M. Ertugrul. "Measurement of K shell radiative transition probabilities and K, L2 and L3 shell/subshell fluorescence yields of some elements in the atomic number range $30 < Z < 40$." In: *Analytica Chimica Acta* 454.2 (2002), pp. 327–334. ISSN: 00032670. DOI: 10.1016/S0003-2670(01)01554-9. URL: https://www.sciencedirect.com/science/article/pii/S0003267001015549.

[137] E. Öz. "Determination of ratios of emission probabilities of Auger electrons and K–L-shell radiative vacancy transfer probabilities for 17 elements from Mn to Mo at 59.5 keV." In: *Journal of Quantitative Spectroscopy and Radiative Transfer* 97.1 (2006), pp. 41–50. ISSN: 0022-4073. DOI: 10.1016/J.JQSRT.2004.12.016. URL: https://www.sciencedirect.com/science/article/pii/S0022407305000415.

[138] I. Han, M. Şahin, L. Demir, and Y. Şahin. "Measurement of K X-ray fluorescence cross-sections, fluorescence yields and intensity ratios for some elements in the atomic range 22<Z<68." In: *Applied Radiation and Isotopes* 65.6 (2007), pp. 669–675. ISSN: 0969-8043. DOI: 10.1016/J.APRADISO.2007.01.009. URL: https://www.sciencedirect.com/science/article/pii/S0969804307000292.

[139] U. Cevik, S. Kaya, B. Ertugral, H. Baltas, and S. Karabıdak. "K-shell X-ray fluorescence cross-sections and intensity ratios for some pure metals at 59.5 and 123.6 keV." In: *Nuclear Instruments and Methods in Physics Research Section B: Beam Interactions with Materials and Atoms* 262.2 (2007), pp. 165–170. ISSN: 0168-583X. DOI: 10.1016/J.NIMB.2007.06.007. URL: https://www.sciencedirect.com/science/article/pii/S0168583X07011731.

[140] B. Ertuğral, G. Apaydın, U. Çevik, M. Ertuğrul, and A. Kobya. "Kβ/Kα X-ray intensity ratios for elements in the range 16Z92 excited by 5.9, 59.5 and 123.6 keV photons." In: *Radiation Physics and Chemistry* 76.1 (2007), pp. 15–22. ISSN: 0969-806X. DOI: 10.1016/J.RADPHYSCHEM.2006.04.003. URL: https://www.sciencedirect.com/science/article/abs/pii/S0969806X06001873.

[141] P. Yalçın. "Measurement of relative K X-ray intensity ratio following radioactive decay and photoionization." In: *Nuclear Instruments and Methods in Physics Research Section B: Beam Interactions with Materials and Atoms* 254.2 (2007), pp. 182–186. ISSN: 0168-583X. DOI: 10.1016/J.NIMB.2006.11.051. URL: https://www.sciencedirect.com/science/article/pii/S0168583X06011530.

[142] N. K. Aylikci, E. Tiraşoğlu, H. Karahan, V. Aylikci, E. Cengiz, and G. Apaydin. "Alloying effect on K shell X-ray fluorescence parameters and radiative Auger ratios of Co and Zn in ZnxCo1x alloys." In: *Chemical Physics Letters* 484.4-6 (2010), pp. 368–373. ISSN: 0009-2614. DOI: 10.1016/J.CPLETT.2009.11.036. URL: https://www.sciencedirect.com/science/article/abs/pii/S0009261409014754.

[143] N. Kup Aylikci, V. Aylikci, A. Kahoul, E. Tiraşoğlu, H. Karahan, and E. Cengiz. "Effect of pH treatment on K-shell x-ray intensity ratios and K-shell x-ray production cross sections in ZnCo alloys." In: *Physical Review A* 84.4 (2011), p. 042509. ISSN: 1050-2947. DOI: 10.1103/PhysRevA.84.042509. URL: https://link.aps.org/doi/10.1103/PhysRevA.84.042509.

[144] A Kahoul, V Aylikci, N. K. Aylikci, E Cengiz, and G Apaydın. "Updated database and new empirical values for K-shell fluorescence yields." In: *Radiation Physics and Chemistry* 81.7 (2012), pp. 713–727. ISSN: 0969-806X. DOI: 10.1016/j.radphyschem.2012.03.006. URL: http://dx.doi.org/10.1016/j.radphyschem.2012.03.006.

[145] U. Safronova, W. Johnson, and J. Albritton. "Auger rates for Ni-, Cu-, and Zn-like ions." In: *Atomic Data and Nuclear Data Tables* 77.2 (2001), pp. 215–275. ISSN: 0092640X. DOI: 10.1006/adnd.2000.0855. URL: http://linkinghub.elsevier.com/retrieve/pii/S0092640X00908556.

[146] J. Bellicard, A. Moussa, and S. Haynes. "Etude des electrons Auger-K emis par le zinc 65." In: *Nuclear Physics* 3.2 (1957), pp. 307–313. ISSN: 0029-5582. DOI: 10.1016/0029-5582(57)90117-7. URL: https://www.sciencedirect.com/science/article/pii/0029558257901177.

[147] M. S. Freedman, F. T. Porter, and F. Wagner. "Internal Conversion, Multipole Mixing, and Auger Spectrum in Zn 67 from Ga 67 Decay." In: *Physical Review* 151.3 (1966), pp. 886–898. ISSN: 0031-899X. DOI: 10.1103/PhysRev.151.886. URL: https://link.aps.org/doi/10.1103/PhysRev.151.886.

[148] Ö. Şimşek, O. Doğan, Ü. Turgut, and M. Ertuğrul. "Measurement of K shell fluorescence yields of some elements in the atomic range 22<Z<30 using photoionisation." In: *Radiation Physics and Chemistry* 58.3 (2000), pp. 207–211. ISSN: 0969-806X. DOI: 10.1016/S0969-806X(99)00382-5. URL: https://www.sciencedirect.com/science/article/pii/S0969806X99003825.

[149] R. Durak and Y. Özdemır. "Measurement of K-shell fluorescence cross-sections and yields of 14 elements in the atomic number range 25<Z<47 using photoionization." In: *Radiation Physics and Chemistry* 61.1 (2001), pp. 19–25. ISSN: 0969-806X. DOI: 10.1016/S0969-806X(00)00353-4. URL: https://www.sciencedirect.com/science/article/pii/S0969806X00003534.

[150] Ö. Şimşek, S. Yilmaz, D. Karagöz, and M. Ertugrul. "Measurement of K shell fluorescence cross sections and K shell fluorescence yields for the atomic region 22<Z<64 by 59.5 keV photons." In: *Journal of Radioanalytical and Nuclear Chemistry* 253.1 (2002), pp. 143–147. ISSN: 02365731. DOI: 10.1023/A:1015833021757. URL: http://link.springer.com/10.1023/A:1015833021757.

[151] S. Gudennavar, N. Badiger, S. Thontadarya, and B. Hanumaiah. "K-shell fluorescence parameters of medium-Z elements." In: *Radiation Physics and Chemistry* 68.5 (2003), pp. 721–726. ISSN: 0969-806X. DOI: 10.1016/S0969-806X(03)00387-6. URL: https://www.sciencedirect.com/science/article/pii/S0969806X03003876.

[152] T. Yashoda, S. Krishnaveni, and R. Gowda. "Measurement of K-shell fluorescence yields for the elements in the range 22 < Z < 52 excited by 14.4 and 122 keV photons." In: *Nuclear Instruments and Methods in Physics Research Section B: Beam Interactions with Materials and Atoms* 240.3 (2005), pp. 607–611. ISSN: 0168-583X. DOI: 10.1016/J.NIMB.2005.04.129. URL: https://www.sciencedirect.com/science/article/pii/S0168583X05008475.

[153] Ö. Sögüt. "Investigation of the K shell fluorescence yields of Cr, Mn, Fe, Co, Ni, Cu, Zn, Mo, Ag, Cd, Ba, La, Ce, and their compounds." In: *Chinese Journal of Physics* 48.2 (2010), pp. 212–221. ISSN: 05779073.

[154] W. Bambynek, B. Crasemann, R. W. Fink, H. U. Freund, H. Mark, C. D. Swift, R. E. Price, and P. V. Rao. "X-Ray Fluorescence Yields, Auger, and Coster-Kronig Transition Probabilities." In: *Reviews of Modern Physics* 44.4 (1972), pp. 716–813. ISSN: 00346861. DOI: 10.1103/RevModPhys.44.716.

[155] M. O. Krause. "Atomic radiative and radiationless yields for K and L shells." In: *Journal of Physical and Chemical Reference Data* 8.2 (1979), pp. 307–327. ISSN: 15297845. DOI: 10.1063/1.555594.

[156] W. Bambynek. "A New Evaluation of K -Shell Fluorescence Yields." In: *X-Ray and Inner-Shell Processes in Atoms, Molecules and Solids*. Leipzig, 1984, pp. 1–2.

[157] S. Daoudi, A. Kahoul, and M. Nekkab. "New K-shell fluorescence yields curve for elements with 3 < Z < 99." In: *Journal of the Korean Physical Society* 67.9 (2015), pp. 1537–1543. DOI: 10.3938/jkps.67.1537.

[158] B. Vekemans, K. Janssens, L. Vincze, F. Adams, and P. Van Espen. "Analysis of X-ray spectra by iterative least squares (AXIL): New developments." In: *X-Ray Spectrometry* 23.6 (1994), pp. 278–285. ISSN: 0049-8246. DOI: 10.1002/xrs.1300230609. URL: http://doi.wiley.com/10.1002/xrs.1300230609.

[159] P. van Espen, H. Nullens, and F. Adams. "A computer analysis of X-ray fluorescence spectra." In: *Nuclear Instruments and Methods* 142.1-2 (1977), pp. 243–250. ISSN: 0029-554X. DOI: 10.1016/0029-554X(77)90834-5. URL: https://www.sciencedirect.com/science/article/abs/pii/0029554X77908345.

[160] P. J. Sempau, J. M. Fern A Andez-Varea, E Acosta, and F Salvat. "Experimental benchmarks of the Monte Carlo code PENELOPE." In: *Nuclear Instruments and Methods in Physics Research Section B: Beam Interactions with Materials and Atoms* 207.2 (2003), pp. 107–123. DOI: 10.1016/S0168-583X(03)00453-1. URL: http://www.nea.fr.

[161] J. Sempau, E. Acosta, J. Baro, J. Fernández-Varea, and F. Salvat. "An algorithm for Monte Carlo simulation of coupled electron-photon transport." In: *Nuclear Instruments and Methods in Physics Research Section B: Beam Interactions with Materials and Atoms* 132.3 (1997), pp. 377–390. ISSN: 0168-583X. DOI: 10.1016/S0168-

583X(97)00414-X. URL: https://www.sciencedirect.com/science/article/pii/S0168583X9700414X.

[162] OECD Nuclear Energy Agency. *Penelope : a code system for Monte Carlo simulation of electron and photon transport*. Nuclear Energy Agency, 2001, p. 234. ISBN: 9264184759. URL: https://www.oecd-nea.org/tools/abstract/detail/nea-1525.

[163] V. O. Kostroun. "Atomic Radiation Transition Probabilities to the 1s State and Theoretical K-Shell Fluorescence Yields." In: *Physical Review A* 3.2 (1971), pp. 533–545. DOI: https://doi.org/10.1103/PhysRevA.3.533.

[164] S. Puri. "Relative intensities for Li (i=1–3) and Mi (i=1–5) subshell X-rays." In: *Atomic Data and Nuclear Data Tables* 93.5 (2007), pp. 730–741. ISSN: 0092640X. DOI: 10.1016/j.adt.2007.05.002.

[165] J. H. Hubbell, P. N. Trehan, N. Singh, B. Chand, D. Mehta, M. L. Garg, R. R. Garg, S. Singh, and S. Puri. "A Review, Bibliography, and Tabulation of K, L, and Higher Atomic Shell X-Ray Fluorescence Yields." In: *Journal of Physical and Chemical Reference Data* 23.2 (1994), pp. 339–364. ISSN: 15297845. DOI: 10.1063/1.555955.

[166] J. H. Hubbell. "Erratum: "A Review, Bibliography, and Tabulation of K, L, and Higher Atomic Shell X-Ray Fluorescence Yields" [J. Phys. Chem. Ref. Data 23, 339 (1994)]." In: *Journal of Physical and Chemical Reference Data* 33.2 (2004), p. 621. ISSN: 00472689. DOI: 10.1063/1.1756152. URL: http://scitation.aip.org/content/aip/journal/jpcrd/33/2/10.1063/1.1756152.

[167] W. Jitschin. "Progress in measurements of L-subshell fluorescence, Coster-Kronig and Auger yields." In: *AIP Conference Proceedings* 215 (1990), pp. 408–423. ISSN: 0094243X. DOI: 10.1063/1.39807. URL: http://scitation.aip.org/content/aip/proceeding/aipcp/10.1063/1.39807.

[168] J. H. Hubbell. *Bibliography and Current Status of K,L, and higher shells fluorescence yields for computations of photon energy-absorption coefficients*. Tech. rep. NIST, 1989.

[169] T. Schoonjans, A. Brunetti, B. Golosio, M. Sanchez Del Rio, V. A. Solé, C. Ferrero, and L. Vincze. "The xraylib library for X-ray-matter interactions. Recent developments." In: *Spectrochimica Acta - Part B Atomic Spectroscopy* 66.11-12 (2011), pp. 776–784. ISSN: 05848547. DOI: 10.1016/j.sab.2011.09.011. URL: http://dx.doi.org/10.1016/j.sab.2011.09.011.

[170] J. M. Sampaio, T. I. Madeira, M. Guerra, F. Parente, J. P. Santos, P. Indelicato, and J. P. Marques. "Dirac-Fock calculations of K-, L-, and M-shell fluorescence and Coster-Kronig yields for Ne, Ar, Kr, Xe, Rn, and Uuo." In: *Physical Review A* 91.5 (2015), p. 052507. ISSN: 1050-2947. DOI: 10.1103/PhysRevA.91.052507. URL: https://link.aps.org/doi/10.1103/PhysRevA.91.052507.

[171] J. M. Sampaio, T. I. Madeira, J. P. Marques, F. Parente, A. M. Costa, P. Indelicato, J. P. Santos, M. C. Lépy, and Y. Ménesguen. "Approaches for theoretical and experimental determinations of K -shell decay rates and fluorescence yields in Ge." In: *Physical Review A - Atomic, Molecular, and Optical Physics* 89.1 (2014), pp. 1–8. ISSN: 10941622. DOI: 10.1103/PhysRevA.89.012512.

[172] T. I. Madeira, J. M. Sampaio, M. Guerra, F. Parente, P. Indelicato, J. P. Santos, and J. P. Marques. "Relativistic calculation of K-, L- and M-shell x-ray fluorescence yields for Ba." In: *Physica Scripta* 90.5 (2015), p. 54009. ISSN: 14024896. DOI: 10.1088/0031-8949/90/5/054009. URL: http://dx.doi.org/10.1088/0031-8949/90/5/054009.

[173] M. Guerra, J. M. Sampaio, F. Parente, P. Indelicato, P. Hönicke, M. Müller, B. Beckhoff, J. P. Marques, and J. P. Santos. "Theoretical and experimental determination of K - And L -shell x-ray relaxation parameters in Ni." In: *Physical Review A* 97.4 (2018), pp. 1–10. ISSN: 24699934. DOI: 10.1103/PhysRevA.97.042501.

APPENDIX

A.1 MCDF transition probability calculations

Table A.1: Zn K-shell radiative transition probability values calculated using Multiconfiguration Dirac-Fock method. Calculations were performed with relaxed orbitals unless if "calculation notes" states that orbitals were frozen. Extra correlation state functions from the 1s orbital up to the 4p orbital were included in the calculations unless "calculation notes" presents a different orbital. In that case, the calculation was performed including extra correlation wavefunctions from the 1s orbital up to the orbital presented in "calculation notes". In the cases were no extra correlation state functions were included "calculation notes" states that no correlation was considered. Transition probabilities are presented in milliatomic units; 1 milliatomic unit = $4.134 \times 10^{-13} s^{-1}$.

Final configuration	State	Transition probability values (s^{-1})
1s2 2s1 2p6 3s2 3p6 3d10 4s2	$^2S_{1/2}$	1.022E+09
1s2 2s2 2p5 3s2 3p6 3d10 4s2	$^2P_{1/2}$	3.620E+14
1s2 2s2 2p5 3s2 3p6 3d10 4s2	$^2P_{3/2}$	7.058E+14
1s2 2s2 2p6 3s1 3p6 3d10 4s2	$^2S_{1/2}$	2.140E+08
1s2 2s2 2p6 3s2 3p5 3d10 4s2	$^2P_{1/2}$	4.899E+13
1s2 2s2 2p6 3s2 3p5 3d10 4s2	$^2P_{3/2}$	9.581E+13
1s2 2s2 2p6 3s2 3p6 3d9 4s2	$^2D_{3/2}$	6.188E+10
1s2 2s2 2p6 3s2 3p6 3d9 4s2	$^2D_{5/2}$	8.958E+10
1s2 2s2 3p6 3s2 3p6 3d10 4s1	$^2S_{1/2}$	1.394E+07

Table A.2: Zn K-shell radiationless transition probability values calculated using Multiconfiguration Dirac-Fock method. Calculations were performed with relaxed orbitals unless if "calculation notes" states that orbitals were frozen. Extra correlation state functions from the 1s orbital up to the 4p orbital were included in the calculations unless "calculation notes" presents a different orbital. In that case, the calculation was performed including extra correlation wavefunctions from the 1s orbital up to the orbital presented in "calculation notes". In the cases were no extra correlation state functions were included "calculation notes" states that no correlation was considered. Transition probability values are presented in milliatomic units; 1 milliatomic unit = $4.134 \times 10^{-13} s^{-1}$.

Final configuration	State	Transition probability (s^{-1})	calculation notes
1s2 2p6 3s2 3p6 3d10 4s2	$^1S_0$	5.796E+13	frozen orbitals
1s2 2s1 2p5 3s2 3p6 3d10 4s2	$^1P_1$	1.514E+14	
1s2 2s1 2p5 3s2 3p6 3d10 4s2	$^3P_0$	1.209E+13	
1s2 2s1 2p5 3s2 3p6 3d10 4s2	$^3P_1$	4.074E+13	
1s2 2s1 2p5 3s2 3p6 3d10 4s2	$^3P_2$	3.672E+13	
1s2 2s1 2p6 3s1 3p6 3d10 4s2	$^1S_0$	3.342E+13	
1s2 2s1 2p6 3s1 3p6 3d10 4s2	$^3S_1$	8.490E+10	
1s2 2s1 2p6 3s2 3p5 3d10 4s2	$^1P_1$	2.168E+13	frozen orbitals
1s2 2s1 2p6 3s2 3p5 3d10 4s2	$^3P_0$	8.607E+11	frozen orbitals
1s2 2s1 2p6 3s2 3p5 3d10 4s2	$^3P_1$	9.295E+12	frozen orbitals
1s2 2s1 2p6 3s2 3p5 3d10 4s2	$^3P_2$	4.694E+12	
1s2 2s1 2p6 3s2 3p6 3d9 4s2	$^1D_2$	9.452E+10	
1s2 2s1 2p6 3s2 3p6 3d9 4s2	$^3D_1$	1.576E+11	
1s2 2s1 2p6 3s2 3p6 3d9 4s2	$^3D_2$	2.172E+11	
1s2 2s1 2p6 3s2 3p6 3d9 4s2	$^3D_3$	4.855E+11	
1s2 2s1 2p6 3s2 3p6 3d10 4s1	$^1S_0$	1.265E+12	4s correlation
1s2 2s1 2p6 3s2 3p6 3d10 4s1	$^3S_1$	9.226E+09	
1s2 2s2 2p4 3s2 3p6 3d10 4s2	$^1S_0$	4.584E+13	
1s2 2s2 2p4 3s2 3p6 3d10 4s2	$^1D_2$	5.080E+14	
1s2 2s2 2p4 3s2 3p6 3d10 4s2	$^3P_0$	2.041E+13	
1s2 2s2 2p4 3s2 3p6 3d10 4s2	$^3P_1$	2.741E+11	
1s2 2s2 2p4 3s2 3p6 3d10 4s2	$^3P_2$	8.379E+13	
1s2 2s2 2p5 3s1 3p6 3d10 4s2	$^1P_1$	1.015E+13	
1s2 2s2 2p5 3s1 3p6 3d10 4s2	$^3P_0$	1.553E+12	
1s2 2s2 2p5 3s1 3p6 3d10 4s2	$^3P_1$	1.046E+13	
1s2 2s2 2p5 3s1 3p6 3d10 4s2	$^3P_2$	3.986E+12	
1s2 2s2 2p5 3s2 3p5 3d10 4s2	$^1S_0$	6.303E+12	no correlation
1s2 2s2 2p5 3s2 3p5 3d10 4s2	$^3P_0$	4.801E+12	no correlation
1s2 2s2 2p5 3s2 3p5 3d10 4s2	$^1P_1$	3.159E+10	

Table A.2 (continued)

1s2 2s2 2p5 3s2 3p5 3d10 4s2	$^3S_1$	1.734E+11	
1s2 2s2 2p5 3s2 3p5 3d10 4s2	$^3P_1$	3.000E+10	
1s2 2s2 2p5 3s2 3p5 3d10 4s2	$^3D_1$	5.036E+10	
1s2 2s2 2p5 3s2 3p5 3d10 4s2	$^1D_2$	6.226E+13	frozen orbitals
1s2 2s2 2p5 3s2 3p5 3d10 4s2	$^3P_2$	1.361E+11	
1s2 2s2 2p5 3s2 3p5 3d10 4s2	$^3D_2$	7.140E+13	frozen orbitals
1s2 2s2 2p5 3s2 3p6 3d9 4s2	$^3P_0$	2.328E+10	
1s2 2s2 2p5 3s2 3p6 3d9 4s2	$^1P_1$	4.503E+10	
1s2 2s2 2p5 3s2 3p6 3d9 4s2	$^3P_1$	4.630E+10	
1s2 2s2 2p5 3s2 3p6 3d9 4s2	$^3D_1$	3.602E+10	
1s2 2s2 2p5 3s2 3p6 3d9 4s2	$^1D_2$	2.262E+11	
1s2 2s2 2p5 3s2 3p6 3d9 4s2	$^3D_2$	1.325E+11	
1s2 2s2 2p5 3s2 3p6 3d9 4s2	$^3P_2$	6.855E+10	
1s2 2s2 2p5 3s2 3p6 3d9 4s2	$^3F_2$	9.154E+11	
1s2 2s2 2p5 3s2 3p6 3d9 4s2	$^3F_3$	8.005E+11	
1s2 2s2 2p5 3s2 3p6 3d9 4s2	$^1F_3$	4.683E+12	
1s2 2s2 2p5 3s2 3p6 3d9 4s2	$^3D_3$	7.987E+11	
1s2 2s2 2p5 3s2 3p6 3d10 4s1	$^3P_1$	6.097E+11	4s correlation
1s2 2s2 2p5 3s2 3p6 3d10 4s1	$^3P_2$	2.100E+11	4s correlation
1s2 2s2 2p6 3p6 3d10 4s2	$^1S_0$	1.643E+12	no correlation
1s2 2s2 2p6 3s1 3p5 3d10 4s2	$^1P_1$	3.139E+12	
1s2 2s2 2p6 3s1 3p5 3d10 4s2	$^3P_0$	1.014E+11	
1s2 2s2 2p6 3s1 3p5 3d10 4s2	$^3P_1$	2.208E+11	
1s2 2s2 2p6 3s1 3p5 3d10 4s2	$^3P_2$	1.931E+11	
1s2 2s2 2p6 3s1 3p6 3d9 4s2	$^3D_1$	2.950E+10	
1s2 2s2 2p6 3s1 3p6 3d9 4s2	$^1D_2$	8.374E+09	
1s2 2s2 2p6 3s1 3p6 3d9 4s2	$^3D_2$	4.356E+10	
1s2 2s2 2p6 3s1 3p6 3d9 4s2	$^3D_3$	5.647E+10	
1s2 2s2 2p6 3s1 3p6 3d10 4s1	$^1S_0$	5.598E+11	4s correlation
1s2 2s2 2p6 3s1 3p6 3d10 4s1	$^3S_1$	2.709E+07	4s correlation
1s2 2s2 2p6 3s2 3p4 3d10 4s2	$^1S_0$	9.639E+11	
1s2 2s2 2p6 3s2 3p4 3d10 4s2	$^3P_0$	9.523E+10	
1s2 2s2 2p6 3s2 3p4 3d10 4s2	$^3P_1$	5.749E+09	
1s2 2s2 2p6 3s2 3p4 3d10 4s2	$^3P_2$	1.452E+11	
1s2 2s2 2p6 3s2 3p4 3d10 4s2	$^1D_2$	6.965E+12	
1s2 2s2 2p6 3s2 3p5 3d9 4s2	$^3P_0$	2.249E+09	
1s2 2s2 2p6 3s2 3p5 3d9 4s2	$^1P_1$	3.857E+09	
1s2 2s2 2p6 3s2 3p5 3d9 4s2	$^3P_1$	5.676E+09	
1s2 2s2 2p6 3s2 3p5 3d9 4s2	$^3D_1$	6.186E+08	

Table A.2 (continued)

1s2 2s2 2p6 3s2 3p5 3d9 4s2	$^3P_2$	8.494E+09	
1s2 2s2 2p6 3s2 3p5 3d9 4s2	$^1D_2$	4.142E+10	
1s2 2s2 2p6 3s2 3p5 3d9 4s2	$^3D_2$	2.990E+09	
1s2 2s2 2p6 3s2 3p5 3d9 4s2	$^3F_2$	7.231E+10	
1s2 2s2 2p6 3s2 3p5 3d9 4s2	$^3D_3$	9.771E+09	
1s2 2s2 2p6 3s2 3p5 3d9 4s2	$^1F_3$	7.691E+11	
1s2 2s2 2p6 3s2 3p5 3d9 4s2	$^3F_3$	1.525E+11	
1s2 2s2 2p6 3s2 3p5 3d10 4s1	$^3P_0$	1.191E+10	4s correlation
1s2 2s2 2p6 3s2 3p5 3d10 4s1	$^1P_1$	1.224E+11	4s correlation
1s2 2s2 2p6 3s2 3p5 3d10 4s1	$^3P_1$	9.523E+10	4s correlation
1s2 2s2 2p6 3s2 3p5 3d10 4s1	$^3P_2$	3.087E+10	4s correlation
1s2 2s2 2p6 3s2 3p6 3d8 4s2	$^1S_0$	1.015E+08	
1s2 2s2 2p6 3s2 3p6 3d8 4s2	$^3P_0$	2.985E+05	
1s2 2s2 2p6 3s2 3p6 3d8 4s2	$^3P_1$	6.678E+05	
1s2 2s2 2p6 3s2 3p6 3d8 4s2	$^3P_2$	4.957E+07	
1s2 2s2 2p6 3s2 3p6 3d8 4s2	$^1D_2$	2.743E+08	
1s2 2s2 2p6 3s2 3p6 3d8 4s2	$^3F_2$	1.553E+06	
1s2 2s2 2p6 3s2 3p6 3d8 4s2	$^3F_3$	9.110E+06	
1s2 2s2 2p6 3s2 3p6 3d8 4s2	$^3F_4$	3.789E+07	
1s2 2s2 2p6 3s2 3p6 3d8 4s2	$^1G_4$	3.351E+10	
1s2 2s2 2p6 3s2 3p6 3d9 4s1	$^3D_1$	2.484E+09	4s correlation
1s2 2s2 2p6 3s2 3p6 3d9 4s1	$^1D_2$	6.574E+08	4s correlation
1s2 2s2 2p6 3s2 3p6 3d9 4s1	$^3D_2$	3.465E+09	4s correlation
1s2 2s2 2p6 3s2 3p6 3d9 4s1	$^3D_3$	4.929E+09	4s correlation
1s2 2s2 2p6 3s2 3p6 3d10	$^1S_0$	8.502E+09	

APPENDIX B

Appendix

B.1 Fluorescence yield and partial fluorescence yield values

Table B.1: Definitions and symbols of atomic quantities of present work and different references.

Present work	"Transition Probability" A	"Total radiative transition probability" $A^{(\mathrm{TR})}$	"Total radiative width" $\Gamma^{(\mathrm{R})}$	"Total radiationless transition probability" $A^{(\mathrm{TA})}$
Kostroun et al. [163]	"transition probability", "transition rate" w	-	"radiative width" Γ_{R}	-
Scofield [105–107]	"transition rate", "decay rate", "emission rate" Γ	"total radiative decay rate"	-	-
Chen *et al.* [95, 97]	"transition rate" T	-	"radiative width"	-
EADL [99]	"transition rate"	-	"radiative width" Γ_{r}	-
Xraylib [169]	"emission rate"	-	-	-
Pia *et al.* [35–37]	"emission rate"	-	-	-
Bambinek *et al.* [40]	"transition probability", "transition probability per unit time", "rate of emission", "decay probability" w	"total radiative transition probability", "total radiative decay rate", "radiative decay probability"	"radiative width" Γ_{A}	"Auger decay probability" + "Coster-Kronig decay probability"
Salem *et al.* [108]	"transition rate"	-	-	-
Hubbell *et al.* [165]	"transition rate"	-	-	-

Table B.2: Continuation of Table I.

Present work	"Total radiationless width" $\Gamma^{(A)}$	"Total transition probability" $A^{(T)}$	"Total state width" $\Gamma^{(T)}$
Kostroun *et al.* [163]	"total radiationless width", "total Auger width", "Auger width" Γ_A	"total transition probability"	"total level width" Γ
Scofield [105–107]	-	"total decay rate"	-
Chen *et al.* [95, 97]	"Auger width" Γ_A	-	"total atomic width" Γ
EADL library [99]	"nonradiative width" Γ_{nr}	-	"total width" Γ_t
Xraylib [169]	-	-	"atomic level width"
Pia *et al.* [35–37]	-	-	-
Bambinek *et al.* [40]	"radiatiationless width", "total Auger width + total Coster-Kronig width" $\Gamma_A + \Gamma_{CK}{}^*$	"decay probability of a state"	"total width", "atomic state energy width" Γ

Table B.3: Continuation of Table II.

Present work	"fluorescence yield" ω	"partial fluorescence yield (normalized without accounting radiationless transitions)" $\omega^{(NA)}$	partial fluorescence yield ω
Kostroun *et al.* [163]	"fluorescence yield" ω	-	-
Scofield [105–107]	"fluorescence yield" ω	-	-
Chen *et al.* [95, 97]	"fluorescence yield" ω	-	-
EADL [99]	"fluorescence yield" ω	-	transition probability
Xraylib [169]	"fluorescence yield" ω	"radiative transition probability"	-
Pia *et al.* [35–37]	-	"radiative transition probability"	-
Bambinek *et al.* [40]	"fluorescence yield" ω	-	-
Hubbell *et al.* [165]	"fluorescence yield" ω	-	-
NIST database [38]	"fluorescence yield"	"relative intensity"	-
Kahoul *et al.* [144]	"fluorescence yield" ω	"transition probability"	-
Daoudi *et al.* [157]	"fluorescence yield" ω	-	-

Table B.4: Theoretical K-shell fluorescence yield values.

Z	Kostroun	DF,DF	DF	EADL	MCDF
10	2.04E-02				1.59E-02 [170]
12	2.72E-02				
14	4.41E-02				
16	7.27E-02				
18	1.11E-01	1.11E-01	1.22E-01		1.17E-01 [170]
20	1.55E-01	1.57E-01	1.69E-01		
22	2.12E-01	2.12E-01	2.26E-01	2.14E-01	
24	2.76E-01	2.74E-01	2.89E-01		
26	3.44E-01	3.41E-01	3.57E-01	3.36E-01	3.78E-01 [133]
28	4.14E-01	4.09E-01	4.24E-01	4.01E-01	4.15E-01 [173]
30	4.82E-01	4.74E-01	4.88E-01	4.66E-01	4.85E-01 [133]
32	5.45E-01	5.34E-01	5.48E-01		5.47E-01 [171]
34	6.02E-01	5.90E-01	6.02E-01		
36	6.55E-01	6.40E-01	6.51E-01		6.49E-01 [170]
38	7.02E-01	6.85E-01	6.94E-01		
40	7.41E-01	7.24E-01	7.32E-01	7.27E-01	
42	7.76E-01	7.58E-01	7.65E-01	7.63E-01	
44	8.07E-01	7.88E-01	7.94E-01		
46	8.33E-01	8.14E-01	8.19E-01		
48	8.55E-01	8.35E-01	8.40E-01		
50	8.74E-01	8.54E-01	8.58E-01	8.63E-01	
52	8.90E-01	8.70E-01	8.74E-01		
54		8.84E-01	8.87E-01		8.90E-01 [170]
56		8.96E-01	8.99E-01		9.02E-01 [172]
58		9.06E-01	9.09E-01		
60		9.16E-01	9.18E-01	9.22E-01	
62		9.23E-01	9.25E-01		
64		9.30E-01	9.32E-01		
66		9.36E-01	9.37E-01		
68		9.41E-01	9.43E-01		
70		9.46E-01	9.47E-01	9.48E-01	
72		9.50E-01	9.51E-01		
74		9.53E-01	9.54E-01		
76		9.56E-01	9.57E-01		
78		9.59E-01	9.59E-01		
80		9.61E-01	9.62E-01	9.60E-01	
82		9.63E-01	9.64E-01	9.61E-01	
84		9.65E-01	9.65E-01		
86		9.66E-01	9.67E-01		9.70E-01 [170]
88		9.67E-01	9.68E-01		
90		9.69E-01	9.69E-01		
92		9.69E-01	9.70E-01		
94		9.70E-01	9.71E-01		
96		9.71E-01	9.71E-01		

Table B.5: Theoretical K-L_2 fluorescence yield values.

Z	DF,DS	DF	EADL
18	3.44E-02	3.69E-02	
20	4.76E-02	5.03E-02	
22	6.40E-02	6.69E-02	6.46E-02
24	8.28E-02	8.59E-02	
26	1.03E-01	1.06E-01	1.01E-01
28	1.23E-01	1.26E-01	1.21E-01
30	1.43E-01	1.45E-01	1.41E-01
32	1.61E-01	1.62E-01	
34	1.76E-01	1.76E-01	
36	1.89E-01	1.89E-01	
38	2.01E-01	2.01E-01	
40	2.12E-01	2.11E-01	2.12E-01
42	2.21E-01	2.20E-01	2.21E-01
44	2.29E-01	2.28E-01	
46	2.36E-01	2.34E-01	
48	2.42E-01	2.40E-01	
50	2.47E-01	2.44E-01	2.48E-01
52	2.51E-01	2.48E-01	
54	2.54E-01	2.51E-01	
56	2.57E-01	2.54E-01	
58	2.60E-01	2.57E-01	
60	2.63E-01	2.60E-01	2.64E-01
62	2.65E-01	2.63E-01	
64	2.67E-01	2.65E-01	
66	2.70E-01	2.67E-01	
68	2.72E-01	2.69E-01	
70	2.74E-01	2.71E-01	2.73E-01
72	2.75E-01	2.73E-01	
74	2.77E-01	2.74E-01	
76	2.79E-01	2.76E-01	
78	2.80E-01	2.78E-01	
80	2.81E-01	2.79E-01	2.81E-01
82	2.83E-01	2.80E-01	2.82E-01
84	2.84E-01	2.82E-01	
86	2.85E-01	2.83E-01	
88	2.87E-01	2.84E-01	
90	2.88E-01	2.86E-01	
92	2.90E-01	2.87E-01	
94	2.91E-01	2.89E-01	
96	2.93E-01	2.91E-01	

Table B.6: Theoretical K-L_3 fluorescence yield values.

Z	DF,DS	DF	EADL
18	6.79E-02	7.30E-02	
20	9.39E-02	9.94E-02	
22	1.26E-01	1.32E-01	1.27E-01
24	1.63E-01	1.69E-01	
26	2.02E-01	2.07E-01	1.99E-01
28	2.41E-01	2.46E-01	2.36E-01
30	2.78E-01	2.82E-01	2.74E-01
32	3.11E-01	3.14E-01	
34	3.40E-01	3.42E-01	
36	3.65E-01	3.65E-01	
38	3.86E-01	3.86E-01	
40	4.05E-01	4.04E-01	4.05E-01
42	4.21E-01	4.19E-01	4.22E-01
44	4.34E-01	4.32E-01	
46	4.46E-01	4.42E-01	
48	4.54E-01	4.51E-01	
50	4.61E-01	4.57E-01	4.64E-01
52	4.66E-01	4.62E-01	
54	4.70E-01	4.66E-01	
56	4.73E-01	4.69E-01	
58	4.76E-01	4.71E-01	
60	4.78E-01	4.74E-01	4.81E-01
62	4.80E-01	4.76E-01	
64	4.81E-01	4.76E-01	
66	4.82E-01	4.78E-01	
68	4.83E-01	4.78E-01	
70	4.83E-01	4.78E-01	4.82E-01
72	4.81E-01	4.78E-01	
74	4.81E-01	4.77E-01	
76	4.80E-01	4.76E-01	
78	4.79E-01	4.74E-01	
80	4.77E-01	4.73E-01	4.76E-01
82	4.75E-01	4.71E-01	4.74E-01
84	4.73E-01	4.69E-01	
86	4.71E-01	4.67E-01	
88	4.68E-01	4.65E-01	
90	4.66E-01	4.62E-01	
92	4.63E-01	4.60E-01	
94	4.61E-01	4.58E-01	
96	4.58E-01	4.55E-01	

Table B.7: Theoretical K-M_2 fluorescence yield values.

Z	DF,DS	DF	EADL
18	2.81E-03	4.01E-03	
20	5.06E-03	6.61E-03	
22	7.26E-03	9.04E-03	7.33E-03
24	9.52E-03	1.14E-02	
26	1.24E-02	1.47E-02	1.22E-02
28	1.51E-02	1.76E-02	1.48E-02
30	1.77E-02	2.03E-02	1.74E-02
32	2.07E-02	2.36E-02	
34	2.38E-02	2.69E-02	
36	2.66E-02	2.94E-02	
38	2.94E-02	3.21E-02	
40	3.19E-02	3.46E-02	3.20E-02
42	3.43E-02	3.70E-02	3.44E-02
44	3.64E-02	3.91E-02	
46	3.84E-02	4.10E-02	
48	4.01E-02	4.27E-02	
50	4.17E-02	4.41E-02	4.19E-02
52	4.30E-02	4.53E-02	
54	4.42E-02	4.64E-02	
56	4.52E-02	4.74E-02	
58	4.63E-02	4.84E-02	
60	4.73E-02	4.93E-02	4.75E-02
62	4.81E-02	5.01E-02	
64	4.89E-02	5.08E-02	
66	4.96E-02	5.15E-02	
68	5.03E-02	5.21E-02	
70	5.08E-02	5.26E-02	5.08E-02
72	5.13E-02	5.30E-02	
74	5.17E-02	5.34E-02	
76	5.21E-02	5.37E-02	
78	5.25E-02	5.40E-02	
80	5.27E-02	5.42E-02	5.26E-02
82	5.29E-02	5.44E-02	5.28E-02
84	5.31E-02	5.45E-02	
86	5.32E-02	5.46E-02	
88	5.33E-02	5.47E-02	
90	5.34E-02	5.48E-02	
92	5.34E-02	5.48E-02	
94	5.34E-02	5.48E-02	
96	5.34E-02	5.48E-02	

Table B.8: Theoretical K-M_3 fluorescence yield values.

Z	DF,DS	DF	EADL
18	5.56E-03	7.95E-03	
20	1.00E-02	1.31E-02	
22	1.43E-02	1.79E-02	1.45E-02
24	1.88E-02	2.26E-02	
26	2.44E-02	2.89E-02	2.40E-02
28	2.96E-02	3.45E-02	2.90E-02
30	3.46E-02	3.98E-02	3.40E-02
32	4.05E-02	4.63E-02	
34	4.64E-02	5.26E-02	
36	5.20E-02	5.74E-02	
38	5.73E-02	6.27E-02	
40	6.22E-02	6.76E-02	6.23E-02
42	6.67E-02	7.22E-02	6.69E-02
44	7.09E-02	7.63E-02	
46	7.46E-02	7.99E-02	
48	7.79E-02	8.30E-02	
50	8.08E-02	8.57E-02	8.13E-02
52	8.34E-02	8.80E-02	
54	8.56E-02	9.00E-02	
56	8.77E-02	9.18E-02	
58	8.96E-02	9.36E-02	
60	9.14E-02	9.54E-02	9.19E-02
62	9.31E-02	9.70E-02	
64	9.45E-02	9.82E-02	
66	9.59E-02	9.96E-02	
68	9.72E-02	1.01E-01	
70	9.82E-02	1.02E-01	9.81E-02
72	9.90E-02	1.02E-01	
74	9.99E-02	1.03E-01	
76	1.01E-01	1.04E-01	
78	1.01E-01	1.04E-01	
80	1.02E-01	1.05E-01	1.02E-01
82	1.03E-01	1.05E-01	1.02E-01
84	1.03E-01	1.06E-01	
86	1.03E-01	1.06E-01	
88	1.04E-01	1.06E-01	
90	1.04E-01	1.07E-01	
92	1.04E-01	1.07E-01	
94	1.05E-01	1.07E-01	
96	1.05E-01	1.08E-01	

Table B.9: Semi-empirical and empirical K-shell fluorescence yield values

Z	Bambynek 1972	Krause 1979	Bambynek 1984	NIST	Kahoul 2012	Daoudi 2015	Min	Max	$\Delta\omega_K$
4	4.51E-04		6.93E-04	3.30E-05		3.60E-04	3.30E-05	6.93E-04	1.82E+02
6	1.98E-03	2.80E-03	2.58E-03	1.40E-03		1.45E-03	1.40E-03	2.80E-03	6.67E+01
8	5.79E-03	8.30E-03	6.91E-03	5.80E-03		4.40E-03	4.40E-03	8.30E-03	6.14E+01
10	1.34E-02	1.80E-02	1.52E-02	1.60E-02		1.09E-02	1.09E-02	2.04E-02	6.09E+01
12	2.65E-02	3.00E-02	2.91E-02	2.60E-02	2.33E-02	2.31E-02	2.31E-02	3.01E-02	2.63E+01
14	4.69E-02	5.00E-02	5.04E-02	4.30E-02	4.32E-02	4.34E-02	4.30E-02	5.14E-02	1.78E+01
16	7.60E-02	7.80E-02	8.04E-02	7.10E-02	7.97E-02	7.34E-02	7.10E-02	8.18E-02	1.41E+01
18	1.15E-01	1.18E-01	1.20E-01	1.09E-01	1.25E-01	1.14E-01	1.09E-01	1.25E-01	1.35E+01
20	1.63E-01	1.63E-01	1.69E-01	1.47E-01	1.54E-01	1.62E-01	1.47E-01	1.71E-01	1.51E+01
22	2.19E-01	2.14E-01	2.26E-01	2.18E-01	2.09E-01	2.15E-01	2.09E-01	2.27E-01	8.44E+00
24	2.81E-01	2.75E-01	2.89E-01	2.86E-01	2.71E-01	2.78E-01	2.71E-01	2.94E-01	8.18E+00
26	3.47E-01	3.40E-01	3.55E-01	3.51E-01	3.35E-01	3.43E-01	3.35E-01	3.62E-01	7.74E+00
28	4.14E-01	4.06E-01	4.21E-01	4.12E-01	4.00E-01	4.09E-01	4.00E-01	4.33E-01	7.85E+00
30	4.79E-01	4.74E-01	4.86E-01	4.69E-01	4.63E-01	4.73E-01	4.63E-01	5.01E-01	7.94E+00
32	5.40E-01	5.35E-01	5.46E-01	5.23E-01	5.23E-01	5.34E-01	5.23E-01	5.65E-01	7.78E+00
34	5.96E-01	5.89E-01	6.02E-01	5.74E-01	5.78E-01	5.90E-01	5.74E-01	6.23E-01	8.19E+00
36	6.46E-01	6.43E-01	6.52E-01	6.21E-01	6.29E-01	6.41E-01	6.21E-01	6.75E-01	8.39E+00
38	6.91E-01	6.90E-01	6.96E-01	6.65E-01	6.75E-01	6.87E-01	6.65E-01	7.21E-01	8.09E+00
40	7.30E-01	7.30E-01	7.34E-01	7.05E-01	7.16E-01	7.27E-01	7.05E-01	7.61E-01	7.65E+00
42	7.64E-01	7.65E-01	7.67E-01	7.42E-01	7.52E-01	7.63E-01	7.42E-01	7.95E-01	6.91E+00
44	7.93E-01	7.94E-01	7.96E-01	7.76E-01	7.84E-01	7.95E-01	7.76E-01	8.24E-01	5.89E+00
46	8.18E-01	8.20E-01	8.20E-01	8.07E-01	8.13E-01	8.22E-01	8.07E-01	8.49E-01	5.08E+00
48	8.40E-01	8.43E-01	8.42E-01	8.36E-01	8.38E-01	8.46E-01	8.35E-01	8.71E-01	4.14E+00
50	8.59E-01	8.62E-01	8.60E-01	8.61E-01	8.60E-01	8.67E-01	8.54E-01	8.89E-01	3.99E+00
52	8.75E-01	8.77E-01	8.75E-01	8.83E-01	8.84E-01	8.65E-01	8.65E-01	9.05E-01	4.44E+00
54	8.88E-01	8.91E-01	8.88E-01	9.03E-01	8.93E-01	8.94E-01	8.84E-01	9.03E-01	2.12E+00
56	9.00E-01	9.02E-01	9.00E-01	9.20E-01	9.01E-01	9.13E-01	8.96E-01	9.20E-01	2.65E+00
58	9.11E-01	9.12E-01	9.10E-01	9.35E-01	9.09E-01	9.26E-01	9.06E-01	9.35E-01	3.09E+00
60	9.20E-01	9.21E-01	9.18E-01	9.47E-01	9.15E-01	9.35E-01	9.15E-01	9.47E-01	3.43E+00
62	9.27E-01	9.29E-01	9.26E-01	9.58E-01	9.22E-01	9.41E-01	9.22E-01	9.58E-01	3.85E+00
64	9.34E-01	9.35E-01	9.32E-01	9.66E-01	9.27E-01	9.46E-01	9.27E-01	9.66E-01	4.12E+00
66	9.40E-01	9.41E-01	9.38E-01	9.72E-01	9.32E-01	9.50E-01	9.32E-01	9.72E-01	4.19E+00
68	9.45E-01	9.47E-01	9.43E-01	9.77E-01	9.37E-01	9.52E-01	9.37E-01	9.77E-01	4.24E+00
70	9.50E-01	9.51E-01	9.47E-01	9.80E-01	9.41E-01	9.54E-01	9.41E-01	9.80E-01	4.12E+00
72	9.54E-01	9.55E-01	9.51E-01	9.82E-01	9.45E-01	9.55E-01	9.45E-01	9.82E-01	3.90E+00
74	9.57E-01	9.58E-01	9.54E-01	9.83E-01	9.48E-01	9.56E-01	9.48E-01	9.83E-01	3.59E+00
76	9.60E-01	9.61E-01	9.57E-01	9.83E-01	9.52E-01	9.57E-01	9.52E-01	9.83E-01	3.23E+00
78	9.63E-01	9.63E-01	9.59E-01	9.82E-01	9.55E-01	9.57E-01	9.55E-01	9.82E-01	2.80E+00
80	9.66E-01	9.65E-01	9.62E-01	9.80E-01	9.57E-01	9.58E-01	9.57E-01	9.80E-01	2.35E+00
82	9.68E-01	9.67E-01	9.63E-01	9.78E-01	9.60E-01	9.58E-01	9.58E-01	9.78E-01	1.99E+00
84	9.70E-01	9.68E-01	9.65E-01	9.76E-01	9.62E-01	9.59E-01	9.59E-01	9.76E-01	1.68E+00
86	9.72E-01	9.69E-01	9.67E-01	9.73E-01	9.64E-01	9.60E-01	9.60E-01	9.73E-01	1.36E+00
88	9.73E-01	9.70E-01	9.68E-01	9.71E-01	9.66E-01	9.61E-01	9.61E-01	9.73E-01	1.20E+00
90	9.75E-01	9.71E-01	9.69E-01	9.70E-01	9.68E-01	9.63E-01	9.63E-01	9.75E-01	1.24E+00
92	9.76E-01	9.72E-01	9.70E-01	9.69E-01	9.70E-01	9.65E-01	9.65E-01	9.76E-01	1.14E+00
94		9.73E-01	9.71E-01	9.69E-01	9.71E-01	9.67E-01	9.67E-01	9.73E-01	5.93E-01
96		9.74E-01	9.72E-01	9.71E-01	9.73E-01	9.70E-01	9.70E-01	9.74E-01	4.27E-01
98		9.75E-01	9.72E-01	9.74E-01	9.74E-01	9.73E-01	9.72E-01	9.75E-01	2.88E-01

Table B.10: Semi-empirical and empirical K-L_2 fluorescence yield values

Z	Bambynek 1972 ,Salem	Krause 1979 ,Salem	Bambynek 1984 ,Salem	NIST ,Salem	Kahoul 2012 ,Salem	Daoudi 2015 ,Salem	Min	Max	$\Delta\omega_{K\text{-}L_2}$
4	1.51E-04	0.00E+00	2.32E-04	1.10E-05		1.20E-04	1.10E-05	2.32E-04	1.82E+02
6	6.62E-04	9.36E-04	8.61E-04	4.68E-04		4.85E-04	4.68E-04	9.36E-04	6.67E+01
8	1.93E-03	2.77E-03	2.31E-03	1.94E-03		1.47E-03	1.47E-03	2.77E-03	6.14E+01
10	4.48E-03	6.02E-03	5.08E-03	5.35E-03		3.64E-03	3.64E-03	6.02E-03	4.93E+01
12	7.88E-03	8.92E-03	8.65E-03	7.73E-03	6.93E-03	6.87E-03	6.87E-03	8.92E-03	2.60E+01
14	1.39E-02	1.48E-02	1.49E-02	1.28E-02	1.28E-02	1.29E-02	1.28E-02	1.49E-02	1.58E+01
16	2.25E-02	2.31E-02	2.38E-02	2.10E-02	2.36E-02	2.17E-02	2.10E-02	2.38E-02	1.24E+01
18	3.39E-02	3.48E-02	3.54E-02	3.22E-02	3.68E-02	3.35E-02	3.22E-02	3.69E-02	1.36E+01
20	4.80E-02	4.80E-02	4.97E-02	4.32E-02	4.52E-02	4.77E-02	4.32E-02	5.03E-02	1.52E+01
22	6.43E-02	6.29E-02	6.63E-02	6.41E-02	6.14E-02	6.31E-02	6.14E-02	6.69E-02	8.60E+00
24	8.26E-02	8.08E-02	8.48E-02	8.41E-02	7.96E-02	8.16E-02	7.96E-02	8.59E-02	7.59E+00
26	1.02E-01	1.00E-01	1.04E-01	1.03E-01	9.86E-02	1.01E-01	9.86E-02	1.06E-01	7.01E+00
28	1.22E-01	1.20E-01	1.24E-01	1.21E-01	1.18E-01	1.20E-01	1.18E-01	1.26E-01	6.67E+00
30	1.41E-01	1.40E-01	1.43E-01	1.38E-01	1.36E-01	1.39E-01	1.36E-01	1.45E-01	6.21E+00
32	1.59E-01	1.58E-01	1.61E-01	1.54E-01	1.54E-01	1.57E-01	1.54E-01	1.62E-01	5.02E+00
34	1.75E-01	1.73E-01	1.77E-01	1.68E-01	1.70E-01	1.73E-01	1.68E-01	1.77E-01	4.75E+00
36	1.88E-01	1.88E-01	1.90E-01	1.81E-01	1.83E-01	1.87E-01	1.81E-01	1.90E-01	4.82E+00
38	2.01E-01	2.01E-01	2.02E-01	1.93E-01	1.96E-01	2.00E-01	1.93E-01	2.02E-01	4.50E+00
40	2.11E-01	2.11E-01	2.13E-01	2.04E-01	2.07E-01	2.11E-01	2.04E-01	2.13E-01	4.03E+00
42	2.21E-01	2.21E-01	2.22E-01	2.14E-01	2.17E-01	2.20E-01	2.14E-01	2.22E-01	3.34E+00
44	2.29E-01	2.29E-01	2.30E-01	2.24E-01	2.26E-01	2.29E-01	2.24E-01	2.30E-01	2.46E+00
46	2.36E-01	2.36E-01	2.37E-01	2.33E-01	2.34E-01	2.37E-01	2.33E-01	2.37E-01	1.85E+00
48	2.42E-01	2.43E-01	2.42E-01	2.41E-01	2.41E-01	2.44E-01	2.40E-01	2.44E-01	1.62E+00
50	2.47E-01	2.48E-01	2.47E-01	2.48E-01	2.48E-01	2.50E-01	2.44E-01	2.50E-01	2.12E+00
52	2.52E-01	2.52E-01	2.52E-01	2.54E-01	2.55E-01	2.49E-01	2.48E-01	2.55E-01	2.54E+00
54	2.55E-01	2.56E-01	2.55E-01	2.59E-01	2.57E-01	2.57E-01	2.51E-01	2.59E-01	3.11E+00
56	2.58E-01	2.59E-01	2.58E-01	2.64E-01	2.59E-01	2.62E-01	2.54E-01	2.64E-01	3.69E+00
58	2.61E-01	2.61E-01	2.61E-01	2.68E-01	2.60E-01	2.65E-01	2.57E-01	2.68E-01	4.03E+00
60	2.63E-01	2.64E-01	2.63E-01	2.71E-01	2.62E-01	2.68E-01	2.60E-01	2.71E-01	4.16E+00
62	2.66E-01	2.66E-01	2.65E-01	2.74E-01	2.64E-01	2.70E-01	2.63E-01	2.74E-01	4.29E+00
64	2.68E-01	2.68E-01	2.67E-01	2.77E-01	2.66E-01	2.71E-01	2.65E-01	2.77E-01	4.41E+00
66	2.69E-01	2.70E-01	2.69E-01	2.78E-01	2.67E-01	2.72E-01	2.67E-01	2.78E-01	4.19E+00
68	2.71E-01	2.72E-01	2.71E-01	2.81E-01	2.69E-01	2.73E-01	2.69E-01	2.81E-01	4.24E+00
70	2.73E-01	2.73E-01	2.72E-01	2.81E-01	2.70E-01	2.74E-01	2.70E-01	2.81E-01	4.12E+00
72	2.75E-01	2.75E-01	2.74E-01	2.83E-01	2.72E-01	2.75E-01	2.72E-01	2.83E-01	3.90E+00
74	2.76E-01	2.76E-01	2.75E-01	2.83E-01	2.73E-01	2.76E-01	2.73E-01	2.83E-01	3.59E+00
76	2.77E-01	2.77E-01	2.76E-01	2.83E-01	2.74E-01	2.76E-01	2.74E-01	2.83E-01	3.23E+00
78	2.78E-01	2.78E-01	2.77E-01	2.83E-01	2.75E-01	2.76E-01	2.75E-01	2.83E-01	2.80E+00
80	2.79E-01	2.79E-01	2.78E-01	2.83E-01	2.77E-01	2.77E-01	2.77E-01	2.83E-01	2.35E+00
82	2.80E-01	2.80E-01	2.79E-01	2.83E-01	2.78E-01	2.78E-01	2.78E-01	2.83E-01	1.99E+00
84	2.81E-01	2.81E-01	2.80E-01	2.83E-01	2.79E-01	2.78E-01	2.78E-01	2.84E-01	2.14E+00
86	2.83E-01	2.82E-01	2.81E-01	2.83E-01	2.81E-01	2.79E-01	2.79E-01	2.85E-01	2.12E+00
88	2.84E-01	2.83E-01	2.83E-01	2.84E-01	2.82E-01	2.81E-01	2.81E-01	2.87E-01	2.08E+00
90	2.86E-01	2.85E-01	2.84E-01	2.84E-01	2.84E-01	2.82E-01	2.82E-01	2.88E-01	1.95E+00
92	2.87E-01	2.86E-01	2.86E-01	2.85E-01	2.86E-01	2.84E-01	2.84E-01	2.90E-01	1.88E+00
94		2.88E-01	2.87E-01	2.87E-01	2.87E-01	2.86E-01	2.86E-01	2.91E-01	1.70E+00
96		2.89E-01	2.89E-01	2.88E-01	2.89E-01	2.88E-01	2.88E-01	2.93E-01	1.62E+00
98		2.90E-01	2.89E-01	2.89E-01	2.89E-01	2.89E-01	2.89E-01	2.90E-01	2.88E-01

Table B.11: Semi-empirical and empirical K-L_3 fluorescence yield values

Z	Bambynek 1972 ,Salem	Krause 1979 ,Salem	Bambynek 1984 ,Salem	NIST ,Salem	Kahoul 2012 ,Salem	Daoudi 2015 ,Salem	Min	Max	$\Delta\omega_{\text{K-L}_3}$
4	3.00E-04	0.00E+00	4.61E-04	2.20E-05	0.00E+00	2.40E-04	2.20E-05	4.61E-04	1.82E+02
6	1.32E-03	1.86E-03	1.71E-03	9.32E-04		9.65E-04	9.32E-04	1.86E-03	6.67E+01
8	3.85E-03	5.53E-03	4.60E-03	3.86E-03		2.93E-03	2.93E-03	5.53E-03	6.14E+01
10	8.92E-03	1.20E-02	1.01E-02	1.07E-02		7.24E-03	7.24E-03	1.20E-02	4.93E+01
12	1.57E-02	1.78E-02	1.72E-02	1.54E-02	1.38E-02	1.37E-02	1.37E-02	1.78E-02	2.60E+01
14	2.77E-02	2.95E-02	2.98E-02	2.54E-02	2.55E-02	2.56E-02	2.54E-02	2.98E-02	1.58E+01
16	4.48E-02	4.60E-02	4.74E-02	4.18E-02	4.70E-02	4.33E-02	4.18E-02	4.74E-02	1.24E+01
18	6.76E-02	6.94E-02	7.05E-02	6.41E-02	7.33E-02	6.67E-02	6.41E-02	7.33E-02	1.35E+01
20	9.56E-02	9.56E-02	9.89E-02	8.61E-02	9.01E-02	9.51E-02	8.61E-02	9.94E-02	1.44E+01
22	1.28E-01	1.25E-01	1.32E-01	1.27E-01	1.22E-01	1.26E-01	1.22E-01	1.32E-01	7.69E+00
24	1.64E-01	1.60E-01	1.68E-01	1.67E-01	1.58E-01	1.62E-01	1.58E-01	1.69E-01	6.73E+00
26	2.01E-01	1.97E-01	2.06E-01	2.04E-01	1.95E-01	1.99E-01	1.95E-01	2.07E-01	6.26E+00
28	2.39E-01	2.35E-01	2.43E-01	2.38E-01	2.31E-01	2.37E-01	2.31E-01	2.46E-01	6.06E+00
30	2.76E-01	2.73E-01	2.80E-01	2.70E-01	2.67E-01	2.73E-01	2.67E-01	2.82E-01	5.65E+00
32	3.10E-01	3.07E-01	3.13E-01	3.00E-01	3.00E-01	3.06E-01	3.00E-01	3.14E-01	4.77E+00
34	3.39E-01	3.35E-01	3.42E-01	3.26E-01	3.29E-01	3.35E-01	3.26E-01	3.42E-01	4.75E+00
36	3.64E-01	3.62E-01	3.67E-01	3.50E-01	3.54E-01	3.61E-01	3.50E-01	3.67E-01	4.82E+00
38	3.86E-01	3.85E-01	3.88E-01	3.71E-01	3.76E-01	3.83E-01	3.71E-01	3.88E-01	4.50E+00
40	4.04E-01	4.04E-01	4.07E-01	3.91E-01	3.96E-01	4.03E-01	3.91E-01	4.07E-01	4.03E+00
42	4.21E-01	4.21E-01	4.22E-01	4.09E-01	4.14E-01	4.20E-01	4.09E-01	4.22E-01	3.34E+00
44	4.34E-01	4.35E-01	4.36E-01	4.25E-01	4.30E-01	4.35E-01	4.25E-01	4.36E-01	2.46E+00
46	4.45E-01	4.46E-01	4.46E-01	4.39E-01	4.42E-01	4.47E-01	4.39E-01	4.47E-01	1.85E+00
48	4.54E-01	4.56E-01	4.55E-01	4.52E-01	4.53E-01	4.58E-01	4.51E-01	4.58E-01	1.51E+00
50	4.62E-01	4.64E-01	4.62E-01	4.63E-01	4.63E-01	4.66E-01	4.57E-01	4.66E-01	1.96E+00
52	4.68E-01	4.69E-01	4.68E-01	4.72E-01	4.73E-01	4.63E-01	4.62E-01	4.73E-01	2.32E+00
54	4.72E-01	4.73E-01	4.72E-01	4.80E-01	4.75E-01	4.75E-01	4.66E-01	4.80E-01	2.97E+00
56	4.75E-01	4.76E-01	4.75E-01	4.85E-01	4.76E-01	4.82E-01	4.69E-01	4.85E-01	3.55E+00
58	4.77E-01	4.78E-01	4.76E-01	4.90E-01	4.76E-01	4.85E-01	4.71E-01	4.90E-01	3.85E+00
60	4.79E-01	4.79E-01	4.78E-01	4.93E-01	4.77E-01	4.87E-01	4.74E-01	4.93E-01	4.02E+00
62	4.80E-01	4.81E-01	4.79E-01	4.96E-01	4.77E-01	4.87E-01	4.76E-01	4.96E-01	4.11E+00
64	4.81E-01	4.81E-01	4.80E-01	4.97E-01	4.77E-01	4.87E-01	4.76E-01	4.97E-01	4.28E+00
66	4.81E-01	4.81E-01	4.79E-01	4.97E-01	4.77E-01	4.86E-01	4.77E-01	4.97E-01	4.19E+00
68	4.80E-01	4.81E-01	4.79E-01	4.97E-01	4.76E-01	4.84E-01	4.76E-01	4.97E-01	4.24E+00
70	4.80E-01	4.80E-01	4.78E-01	4.95E-01	4.75E-01	4.82E-01	4.75E-01	4.95E-01	4.12E+00
72	4.79E-01	4.80E-01	4.78E-01	4.93E-01	4.75E-01	4.80E-01	4.75E-01	4.93E-01	3.90E+00
74	4.78E-01	4.79E-01	4.77E-01	4.91E-01	4.74E-01	4.78E-01	4.74E-01	4.91E-01	3.59E+00
76	4.77E-01	4.77E-01	4.75E-01	4.88E-01	4.73E-01	4.75E-01	4.73E-01	4.88E-01	3.23E+00
78	4.75E-01	4.75E-01	4.73E-01	4.84E-01	4.71E-01	4.72E-01	4.71E-01	4.84E-01	2.80E+00
80	4.74E-01	4.73E-01	4.71E-01	4.80E-01	4.69E-01	4.70E-01	4.69E-01	4.80E-01	2.35E+00
82	4.71E-01	4.70E-01	4.69E-01	4.76E-01	4.67E-01	4.66E-01	4.66E-01	4.76E-01	1.99E+00
84	4.69E-01	4.68E-01	4.67E-01	4.72E-01	4.65E-01	4.64E-01	4.64E-01	4.73E-01	2.03E+00
86	4.67E-01	4.66E-01	4.64E-01	4.68E-01	4.63E-01	4.61E-01	4.61E-01	4.71E-01	1.98E+00
88	4.65E-01	4.63E-01	4.62E-01	4.64E-01	4.62E-01	4.59E-01	4.59E-01	4.68E-01	1.92E+00
90	4.63E-01	4.61E-01	4.60E-01	4.61E-01	4.60E-01	4.57E-01	4.57E-01	4.66E-01	1.77E+00
92	4.61E-01	4.59E-01	4.58E-01	4.58E-01	4.58E-01	4.56E-01	4.56E-01	4.63E-01	1.59E+00
94		4.57E-01	4.56E-01	4.55E-01	4.56E-01	4.55E-01	4.55E-01	4.61E-01	1.37E+00
96		4.55E-01	4.53E-01	4.53E-01	4.54E-01	4.53E-01	4.53E-01	4.58E-01	1.25E+00
98		4.53E-01	4.52E-01	4.52E-01	4.53E-01	4.52E-01	4.52E-01	4.53E-01	2.88E-01

Table B.12: Semi-empirical and empirical K-M_2 fluorescence yield values

Z	Bambynek 1972 ,Salem	Krause 1979 ,Salem	Bambynek 1984 ,Salem	NIST ,Salem	Kahoul 2012 ,Salem	Daoudi 2015 ,Salem	Min	Max	$\Delta\omega_{K\text{-}M_2}$
12	9.99E-04	1.13E-03	1.10E-03	9.81E-04	8.79E-04	8.71E-04	8.71E-04	1.13E-03	2.60E+01
14	1.80E-03	1.92E-03	1.94E-03	1.65E-03	1.66E-03	1.67E-03	1.65E-03	1.94E-03	1.58E+01
16	2.98E-03	3.05E-03	3.15E-03	2.78E-03	3.12E-03	2.87E-03	2.78E-03	3.15E-03	1.24E+01
18	4.59E-03	4.70E-03	4.78E-03	4.35E-03	4.97E-03	4.53E-03	2.81E-03	4.97E-03	5.55E+01
20	6.62E-03	6.62E-03	6.85E-03	5.96E-03	6.24E-03	6.58E-03	5.06E-03	6.85E-03	3.00E+01
22	9.04E-03	8.83E-03	9.31E-03	8.99E-03	8.62E-03	8.86E-03	7.26E-03	9.31E-03	2.48E+01
24	1.18E-02	1.15E-02	1.21E-02	1.20E-02	1.13E-02	1.16E-02	9.52E-03	1.21E-02	2.38E+01
26	1.48E-02	1.45E-02	1.51E-02	1.49E-02	1.43E-02	1.46E-02	1.22E-02	1.51E-02	2.11E+01
28	1.79E-02	1.75E-02	1.82E-02	1.78E-02	1.73E-02	1.77E-02	1.48E-02	1.82E-02	2.05E+01
30	2.10E-02	2.08E-02	2.13E-02	2.06E-02	2.03E-02	2.07E-02	1.74E-02	2.13E-02	2.02E+01
32	2.40E-02	2.38E-02	2.43E-02	2.33E-02	2.32E-02	2.37E-02	2.07E-02	2.43E-02	1.59E+01
34	2.68E-02	2.64E-02	2.70E-02	2.58E-02	2.59E-02	2.65E-02	2.38E-02	2.70E-02	1.28E+01
36	2.92E-02	2.91E-02	2.95E-02	2.81E-02	2.84E-02	2.90E-02	2.66E-02	2.95E-02	1.01E+01
38	3.15E-02	3.14E-02	3.17E-02	3.03E-02	3.07E-02	3.13E-02	2.94E-02	3.21E-02	8.73E+00
40	3.36E-02	3.36E-02	3.37E-02	3.24E-02	3.29E-02	3.34E-02	3.19E-02	3.46E-02	8.09E+00
42	3.55E-02	3.55E-02	3.57E-02	3.45E-02	3.49E-02	3.55E-02	3.43E-02	3.70E-02	7.59E+00
44	3.72E-02	3.73E-02	3.74E-02	3.65E-02	3.68E-02	3.73E-02	3.64E-02	3.91E-02	7.17E+00
46	3.88E-02	3.89E-02	3.89E-02	3.83E-02	3.86E-02	3.90E-02	3.83E-02	4.10E-02	6.86E+00
48	4.03E-02	4.05E-02	4.04E-02	4.01E-02	4.02E-02	4.06E-02	4.01E-02	4.27E-02	6.19E+00
50	4.17E-02	4.18E-02	4.17E-02	4.18E-02	4.17E-02	4.21E-02	4.17E-02	4.41E-02	5.67E+00
52	4.28E-02	4.29E-02	4.28E-02	4.32E-02	4.33E-02	4.23E-02	4.23E-02	4.53E-02	6.85E+00
54	4.38E-02	4.39E-02	4.38E-02	4.45E-02	4.41E-02	4.41E-02	4.38E-02	4.64E-02	5.79E+00
56	4.47E-02	4.48E-02	4.47E-02	4.57E-02	4.48E-02	4.53E-02	4.47E-02	4.74E-02	5.83E+00
58	4.56E-02	4.56E-02	4.55E-02	4.68E-02	4.55E-02	4.63E-02	4.55E-02	4.84E-02	6.19E+00
60	4.64E-02	4.64E-02	4.63E-02	4.78E-02	4.62E-02	4.71E-02	4.62E-02	4.93E-02	6.58E+00
62	4.71E-02	4.72E-02	4.71E-02	4.87E-02	4.69E-02	4.79E-02	4.69E-02	5.01E-02	6.75E+00
64	4.80E-02	4.80E-02	4.79E-02	4.96E-02	4.76E-02	4.86E-02	4.76E-02	5.08E-02	6.43E+00
66	4.93E-02	4.94E-02	4.92E-02	5.10E-02	4.89E-02	4.98E-02	4.89E-02	5.15E-02	5.13E+00
68	5.09E-02	5.10E-02	5.07E-02	5.26E-02	5.04E-02	5.12E-02	5.03E-02	5.26E-02	4.54E+00
70	5.22E-02	5.23E-02	5.20E-02	5.39E-02	5.17E-02	5.24E-02	5.08E-02	5.39E-02	5.92E+00
72	5.33E-02	5.33E-02	5.31E-02	5.48E-02	5.27E-02	5.33E-02	5.13E-02	5.48E-02	6.74E+00
74	5.41E-02	5.42E-02	5.39E-02	5.56E-02	5.36E-02	5.41E-02	5.17E-02	5.56E-02	7.21E+00
76	5.48E-02	5.49E-02	5.46E-02	5.61E-02	5.43E-02	5.46E-02	5.21E-02	5.61E-02	7.40E+00
78	5.53E-02	5.53E-02	5.51E-02	5.64E-02	5.48E-02	5.50E-02	5.25E-02	5.64E-02	7.20E+00
80	5.57E-02	5.57E-02	5.54E-02	5.65E-02	5.52E-02	5.52E-02	5.26E-02	5.65E-02	7.26E+00
82	5.59E-02	5.59E-02	5.56E-02	5.65E-02	5.54E-02	5.54E-02	5.28E-02	5.65E-02	6.75E+00
84	5.61E-02	5.60E-02	5.58E-02	5.64E-02	5.57E-02	5.55E-02	5.31E-02	5.64E-02	6.06E+00
86	5.63E-02	5.61E-02	5.60E-02	5.64E-02	5.59E-02	5.56E-02	5.32E-02	5.64E-02	5.78E+00
88	5.64E-02	5.62E-02	5.61E-02	5.63E-02	5.60E-02	5.57E-02	5.33E-02	5.64E-02	5.64E+00
90	5.67E-02	5.64E-02	5.63E-02	5.64E-02	5.63E-02	5.60E-02	5.34E-02	5.67E-02	5.99E+00
92	5.68E-02	5.66E-02	5.65E-02	5.64E-02	5.64E-02	5.62E-02	5.34E-02	5.68E-02	6.12E+00
94		5.68E-02	5.66E-02	5.65E-02	5.67E-02	5.64E-02	5.34E-02	5.68E-02	6.04E+00
96		5.70E-02	5.69E-02	5.68E-02	5.69E-02	5.67E-02	5.34E-02	5.70E-02	6.46E+00
98		5.71E-02	5.69E-02	5.70E-02	5.70E-02	5.69E-02	5.69E-02	5.71E-02	2.88E-01

Table B.13: Semi-empirical and empirical K-M_3 fluorescence yield values

Z	Bambynek 1972 ,Salem	Krause 1979 ,Salem	Bambynek 1984 ,Salem	NIST ,Salem	Kahoul 2012 ,Salem	Daoudi 2015 ,Salem	Min	Max	$\Delta\omega_{\text{K-M}_3}$
12	1.93E-03	2.18E-03	2.12E-03	1.89E-03	1.70E-03	1.68E-03	1.68E-03	2.18E-03	2.60E+01
14	3.48E-03	3.71E-03	3.74E-03	3.19E-03	3.21E-03	3.22E-03	3.19E-03	3.74E-03	1.58E+01
16	5.74E-03	5.90E-03	6.08E-03	5.37E-03	6.02E-03	5.55E-03	5.37E-03	6.08E-03	1.24E+01
18	8.85E-03	9.08E-03	9.23E-03	8.39E-03	9.60E-03	8.74E-03	5.56E-03	9.60E-03	5.33E+01
20	1.28E-02	1.28E-02	1.32E-02	1.15E-02	1.20E-02	1.27E-02	1.00E-02	1.32E-02	2.77E+01
22	1.74E-02	1.70E-02	1.80E-02	1.74E-02	1.66E-02	1.71E-02	1.43E-02	1.80E-02	2.25E+01
24	2.27E-02	2.22E-02	2.33E-02	2.31E-02	2.19E-02	2.25E-02	1.88E-02	2.33E-02	2.17E+01
26	2.85E-02	2.79E-02	2.91E-02	2.88E-02	2.76E-02	2.82E-02	2.40E-02	2.91E-02	1.93E+01
28	3.45E-02	3.39E-02	3.51E-02	3.44E-02	3.34E-02	3.41E-02	2.90E-02	3.51E-02	1.90E+01
30	4.05E-02	4.01E-02	4.11E-02	3.97E-02	3.92E-02	4.01E-02	3.40E-02	4.11E-02	1.89E+01
32	4.64E-02	4.59E-02	4.69E-02	4.49E-02	4.49E-02	4.58E-02	4.05E-02	4.69E-02	1.46E+01
34	5.16E-02	5.10E-02	5.22E-02	4.97E-02	5.01E-02	5.11E-02	4.64E-02	5.26E-02	1.25E+01
36	5.64E-02	5.61E-02	5.69E-02	5.42E-02	5.49E-02	5.60E-02	5.20E-02	5.74E-02	9.99E+00
38	6.08E-02	6.07E-02	6.12E-02	5.85E-02	5.93E-02	6.04E-02	5.73E-02	6.27E-02	9.05E+00
40	6.48E-02	6.48E-02	6.51E-02	6.26E-02	6.35E-02	6.45E-02	6.22E-02	6.76E-02	8.37E+00
42	6.85E-02	6.86E-02	6.88E-02	6.66E-02	6.75E-02	6.85E-02	6.66E-02	7.22E-02	8.12E+00
44	7.19E-02	7.20E-02	7.21E-02	7.04E-02	7.11E-02	7.20E-02	7.04E-02	7.63E-02	8.02E+00
46	7.49E-02	7.51E-02	7.51E-02	7.39E-02	7.45E-02	7.53E-02	7.39E-02	7.99E-02	7.74E+00
48	7.76E-02	7.79E-02	7.78E-02	7.73E-02	7.75E-02	7.82E-02	7.73E-02	8.30E-02	7.14E+00
50	8.03E-02	8.05E-02	8.03E-02	8.04E-02	8.04E-02	8.10E-02	8.03E-02	8.57E-02	6.54E+00
52	8.26E-02	8.28E-02	8.26E-02	8.33E-02	8.34E-02	8.17E-02	8.17E-02	8.80E-02	7.47E+00
54	8.45E-02	8.48E-02	8.45E-02	8.59E-02	8.50E-02	8.50E-02	8.45E-02	9.00E-02	6.32E+00
56	8.63E-02	8.65E-02	8.63E-02	8.82E-02	8.64E-02	8.75E-02	8.63E-02	9.18E-02	6.24E+00
58	8.80E-02	8.81E-02	8.79E-02	9.03E-02	8.78E-02	8.94E-02	8.78E-02	9.36E-02	6.45E+00
60	8.95E-02	8.96E-02	8.94E-02	9.22E-02	8.91E-02	9.10E-02	8.91E-02	9.54E-02	6.84E+00
62	9.10E-02	9.12E-02	9.09E-02	9.40E-02	9.05E-02	9.24E-02	9.05E-02	9.70E-02	6.94E+00
64	9.17E-02	9.18E-02	9.15E-02	9.49E-02	9.10E-02	9.29E-02	9.10E-02	9.82E-02	7.61E+00
66	9.51E-02	9.52E-02	9.48E-02	9.83E-02	9.43E-02	9.60E-02	9.43E-02	9.96E-02	5.48E+00
68	9.80E-02	9.82E-02	9.77E-02	1.01E-01	9.71E-02	9.87E-02	9.71E-02	1.01E-01	4.24E+00
70	1.00E-01	1.01E-01	1.00E-01	1.04E-01	9.95E-02	1.01E-01	9.81E-02	1.04E-01	5.49E+00
72	1.03E-01	1.03E-01	1.02E-01	1.06E-01	1.02E-01	1.03E-01	9.90E-02	1.06E-01	6.54E+00
74	1.04E-01	1.04E-01	1.04E-01	1.07E-01	1.03E-01	1.04E-01	9.99E-02	1.07E-01	6.85E+00
76	1.05E-01	1.06E-01	1.05E-01	1.08E-01	1.05E-01	1.05E-01	1.01E-01	1.08E-01	7.00E+00
78	1.06E-01	1.06E-01	1.06E-01	1.08E-01	1.05E-01	1.06E-01	1.01E-01	1.08E-01	6.63E+00
80	1.07E-01	1.07E-01	1.06E-01	1.09E-01	1.06E-01	1.06E-01	1.02E-01	1.09E-01	6.46E+00
82	1.07E-01	1.07E-01	1.07E-01	1.08E-01	1.06E-01	1.06E-01	1.02E-01	1.08E-01	5.80E+00
84	1.07E-01	1.07E-01	1.07E-01	1.08E-01	1.07E-01	1.06E-01	1.03E-01	1.08E-01	4.77E+00
86	1.08E-01	1.07E-01	1.07E-01	1.08E-01	1.07E-01	1.06E-01	1.03E-01	1.08E-01	4.08E+00
88	1.08E-01	1.07E-01	1.07E-01	1.07E-01	1.07E-01	1.06E-01	1.04E-01	1.08E-01	3.66E+00
90	1.08E-01	1.07E-01	1.07E-01	1.07E-01	1.07E-01	1.06E-01	1.04E-01	1.08E-01	3.35E+00
92	1.08E-01	1.07E-01	1.07E-01	1.07E-01	1.07E-01	1.06E-01	1.04E-01	1.08E-01	3.05E+00
94	0.00E+00	1.07E-01	1.07E-01	1.07E-01	1.07E-01	1.07E-01	1.05E-01	1.07E-01	2.40E+00
96	0.00E+00	1.07E-01	1.07E-01	1.07E-01	1.07E-01	1.07E-01	1.05E-01	1.08E-01	2.35E+00
98	0.00E+00	1.07E-01	1.07E-01	1.07E-01	1.07E-01	1.07E-01	1.07E-01	1.07E-01	2.88E-01